



HAL
open science

Modeling and Design of Passive Planar Components for EMI Filters

Wenhua Tan

► **To cite this version:**

Wenhua Tan. Modeling and Design of Passive Planar Components for EMI Filters. Other. Ecole Centrale de Lille, 2012. English. NNT : 2012ECLI0026 . tel-00776515

HAL Id: tel-00776515

<https://theses.hal.science/tel-00776515v1>

Submitted on 15 Jan 2013

HAL is a multi-disciplinary open access archive for the deposit and dissemination of scientific research documents, whether they are published or not. The documents may come from teaching and research institutions in France or abroad, or from public or private research centers.

L'archive ouverte pluridisciplinaire **HAL**, est destinée au dépôt et à la diffusion de documents scientifiques de niveau recherche, publiés ou non, émanant des établissements d'enseignement et de recherche français ou étrangers, des laboratoires publics ou privés.

N° d'ordre: 205

ECOLE CENTRALE DE LILLE

THESE

présentée en vue d'obtenir le grade de

DOCTEUR

en

Génie Electrique

par

Wenhua TAN

DOCTORAT DELIVRE PAR L'ECOLE CENTRALE DE LILLE

**Modeling and Design of Passive Planar
Components for EMI Filters**

**Modélisation et Conception des Composants
Passifs Planar pour Filtres CEM**

Soutenue le 30 novembre 2012 devant le jury :

Président	François Forest, <i>Professeur des universités, IES – Université de Montpellier 2</i>
Rapporteur	Eric Labouré, <i>Professeur des universités, LGEP – Université de Paris SUD 11</i>
Rapporteur	Jean-Luc Schanen, <i>Professeur des universités, G2ELab – Grenoble INP</i>
Examineur	Ambroise Schellmanns, <i>Maître de conférences, LMP – Université de Tours</i>
Examineur	Christian Martin, <i>Maître de conférences, Ampère – Université de Lyon 1</i>
Directeur de thèse	Nadir Idir, <i>Professeur des universités, L2EP – Université de Lille 1</i>
Co-encadrant de thèse	Xavier Margueron, <i>Maître de conférences, L2EP – Ecole Centrale de Lille</i>

Thèse préparée au Laboratoire d'Electrotechnique et d'Electronique de Puissance (L2EP)

Ecole Doctorale SPI 072

PRES – Université Lille Nord-de-France

Abstract

The high switching frequency of power converters makes the electromagnetic interferences (EMI) a critical problem for engineers. EMI filter are thus widely implemented in electronic systems for the compliance with stringent electromagnetic compatibility (EMC) standards. Meanwhile, due to the pursuit of the integration and miniaturization of systems, planar magnetic components become a promising technology for future power electronics and gain a growing application area, including their applications in EMI filters.

To use a component, reliable model are necessary. In particular for the planar magnetic components dedicated to EMI applications, effective models containing all the parasitic elements can help the designers to predict the high frequency performances of the filters using these planar components. However, the existing research work on this topic seems very limited, which becomes the motivation of this PhD work. Therefore, a major part of this dissertation attempts to study several important modeling aspects of the planar inductor (or choke) for EMI filter applications.

The construction of the equivalent circuit for planar components in EMI filters via experimental approach is studied first. An improved model for planar common mode (CM) chokes is presented together with a systematic procedure for parameter extraction based on impedance measurements and fitting algorithm. Detailed explanation and experimental tests are given for validating the model and the extraction procedure.

Next, the modeling of parasitic capacitances through theoretical approach is explored. An analytical procedure based on electric field decomposition (EFD) method and energy approach is introduced. The EFD method analyzes the 2D capacitance matrix for the PCB structures of studied planar components. The influence of ferrite core is also considered by using simple formulation. Finally, an energy approach is applied for finding the equivalent parasitic capacitances of the component of interest.

In order to develop a tool that is more general and more adapted for computer calculation, the third part of this dissertation is dedicated to a semi-analytical 2D modeling method of the parasitic capacitances and leakage inductance of a planar CM choke. For the calculation of the parasitic capacitances, analytical multilayered Green's function is obtained to solve the Poisson's equations in electrostatic. The method of moment (MoM) is then employed to calculate the 2D capacitance matrix for the cross-section of the studied component. For calculating the leakage inductance, the multilayered Green's function method is extended for magnetostatic analysis. Numerical integration is then implemented for obtaining the information on the magnetic field. Both of these methods are verified by simulation results.

Apart from the modeling, this PhD work also proposes two conceptions for EMI filter design. The first one consists in an improved parasitic capacitance cancellation technique using structural parasitic elements. The second conception introduces the association of two magnetic cores with different materials and geometries to realize a compact common mode (CM) and differential mode (DM) choke for EMI filtering.

Keywords:

- Analytical modeling
- Common-mode choke
- Electromagnetic interference filter
- Equivalent circuit
- Integration
- Leakage inductance
- Parasitic capacitance
- Planar component

Résumé

L'utilisation de composants actifs, de plus en plus rapides et performants laisse entrevoir un renouveau à venir de l'Electronique de Puissance (EP) en termes d'application, d'efficacité et de compacité. Ces nets progrès entraînent deux tendances qu'il faut être capable de maîtriser pour concevoir des convertisseurs « optimaux » sur différents critères.

La première tendance est liée au comportement électromagnétique des structures de puissance. En effet, les convertisseurs d'électronique de puissance (EP) sont naturellement sources de perturbations électromagnétiques qui sont aggravées en raison de l'utilisation de fréquences de découpage élevées. Cette tendance impose des contraintes fortes en termes de Compatibilité Electromagnétique (CEM) des équipements envers leur environnement, qui doivent être prises en compte par les ingénieurs dès la phase de conception des convertisseurs. Différentes solutions peuvent ainsi être mises en œuvre afin d'atténuer ces perturbations électromagnétiques, parmi lesquelles les filtres CEM sont une des solutions les plus pratiques et les plus fiables.

La seconde tendance vise à miniaturiser et à intégrer les systèmes et, par la même, les composants. Concernant les composants magnétiques, la technologie planar semble être une solution très prometteuse en termes d'encombrement pour l'électronique de puissance du futur car elle permet de réduire les dimensions des composants passifs et ainsi, d'augmenter la densité de puissance. L'utilisation de composants planar en EP se développe depuis quelques années pour réaliser des systèmes très compacts et peut être envisagée, à terme, pour les filtres CEM.

Afin d'utiliser un composant dans les meilleures conditions possibles, des modèles fiables sont toujours nécessaires. En particulier concernant les aspects CEM, des modèles prenant en compte tous les éléments parasites (capacités parasites, inductance de fuite et couplages magnétiques parasites) sont très utiles, puisqu'ils permettent la prévision des performances en haute fréquence (HF) des filtres. Les modèles appliqués aux composants magnétiques planar, sont souvent

limités et peu développés dans la littérature scientifique. Par conséquent, une grande partie de cette thèse est dédiée à l'étude de plusieurs aspects importants de la modélisation des éléments parasites des inductances (ou inductances couplées) planar pour les filtres CEM. Pour ces modélisations, deux principales approches seront utilisées ; la première étant une méthode expérimentale via des mesures, tandis que la seconde est basée sur des méthodes théoriques via des analyses mathématiques et physiques. Le manuscrit de cette thèse est découpé en cinq chapitres, de l'étude bibliographique aux applications innovantes.

Après un premier chapitre dédié à la présentation des problématiques et à une analyse bibliographique des différents thèmes traités, le second chapitre se focalise sur la construction de circuits équivalents pour les composants planar, utilisés dans les filtres CEM, par une approche expérimentale. Les méthodes traditionnellement utilisées pour élaborer des circuits équivalents, sont basées sur l'observation des résultats de mesures associée à un processus d'ajustement manuel des valeurs des éléments du schéma équivalent. Ce dernier exige beaucoup d'essais à réaliser et d'itérations de type essais/erreurs pour obtenir une précision satisfaisante pour le modèle obtenu. Afin d'éviter ces inconvénients, un modèle amélioré pour les inductances de mode commun (MC) a été donc proposé avec une procédure systématique d'identification des paramètres du modèle. Cette méthode est basée sur des mesures d'impédances associées à un algorithme de fitting par approximation itérative de fonctions rationnelles (IRFA). Cet algorithme provient de l'algorithme RFA originalement développé pour extraire des modèles de type « boîte-noire » pour les interconnexions en micro-électronique. Dans ce travail de thèse, cette méthode a donc été améliorée en s'aidant de l'itération « Sanathanan-Koerner » pour résoudre le problème du déséquilibre fréquentiel de fitting. En conséquence, la procédure introduite permet d'obtenir un modèle précis sur une large bande fréquentielle. Cette méthode est donc détaillée dans ce premier chapitre et des essais expérimentaux sont présentés afin de valider le modèle et la procédure d'identification IRFA.

Par la suite, la modélisation des capacités parasites des composants planar, via une approche théorique, est examinée. Une procédure analytique, basée sur la méthode de décomposition de champ électrique (DCE) combinée à une approche

énergétique, est proposée. La méthode DCE, couplée à une combinaison de résultats issus de la transformation conforme, permet d'effectuer des analyses en 2D des structures de type PCB (circuit imprimé) en utilisant quelques principes de décompositions en capacités élémentaires. Des formules assez précises peuvent ainsi être déduites pour calculer la matrice des capacités de la structure PCB étudiée. Par ailleurs, l'influence du noyau magnétique est également investiguée à l'aide d'une technique simple de transformation, qui suppose une équivalence entre un noyau magnétique et un noyau en conducteur électrique parfait (CEP). La validité des formules proposées ainsi que la technique de transformation sont vérifiées par des comparaisons de résultats sur différentes structures avec des simulations éléments finis. Enfin, une approche énergétique est mise en œuvre pour évaluer les capacités parasites équivalentes des composants planar. En décomposant les enroulements du composant planar en segments indépendants, l'énergie électrique stockée est calculée à partir de la matrice de capacités de la section du composant et la distribution du potentiel sur les enroulements. Cette procédure est validée par des résultats de mesures d'impédances sur trois exemples : inductance à 8 spires sans noyau magnétique, inductance à 8 spires avec noyau magnétique et inductance de MC à 8 spires.

Devant les limitations obtenues par la méthode EFD, et afin de développer un outil plus général et plus adapté aux calculs et optimisations de composants planar, le quatrième chapitre de cette thèse est consacré à l'étude d'une méthode semi-analytique de modélisation en 2D des capacités parasites et de l'inductance de fuite d'une inductance de MC. Pour calculer ces capacités parasites dans le cas d'un composant planar possédant une structure de PCB en multicouche, la fonction de Green multicouche, appliquée avec des conditions aux limites de type Dirichlet, est mise en œuvre en vue de résoudre l'équation de Poisson en électrostatique pour la partie d'enroulement dans le noyau magnétique. La Méthode des Moments (MoM) à collocation des points est alors appliquée pour déduire la matrice des capacités en 2D de la section transversale du composant étudié. Une approximation est mise en place pour déduire la matrice de capacités pour la partie de l'enroulement en dehors du noyau magnétique. Avec ces matrices de capacités calculées, l'approche d'énergie présentée dans le chapitre 3 peut de nouveau être appliquée pour évaluer les valeurs

des capacités parasites du composant. Cette méthode a été programmée avec le logiciel Matlab et les résultats obtenus démontrent une bonne cohérence avec les simulations éléments finis.

Après l'aspect capacitif, la deuxième partie de ce chapitre s'intéresse au calcul de l'inductance de fuite. La méthode des fonctions de Green est ainsi étendue aux analyses en magnétostatique pour le calcul de l'inductance de fuite d'une inductance de MC où une couche composite de ferrite-polymère (CFP) est insérée. Une mesure particulière est introduite pour construire la fonction de Green multicouche pour les conditions aux limites de type Neumann du problème original. Une intégration numérique est ensuite couplée à la fonction de Green pour permettre d'obtenir des informations sur le champ magnétique dans la fenêtre d'un composant planar. Un programme Matlab a également été réalisé pour effectuer les calculs et les résultats ont été validés par les simulations éléments finis sur un exemple : une inductance de MC à 8 spires avec une couche de CFP.

En plus de ces aspects modélisation, deux conceptions innovantes autour des filtres CEM ont aussi été proposées. La première consiste en une technique permettant d'améliorer la compensation des capacités parasites des inductances de mode différentiel (MD). A la différence des méthodes de compensation existantes, qui nécessitent l'ajout de composants supplémentaires, la technique développée ici utilise les capacités parasites structurales pour améliorer la robustesse et réduire le coût des composants. Cette compensation « optimale » se base sur les principes et les méthodes introduits au chapitre 3 pour le calcul des capacités parasites par la méthode de type EFD. Des mesures ont été réalisées afin de démontrer les avantages de cette technique de compensation.

La seconde conception consiste à réaliser une inductance de MC et de MD compacte pour le filtrage CEM, en associant deux noyaux magnétiques différents. Un noyau torique en nanocristallin, bobiné comme une inductance classique de MC est implémentée dans un noyau planar en ferrite. Ce dernier a pour objectif d'augmenter l'inductance de fuite de l'inductance de MC et de diminuer les couplages parasites existants envers son environnement. Des essais comparatifs en conditions réelles montrent que le composant proposé est une solution très intéressante pour l'intégration des filtres CEM.

Une synthèse des travaux réalisés est présentée en guise de conclusion et des perspectives sont listées pour ouvrir le champ à de futurs travaux.

Mots-clés :

- Modélisation analytique
- Inductance de mode commun
- Filtre compatibilité électromagnétique
- Circuit équivalent
- Intégration
- Inductance de fuite
- Capacité parasite
- Composant planar

Table of Contents

Abstract	3
Résumé.....	5
Table of Contents	11
List of Figures	15
List of Tables.....	20
General Introduction	23
Scope of the Work	23
Organization of the Dissertation	25
Chapter 1. Introduction.....	29
1.1 EMI in Power Electronics.....	29
1.1.1 EMI Sources in Power Electronics.....	29
1.1.2 EMC Standards and Conducted EMI Measurements.....	30
1.2 Power Line EMI Filters.....	32
1.2.1 Overview	32
1.2.2 Passive EMI Filters	33
1.2.3 Technologies for Passive EMI Filters.....	36
1.2.4 Design of Planar EMI Filters.....	39
1.3 Modeling of Planar EMI Filters.....	40
1.3.1 Global View of the Modeling Issue	40
1.3.2 Experimental Modeling Methods	42
1.3.3 Analytical Methods	43
1.4 Conclusion.....	46
Chapter 2. Experimental Modeling of CM Chokes.....	49
2.1 HF Equivalent Circuits of CM Chokes	49
2.1.1 Brief Review of Existing Models	49
2.1.2 Equivalent Circuit Model for CM Chokes with More Physical Meanings.....	51
2.1.3 Introduction to the Developed Modeling Method.....	53
2.2 Iterative Rational Function Approximation Approach.....	53
2.2.1 Reminder on Rational Functions	53
2.2.2 Rational Function Approximation	54
2.2.3 Introduction of Iterative Rational Function Approximation Method	57
2.3 IRFA Adapted Equivalent Circuit Synthesis.....	60
2.3.1 Foster Expansion General Expression.....	61

2.3.2	General Topology and Terms d and e 's	61
2.3.3	Real Pole-Residue Terms.....	61
2.3.4	Complex Pole-Residue Pair Terms	63
2.4	Complete Identification Process.....	65
2.4.1	Improved HF Equivalent Circuit Model	65
2.4.2	General Parameter Extraction Procedure	66
2.4.3	Application Example	68
2.5	Experimental Validations	75
2.5.1	Impedance Measurements and Sensitivity Analysis	75
2.5.2	Insertion Loss Measurements.....	77
2.6	Discussion.....	78
2.7	Conclusion.....	81
Chapter 3.	Analytical Modeling of Parasitic Capacitances of Planar Components.....	85
3.1	Review of Analytical Methods for Parasitic Capacitances Modeling	85
3.1.1	Plate Capacitance Formula and Other Empirical Formulas.....	85
3.1.2	Conformal Mapping.....	87
3.2	Electric Field Decomposition Method	90
3.2.1	Overview of EFD Method.....	90
3.2.2	Field-Based Stray Capacitance Modeling.....	91
3.3	Parasitic Capacitance Analysis of Planar Components based on EFD.....	95
3.3.1	Basic Structures	95
3.3.2	Configuration of PCB Structure with Six Conductors	99
3.3.3	Numerical Validation.....	105
3.3.4	Configuration of PCB structure with Eight Conductors	105
3.4	Influence of Ferrite Core.....	106
3.4.1	Permittivity of Ferrite Core	106
3.4.2	Perfect Electric Conductor	107
3.4.3	Transformation Technique for Handling Floating PEC Core.....	109
3.4.4	Combination of EFD Method and Transformation Technique.....	111
3.5	Energy Approach.....	115
3.5.1	Derivation of Self-parasitic Capacitance	116
3.5.2	Calculation of Electric Energy in a Single Port Component	117
3.5.3	Procedure for Calculating the Parasitic Capacitances of Planar CM Chokes 120	
3.6	Applications	121
3.6.1	Planar Inductor without Ferrite Core.....	122
3.6.2	Planar Inductor with Ferrite Core.....	123

3.6.3	Planar CM Choke with Ferrite Core	126
3.7	Discussion.....	129
3.8	Conclusion.....	130
Chapter 4.	Modeling of Parasitic Elements of Planar CM Choke via Multilayered Green's Function	135
4.1	Green's Function Theory.....	135
4.1.1	Introduction to Green's Function	135
4.1.2	2D Green's Function for Homogenous Space	137
4.2	Parasitic Capacitance Calculation Using Multilayered Green's Function.....	138
4.2.1	Declaration of Problem: PCB Structure with Ferrite Core	138
4.2.2	Multilayered Green's Function for Rectangular Region	140
4.2.3	Numerical Stability of the Green's Function.....	142
4.2.4	Moment Method for Calculating the Capacitance Matrix.....	144
4.2.5	Numerical Validation.....	147
4.2.6	Applications on Planar Components.....	149
4.2.7	Discussion.....	150
4.3	Static Leakage Inductance Calculation Using Multilayered Green's Function....	153
4.3.1	Energy Base Method for Calculating Static Leakage Inductance	153
4.3.2	Review of Existing Methods	154
4.3.3	Multilayered Green's Function in Magnetostatic	155
4.3.4	Application on Planar CM Choke with FPC Leakage Layer.....	164
4.3.5	Discussion.....	165
4.4	Conclusion.....	166
Chapter 5.	Designs of Planar Components for EMI Filters.....	171
5.1	Improved Parasitic Capacitance Cancellation with Planar Components	171
5.1.1	Overview of Parasitic Capacitance Cancellation Techniques.....	172
5.1.2	Improved Parasitic Capacitance Cancellation for Planar DM Chokes.....	176
5.1.3	Experimental Validations	179
5.1.4	Discussion.....	181
5.2	Toroid-EQ Mixed Structured CM Choke.....	183
5.2.1	Review of Integration Techniques of CM and DM Chokes.....	183
5.2.2	Design of the Toroid-EQ CM Choke.....	185
5.2.3	Experimental Validations and Discussion	191
5.2.4	Discussion.....	193
5.3	Conclusion.....	194
Conclusion and Perspectives.....		199
Realized Work		199

Future Work.....	201
Appendix.....	207
Appendix I. Householder Transformation	207
Appendix II. Derivation of (2.16)-(2.17)	209
Appendix III. Derivation of Eq.(3.5)	210
III.1 Elliptic Integral of the First Kind	210
III.2 Demonstration of (3.4) and (3.5).....	211
Appendix IV. Derivation of (3.45)	212
Appendix V. Derivation of Multilayered Green's Function for Electrostatic	213
V.1 General Solution by Separation of Variable.....	213
V.2 Derivation of (4.16)-(4.19).....	214
Appendix VI. Derivation of Multilayered Green's Function for Magnetostatic.....	216
References.....	221
Remerciements	227

List of Figures

Figure 1.1. EMI sources in power converters. (a) Buck converter. (b) Switching wave forms.	30
Figure 1.2. Conducted emission measurement. (a) Measurement setup. (b) Circuit of LISN.	31
Figure 1.3. HF conducted emission levels defined by CISPR 22 [7].....	32
Figure 1.4. CM and DM conducted noise in a single phase application.....	32
Figure 1.5. Typical EMI filter. (a) Schematic. (b) Photo of an example.	34
Figure 1.6. Definition of insertion loss. (a) Without EMI filter. (b) With EMI filter.	35
Figure 1.7. Insertion loss of a LC low pass filter. (a) Ideal filter. (b) Realistic filter with parasitic elements. (c) Comparison of the IL of the two cases.....	35
Figure 1.8. HF models proposed in literature. (a) Modal Model for CM chokes [28]. (b) DM EMI Filter Model Containing Parasitic Elements [29].....	43
Figure 1.9. HF model for CM choke [30]. (a) Toroidal CM choke under study. (b) Equivalent circuit.	43
Figure 1.10. Parasitic capacitance calculation. (a) Winding structure. (b) Cross-section view of conductors. (c) Plate capacitance model.	45
Figure 1.11. PEEC-like methods for calculating leakage inductance [39]. (a) Rectangular conductor. (b) Transformer window with two rectangular conductors. (c) Image methods.	46
Figure 2.1. Equivalent circuit models of CM chokes. (a) Simplified circuit presentation. (b) Model used in [56]. (c) Model used in [33].....	50
Figure 2.2. HF equivalent circuit of CM chokes proposed in [30]. (a) Equivalent circuit. (b) Circuit of Z_2 . (c) Circuit of Z_1	51
Figure 2.3. Different measurement configurations used for the parameter identification. (a) T_0 . (b) T_1 . (c) T_2 . (d) T_3 . (e) T_4	51
Figure 2.4. Algorithm of the IRFA method.....	59
Figure 2.5. Impedance measurements for the IRFA method. (a) 8-turn planar inductor. (b) HP4294A impedance analyzer.....	59
Figure 2.6. Comparison of the fitting results. (a) RFA with frequency bias problem. (b) IRFA without balanced weighting. (c) Proposed IRFA with balanced weighting.....	60
Figure 2.7. Synthesized equivalent circuit from rational functions. (a) Impedance $Z(s)$. (b) Admittance $Y(s)$	64
Figure 2.8. Synthesized equivalent circuit for the 8-turn planar inductor. (a) Equivalent circuit with negative branches. (b) Equivalent circuit after transformation. (c) Comparison of simulated and measured impedances.....	64
Figure 2.9. Improved IRFA-based equivalent circuit.....	66
Figure 2.10. Planar CM choke under study.	67
Figure 2.11. Measured impedances for the identification. (a) Z_{T3} . (b) Z_{T0} . (c) Z_{T2}	67
Figure 2.12. Equivalent circuit for extracting the capacitance. (a) R - C in parallel. (b) R - C in parallel with ESL and ESR.....	69
Figure 2.13. Equivalent circuit for Z_{T0} . (a) Without approximation. (b) With approximation.	71

Figure 2.14. Comparison between simulation and measurement for Z_{T0} . (a) Impedance magnitude. (b) Real part.....	72
Figure 2.15. Comparison between simulation and measurement for Z_{T2} . (a) Impedance magnitude. (b) Real part.....	73
Figure 2.16. Equivalent circuit for Z_{T2}	74
Figure 2.17. Extracted equivalent circuit for the planar CM choke.....	74
Figure 2.18. Comparison between simulations and measurements. (a) Open circuit impedance Z_0 . (b) Short circuit impedance Z_{SC}	75
Figure 2.19. Circuit of Z_{T2} for sensitivity analysis.....	76
Figure 2.20. Sensitivity analysis results for Z_{T2}	76
Figure 2.21. Realized EMI filter for validation.....	78
Figure 2.22. Insertion loss measurement configuration. (a) Schematic. (b) Implementation.....	78
Figure 2.23. Insertion loss comparison between measurements and simulations. (a) CM. (b) DM.....	79
Figure 3.1. (a) Plate capacitor. (b) Uniform electric field between two electrodes.....	86
Figure 3.2. Conformal mapping of the simple example. (a) Original structure. (b) Simplified structure. (c) Mapping results in ω -plane. (d) Mapping results in φ -plane.....	88
Figure 3.3. Comparison of calculated and simulated results.....	89
Figure 3.4. Simulated equipotential lines of one conductor over ground plane.....	91
Figure 3.5. Electric field decomposition results.....	91
Figure 3.6. (a) Dimensions of the structure. (b) Electric field decomposition [37].....	93
Figure 3.7. Principle for EFD method. (a) Charge sharing. (b) Field shielding [37].....	94
Figure 3.8. (a) One vertical conductor over ground plane. (b) Two conductors side by side.....	96
Figure 3.9. Comparison of the results of conformal mapping and EFD.....	96
Figure 3.10. (a) Field decomposition for one conductor over ground plane. (b) The equivalent circuit for calculating the capacitance.....	97
Figure 3.11. Derived cases for one conductor over ground plane. (a) Two conductors face to face. (b) One conductor over ground plane with epoxy. (c) Two conductors face to face with epoxy.....	97
Figure 3.12. Comparison between calculation and FEM simulation. (a) One horizontal conductor over ground plane without epoxy ($W=4$ mm). (b) One horizontal conductor over ground plane with epoxy ($W=4$ mm, $\epsilon_r=5$).....	99
Figure 3.13. PCB structure with 6 conductors.....	100
Figure 3.14. Electric field decomposition for calculating C_{21} and C_{25} . (a) Exterior coupling. (b) Interior coupling.....	101
Figure 3.15. Electric field decomposition for calculating C_{21} and C_{25} ; terminal capacitances.....	101
Figure 3.16. Electric field decomposition for calculating C_{14} ; interior coupling.....	104
Figure 3.17. Electric field decomposition for calculating C_{14} ; terminal capacitance.....	104
Figure 3.18. FEM model for validation.....	105
Figure 3.19. PCB structure with 8 conductors.....	107
Figure 3.20. Decomposition of the configuration with 8 conductors.....	107
Figure 3.21. Measurement of the relative permittivity of ferrite material. (a) Agilent 16451B fixture. (b) Measurement results.....	108

Figure 3.22. Verification of the equivalent between ferrite core and PEC core. (a) PCB structure in ferrite core. (b) Simulation results for (a). (c) PCB structure in PEC core. (d) Simulation results for (c).	109
Figure 3.23. Treatment of PEC core. (a) Two conductors with grounded PEC core. (b) Two conductors with floating PEC core. (c) N conductors with floating PEC core (only the capacitances for conductors 1, 2, and 3 are drawn).....	109
Figure 3.24. Validation of the procedure for handling ferrite core. (a) Grounded PEC core. (b) Floating PEC core.	110
Figure 3.25. 6-conductor PCB structure in ferrite core. (a) Structure. (b) Decomposition of the field between conductors and the grounded PEC core: plate and terminal capacitances. (c) Decomposition of the field between the conductors and the grounded PEC core: fringe capacitance.	112
Figure 3.26. Simulation model for the 6-conductor PCB structure.....	116
Figure 3.27. Procedure to handle ferrite core.	116
Figure 3.28. (a) Variation of potential without core. (b) Variation of potential with core. (c) Variation of potential of a 2-turn inductor: with and without core.....	118
Figure 3.29. Example: 6-turn inductor without ferrite core. (a) 3D view. (b) Cross-section at the cut point. (c) Trace on the top layer. (d) Trace on the bottom layer.	120
Figure 3.30. The common length L_{ij} for segments i and j . (a) Segments i and j with different lengths. (b) Segments i and j not aligned.....	120
Figure 3.31. Winding structure of an 8-turn planar inductor generated in Matlab.....	121
Figure 3.32. Parasitic capacitances calculation for planar CM choke. (a) Equivalent circuit for planar CM choke. (b) Test configurations.	122
Figure 3.33. 8-turn planar inductor without ferrite core. (a) Component. (b) Cross-section. (c) Measured impedance.	123
Figure 3.34. 8-turn planar inductor with ferrite core. (a) Component. (b) Cross-section in the core.....	124
Figure 3.35. Transformation for handling the multilayered isolator.	124
Figure 3.36. Decomposition of the field between conductors and the PEC core: conductor 1 and conductor 6.....	124
Figure 3.37. Simulation of the 8-turn planar inductor. (a) Equivalent circuit for the ferrite core. (b) Equivalent circuit for simulation. (c) Comparison between simulation and measurement.	126
Figure 3.38. Decomposition of the field for conductor 5 and 6: (a) Cross-section in air. (b) Cross-section in core.	127
Figure 3.39. Planar CM choke under study. (a) Component. (b) Geometry models constructed in Matlab.....	128
Figure 3.40. Comparison between simulations and measurements for the CM choke. (a) Open-circuit impedance Z_0 . (b) Short-circuit impedance Z_{SC}	129
Figure 4.1. Dirac charge source in a rectangular region with homogenous Dirichlet B.C..	138
Figure 4.2. PCB structure in ferrite core. (a) Original problem. (b) Transformed Dirichlet B.C. problem.	139
Figure 4.3. Multilayered structure under study.....	140
Figure 4.4. Moment method by point collocation. (a) Discretized conductor with pulse-like charge density function. (b) Source point and verification point on the segment.	145
Figure 4.5. Test configuration with 4 conductors and 4 layers: (a) grounded PEC core; (b) ferrite core (unit: mm).....	147
Figure 4.6 Cross-section of the 8-turn planar inductor in the ferrite core.....	150

Figure 4.7. Effect of side wall.	151
Figure 4.8. Cross-section of the planar CM choke in the ferrite core.....	152
Figure 4.9. Planar CM choke with FPC leakage layer. (a) Top view (b) Cross-section (one magnetic window). (c) Cross-section for magnetostatic analysis.	156
Figure 4.10. Boundary conditions on the inner surface of the magnetic window.	157
Figure 4.11. 4-layer structure for Green’s function deduction. (a) Source point higher than FPC layer. (b) Source point lower than FPC Layer.	159
Figure 4.12. Calculation of the magnetic field. (a) Discretization along y -axis of the source conductor. (b) Analytical integration on the observation conductor-three cases	162
Figure 4.13. Test configurations for validation (unit: mm).	163
Figure 4.14. Comparison between calculated results and simulated results. (a) Before removing the constant. (b) After removing the constant.	163
Figure 4.15. Comparison between calculated results and simulated results for the test case. (a) Test cut 1: B_x . (b) Test cut 1: B_y . (c) Test cut 2: B_x . (d) Test cut 2: B_y	164
Figure 4.16. Cross-section of the studied planar CM choke.....	165
Figure 4.17. Comparison between calculated results and simulated results. (a) Test cut: B_x . (b) Test cut: B_y	165
Figure 5.1. Methods for reducing parasitic capacitances. (a) Staggered winding structure. (b) Alternating winding method: left-traditional winding; right-alternating winding.	172
Figure 5.2. Parasitic capacitance cancellation technique for CM chokes.....	172
Figure 5.3. Parasitic capacitance cancellation technique for DM inductors: method 1.	174
Figure 5.4. Parasitic capacitance cancellation technique for DM inductors: method 2.	175
Figure 5.5. Simulation results of the parasitic cancellation technique for DM inductors: method 2.	176
Figure 5.6. Equivalent circuit for DM chokes.....	177
Figure 5.7. Parasitic capacitance cancellation for planar DM choke. (a) Realized DM choke. (b) Cross-section without core. (c) Cross-section with core.....	178
Figure 5.8. Calculated variation of the capacitances. (a) Without ferrite core. (b) With ferrite core.	179
Figure 5.9. Test setup for the cancellation. (a) Schematic. (b) Photo of the fixture.....	180
Figure 5.10. Measurement results for the parasitic cancellation technique. (a) Without ferrite core. (b) With ferrite core.	181
Figure 5.11. Measurement setup for testing the LC filter.....	182
Figure 5.12. Measured IL of the LC filter.	182
Figure 5.13. Integration techniques for EMI filters. (a) [88]. (b) [1]. (c) [89]. (d) [90]. (e) [91].	185
Figure 5.14. T-EQ CM choke. (a) Structure: top view. (b) Structure: front view. (c) Realized T-EQ choke: top view. (d) Realized T-EQ choke: front view.....	186
Figure 5.15. T-EQ CM choke model for simulation. (a) One-turn equivalent model. (b) Cross section view.	187
Figure 5.16. Finite element simulation results for the CM choke models. (a) Ordinary toroidal choke. (b) T-EQ choke.	187
Figure 5.17. Impedance measurement results. (a) Short-circuit configuration. (b) Open-circuit configuration.....	188
Figure 5.18. Measurements of the parasitic magnetic coupling between the choke and DM capacitors. (a) Test setup. (b) Measurement results.	189

Figure 5.19. Four different EMI filters for comparison..... 190
Figure 5.20. Configuration of the four-port mixed-mode S parameter measurements. 190
Figure 5.21. Comparison of the insertion losses of the four EMI filters. (a) DM. (b) CM. 192
Figure 5.22. Setup for conducted noise measurements..... 192
Figure 5.23. Conducted noise measurement results. (a) DM noise. (b) CM noise..... 193

List of Tables

Table 1.1 Different Magnetic Materials for EMI Filtering Applications	38
Table 1.2 Different core geometries for EMI Filtering Applications [25].....	39
Table 1.3 Planar EMI Filter Designs in Literatures.....	40
Table 2.1 Correspondence Between the Impedance Measurements and Parameters to Determine.....	52
Table 2.2 Equivalent Circuit Synthesis with Rational Functions.....	62
Table 2.3 IRFA Fitting Results for the 8-turn Planar Inductor.....	64
Table 2.4 Measurement Configurations for the Extraction Procedure.....	66
Table 2.5 Fitting Results of $Y_{T0}(s)$	71
Table 2.6 Fitting Results of $Y_{T2}(s)$ and $2Y_2(s)$	73
Table 3.1 Simulated Capacitance Matrix for the Case with 6 Conductors (Unit: pF/m). 100	
Table 3.2 Comparison between Calculations and Simulations for the Case of 6 Conductors	105
Table 3.3 Simulated Capacitance Matrix for the Case of 8 Conductors (Unit: pF/m).	107
Table 3.4 Simulation Results for Grounded PEC Core and Floating PEC Core.	111
Table 3.5 Simulation Results for the 6-conductor PCB Structure.....	116
Table 3.6 Comparison between Calculation and Simulation for the Capacitance Between Conductors and Grounded PEC Core.....	125
Table 3.7 Comparison between Calculation and Simulation for the 8-conductor Configuration in Ferrite Core.	125
Table 4.1 Comparison between Calculated Results and Simulation Results for the Configuration with Grounded PEC Core.....	148
Table 4.2 Comparison between Calculated Results and Simulation Results for the Configuration of Ferrite Core with High Relative Permittivity ($\epsilon_r=10^4$)	148
Table 4.3 Comparison between Calculated Results and Simulation Results for the Configuration of Ferrite Core with Lower Relative Permittivity ($\epsilon_r=10^3$).....	148
Table 4.4 Comparison between Calculated Results and Simulation Results for the Cross-section of the 8-turn Planar Inductor in the Core.....	150
Table 4.5 Comparison between Analytical Method and FEM Results for the Cross-section of the 8-turn Planar Inductor in Air.....	151
Table 4.6 Comparison between Calculated Results and Simulation Results for the Cross-section of the Planar CM choke in the Ferrite Core.....	152
Table 4.7 Comparison between Calculated Results and Simulation Results for the Cross-section of the Planar CM choke in Air.....	152
Table 5.1 Test Configurations for Calculating the Parasitic Capacitances.....	177
Table 5.2 Geometry and Material Properties of the Component.....	178
Table 5.3 Variation of the Capacitances with H_{iso}	179
Table 5.4 H_{opt} for the Cancellation.....	181
Table 5.5 Parameters of the Magnetic Cores Used in the T-EQ CM Choke.....	186
Table 5.6 Parameters of the Chokes	188

General Introduction

The research work presented in this dissertation had been carried out from Sep., 2009 to Oct., 2012, under the PhD program of CSC-CENTRALE managed by China Scholarship Council (CSC) and the Ecole Centrale Group, and is financially supported by the CSC and Ecole Centrale de Lille. This PhD work was performed inside L2EP (Laboratoire d'Electrotechnique et d'Electronique de Puissance de Lille) at the sites of the Ecole Centrale de Lille and the University of Lille 1.

Scope of the Work

Driven by the interests of power converters with high power density, the power electronics industry looks for solutions to integrate and miniaturize components and systems. This tendency makes planar magnetic components a very promising solution for realizing highly compact system. During the past decades, particular attention has been drawn on the integration of power line EMI filters using planar components [1, 2, 3], especially on the common mode (CM) choke. The main advantages of “planar” CM chokes comparing to traditional wire-wound chokes, is that the self-parasitic elements can be modeled more easily by analytical or numerical approaches. Moreover, as the planar components are automatically manufactured, a very good repeatability of performances can be expected in mass production.

The main topic treated in this research work is to model the parasitic elements of a planar CM choke because they are very critical for the performances of EMI filters. In particular, a focus is made on the parasitic capacitances and the leakage inductance of planar CM chokes. For this purpose, two different approaches are followed: the first one is experimental and the second one is analytical.

1. ***Experimental approach:*** This approach can be used when prototypes are available and the modeling is based on measurement results. It consists in using measured data to extract the equivalent circuit model of a planar CM choke. The parasitic capacitances, leakage inductance as well as the magnetizing part

are all extracted by a set of selected impedance measurements. The major concerns in this approach are the following:

- a. The configurations of the impedance measurements required for the extraction;
- b. The equivalent circuit topology for modeling the planar CM choke;
- c. The extraction method to obtain the parameters of the equivalent circuit.

With this experimental approach, accurate HF equivalent circuit model can be obtained for circuit simulations or validations purposes.

2. **Theoretical approaches:** To reduce the number of prototypes, virtual modeling is also necessary. Instead of using numerical methods, this work proposed analytical methods which compute much faster and require less computing resources. The first modeling objective involves the parasitic capacitances, which are very critical parameters for CM chokes used EMI filters. However, the research work on this topic in the literature is very limited. Therefore, this PhD work tries to propose original systematic approaches for calculating the parasitic capacitances, considering many factors such as the geometry of the winding, the characteristics of epoxy material and also the influence of ferrite magnetic core. Moreover, this dissertation also presents a method for calculating the leakage inductance of planar CM chokes. This problem has been originally studied in the dissertation of my co-advisor Xavier Margueron and is significantly extended and improved in this work for multilayered structures.

Using the theoretical approaches, parasitic capacitances and leakage inductance can be calculated analytically without prototyping, making the presented methods very interesting for component designers.

Besides, these modeling methods are quite general so their applications are not limited to planar CM chokes but can be extended to other types of planar magnetic components.

Apart from these modeling issues, some new design conceptions are introduced for planar components. First, based on the parasitic capacitance

modeling method, an improved parasitic capacitance cancellation technique is suggested for improving the HF performances of a planar differential mode (DM) choke. The second conception presented in this dissertation consists in the association of two magnetic cores with different geometries, i.e. toroidal core and planar EQ core for realizing a mixed T-EQ integrated CM and DM choke.

Organization of the Dissertation

This dissertation is organized as follows. In Chapter 1, the scientific background of the research work is briefly reviewed. For both experimental and analytical approach, different methods in the literature are compared and their pros and cons are analyzed.

In Chapter 2, the experimental modeling method for planar CM choke is presented. An HF equivalent circuit model is suggested together with its parameter extraction procedure. The latter is based on experimental impedance measurements and rational function approximation fitting algorithm. The equivalent circuit is extracted systematically from the fitting algorithm with good accuracy and short computation time.

Chapter 3 studies the analytical modeling methods of parasitic elements in planar components. The study starts with 2D analytical analysis, based on the Electric Field Decomposition (EFD) method, for calculating the capacitance matrix. Formulas for treating PCB structures and ferrite cores are proposed. With the calculated capacitance matrix, an energy approach is applied for deriving the parasitic capacitances of the studied component.

Chapter 4 focuses on the application of multilayered Green's function for extracting the parasitic elements of planar CM choke. First, the multilayered Green's function in electrostatic is applied for extracting the capacitance matrix of the cross-section of planar components. Next, the multilayered Green's function method is extended in magnetostatic for obtaining the 2D magnetic field information of a planar CM choke.

In Chapter 5, several new design conceptions for planar EMI filters are presented. First, an improved parasitic capacitance cancellation method using

structural parasitic elements is proposed for planar DM choke. Second, a CM choke using Toroid-EQ mixed structure is introduced. Theoretical analyses and experimental tests are given for validating the design conceptions.

Finally, the conclusion is drawn and some future works are discussed.

The derivation of several important formulas is detailed in Appendix.

Chapter 1. Introduction

1.1 EMI in Power Electronics

In the past decades, the prevalence of switching mode power converters greatly improves the performances of power supplies. During recent years, the miniaturization of these systems has been one major concern for power electronics (PE) designers. Developments of new power semiconductor components, power module packaging, passive components, converter topologies and control strategies allow improving the performances of power converters with higher switching frequency, higher power density, better efficiency and more compact volume. However, the fast switching semiconductor components used in the power converters allow to reduce the volume but cause severe high frequency (HF) Electromagnetic Interferences (EMI), which might subsequently disturb other electric or electronic equipments in their vicinity. For any EMI problems, three elements have to be identified and analyzed: the interference source, the propagation path and the victims. This section will focus on the first two elements.

1.1.1 EMI Sources in Power Electronics

Switching mode power converters are naturally EMI generators due to the commutation of power switches. The main EMI sources in a power converter are the high dV/dt and dI/dt caused by the fast switching semiconductors. Figure 1.1(a) illustrates a buck converter whereas Figure 1.1(b) depicts the trapezoidal waveforms of voltage V_x and current I under working condition. During the switching phase, V_x and I change abruptly. In fact, these abrupt rising and falling signals contain very rich HF harmonics, which can further transmits to the other equipment (regarded as the victims) through two types of propagation paths: conductions and radiation. Accordingly, two kinds of HF EMIs are defined [4]:

- ***HF Conducted Emissions***: These emissions are transmitted through resistive, capacitive and inductive couplings. The frequency range of interest for

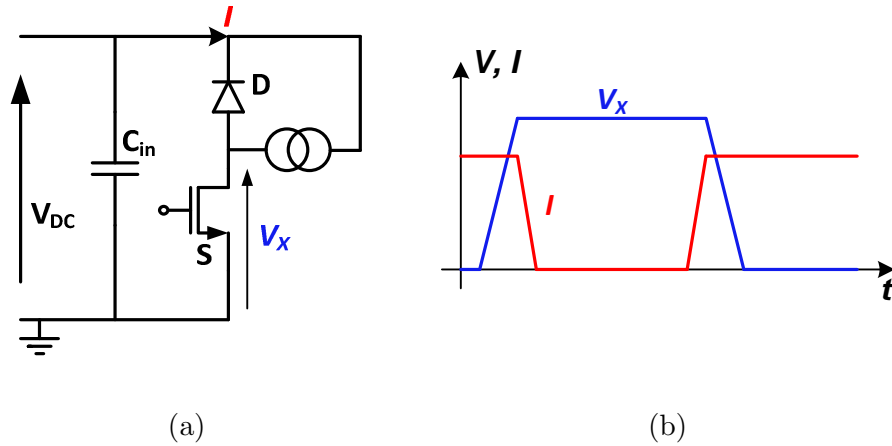


Figure 1.1. EMI sources in power converters. (a) Buck converter. (b) Switching wave forms.

conducted emissions is normally covered from 150 kHz to 30 MHz.

- **HF Radiated Emissions:** These emissions are transmitted by electromagnetic waves. Their frequency range of interests is included between 30 MHz and 40 GHz. For power electronics applications, the upper limit is at 1GHz [5].

1.1.2 EMC Standards and Conducted EMI Measurements

To reduce the potential harm of EMI, organizations such as Federal Communication Commission (FCC) in USA or Comité International Spécial des Perturbations Radioélectrique (CISPR) in Europe, define Electromagnetic Compatibility (EMC) regulations which must be strictly respected. These standards define the limit of the measured interference level, the specific equipments for EMC test as well as the corresponding measurement setup for these tests.

The studies presented in this dissertation concern only the HF conducted emissions (referred as conducted noises). The common setup for conducted noise measurement is illustrated in Figure 1.2(a). The equipment under test (EUT) is placed on a non-conductive table and it is connected to the power supply through a line impedance stabilization network (LISN). Then an EMI test receiver captures the conducted emissions sent from output of the LISN. The LISN is in fact a low pass filter that sends energy to the EUT but blocks high frequency noises coming from the power grid. Besides, the LISN provides a fixed characteristic impedance for the EUT and it can send the conducted noises to spectrum analyzer or EMI

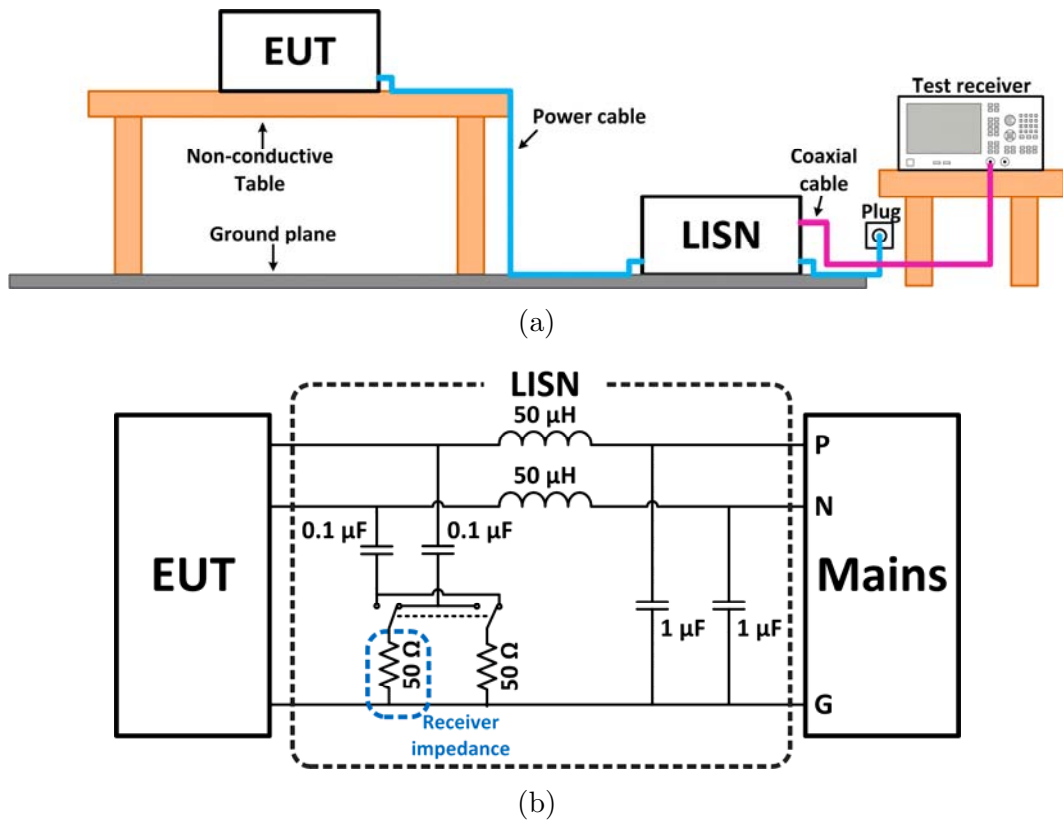


Figure 1.2. Conducted emission measurement. (a) Measurement setup. (b) Circuit of LISN.

receiver. In Figure 1.2(b), the circuit topology of LISN suggested by CISPR 22 is presented [6]. In Figure 1.3, the commonly used conducted emission limits defined by CISPR 22 are illustrated [7], where QP signifies quasi-peak detection mode while AVG for average detection mode. The “Class A” limits apply on devices for commercial, industrial or business use whereas the “Class B” limits apply for residential environments.

For better understanding the conducted emissions and EMI diagnosis, the noises can be separated into common mode (CM) and differential mode (DM) parts according to the nature of their transmission (see Figure 1.4):

- **Common mode:** the noise current I_{CM} goes through both the phase and the neutral lines and return from the ground line.
- **Differential mode:** the noise current I_{DM} goes through the phase line and returns from the neutral line.

With these separations, the conducted noises can be studied separately for CM and DM. However, it should be noted that the conducted emissions limits deal with the

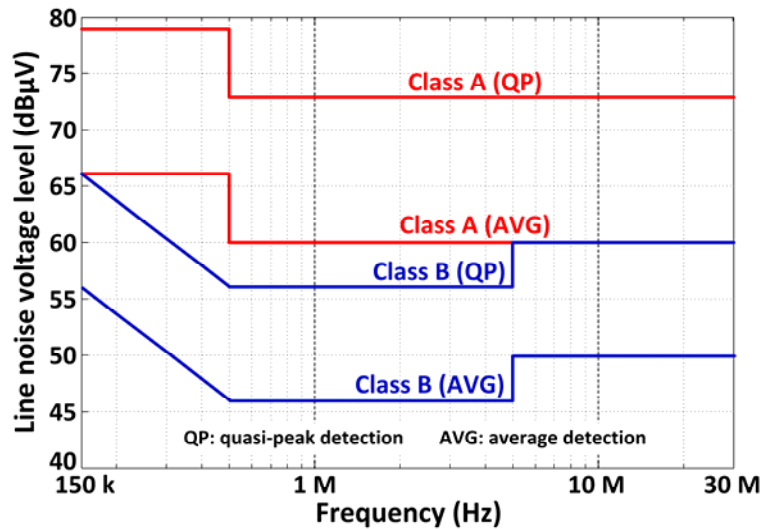


Figure 1.3. HF conducted emission levels defined by CISPR 22 [7].

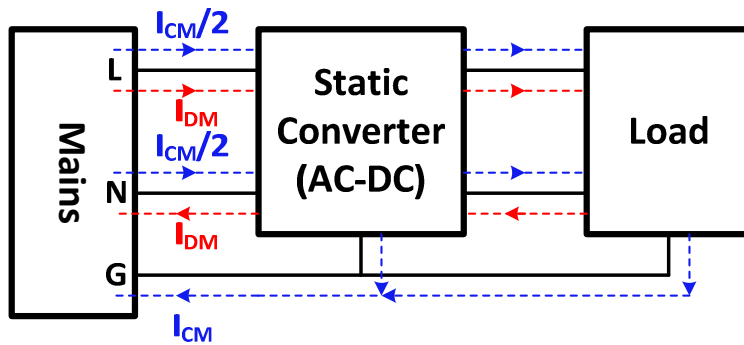


Figure 1.4. CM and DM conducted noise in a single phase application.

overall effect of CM and DM noises at the receiver output of the LISN.

1.2 Power Line EMI Filters

1.2.1 Overview

To mitigate the conducted noises, many solutions have been reported [8]. At the EMI source, techniques such as soft switching [9], snubber circuit [10], spread-spectrum control scheme [11] can effectively reduce the noise level. On the propagation path, improvements on the layout and implementation of EMI filters can further reduce the outgoing noises. Among all these techniques, using an EMI filter is one of the most practical and reliable solution to achieve the compliance with EMC standards. EMI filters are basically low-pass filters which are

transparent to nominal current (e.g. 50 Hz) but that have large suppression for conducted noises between 150 kHz to 30 MHz. In general, EMI filters can be classified into three types:

- **Passive filter:** In passive filter, only passive elements are used such as inductors, capacitors and resistors. No external power is needed for the filtering.
- **Active filter:** In these filters, active elements like transistors or operational amplifiers are implemented, which requires an external power source and proper circuit design for achieving the desired attenuation.
- **Hybrid filter:** Hybrid filters combines together the passive and active filter solutions.

The latter two types of filters are generally of smaller dimensions and thus are very promising for realizing compact power electronic systems. However, the use of active components such as operational amplifiers increases the design complexity and failure risks, hence reduces the reliability. Besides, the large signal characteristics of the active components have not been profoundly investigated for practical uses. Though several works have been reported on the EMI filtering using active [12] or hybrid filters [2], EMI filters with active components is still far from wide industrial applications. Therefore, the passive filters are more practical solutions. With some recent development in magnetic material [13] and filter design [14, 15, 16], passive filters become more and more efficient and remain the most common choice for EMI filtering applications. In this dissertation, the focus will be these passive filters.

1.2.2 Passive EMI Filters

In Figure 1.5(a), a typical topology of a passive EMI filter is shown. The capacitors used in the filters are generally standard components with strict safety requirements. The CM capacitors, also called Y-capacitors, are connected between line and ground and between neutral and ground for filtering the CM noises. The DM capacitors, or X-capacitors, are connected between line and neutral for filtering the DM noises. The common mode chokes are realized by coupled inductors, as shown by L_{CM} in Figure 1.5(a). They are indeed two inductors wound on the same

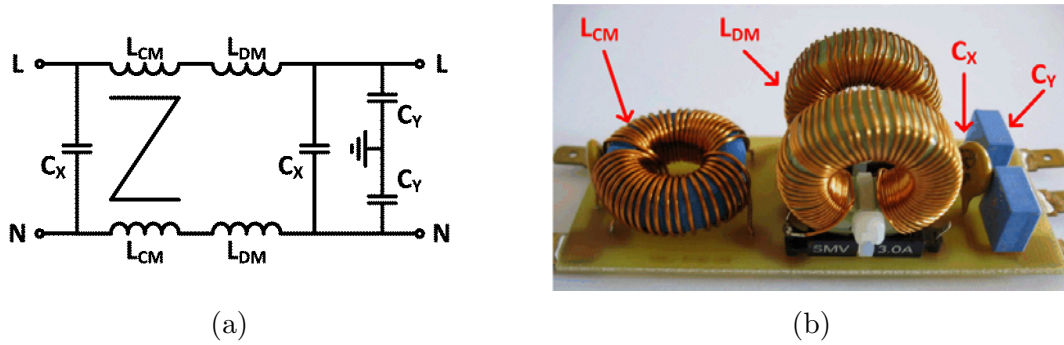


Figure 1.5. Typical EMI filter. (a) Schematic. (b) Photo of an example.

magnetic core in such a way that the component exhibits high impedance for CM currents while it has little influence on DM current (including DM noise current). The DM inductors can be realized by independent inductors or by using the leakage inductance of the CM chokes. In an EMI filter, the elements for attenuating CM and DM noises are quite independent, so that the design of EMI filters is usually carried out separately for CM and DM filtering parts.

To describe the noise-attenuating performances of an EMI filter, the term insertion loss (IL) is defined. Figure 1.6 shows two configurations before and after the insertion of the EMI filter. The IL is given by the ratio of the load voltage level without the EMI filter $V_{L,W0}$ and that with the EMI filter $V_{L,W}$, as given by (1.1). This value is positive in dB by its definition. However, its reversed value (1.2) is commonly used for presenting the IL since a negative value is intuitively related to “loss” (actually, the negative value should be called insertion gain). Throughout this dissertation, the negative-valued IL form (1.2) is chosen for presentation. Note that the IL of an EMI filter is dependent to the source impedance Z_S and load impedance Z_L , so it is meaningless to give IL without defining Z_S and Z_L .

$$\text{IL} = 20 \log \left(\frac{V_{L,W0}}{V_{L,W}} \right) \quad [\text{dB}] \quad (1.1)$$

$$\text{IL} = -20 \log \left(\frac{V_{L,W0}}{V_{L,W}} \right) \quad [\text{dB}] \quad (1.2)$$

In the literature, many works have been reported on the design of EMI filters. In [17], a systematic procedure is presented for designing an EMI filter according to the CM and DM noises information. However, this method supposes

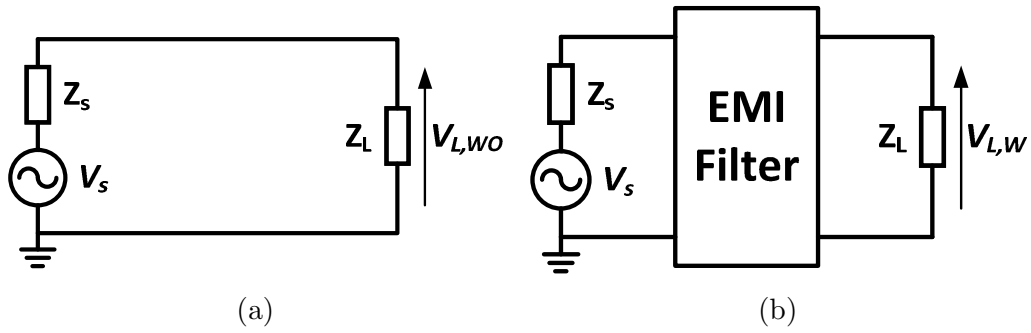


Figure 1.6. Definition of insertion loss. (a) Without EMI filter. (b) With EMI filter.

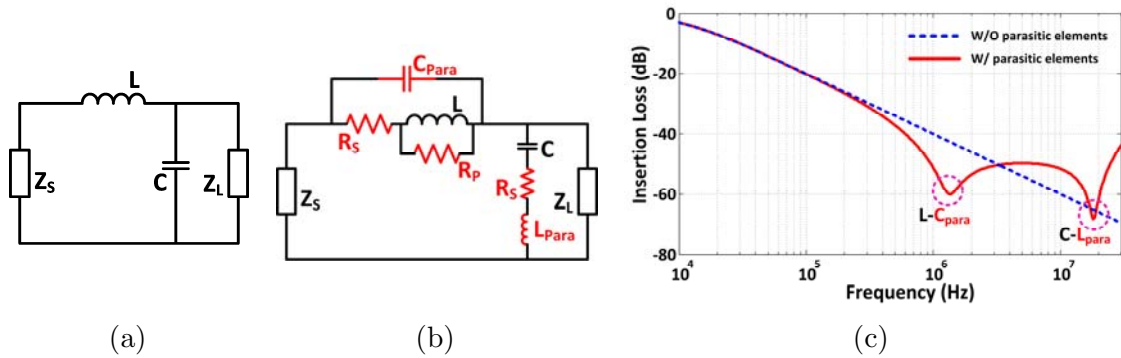


Figure 1.7. Insertion loss of a LC low pass filter. (a) Ideal filter. (b) Realistic filter with parasitic elements. (c) Comparison of the IL of the two cases ($Z_s=50 \Omega$, $Z_L=50 \Omega$).

that the source and load impedances are both 50Ω . It has been stated that the insertion loss of an EMI filter is related to Z_s and Z_L . The $50 \Omega/50 \Omega$ (Z_s/Z_L) assumption is seldom satisfied in practical applications, especially for the noise source impedance Z_s . As a result, EMI filters designed by this method may fail to provide the specified attenuation to the conducted noises in real environment. Usually, the $100 \Omega/0.1 \Omega$ and $0.1 \Omega/100 \Omega$ impedance setups are also tested to verify the performances of EMI filters under unfavorable conditions. In recent years, several research works have been carried out for measuring the noise source impedance, which allows for the acquisition of the information on Z_s [18, 19] (Z_L is known from LISN). With this information, the design of EMI filters becomes more effective and robust [20].

However, EMI filters are never as ideal as are presented in Figure 1.5(a). First, the inductances of the filtering inductors strongly depend on the characteristics of the magnetic core. The complex permeability $\mu = \mu' - j\mu''$ of magnetic materials is frequency dependent, making the impedances varying with frequency. Second, the inductors work under flux bias, which may cause saturation

of the magnetic material. Therefore, the filter may not provide sufficient suppression under working condition, due to the decrease of the inductance value. Third, the components in EMI filters have parasitic elements which will degrade the performances of the filters. In Figure 1.7(a) and (b), an ideal LC low pass and its counterpart with parasitic elements are illustrated. Their insertion losses are compared in Figure 1.7(c). The first resonance of the IL for the filter with parasitic elements is due to the parasitic capacitance of the inductor C_{para} whereas the second one is due to the parasitic inductance of the capacitor L_{para} . It can be seen that these elements will deteriorate the IL of the filters at high frequencies. Last but not least, the parasitic coupling between components, grounds and loops inside the filter will also significantly influence the HF performances of the filter [21]. In view of these points, the behavior of an EMI filter is much more complicated than the circuit shown in Figure 1.5(a). As a result, more accurate models for the components in an EMI filter are needed to correctly describe the real behavior of the filter in a wide frequency band. These models are generally in frequency domain and can be classified in two categories: black-box modeling and equivalent circuit modeling. For the black-box modeling, characteristics of the filter are presented by tabulated data or rational functions, which hide completely the physical meanings. Consequently, equivalent circuit models are preferred since they can provide rich and direct insight about the performances of the filter. One major task of this dissertation will be dedicated to the construction of the equivalent circuit model of an EMI filter by experimental and theoretical approaches.

1.2.3 Technologies for Passive EMI Filters

In this section, some of the available technologies for fabricating passive EMI filters will be reviewed. As stated previously, the capacitors are the devices imposed by safety requirements. As a result, the capacitors are generally chosen in the catalogue of manufacturers. Three types of capacitors are widely used in EMI filters: film capacitors, ceramic capacitors and electrolytic capacitors. Thin plate capacitors with high permittivity dielectric material become more popular in recent years [1, 2]. However, the safety property of thin plate capacitors should be further studied to make them commercially mature. Another issue that should be

mentioned is that the filtering capacitors are usually small so that they impose little constraint on the volume of EMI filters. In a word, the design freedom on filtering capacitors is limited in the states of art. On the contrary, there are numerous design choices for magnetic components in passive EMI filters.

1.2.3.1 Magnetic Materials for Inductors

Magnetic materials are first investigated. The most frequently used material is ferrite and there are mainly two types: MnZn and NiZn [22]. In common practice, the former ones are dedicated for frequency range up to several megahertz. Beyond these frequencies, the NiZn ferrites are more efficient. For conducted EMI noise suppression in power electronics, MnZn ferrites are more prevalently used to make CM chokes. Nevertheless, these ferrite materials suffer from low saturation flux density. Therefore, when designing DM inductors, air-gaped ferrite should be chose to avoid the saturation of the cores.

Powder core is an alternative to solve the saturation problem. As the name implies, these cores are a mixture of magnetic material powder, in which the air-gap is distributed in the material. Four main types of powder material exist: Iron powder (Fe), Sendust powder (Fe-Al-Si), High Flux (Fe-Ni) and Molypermalloy (Mo-Ni-Fe) [23]. In general, powder cores have a very high saturation level B_{sat} (higher than 1 T) and low temperature sensibility, so they can be used to realize DM inductors in EMI filters.

The last material family is the magnetic alloy. These materials are basically the alloy of Fe, Ni, Co and some other elements. Due to the low resistivity, these materials are usually in the form of thin tape to reduce eddy current losses. Commonly used magnetic alloys consist of silicon-steel, permalloy and amorphous alloy [24]. They have very high relative permeability ($>10^4$) and high saturation level. It should be noted that one particular amorphous alloy called nanocrystalline is receiving more and more interest for EMI filtering applications. This material has a very high initial permeability μ_i ($>10^4$), high saturation level B_{sat} (up to 3 times higher than ferrite), high operating temperature and low temperature sensibility. Though the nanocrystalline materials are very suitable for realizing CM inductors in EMI filters, they are more expensive than ferrites. The properties of commonly

Table 1.1 Different Magnetic Materials for EMI Filtering Applications

Material	Initial Permeability	Saturation Level	Max. Operating Temperature	Temperature Sensibility
<i>MnZn Ferrite</i>	$10^2 \sim 10^4$	~ 0.4 T	< 100 °C	High
<i>Powder (Iron)</i>	$\sim 10^2$	1.3 T \sim 1.7 T	> 120 °C	Low
<i>Nanocrystalline</i>	$\sim 10^5$	1.2 T \sim 1.8 T	> 120 °C	Low




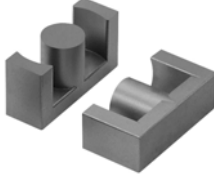
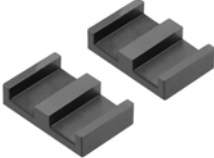
used materials for EMI filtering are summarized in Table 1.1.

1.2.3.2 Geometry of Magnetic Cores

A wide diversity of core geometries are commercially available, as presented in Table 1.2. [25]. For EMI filtering applications, the most frequently used geometry of magnetic cores is toroid. The prevalence of toroidal core is due to their low fabrication cost and wide commercial availability. One can find toroidal core with almost all the magnetic materials presented in the previous section. However, the winding process on toroidal cores is quite difficult so that special machine or manual winding may be required. Besides, the magnetic components in EMI filters can also be realized with other types of cores such as U styles (UI, UU, etc.) and E styles (EI, EE, EP, etc.). Another important core type, the E-Planar (referred as planar afterward) cores have gained a lot of interests from power electronics industry during the past decades. The E-Planar cores are, in fact, the flattened version of EE or EI cores and their windings are often realized by Printed circuit board (PCB) traces or copper foil. Since 90s, planar magnetic components have been widely used in transformers for switch-mode power converters, since they have the following advantages:

- **Low profile:** the use of PCB structure can effectively reduce the height of the components.
- **Low fabrication cost:** The large quantity fabrication of PCB structures can greatly reduce the cost in modern industry.
- **High repeatability:** The PCB winding of planar components is highly repeatable with available technology thereby ensuring stable HF parasitic

Table 1.2 Different core geometries for EMI Filtering Applications [25].

Toroid	UU	Pot	EER	E-Planar
				

characteristics.

- **High power density:** The current density limit for planar trace is generally 20 A/mm², which is 4 times larger than that of a round wire (5 A/mm²).

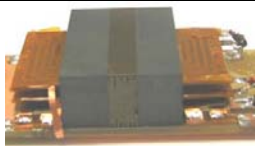
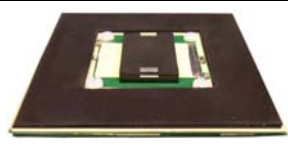
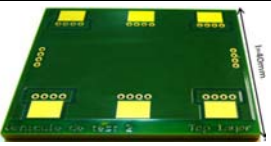
These advantages make the planar components very suitable for realizing highly compact power electronics converters [26]. Lately, driven by the integration and miniaturization motivations, planar EMI filters become one important research interest [1, 2, 27].

This dissertation is dedicated to the study of the planar components. As nanocrystalline material is not commercially available for planar cores due to the fabrication process, the components under study are planar components using MnZn ferrite cores.

1.2.4 Design of Planar EMI Filters

During the past decades, many research works have been reported on the design of planar coupled inductors (see Table 1.3). In [1], R. Chen et al. presented an integrated EMI filter. The CM choke is realized by two coupled spiral planar windings. Between these two CM windings, a leakage layer of ferrite polymer composite (FPC) is added for increasing the leakage inductance of the CM choke [1]. To circumvent the parasitic capacitances of the winding, a cancellation technique is proposed to improve its high frequency performances. In [2], the authors put the differential mode choke outside of the CM choke, still using leakage layers (μ -metal and FPC materials) to enlarge the leakage inductance, realizing a very low-profile integrated EMI filter. In 2011, a hybrid planar EMI filter has been presented (Table 1.3) [3]. The CM choke is realized by sliced ferrite core, which is indeed a flattened toroidal core. As the inductance value is very small, the passive

Table 1.3 Planar EMI Filter Designs in Literatures.

Type		Passive		Hybrid
Author/Year		R. Chen/2004 [1]	J. Biela/2009 [2]	M. Ali/2011 [3]
Prototype				
Parameters	L_{CM}	3.1 mH	1.5 mH	3 μ H (@1 MHz)
	L_{DM}	21 μ H	182 μ H	3.5 μ H
	C_X	0.7 μ F	0.8 μ F	18 nF
	C_Y	6.6 nF	N/A	9 nF
	Size	Height = 1.2 cm; Volume = 20 cm ³	80×80×7.2 (mm); Volume = 46.1 cm ³	50×40×2.8 (mm); Volume = 5.6 cm ³

part is used to filter the high frequency noises while the low frequency noises are filtered using an active EMI filter. The characteristics of these EMI filters are summarized in Table 1.3. It can be seen that all these filters have low profile and small volume, which are very promising solutions for power system integration.

1.3 Modeling of Planar EMI Filters

1.3.1 Global View of the Modeling Issue

1.3.1.1 Modeling Contents

The performances of EMI filters depend on many factors such as the characteristics of the components, the parasitic couplings between components and the grounding patterns etc. As said before, this work will focus on the modeling of planar CM chokes for EMI filters. The modeling of such components includes many aspects:

- **Magnetizing impedance:** the magnetizing impedance determines the CM inductance for the attenuation of the CM conducted noises;
- **Parasitic capacitances:** the parasitic capacitances of CM chokes bypass the HF noises so that they deteriorate the HF performances of the filters;
- **Leakage inductance:** the leakage inductance is a useful stray element in planar CM chokes that can be used for DM noise filtering.

These elements are critical for the performance of the CM choke and the EMI filter. Therefore, simple and reliable modeling method to determine these elements are very important for the design of EMI filters. Though parasitic couplings and grounding pattern are also crucial for the HF performance of EMI filters [15, 21], they are out of the concern of this PhD work.

1.3.1.2 Methods for Modeling CM Chokes

In this section, a brief review of modeling methods for planar CM chokes is presented. Generally speaking, the modeling methods for CM chokes can be separated into two classes: experimental methods and theoretical ones. Experimental methods consist in building models on the basis of measurements on real devices, whereas theoretical methods refer to strict or approximate analyses of components with electromagnetic theory.

The experimental methods are direct and accurate. However, one main drawback of these methods is that they require prototype realizations, which may be time-consuming and expensive. Therefore, these modeling methods are normally applied at the ending step of a design cycle for validation purposed. At the starting stage of a design, theoretical modeling methods are prevalently used to avoid blind designs.

The theoretical methods can be further divided into two families: numerical approaches and analytical ones. As always, both approaches have their pros and cons. Numerical modeling such as Finite Element Analysis (FEA) and Partial Electric Equivalent Circuit (PEEC) are quite mature for which a lot of commercial general solvers are available (e.g. Maxwell, COMSOL multiphysics, InCAD etc.). They can give accurate results but can also be considerably expensive in terms of computing resources and time, especially for HF simulations.

Analytical methods usually analyze a device with approximations. Consequently, the models are simplified and the obtained results are normally less accurate. Nevertheless, these analytical models can be solved in short time and they can provide very rich insight into the influence of different parameters on the global performance of the studied component. Just like circuit design, SPICE simulations can never replace analytical analysis. Designers can apply analytical models to

make a coarse design or coarse turning and subsequently perform fine optimization or validation of its design using numerical tools.

Based on the above statements, the advancement in experimental modeling methods and the analytical modeling methods will be reviewed hereinafter.

1.3.2 Experimental Modeling Methods

Experimental methods build general models that can be applied to planar EMI filters as well as other types of EMI filters. In fact, the magnetizing impedance, the parasitic capacitances and the leakage inductance can all be modeled by such methods. They consist in building models on the basis of measurements such as impedance (admittance) measurements or network measurements. The obtained measured data are post-processed to generate black-box or equivalent circuit models. The authors proposed in [28] a black-box model of EMI filter using S parameter measurement results [see Figure 1.8(a)]. Despite its high accuracy, the model is not direct in physic meanings. As a result, it is hard to use the model at the design step. In [29], the authors introduced an equivalent circuit model for EMI filters using S parameter measurements [see Figure 1.8(b)]. The model can effectively capture the parasitic elements of the filter including the parasitic couplings. However, the identification procedure requires complex measurement setups. J.-L. Kotny and al. present in [30] a simple approach to establish the HF equivalent circuit model of EMI filter by impedance measurements, as shown in Figure 1.9. The obtained model is accurate and has more physical meanings. However, the parameters of this model are extracted through observations and manual trials, making the procedure somehow heuristic and time consuming. Numerical methods are alternatives to build accurate and broadband equivalent circuit models. For this purpose, many methods based on optimization techniques are reported. It consists in curve fitting of the measurement data and then post-processing on the fitting results to generate the equivalent circuit. These methods can generally be categorized into three families: linear optimization techniques [31], nonlinear optimization techniques [32] and heuristic optimization techniques [33]. With these methods, accurate models can be extracted from measurements results in a short computing time.

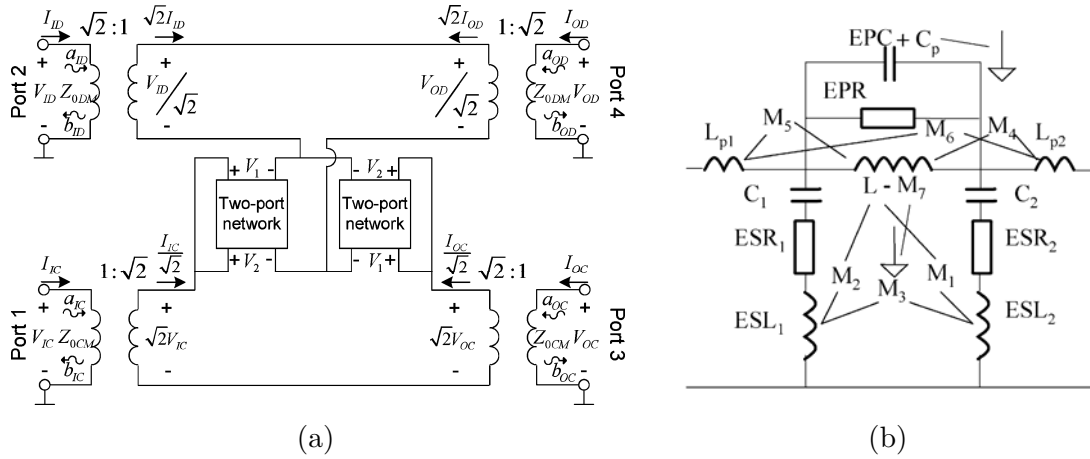


Figure 1.8. HF models proposed in literature. (a) Modal Model for CM chokes [28]. (b) DM EMI Filter Model Containing Parasitic Elements [29].

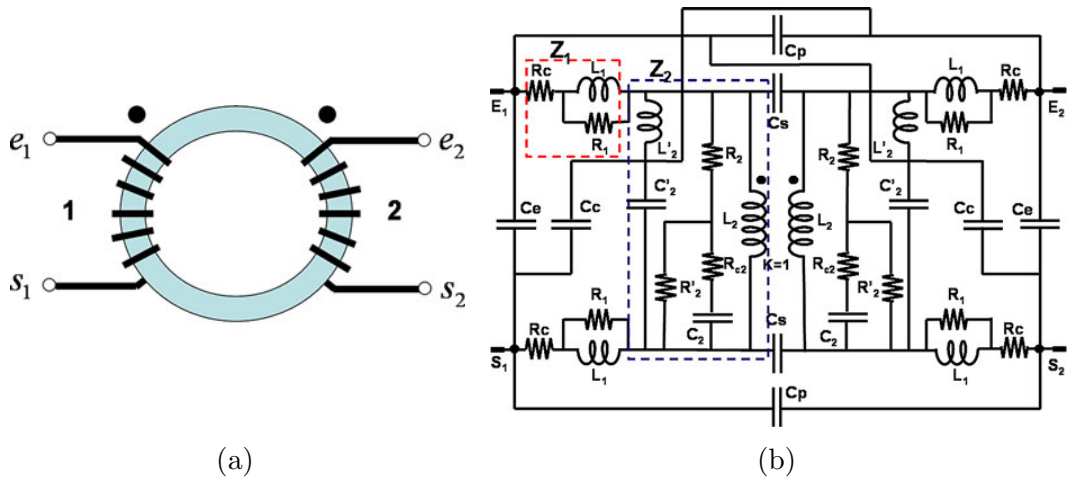


Figure 1.9. HF model for CM choke [30]. (a) Toroidal CM choke under study. (b) Equivalent circuit.

1.3.3 Analytical Methods

The magnetizing impedance of a CM choke depends strongly on the characteristics of the magnetic core, so it is normally modeled through measurements of the magnetic material. Therefore, only the analytical modeling of parasitic capacitances and leakage inductance is presented in this section.

1.3.3.1 Modeling of Parasitic Capacitances

As the winding length of planar CM chokes is much larger than that of a toroidal choke, the parasitic capacitances are more stringent for planar CM chokes. To determine analytically the parasitic capacitances of planar components, two

steps are necessary.

The first step is to calculate the 2D distributed capacitance matrix for the cross-section of the winding trace, as presented in Figure 1.10(a) and (b). In this step, the length of the conductors in the studied cross-section is supposed to be infinite so that the third dimension effect is neglected. Traditionally, the simplest method for modeling the 2D parasitic capacitances are based on the empirical formulas for plate capacitor [Figure 1.10(c)] given by:

$$C = k\varepsilon \frac{W}{H} \quad [\text{F/m}] \quad (1.3)$$

where k is a fitting parameter for adjust the results, ε is the permittivity of the PCB epoxy, W is the width of conductors and H is the distance between two conductors. This formula is only precise when W/H ratio is large. Otherwise, the formulas will give inaccurate results since it neglects fringe effects. Besides, this formula can only evaluate the capacitance between two face-to-face conductors such as C_{14} (between conductor 1 and 4). It cannot be used for calculating the 2D capacitances of C_{12} or C_{15} for example [see Figure 1.10(b)]. A common practice is to neglect the capacitances C_{12} and C_{15} in the calculation, just as done in [1]. However, this simplification will cause significant errors, especially when W/H ratio is small. An alternative to calculate 2D capacitance matrix is the conformal mapping [34]. It involves strict mathematical treatment in complex analysis and it is thereby very accurate. In [35], this method is applied for calculating the capacitance matrix of a planar LCT device. However, the conformal mapping requires very complex calculations and can only be applied on simple planar structures or with strong simplifications. Some other work combines the conformal mapping results with empirical fitting parameters to study simple structures [36, 37], but no results are available for studying such structures of power planar components, as illustrated in Figure 1.10(a).

Once the 2D capacitance matrix is known, the second step using an energy approach can be applied to obtain the equivalent capacitance. It consists of calculating the electric energy W_E stored in the component and deriving the equivalent capacitance C_{eq} by:

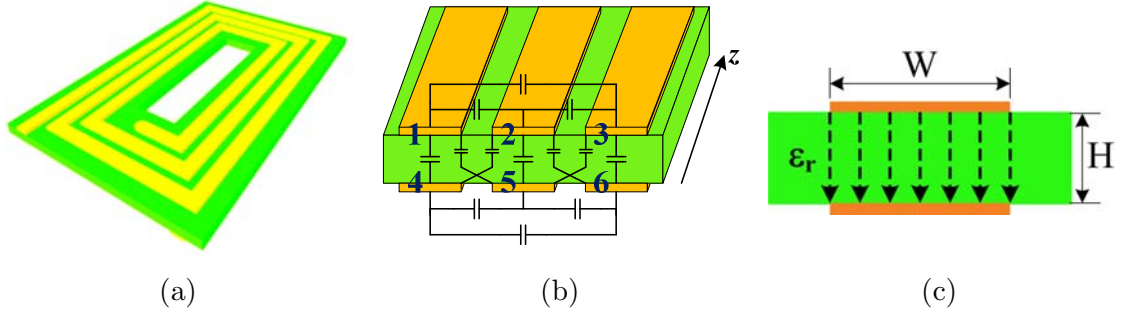


Figure 1.10. Parasitic capacitance calculation. (a) Winding structure. (b) Cross-section view of conductors. (c) Plate capacitance model.

$$C_{eq} = 2W_E / U^2 \quad [\text{F}] \quad (1.4)$$

where U is the input voltage of the studied component.

1.3.3.2 Modeling of Leakage Inductance

First of all, studies about magnetic aspects are presented. In [1], an FPC layer is added in the CM choke to create a leakage path, which increases the leakage inductance. The author proposes an analytical formula based on Dowell method [38]. However, this formula assumed that the magnetic field is parallel to the planar conductor, which is not true in reality. Authors in [39] proposed a more general method to calculate the static leakage inductance for planar structure. The method uses 2D PEEC (Partial Electric Equivalent Circuit) formulas (1.5) to calculate the vector potential generated by a rectangular conductor, as presented by Figure 1.11(a) and (b).

$$A_z(x, y; a, b) = \frac{-\mu_0 I}{16\pi ab} \left[F(X, Y) \Big|_{X=x+a}^{X=x-a} \Big|_{Y=y+b}^{Y=y-b} \right] \quad (1.5)$$

with $F(X, Y) = XY \ln(X^2 + Y^2) + X^2 \arctan\left(\frac{Y}{X}\right) + Y^2 \arctan\left(\frac{X}{Y}\right)$

These formulas are coupled with image method to evaluate the influence of ferrite core [see Figure 1.11(c)] [40]. The magnetic energy per unit length stored in the component's cross-section W_l can thus be calculated by:

$$W_l = \iint A_z J_z dS \quad [\text{J/m}] \quad (1.6)$$

where J_z is the current density on the cross-section of the conductors in the window. The leakage inductance L_f is determined through total magnetic energy stored in

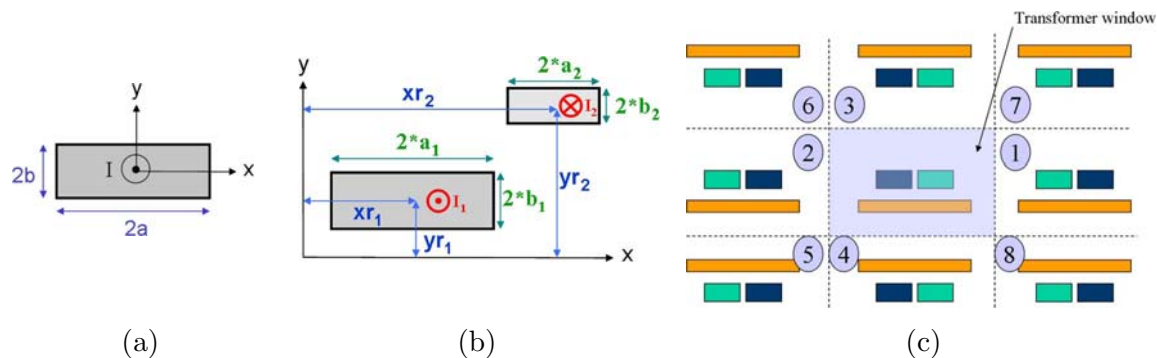


Figure 1.11. PEEC-like methods for calculating leakage inductance [39]. (a) Rectangular conductor. (b) Transformer window with two rectangular conductors. (c) Image methods.

the component:

$$\frac{1}{2} L_f I^2 \approx l_{mean} W_l \quad (1.7)$$

where l_{mean} is a well-chosen mean winding length of the component. One limitation of such method is that it can only be applied on magnetically homogenous space. For planar CM chokes that use FPC layer to increase their leakage inductance, the implementation of image method for FPC layer can be very cumbersome.

1.4 Conclusion

In this chapter, the general notions of EMC in power electronics are presented. The conducted noise of a power converter should comply with strict EMC standards and are thereby a critical issue for designers. To suppress the conducted noise level below the limits, EMI filters are widely used for filtering the CM and DM noise. The interests of integration and miniaturization of power electronic systems calls for realization of chokes in EMI filters with the recent technology: planar components. The existing models for such components are quite limited, which become the motivation of this work. As will be seen in the following chapters, different methods will be presented for modeling a planar CM choke, including the experimental approach and theoretical ones. In the theoretical modeling parts, elements including parasitic capacitances and leakage inductance will be profoundly studied.

Chapter 2. Experimental Modeling of CM Chokes

This chapter treats an experimental modeling method of CM chokes used in EMI filters. This method involves the build of a choke model through impedance measurements, which are frequency domain small-signal analysis in essence. Under real working conditions, the large signal performances of the choke will be affected due to saturation effects in magnetic material. However, the small signal modeling approach is still widely used as the first step for EMI filter design, since they can reveal many important physic insights of the filter or components such as CM filtering inductance, DM filtering inductance as well as the parasitic capacitances and other HF effects.

In the following parts, the existing models of CM chokes will first be reviewed. Next, the IRFA fitting method will be presented before introducing the proposed HF equivalent circuit model for CM chokes. A simple parameter extraction procedure is described by an example and experimental validations are given at the end to show the effectiveness of the proposed model and the extraction algorithm.

2.1 HF Equivalent Circuits of CM Chokes

2.1.1 Brief Review of Existing Models

Figure 2.1(a) illustrates the electric symbol of a CM choke, which is the simplest form for representation and is hardly used in simulations. During the past decades, many physic-based and measurement-based models are studied. For the reasons stated in the first chapter, measurement-based models relying on black-box are not covered in this section but only equivalent circuit models are discussed. A commonly used equivalent circuit for CM chokes is given in Figure 2.1(b). It is a coarse model since it does not consider the frequency dependent losses of the choke

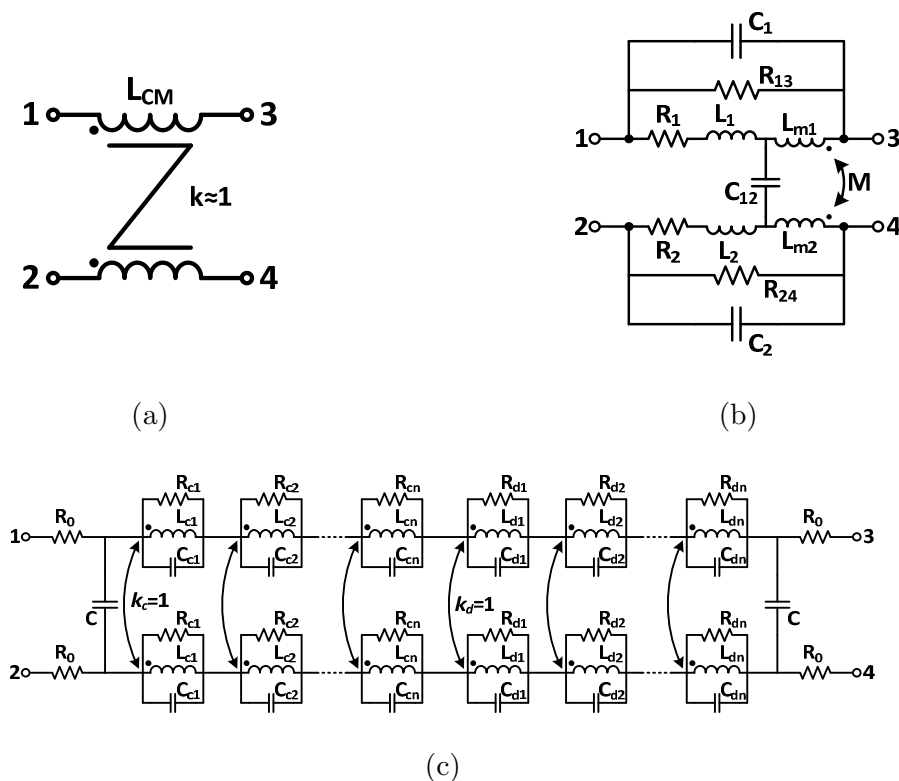


Figure 2.1. Equivalent circuit models of CM chokes. (a) Simplified circuit presentation. (b) Model used in [56]. (c) Model used in [33].

due to the characteristics of magnetic core and winding losses. Moreover, the parasitic capacitances network is not sufficient to fully represent the electrostatic behavior of the component. Indeed, note that three independent voltages (V_{13} , V_{24} , V_{34}) can be established between the terminals of the component, and three independent capacitances are thereby necessary to completely describe the electric energy stored in the component [41]. In common practice, the parameters of such models are determined from measured data on several frequency points, so it will not provide high accuracy on a wide frequency band.

In [33], a more sophisticated equivalent circuit model is proposed for CM chokes [see Figure 2.1(c)] and its parameters are extracted by optimization with genetic algorithms. This equivalent circuit allows a high modeling accuracy over the HF resonances. However, the LF part accuracy is really poor as it can be seen from the validation results given in [33]. Besides, it does not provide any clear physic interpretations for the elements in the model so that it remains somehow a black-box model for designers. Though the parameters of the model are extracted through an optimization process instead of manual trials, using heuristic methods such as

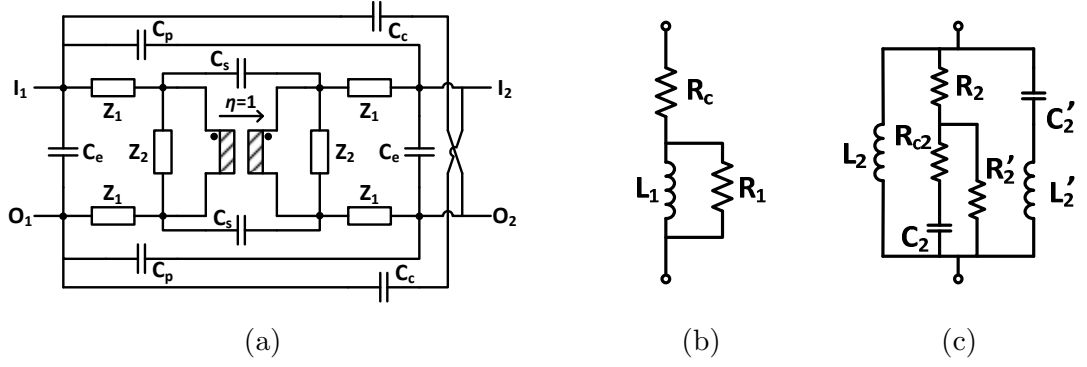


Figure 2.2. HF equivalent circuit of CM chokes proposed in [30]. (a) Equivalent circuit. (b) Circuit of Z_2 . (c) Circuit of Z_1 .

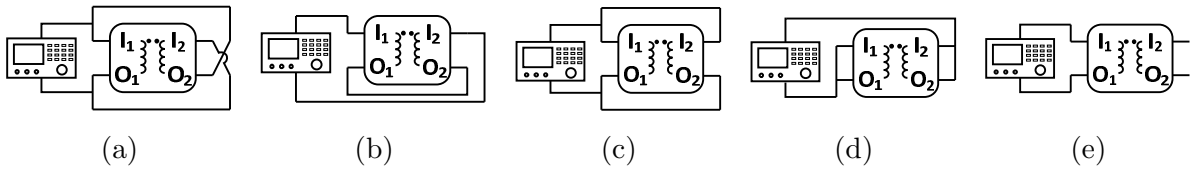


Figure 2.3. Different measurement configurations used for the parameter identification. (a) T_0 . (b) T_1 . (c) T_2 . (d) T_3 . (e) T_4 .

genetic algorithms requires relatively long time for searching the results and may suffer from convergence problems.

2.1.2 Equivalent Circuit Model for CM Chokes with More Physical Meanings

2.1.2.1 Model Structure and Parameter Extraction

Recently, a HF equivalent circuit model for CM chokes with more physical meanings has been reported in [30] [see Figure 2.2(a)]. This symmetrical structure consists in a special case of a 2-winding transformer equivalent circuit [41]. The main elements in this model are:

- η : transformation ratio that is assumed to be unity;
- Z_1 : leakage impedance including frequency-variant winding resistance $R_w(f)$, leakage inductance $L_l(f)$ due to skin and proximity effects of the winding wire [see Figure 2.2(b)]
- Z_2 : magnetizing impedance including the frequency-dependent inductance and magnetic core losses [see Figure 2.2(c)].

Table 2.1 Correspondence Between the Impedance Measurements and Parameters to Determine.

<i>Impedance measurements</i>	<i>Parameters to determine</i>
T_0, T_1, T_2 and T_3	Parasitic capacitances $C_e, C_{e'}, C_p$ and C_s
T_0 and T_1	Leakage impedance Z_1
T_2 and T_4	Magnetizing impedance Z_2

- C_e, C_s and C_p : parasitic capacitances of the CM choke.

To extract these equivalent circuit parameters, five specific impedance measurements are performed, as presented in Figure 2.3. Table 2.1 summarizes the correspondences between these measurements and the parameters that can be determined.

The extraction procedure consists in observations on the variation of the measured impedances, while some typical frequency responses are identified to extract the searched parameters. For example, 20 dB/dec. and -20 dB/dec. slopes symbolize an inductance and a capacitance respectively. The resonance frequency can also be used to determine the parasitic capacitance through the well-known formula (2.1):

$$f_{res} = \frac{1}{2\pi\sqrt{LC_{para}}} \quad (2.1)$$

where f_{res} denotes the resonance frequency, L the inductance and C_{para} the parasitic capacitance. Regarding the determination of impedances Z_1 and Z_2 , some manual adjustments on the parameters are necessary to further improve the accuracy of the results. Once these parameters are determined, the large frequency band behavior of the CM choke can be accurately modeled by the obtained equivalent circuit.

2.1.2.2 Limits of Application

Though the previous HF equivalent circuit model can effectively describe the behavior of a CM choke, this model and its parameter extraction procedure can still be improved for the following reasons:

- The choice of the circuit topology is based on observations. For example, the admittance $Y_2 = (Z_2)^{-1}$ in Figure 2.2(c) contains:
 - One pole at origin: the branch of L_2 ;

- One stable real pole: the branch of R_2 , R_{C2} , C_2 and R'_2 ;
- One pure imaginary pole-pair: the branch of L'_2 and C'_2 .

In fact, choosing such circuit topology through observations requires a lot of experience, making this model less accessible to novice designers. Therefore, a clear and systematic procedure is needed for synthesizing the equivalent circuit.

- b.* Manual tweaking on the parameters are needed in [30] to achieve a high accuracy. As a result of numerous trial/error iterations, this procedure becomes complex and time-consuming. Therefore, a computer-aided procedure seems more attractive for practical applications.

2.1.3 Introduction to the Developed Modeling Method

In consideration with the previous necessities, the HF equivalent circuit model for CM chokes proposed in [30] will be improved so that its circuit topology can be determined systematically. Besides, the parameters of the model will be extracted by a numerical method called Iterative Rational Function Approximation (IRFA). Using an unfixed topology coupled with IRFA algorithm, the equivalent circuits can be generated automatically, based on well-chosen impedance measurements. With decent treatment, the obtained equivalent circuit allows to have a good accuracy over a wide frequency range.

For better understanding, the IRFA method will be presented at first step and the improved HF equivalent circuit model will be introduced subsequently.

2.2 Iterative Rational Function Approximation Approach

2.2.1 Reminder on Rational Functions

Transfer function characterizes the input-output relation of a linear system and it has long been used in automatic and electronic engineering. It represents the Laplace (or Fourier) transform of the impulse response of a linear time-invariant system with zero initial conditions and zero equilibrium point. This function is

expressed by a rational function that is given in the following form:

$$H(s) = \frac{N(s)}{D(s)} \quad (2.2)$$

where the numerator $N(s)$ and the denominator $D(s)$ are both polynomials of s . The roots of the numerator $N(s)$ is called the zeros of the rational function and the roots of the denominator $D(s)$ is called the poles.

For single-port components, the current and the voltage on the terminals of the components are regarded as the input and the output, so their transfer functions take the form of impedance or admittance. Throughout this chapter, the term rational function is used instead of transfer function since the former one is more mathematical and the latter one is more physical.

2.2.2 Rational Function Approximation

Rational Function Approximation (RFA) method has long been studied for linear system identification in automatic control fields [42].

For our case of interest, the impedance $Z(s)$ (or admittance $Y(s)$) of a linear circuit network can be expressed by a rational function given by equation (2.3)

$$Z(s) = \frac{N(s)}{D(s)} = \frac{b_m s^m + b_{m-1} s^{m-1} + \dots + b_1 s + b_0}{a_n s^n + a_{n-1} s^{n-1} + \dots + a_1 s + 1} \quad (2.3)$$

with $|m-n| \leq 1$ and $s = j\omega$. Note that only the analysis on $Z(s)$ is given in this section but the same analysis can be conducted for the admittance $Y(s)$. From one measured impedance $Z_{meas}(s)$, the corresponding $Z(s)$ can be identified by the RFA method through a nonlinear optimization process. It consists in searching coefficients a_i and b_j in order to minimize the following cost function (2.4)

$$\arg \min_{a_i, b_j} \sum_k |\varepsilon_k|^2 = \arg \min_{a_i, b_j} \sum_k \left| Z_{meas}(s_k) - \frac{N(s_k)}{D(s_k)} \right|^2 \quad (2.4)$$

where $s_k = j\omega_k$ ($k=1\dots N$) with ω_k the sample frequencies.

To solve this problem, nonlinear methods such as Newton-Gauss or Levenberg-Marquardt algorithm can be used [43]. However, the slow convergence of these methods is quite troublesome, and the obtained results may be incorrect due

to the convergence to some local optimal points. In [44], Levy proposed a linearization technique to circumvent this problem. Stemming from Levy's technique, the authors introduced in [45] an RFA method to build the macro-models of HF interconnects. Reformulating (2.4) by multiplying the equation with the denominator $D(s_k)$ gives a linearized cost function (2.5).

$$\arg \min_{a_i, b_j} \sum_k |D(s_k) \varepsilon_k|^2 = \arg \min_{a_i, b_j} \sum_k |D(s_k) Z_{meas}(s_k) - N(s_k)|^2 \quad (2.5)$$

It implies solving the following linear system (2.6), which can be written into real and imaginary parts separately (2.7).

$$N(s_k) - Z_{meas}(s_k)D(s_k) = 0 \quad (2.6)$$

$$\begin{cases} \operatorname{Re}[N(s_k)] - \operatorname{Re}[Z_{meas}(s_k)D(s_k)] = 0 \\ \operatorname{Im}[N(s_k)] - \operatorname{Im}[Z_{meas}(s_k)D(s_k)] = 0 \end{cases} \quad (2.7)$$

For example, suppose that m and n are even numbers and $Z_{meas}(s_k) = x_k + jy_k$, the matrix form of (2.7) can be written as (2.8).

$$\begin{pmatrix} 1 & 0 & -\omega_1^2 & 0 & \cdots & 0 & j^m \omega_1^m & \omega_1 y_1 & \omega_1^2 x_1 & \cdots & -j^n \omega_1^n x_1 \\ 1 & 0 & -\omega_2^2 & 0 & \cdots & 0 & j^m \omega_2^m & \omega_2 y_2 & \omega_2^2 x_2 & \cdots & -j^n \omega_2^n x_2 \\ \vdots & \vdots & \vdots & \vdots & \vdots & \vdots & \vdots & \vdots & \vdots & \vdots & \vdots \\ 1 & 0 & -\omega_N^2 & 0 & \cdots & 0 & j^m \omega_N^m & \omega_N y_N & \omega_N^2 x_N & \cdots & -j^n \omega_N^n x_N \\ 0 & 1 & 0 & -\omega_1^3 & \cdots & j^{m-2} \omega_1^{m-1} & 0 & -\omega_1 x_1 & \omega_1^2 y_1 & \cdots & -j^n \omega_1^n y_1 \\ 0 & 1 & 0 & -\omega_2^3 & \cdots & j^{m-2} \omega_2^{m-1} & 0 & -\omega_2 x_2 & \omega_2^2 y_2 & \cdots & -j^n \omega_2^n y_2 \\ \vdots & \vdots & \vdots & \vdots & \vdots & \vdots & \vdots & \vdots & \vdots & \vdots & \vdots \\ 0 & 1 & 0 & -\omega_N^3 & \cdots & j^{m-2} \omega_N^{m-1} & 0 & -\omega_N x_N & \omega_N^2 y_N & \cdots & -j^n \omega_N^n y_N \end{pmatrix} \begin{pmatrix} b_0 \\ b_1 \\ \vdots \\ b_m \\ a_1 \\ a_2 \\ \vdots \\ a_n \end{pmatrix} = \begin{pmatrix} a_0 x_1 \\ a_0 x_2 \\ \vdots \\ a_0 x_N \\ a_0 y_1 \\ a_0 y_2 \\ \vdots \\ a_0 y_N \end{pmatrix} \quad (2.8)$$

Due to the large number of measured points (at least 200 points for an impedance analyzer), this system (2.8) is over-determined and should be solved in a least-square sense.

To determine the values of coefficients a_i and b_j , QR factorization using Householder transformation [46] has to be applied to solve the over-determined system (2.7). This method is proved to be stable and has a median computation complexity. The detail of Householder transformation is omitted here but can be found in Appendix I. After the factorization, \mathbf{A} is transformed into an upper-

triangle matrix with which the systems $\mathbf{AX}=\mathbf{B}$ can be solved.

With the denominator parameters b_j known, the poles p_i of $Z(s)$ can then be solved using Matlab function “roots”. The next step is to express $Z(s)$ into a pole-residue form (2.9).

$$Z(s) = d + e \cdot s + \underbrace{\sum_{k=1}^R \frac{r_k}{s - p_k}}_{\text{Real poles}} + \underbrace{\sum_{k=R+1}^{I+R} \left(\frac{r_k}{s - p_k} + \frac{r_k^*}{s - p_k^*} \right)}_{\text{Complex conjugate pole pairs}} \quad (2.9)$$

where p_k and r_k indicate the pole and the residue, the superscript $*$ denotes the complex conjugate, d denotes the direct term and e the s -proportional term.

Here, one can establish again a linear over-determined system $\mathbf{AX}=\mathbf{B}$, where \mathbf{A} , \mathbf{X} and \mathbf{B} are given by (2.10), (2.11) and (2.12) respectively. Using the previous stated QR factorization method, the values of d , e , residues r_k (real and complex) can finally be calculated.

$\mathbf{A} =$

$$\begin{pmatrix} 1 & 0 & \operatorname{Re}\left(\frac{1}{j\omega_1 - p_1}\right) & \cdots & \operatorname{Re}\left(\frac{1}{j\omega_1 - p_R}\right) & \operatorname{Re}\left(\frac{1}{j\omega_1 - p_{R+1}} + \frac{1}{j\omega_1 - p_{R+1}^*}\right) & \operatorname{Im}\left(\frac{-1}{j\omega_1 - p_{R+1}} + \frac{-1}{j\omega_1 - p_{R+1}^*}\right) & \cdots & \operatorname{Re}\left(\frac{1}{j\omega_1 - p_I} + \frac{1}{j\omega_1 - p_I^*}\right) & \operatorname{Im}\left(\frac{-1}{j\omega_1 - p_I} + \frac{-1}{j\omega_1 - p_I^*}\right) \\ 1 & 0 & \operatorname{Re}\left(\frac{1}{j\omega_2 - p_1}\right) & \cdots & \operatorname{Re}\left(\frac{1}{j\omega_2 - p_R}\right) & \operatorname{Re}\left(\frac{1}{j\omega_2 - p_{R+1}} + \frac{1}{j\omega_2 - p_{R+1}^*}\right) & \operatorname{Im}\left(\frac{-1}{j\omega_2 - p_{R+1}} + \frac{-1}{j\omega_2 - p_{R+1}^*}\right) & \cdots & \operatorname{Re}\left(\frac{1}{j\omega_2 - p_I} + \frac{1}{j\omega_2 - p_I^*}\right) & \operatorname{Im}\left(\frac{-1}{j\omega_2 - p_I} + \frac{-1}{j\omega_2 - p_I^*}\right) \\ \vdots & \vdots & \vdots & \vdots & \vdots & \vdots & \vdots & \vdots & \vdots & \vdots \\ 1 & 0 & \operatorname{Re}\left(\frac{1}{j\omega_N - p_1}\right) & \cdots & \operatorname{Re}\left(\frac{1}{j\omega_N - p_R}\right) & \operatorname{Re}\left(\frac{1}{j\omega_N - p_{R+1}} + \frac{1}{j\omega_N - p_{R+1}^*}\right) & \operatorname{Im}\left(\frac{-1}{j\omega_N - p_{R+1}} + \frac{-1}{j\omega_N - p_{R+1}^*}\right) & \cdots & \operatorname{Re}\left(\frac{1}{j\omega_N - p_I} + \frac{1}{j\omega_N - p_I^*}\right) & \operatorname{Im}\left(\frac{-1}{j\omega_N - p_I} + \frac{-1}{j\omega_N - p_I^*}\right) \\ 0 & \omega_1 & \operatorname{Im}\left(\frac{1}{j\omega_1 - p_1}\right) & \cdots & \operatorname{Im}\left(\frac{1}{j\omega_1 - p_R}\right) & \operatorname{Im}\left(\frac{1}{j\omega_1 - p_{R+1}} + \frac{1}{j\omega_1 - p_{R+1}^*}\right) & \operatorname{Re}\left(\frac{1}{j\omega_1 - p_{R+1}} + \frac{1}{j\omega_1 - p_{R+1}^*}\right) & \cdots & \operatorname{Im}\left(\frac{1}{j\omega_1 - p_I} + \frac{1}{j\omega_1 - p_I^*}\right) & \operatorname{Re}\left(\frac{1}{j\omega_1 - p_I} + \frac{1}{j\omega_1 - p_I^*}\right) \\ 0 & \omega_2 & \operatorname{Im}\left(\frac{1}{j\omega_2 - p_1}\right) & \cdots & \operatorname{Im}\left(\frac{1}{j\omega_2 - p_R}\right) & \operatorname{Im}\left(\frac{1}{j\omega_2 - p_{R+1}} + \frac{1}{j\omega_2 - p_{R+1}^*}\right) & \operatorname{Re}\left(\frac{1}{j\omega_2 - p_{R+1}} + \frac{1}{j\omega_2 - p_{R+1}^*}\right) & \cdots & \operatorname{Im}\left(\frac{1}{j\omega_2 - p_I} + \frac{1}{j\omega_2 - p_I^*}\right) & \operatorname{Re}\left(\frac{1}{j\omega_2 - p_I} + \frac{1}{j\omega_2 - p_I^*}\right) \\ \vdots & \vdots & \vdots & \vdots & \vdots & \vdots & \vdots & \vdots & \vdots & \vdots \\ 0 & \omega_N & \operatorname{Im}\left(\frac{1}{j\omega_N - p_1}\right) & \cdots & \operatorname{Im}\left(\frac{1}{j\omega_N - p_R}\right) & \operatorname{Im}\left(\frac{1}{j\omega_N - p_{R+1}} + \frac{1}{j\omega_N - p_{R+1}^*}\right) & \operatorname{Re}\left(\frac{1}{j\omega_N - p_{R+1}} + \frac{1}{j\omega_N - p_{R+1}^*}\right) & \cdots & \operatorname{Im}\left(\frac{1}{j\omega_N - p_I} + \frac{1}{j\omega_N - p_I^*}\right) & \operatorname{Re}\left(\frac{1}{j\omega_N - p_I} + \frac{1}{j\omega_N - p_I^*}\right) \end{pmatrix} \quad (2.10)$$

$$\mathbf{X} = \left(d \quad e \quad r_1 \quad \cdots \quad r_R \quad \operatorname{Re}(r_{R+1}) \quad \operatorname{Im}(r_{R+1}) \quad \cdots \quad \operatorname{Re}(r_I) \quad \operatorname{Im}(r_I) \right)^T \quad (2.11)$$

$$\mathbf{B} = \left(x_1 \quad x_2 \quad \cdots \quad x_N \quad y_1 \quad y_2 \quad \cdots \quad y_N \right)^T \quad (2.12)$$

Till now, the rational function $Z(s)$ is identified by the RFA method and is ready for further process.

2.2.3 Introduction of Iterative Rational Function Approximation Method

2.2.3.1 Limitations of the RFA Method

Though the RFA method is able to identify the rational function for a specified frequency response, it cannot be directly applied in our applications because Levy's linearization technique leads to a frequency bias problem [47]. Indeed, according to (2.4) and (2.5), the original cost function is linearized with multiplying by the denominator $D(s_k)$. As a result, the new cost function (2.5) is weighted by $D(s_k)$ that increases rapidly with frequency ($s_k = j\omega_k$), making the errors over HF more important than those over LF. As a consequence, the frequency bias of the RFA method will cause poor fitting accuracy at LF. Besides, when treating measured data that contains irrational noises, the RFA method will have severer frequency bias problem and thereby gives even wrong fitting results at LF. These properties are undesirable for identifying the DC resistance part of magnetic components in power electronics. As a result, the simple RFA method cannot be applied if accuracy is required over wide frequency range.

2.2.3.2 The IRFA Method

To alleviate the frequency bias of the RFA method, an iterative rational function approximation using Sanathanan-Koerner (SK) iteration is implemented in this work. It consists in dividing the expression (2.6) by the previous iteration $t-1$ of $D^{[t-1]}(s_k)$. For the iteration t , the expression (2.6) can then be written as (2.13).

$$\frac{N^{[t]}(s_k)}{D^{[t-1]}(s_k)} - \frac{Z_{meas}(s_k)D^{[t]}(s_k)}{D^{[t-1]}(s_k)} = 0 \quad (2.13)$$

Therefore, the new cost function for this problem becomes:

$$\arg \min_{a_i, b_j} \sum_k \left| \frac{D^{[t]}(s_k)}{D^{[t-1]}(s_k)} \varepsilon_k \right|^2 = \arg \min_{a_i, b_j} \sum_k \left| \frac{D^{[t]}(s_k)}{D^{[t-1]}(s_k)} Z_{meas}(s_k) - \frac{N^{[t]}(s_k)}{D^{[t-1]}(s_k)} \right|^2 \quad (2.14)$$

When the algorithm converges, $D^{[t]}(s_k) \rightarrow D^{[t-1]}(s_k)$, so the above cost function asymptotically converges to (2.4). Therefore, the frequency bias introduced by Levy's technique is significantly alleviated and better fitting accuracy over LF can

be obtained. The basic IRFA formulation is given by (2.15).

$$\begin{cases} \operatorname{Re}\left[\frac{N^{[t]}(s_k)}{D^{[t-1]}(s_k)}\right] - \operatorname{Re}\left[\frac{D^{[t]}(s_k)}{D^{[t-1]}(s_k)}Z_{meas}(s_k)\right] = 0 \\ \operatorname{Im}\left[\frac{N^{[t]}(s_k)}{D^{[t-1]}(s_k)}\right] - \operatorname{Im}\left[\frac{D^{[t]}(s_k)}{D^{[t-1]}(s_k)}Z_{meas}(s_k)\right] = 0 \end{cases} \quad (2.15)$$

As the real and the imaginary parts of (2.15) are solved together, normalization is necessary for achieving balanced fitting accuracy between the both parts. Instead of using $1/|Z_{meas}(s_k)|$ as the normalization factor, the real part and imaginary part of (2.15) are normalized by $1/\operatorname{Re}[Z^{[t]}(s_k)]$ and $1/\operatorname{Im}[Z^{[t]}(s_k)]$.

Based on the above analysis, the developed IRFA formulation is given as:

$$\begin{cases} \operatorname{Re}\left[W_{\operatorname{Re}}^{[t]}(s_k)N^{[t]}(s_k)\right] - \operatorname{Re}\left[W_{\operatorname{Re}}^{[t]}(s_k)Z_{meas}(s_k)D^{[t]}(s_k)\right] = 0 \\ \operatorname{Im}\left[W_{\operatorname{Im}}^{[t]}(s_k)N^{[t]}(s_k)\right] - \operatorname{Im}\left[W_{\operatorname{Im}}^{[t]}(s_k)Z_{meas}(s_k)D^{[t]}(s_k)\right] = 0 \end{cases} \quad (2.16)$$

with the normalization factors $W_{\operatorname{Re}}^{[t]}(s_k)$ and $W_{\operatorname{Im}}^{[t]}(s_k)$ given by:

$$\begin{cases} W_{\operatorname{Re}}^{[t]}(s_k) = \frac{[D^{[t-1]}(s_k)]^*}{\operatorname{Re}[D^{[t-1]}(s_k)]\operatorname{Re}[N^{[t-1]}(s_k)] + \operatorname{Im}[D^{[t-1]}(s_k)]\operatorname{Im}[N^{[t-1]}(s_k)]} \\ W_{\operatorname{Im}}^{[t]}(s_k) = \frac{[D^{[t-1]}(s_k)]^*}{\operatorname{Re}[D^{[t-1]}(s_k)]\operatorname{Im}[N^{[t-1]}(s_k)] - \operatorname{Im}[D^{[t-1]}(s_k)]\operatorname{Re}[N^{[t-1]}(s_k)]} \end{cases} \quad (2.17)$$

The derivation of (2.17) is detailed in Appendix II.

The complete algorithm of IRFA is given in Figure 2.4, where the iteration error tolerance $\varepsilon_{\text{iter}}$ is defined as:

$$\varepsilon_{\text{iter}} = \max_k \left\{ \left| \frac{Z_{fit}(j\omega_k) - Z_{meas}(j\omega_k)}{Z_{meas}(j\omega_k)} \right| \right\} \quad (2.18)$$

where $Z_{fit}(j\omega_k)$ denotes the fitted rational function by the IRFA method. Apart from this choice, there are many other options for defining the iteration error tolerance such as relative error on real parts or absolute error. Depending on different applications, the designer can choose the most appropriate error tolerance for the fitting algorithm.

The algorithm (see Figure 2.4) first launches the RFA method to obtain a starting point. Then, the IRFA with normalization is executed until the stopping conditions (ε_{max} and N_{max}) are satisfied. During these iterations, unstable poles (with $\operatorname{Re}(p_k) > 0$) may occur. To avoid this problem, unstable poles are flipped to the other

Algorithm IRFA**Input:** n (Denominator Order), m (Numerator Order)**Input:** N_{\max} (Stopping iteration number), ε_{\max} (Stopping error)**Input:** normalization options**RFA:**

1. Computation of the poles using (2.7)(2.8)
2. Computation of the pole-residue expression using (2.9)

IRFA:

3. **while** $\varepsilon_{\text{iter}} > \varepsilon_{\max}$ **and** $N_{\text{iter}} < N_{\max}$ **do**
4. Computation of $W_{\text{Re}}^{[t]}(s_k)$ and $W_{\text{Im}}^{[t]}(s_k)$ for iteration t via (2.17)
5. Computation of the poles using (2.16)
6. Computation of the pole-residue expression using (2.9)-(2.12)
7. **end while**

END

Figure 2.4. Algorithm of the IRFA method.

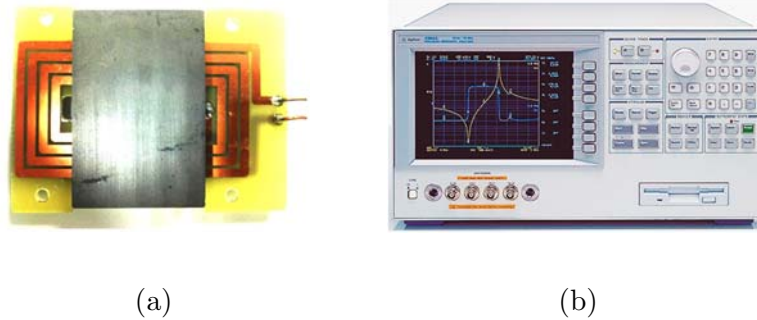


Figure 2.5. Impedance measurements for the IRFA method. (a) 8-turn planar inductor. (b) HP4294A impedance analyzer.

side of imaginary axis [48].

2.2.3.3 Algorithm Comparisons

In order to show the efficiency of the IRFA method and the normalization technique, a comparative study is performed. The impedance of an 8-turn planar inductor with Ferroxcube 3F3 ferrite planar E38 core [Figure 2.5(a)] is first measured (from 40 Hz to 70 MHz) with an impedance analyzer HP4294A [Figure 2.5(b)] and then fitted by different approaches using a rational function with $m=n=6$.

The fitting results are compared in Figure 2.6. Due to the frequency bias problem, the RFA method [Figure 2.6(a)] gives good fitting results over HF side but completely wrong results in LF band. With the IRFA method [Figure 2.6(b)]

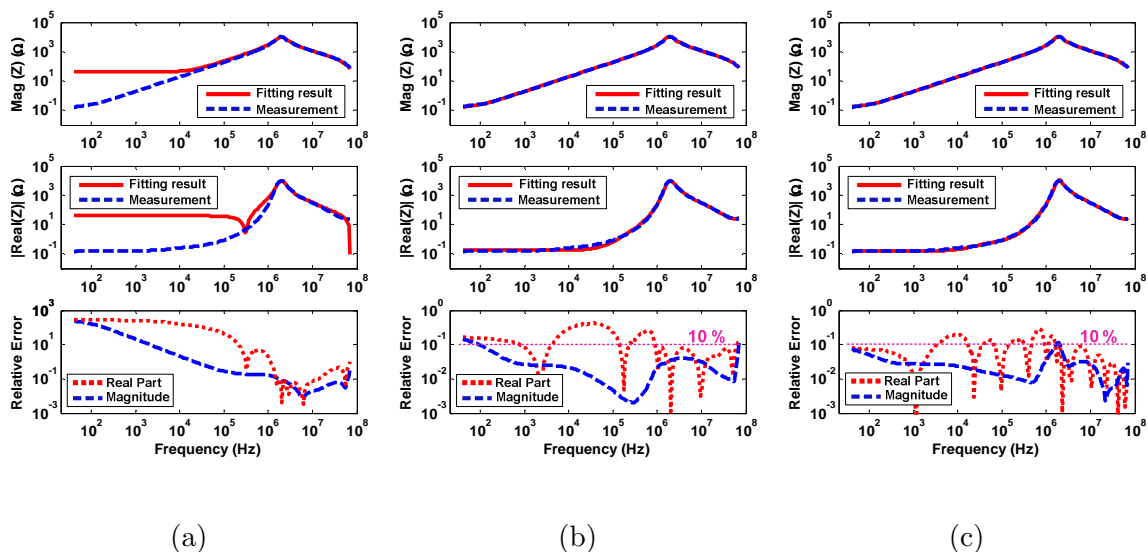


Figure 2.6. Comparison of the fitting results. (a) RFA with frequency bias problem. (b) IRFA without balanced weighting. (c) Proposed IRFA with balanced weighting.

and (c)], the frequency bias is alleviated so that the fitting accuracy is much better, especially over LF band. The difference between Figure 2.6 (b) and Figure 2.6 (c) is the normalization technique that is applied: On Figure 2.6 (b), the IRFA algorithm is tested without any balanced technique while on Figure 2.6 (c), a balanced normalization is held. From the error curves, it can be seen that the fitting accuracy of the real part is further improved when the balanced normalization technique is applied.

As the impedance curves for magnetic components are generally very smooth (with very few resonances), the fitting accuracy of IRFA leads to very good results on a wide frequency band. Generally speaking, the accuracy that can be achieved directly depends on the order of the rational function for computation. To further improve this accuracy, higher order rational function (with larger m and n) should be employed. However, as will be shown in the next section, the resulting equivalent circuit will also be more bulky. This trade-off between the fitting accuracy and complexity should be carefully considered by the designer.

2.3 IRFA Adapted Equivalent Circuit Synthesis

In the previous section, the IRFA method has been used for identifying the rational function of a measured impedance (or admittance). To transform the

rational function into an equivalent circuit form, a systematic synthesis method will be discussed in the following parts.

2.3.1 Foster Expansion General Expression

The rational function (2.9) identified by the IRFA method is the sum of direct terms d and $e \cdot s$, real pole-residue terms and complex pole-residue pair terms. Rearranging the complex pole-residue terms, the expression (2.9) can be transformed into its Foster expansion form (2.19).

$$Z(s) = d + e \cdot s + \overbrace{\sum_{k=1}^R \frac{r_k}{s - p_k}}^{\text{Real poles}} + \overbrace{\sum_{k=R+1}^{I+R} \left(\frac{a_k s + b_k}{s^2 + m_k s + n_k} \right)}^{\text{Complex conjugate pole pairs}} \quad (2.19)$$

Note that the parameters a_k and b_k listed here are different from those in (2.3). Based on this expression (2.18), a systematic synthesis method is introduced in [49] to generate the corresponding equivalent circuit. The Table 2.2 summarizes the detailed equivalent circuits for impedance or admittance expressions. Each term is discussed in the following sections.

2.3.2 General Topology and Terms d and $e \cdot s$

For impedance $Z(s)$, the “+” sign implies a series connection. The constant d corresponds to a resistance $R=d$ whereas the s -asymptotical term $e \cdot s$ can be represented by an inductance $L=e$.

For admittance $Y(s)$, the circuit can be obtained by a similar analysis. First of all, the connection style becomes parallel. Next, d corresponds to a resistance $R=1/d$ and the $e \cdot s$ term denotes a capacitance $C=e$.

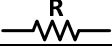
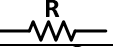

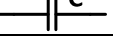
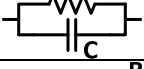
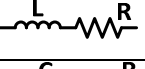

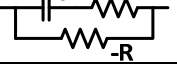
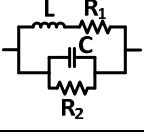
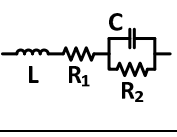
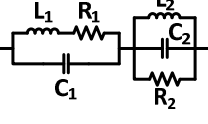
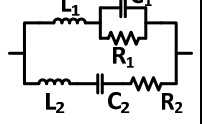
2.3.3 Real Pole-Residue Terms

Real poles come together with real residues. Therefore, the equivalent circuit for these terms is R - C in parallel for $Z(s)$ or R - L in series for $Y(s)$, as given by

$$Z(s) = \frac{\frac{1}{C}}{s + \frac{1}{RC}} \quad \text{or} \quad Y(s) = \frac{\frac{1}{L}}{s + \frac{R}{L}} \quad (2.20)$$

Sometimes, the IRFA method gives negative residues as results, which will

Table 2.2 Equivalent Circuit Synthesis with Rational Functions.

Term		Z(s)		Y(s)	
		Circuit	Expression	Circuit	Expression
Constant	d		$R=d$		$R=1/d$
s-asymptotical	e/s		$L=e$		$C=e$
Real pole $\frac{r_k}{s-p_k}$	$r_k > 0$		$C=1/r_k$ $R=-r_k/p_k$		$L=1/r_k$ $R=-p_k/r_k$
	$r_k < 0$		$R=r_k/p_k$ $L=-R/p_k$		$R=p_k/r_k$ $C=-1/(p_k R)$
Complex-pole Pair $\frac{a_k s + b_k}{s^2 + m_k s + n_k}$	Minimum type		$C=1/a_k$, $R_2=(Cm_k - C^2 b_k)^{-1}$, $R_1=(n_k/b_k - 1/R_2)^{-1}$, $L=R_1/(b_k C)$		$L=1/a_k$, $R_1=Lm_k - L^2 b_k$, $R_2=n_k/b_k - R_1$, $C=1/(b_k L R_2)$
	Extended type		$R_1=b_k/n_k$, $L_1=R_1/m_k$, $C_1=(n_k L_1)^{-1}$, $C_2=(a_k - 1/C_1)^{-1}$, $R_2=(m_k C_2)^{-1}$, $L_2=(n_k C_2)^{-1}$		$R_1=n_k/b_k$, $C_1=(m_k R_1)^{-1}$, $L_1=(n_k C_1)^{-1}$, $L_2=(a_k - 1/L_1)^{-1}$, $R_2=m_k L_2$, $C_2=(n_k L_2)^{-1}$

yield negative-component values (see Table 2.2). Strictly speaking, these negative elements are not feasible for designing purposes (except for using active circuits) and thereby should be avoided. However, if these negative elements are not directly measurable, they can be accepted for modeling and simulation purposes because they allow obtaining accurate equivalent circuits.

Negative elements can be simulated in frequency analysis without problem. However, to introduce negative elements into circuit simulation softwares for time-domain analysis, techniques such as phase-inverting transformer or controlled-source can be used. Here, another topology is suggested: a positive-valued cell combined together with a negative resistance, as illustrated in Table 2.2. The corresponding rational functions for these equivalent circuits are:

$$Z(s) = \frac{-R^2/L}{s + R/L} \quad \text{or} \quad Y(s) = \frac{-(CR^2)^{-1}}{s + (CR)^{-1}} \quad (2.21)$$

Taking admittance $Y(s)$ as example and supposing that a stable real pole p_k is extracted with a negative residue r_k , the parameters of the $Y(s)$ equivalent circuit can be derived by (2.22).

$$\begin{cases} R = p_k / r_k & \text{positive} \\ C = -1 / (p_k R) & \text{positive} \\ -R = -p_k / r_k & \text{negative} \end{cases} \quad (2.22)$$

It can be seen that the R - C series cell is now positive and the negative resistance can be subsequently merged into the resistance for the constant term d with:

$$R^* = \left(d - \frac{1}{R} \right)^{-1} \quad (2.23)$$

where R^* is the new resistance after the transformation. Similar analysis can be performed for $Z(s)$ as well. With these circuits, the negative elements for real pole-residue terms can be reduced to minimum.

2.3.4 Complex Pole-Residue Pair Terms

To convert complex-pole pairs, two types of equivalent circuit are well known in the literatures [49, 50]. The first one consists in a four-element circuit and is referred as “minimum” type since its rational function has only four free variables: a_k , b_k , m_k and n_k (see Table 2.2). The other one, referred as “Extended” type, uses a six-element circuit with easier parameter calculation formulas [50]. The detailed expressions for calculating the equivalent circuit parameters for a given rational function are detailed in Table 2.2.

With this synthesis method, the equivalent circuit of the rational function (2.19) can be generated systematically, as shown in Figure 2.7(a). The equivalent circuits for admittance $Y(s)$ can be built in a similar way [Figure 2.7(b)].

Now the planar 8-turn inductor with Ferroxcube 3F3 ferrite Planar E38 core [Figure 2.5(a)] is revisited. The IRFA program is executed firstly to identify the rational function of its measured admittance $Y_{meas}(j\omega_k) = 1/Z_{meas}(j\omega_k)$. A rational function (2.3) with parameters $m=7$ and $n=6$, is fixed to fit the admittance from 40 Hz to 70 MHz. The obtained fitting results are listed in Table 2.3 where two real poles with negative residues are found. Based on the previous equivalent circuit synthesis method, the circuit representing this admittance can be obtained, as shown in Figure 2.8(a). Two negative R - L branches are then extracted in this circuit to be modified into positive elements using the preceding transformation,

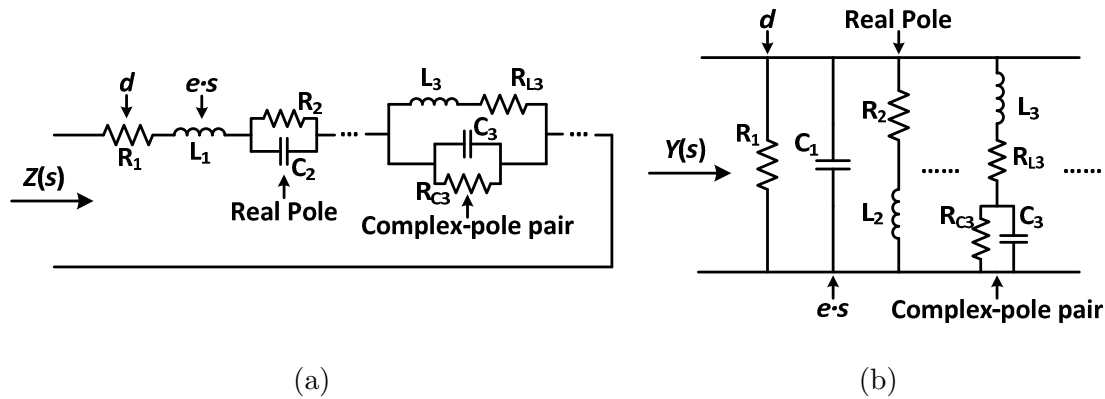


Figure 2.7. Synthesized equivalent circuit from rational functions. (a) Impedance $Z(s)$. (b) Admittance $Y(s)$.

Table 2.3 IRFA Fitting Results for the 8-turn Planar Inductor.

	<i>Poles</i>	<i>Residues</i>
<i>Real poles</i>	-5.3359E2	3.2573E3
	-2.0630E5	2.2961E1
	-1.5789E7	-2.9894E3
	-2.6953E8	-1.9200E5
<i>Complex poles</i>	$-3.5349E7 \pm j1.2863E8$	$3.1701E2 \mp j1.6733E3$
	$d = 8.8364E-4$; $e = 1.1138E-11$	

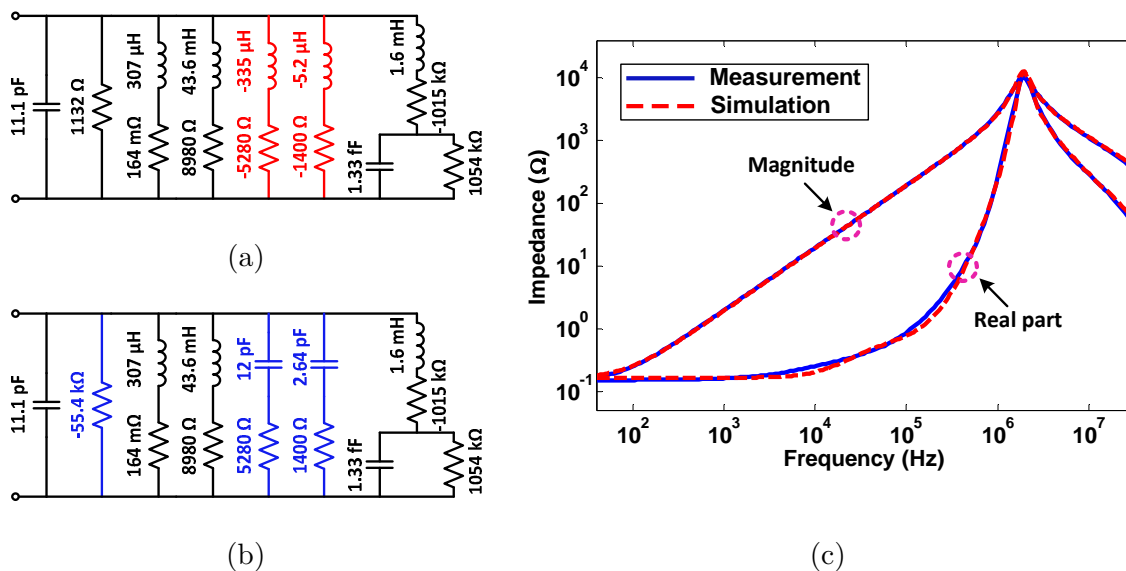


Figure 2.8. Synthesized equivalent circuit for the 8-turn planar inductor. (a) Equivalent circuit with negative branches. (b) Equivalent circuit after transformation. (c) Comparison of simulated and measured impedances.

resulting in a new equivalent circuit Figure 2.8(b). This circuit is finally introduced into Pspice for AC analysis and the obtained frequency response of its impedance

$Z_{sim}(s)$ is compared with the measured one in Figure 2.8(c). It can be seen that the frequency response of the synthesized equivalent circuit matches very well with the measured data, which validates the circuit synthesis approach.

The above analysis shows the effectiveness of the equivalent circuit synthesis based on the IRFA method. From measured impedances or admittances, a flexible equivalent circuit can be automatically generated.

Based on these techniques, the complete HF equivalent circuit for CM chokes will be introduced in the next section.

2.4 Complete Identification Process

Recall that the HF equivalent circuit model for CM chokes presented in [30] can be improved in the following two aspects:

- Providing a systematic equivalent circuit synthesis method;
- Using computer-aided parameter extraction.

In this section, an improved HF equivalent circuit model of CM chokes, combined with its parameter identification process, is presented.

2.4.1 Improved HF Equivalent Circuit Model

The equivalent circuit model is illustrated in Figure 2.9 and it is built on the basis of the IRFA fitting results and the circuit synthesis technique presented in Section 2.3. Like the equivalent circuit of [30], it keeps a symmetrical structure and the parasitic capacitances are assumed to be lossless as well. However, as C_e , C_p and C_c are sufficient for characterizing the electrostatic behavior of a two-winding transformer that is strongly coupled [41], the capacitance C_s in Figure 2.2 can be neglected and is no longer included in our applications. The major improvement of this new model in comparison with [30], is that the leakage impedance Z_1 and the magnetizing one Z_2 are completely determined by the IRFA method. Therefore, the obtained equivalent circuit is guaranteed to be accurate over a broad band of frequency since both topology and parameter values are determined via mathematical calculations.

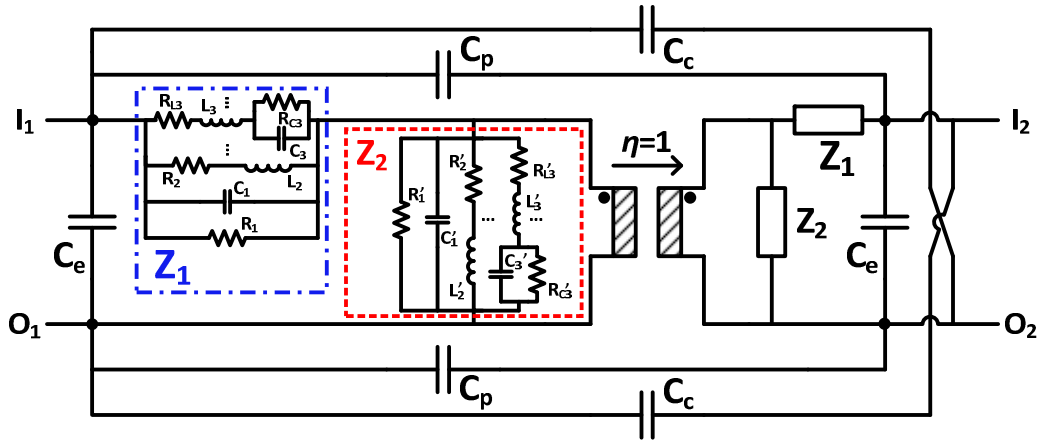


Figure 2.9. Improved IRFA-based equivalent circuit.

Table 2.4 Measurement Configurations for the Extraction Procedure.

Notation	Measurement Configuration	Element	Equivalent Circuit
T_3		$2C_p + 2C_c$	
T_0		$Z_1 / 2;$ $2(C_e + C_p)$	
T_2		$(Z_1 + Z_2) / 2 ;$ $2(C_e + C_c)$	

2.4.2 General Parameter Extraction Procedure

The parameter extraction procedure in [30] employs five impedance measurements to determine the equivalent circuit parameters. As C_s is discarded from the capacitances network of the improved model, the extraction procedure is accordingly simplified with only three impedance measurements, as summarized in Table 2.4. To extract the impedances Z_1 and Z_2 , two measurements T_0 and T_2 have to be carried out (Table 2.4). To obtain the three parasitic capacitances C_e , C_c and C_p , three independent equations are also needed. Thus, apart from T_0 and T_2 , one more measurement T_3 is provided, from which the system (2.24) is obtained.

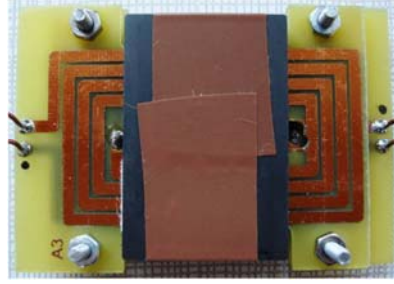
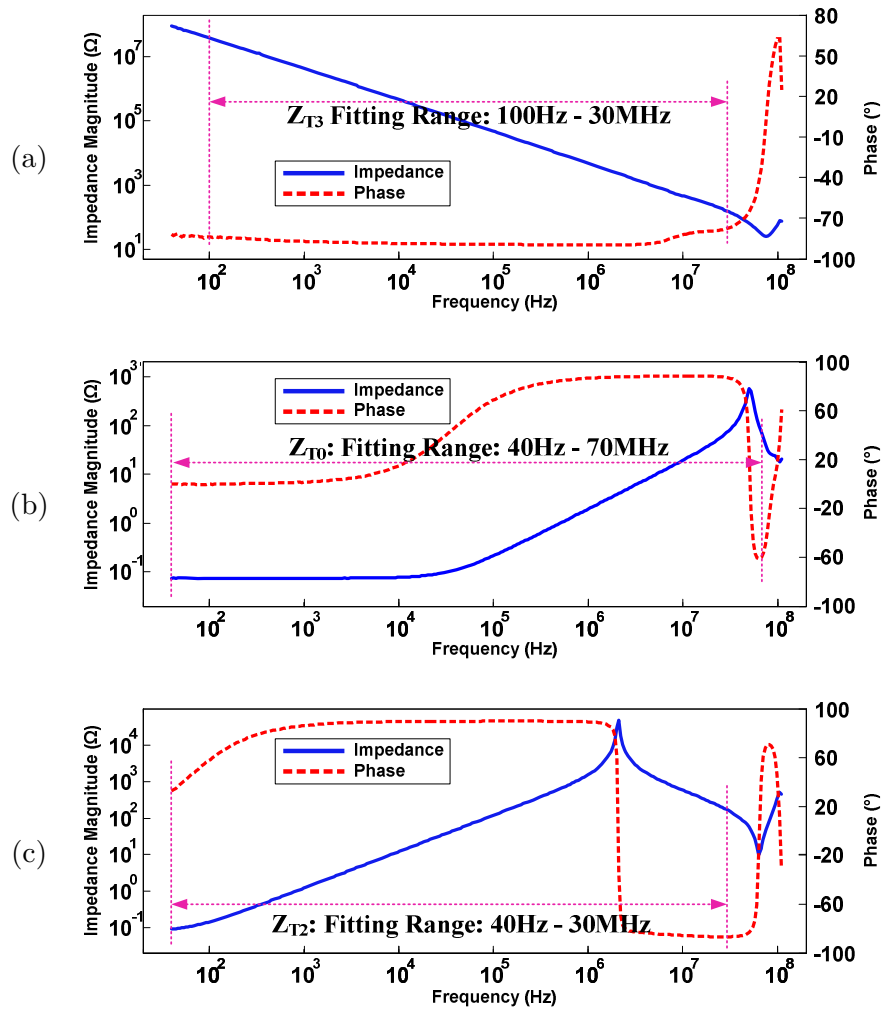


Figure 2.10. Planar CM choke under study.


 Figure 2.11. Measured impedances for the identification. (a) Z_{T3} . (b) Z_{T0} . (c) Z_{T2} .

$$\begin{cases} C_e + C_p = a & \text{Measurement } T_0 \\ C_e + C_c = b & \text{Measurement } T_2 \\ C_p + C_c = c & \text{Measurement } T_3 \end{cases} \quad (2.24)$$

Solving these equations, the values of the three parasitic capacitances can

then be derived. Note that when extracting Z_2 , Z_1 should be subtracted from the result of measurement T_2 since Z_2 is not directly measurable.

2.4.3 Application Example

For better understanding, the parameter extraction procedure is applied step by step on an example. The studied component is an 8-turn planar CM choke using Ferroxcube 3F4 ferrite planar E38 core (Figure 2.10). The first step consists in measuring the impedances Z_{T0} , Z_{T2} and Z_{T3} with the better accuracy as possible [51]. The measured impedances from 40 Hz to 110 MHz are presented in Figure 2.11. Next, these three impedances are processed successively in the following sections.

2.4.3.1 Analysis of Measurement T_3

With this configuration, the inter-winding parasitic capacitance $2(C_c + C_p)$ can be extracted. Traditional manual method extracts the capacitance by using the formula:

$$Z_{T3}(s_t) = \frac{1}{s_t C} \quad \text{or} \quad Y_{T3}(s_t) = s_t C \quad (2.25)$$

where $s_t = j2\pi f_t$ with f_t the sample frequency. In our extraction approach, the admittance $Y_{T3} = 1/Z_{T3}$ is preferred for the fitting process with the following expression:

$$Y_{T3} = 1 / Z_{T3} = d + e \cdot s = \frac{1}{R_p} + sC \quad (2.26)$$

where constant d denotes the dielectric losses and s -asymptotical term e denotes the capacitance $2(C_c + C_p)$. The resulting equivalent circuit is given by Figure 2.12(a). However, it can be seen from Figure 2.11(a) that the impedance is capacitive (-20 dB/Dec.) below several tens of megahertz and beyond that frequency, a series resonance appears and the impedance becomes inductive. This is well known that any capacitor has an equivalent series inductance (ESL) and an equivalent series resistance (ESR). Therefore, the equation will not be appropriate for fitting the impedance over the whole measured frequency band but only on a selected range. According to Figure 2.11(a), the upper limit of the fitting range is fixed at 30MHz where the phase is starting to rise abruptly. As the parasitic capacitances are

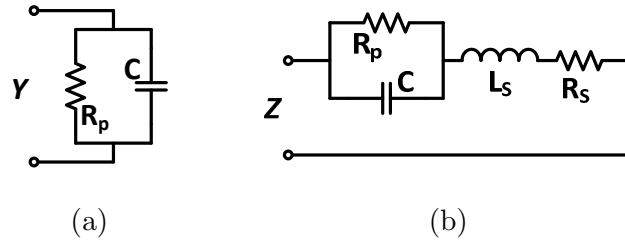


Figure 2.12. Equivalent circuit for extracting the capacitance. (a) R - C in parallel. (b) R - C in parallel with ESL and ESR.

assumed to be lossless, the constant term d is neglected and the extracted results for $2(C_c + C_p)$ is 29.98 pF.

A more sophisticated method for extracting the capacitance values can be performed with a more complete model, as given in Figure 2.12(b). It can be seen that an R_s - L_s series is added to represent the effects of the ESR and the ESL. To extract the parameters of this circuit, its impedance Z_{T3} is used for the fitting, as expressed by (2.27).

$$Z_{T3}(s) = R_s + sL_s + \frac{R_p}{sCR_p + 1} \quad (2.27)$$

Using a rational function with $m=2$ and $n=1$, the pole-residue expression can be fitted. Meanwhile, it should be mentioned that this rational function can be manually fitted without the fitting program. As the parasitic capacitances are lossless, the terms R_s , L_s and R_p have to be discarded after fitting anyway. However, this model is very useful for extracting the parameters of filter capacitors, as will be shown in the next section.

2.4.3.2 Analysis of Measurement T_0

In this measurement configuration, the magnetic flux generated by both the windings cancel in the ferrite core so the leakage impedance $Z_1/2$ and the capacitance $2(C_e + C_p)$ can be determined (see Table 2.4). Like what is done for measurement T_3 , the admittance Y_{T0} is treated instead of Z_{T0} in the IRFA fitting to extract the capacitance $2(C_e + C_p)$, which corresponds the e 's term in Figure 2.7(b). As a result, the order of the rational function $Y_{T0}(s)$ must verify: $m-n=1$. As said previously, choosing the order of the rational function consists in a trade-off

between accuracy and complexity of the obtained circuit. In this example, $m=6$ and $n=5$ are fixed as the order after a few trials. The frequency range for the fitting is from 40 Hz to 70 MHz to extract both DC resistance and the parasitic capacitances. The fitting results are given in Table 2.5 and the corresponding equivalent circuit is shown in Figure 2.13(a). The circuit for the impedance $Z_1/2$ is enclosed by the dashed box. The R - L branches are calculated with the real pole-residue pairs listed in Table 2.5. These elements can be interpreted as the reduced Partial Element Equivalent Circuits (PEEC) model considering the eddy current effect [52].

It is also interesting to study the importance of each branches of Y_{T0} . For this, the definition dominant pole is revised: a pole p_i with its residue r_i is called dominant pole if its $F_i = |r_i/\text{Re}(p_i)|$ is much larger than the other ones. According to this definition, the F_i for each pole is calculated and listed in Table 2.5. One can immediately find that the pole $p=-2.3224\text{E}+05$ is the dominate one, which corresponds to the $R(76 \text{ m}\Omega)$ - $L(330 \text{ nH})$ series branch. Therefore, this branch has the largest influence on the leakage admittance Y_{T0} . Note that with the obtained results, a negative capacitance is extracted since $e_{T0}<0$. Even if this negative capacitance is not directly measurable, it may cause instabilities in circuit simulations [53]. From the phase plot of Z_{T0} shown in Figure 2.11(b), it can also be observed that the impedance is not capacitive beyond the resonance frequency $f_r \approx 51 \text{ MHz}$. In fact, for f_r frequency, the PCB characteristic wave length can be calculated by [54]:

$$\lambda_{\text{PCB}} = \frac{c}{\sqrt{\varepsilon_{\text{eff}} f_r}} = \frac{3 \cdot 10^8 \text{ m/s}}{\sqrt{\varepsilon_{\text{eff}} 51 \text{ MHz}}} \approx \frac{6 \text{ m}}{\sqrt{\varepsilon_{\text{eff}}}} \quad (2.28)$$

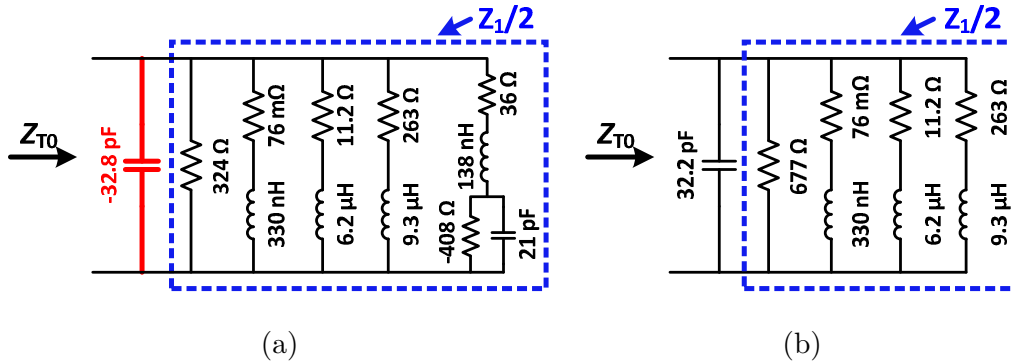
where c is the velocity of light in vacuum and ε_{eff} is the effective relative permittivity of the epoxy material of the PCBs. According to [54], ε_{eff} can be calculated empirically by (2.29):

$$\varepsilon_{\text{eff}} = \frac{\varepsilon_r + 1}{2} + \frac{\varepsilon_r - 1}{2} \left[\sqrt{\frac{w}{w + 12h}} + 0.04 \left(1 - \frac{w}{h} \right)^2 \right] \quad \text{for } \frac{w}{h} < 1 \quad (2.29)$$

where ε_r is the relative permittivity of the epoxy material, w is the width of conductors and h is the thickness of epoxy. For the FR-4 epoxy used in the studied

Table 2.5 Fitting Results of $Y_{T_0}(s)$.

$Y_{T_0}(s) = 1/Z_{T_0}(s)$		
$d_{T_0} = 3.0893\text{E-}3; e_{T_0} = -3.2803\text{E-}12$		
Poles	Residues	F_i
-7.3080E+07	3.6178E+06	0.05
+j5.5497E+08	+j1.2356E+06	
-7.3080E+07	3.6178E+06	3.8E-3
-j5.5497E+08	-j1.2356E+06	
-2.8458E+07	1.0814E+05	0.09
-1.8105E+06	1.6114E+05	
-2.3224E+05	3.0680E+06	13.2


 Figure 2.13. Equivalent circuit for Z_{T_0} . (a) Without approximation. (b) With approximation.

planar component, the value of ϵ_{eff} is about 3, so the resulting λ_{PCB} is around 3.8 m. Note that the total trace length for one winding of this component is about 1 m, which is already comparable to λ_{PCB} . Accordingly, the measured Y_{T_0} is affected by distributed effects beyond 51 MHz which cannot be described by a simple parallel resonator shown in Table 2.4. Due to the insufficiency of this circuit, negative capacitance appears for fitting Y_{T_0} . This is also the main limit of the lumped-element equivalent circuit modeling method.

In order to obtain a positive capacitance, some approximations can be made. First, we recombine together the complex pole-residue pair $(p_{T_0}, r_{T_0}) - (p_{T_0}^*, r_{T_0}^*)$, $d_{T_0}=3.0893\text{E-}3$ and $e_{T_0}=-3.2803\text{E-}12$ terms of $Y_{T_0}(s)$ in Table 2.5 to form a new admittance $Y_{CT_0}(s)$:

$$Y_{CT_0}(s) = d_{T_0} + e_{T_0} \cdot s + \frac{r_{T_0}}{s - p_{T_0}} + \frac{r_{T_0}^*}{s - p_{T_0}^*} \quad (2.30)$$

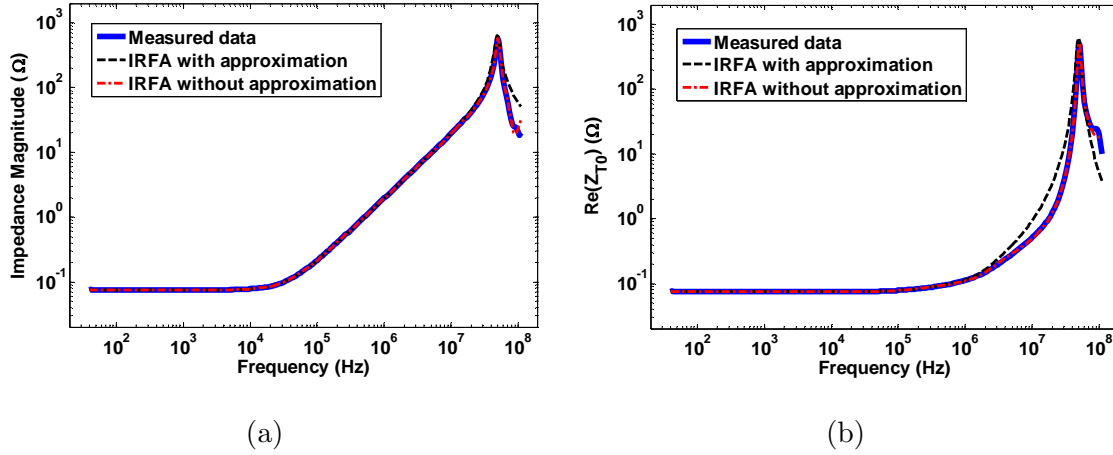


Figure 2.14. Comparison between simulation and measurement for Z_{T0} . (a) Impedance magnitude. (b) Real part.

In fact, the “true” parasitic capacitance is merged in $Y_{CT0}(s)$. The expression (2.30) is further simplified using $Y'_{CT0}(s)=d'+e's$ by making the value of $Y_{CT0}(s)$ equal to $Y'_{CT0}(s)$ at the resonance frequency $s_r = j2\pi f_r$, as given by:

$$d_{T0} + e_{T0} \cdot s_r + \frac{r_{T0}}{s_r - p_{T0}} + \frac{r_{T0}^*}{s_r - p_{T0}^*} = d'_{T0} + e'_{T0} \cdot s_r \quad (2.31)$$

From (2.31), we have: $e'_{T0}=3.22\text{E-}11$ and $d'_{T0}=1.48\text{E-}03$, which can be transformed into an R - C parallel cell. After this simplification, a positive-valued capacitance $2(C_e+C_p)$ is obtained. The final extracted equivalent circuit is shown in Figure 2.13(b), where the impedance $Z_1/2$ is enclosed in the dashed box.

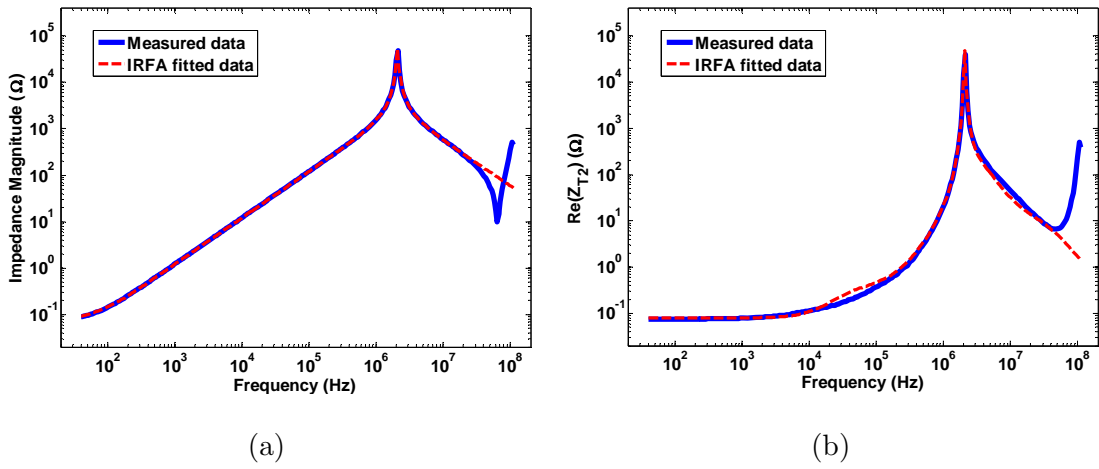
The impedance of the synthesized circuit is simulated in Pspice and compared with the measured data, as illustrated in Figure 2.14. With the approximation, the fitting precision of the real part of Z_{T0} is impaired at HF compared to that without approximation because the complex pole pair is discarded. However, trade-offs have to be accepted with this lumped-element equivalent circuit model.

2.4.3.3 Analysis of Measurement T_2

As the last step, Z_{T2} is identified to extract the circuit of Z_2 and C_e+C_c . Before launching the fitting, a coarse calculation is performed to estimate the CM inductance by the following formula:

Table 2.6 Fitting Results of $Y_{T_2}(s)$ and $2Y_2(s)$.

$Y_{T_2}(s) = 1/Z_{T_2}(s)$		$2Y_2(s) = 2/Z_2(s)$		
$d_{T_2} = 5.2701\text{E-}04; e_{T_2} = 2.6690\text{E-}11$		$d_2 = 4.9593\text{E-}04; e_2 = 8.2615\text{E-}14$		
<i>Poles</i>	<i>Residues</i>	<i>Poles</i>	<i>Residues</i>	F_i
-1.6659E+07 +j1.8259E+07	-2.1578E+02 +j6.3580E+02	-1.6679E+07 +j1.8265E+07	-2.1486E+02 +j6.3909E+02	4.0E-5
-1.6659E+07 -j1.8259E+07	-2.1578E+02 -j6.3580E+02	-1.6679E+07 -j1.8265E+07	-2.1486E+02 -j6.3909E+02	
-2.2332E+08	-1.0501E+05	-2.1616E+08	-9.4903E+04	4.4E-4
-2.0256E+05	4.2972E+01	-2.0165E+05	4.2780E+01	2.1E-5
-4.1835E+02	5.2350E+03	-2.4875E+01	5.2440E+03	211

Figure 2.15. Comparison between simulation and measurement for Z_{T_2} . (a) Impedance magnitude. (b) Real part.

$$\text{Im}(Z_{T_2}) = 2\pi f \frac{L_{CM}}{2} \quad (2.32)$$

At 100 kHz, the value of L_{CM} is derived to be about 382 μH . Similarly to Z_{T_0} , the admittance Y_{T_2} is fitted using a rational function with $m=6$ and $n=5$. As the lumped-element equivalent circuit in Table 2.4 cannot correctly model the second resonance in Figure 2.11(c), the fitting must stop before this resonance. Therefore, the fitting range covers from 40 Hz to 30 MHz. The fitting results are shown in Table 2.6, where e_{T_2} corresponds to the parasitic capacitance $2(C_e + C_c)$. The remaining part (including d_{T_2} , the real poles and complex poles) is the admittance $2(Z_1 + Z_2)^{-1}$. As Z_1 has been identified before, the magnetizing impedance Z_2 is calculated by subtracting the contribution of Z_1 . The IRFA fitting is then applied again on $Y_2(s) = 1/Z_2(s)$ with $m=6$ and $n=5$. The results are given in Table 2.6

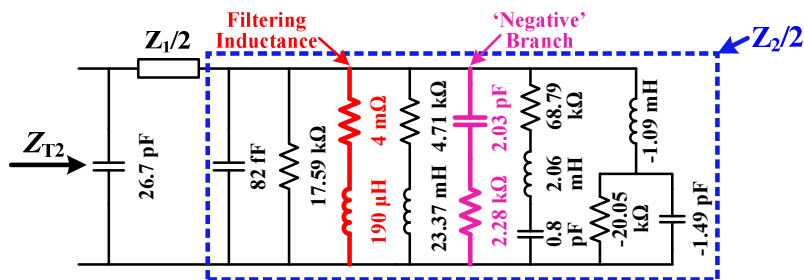
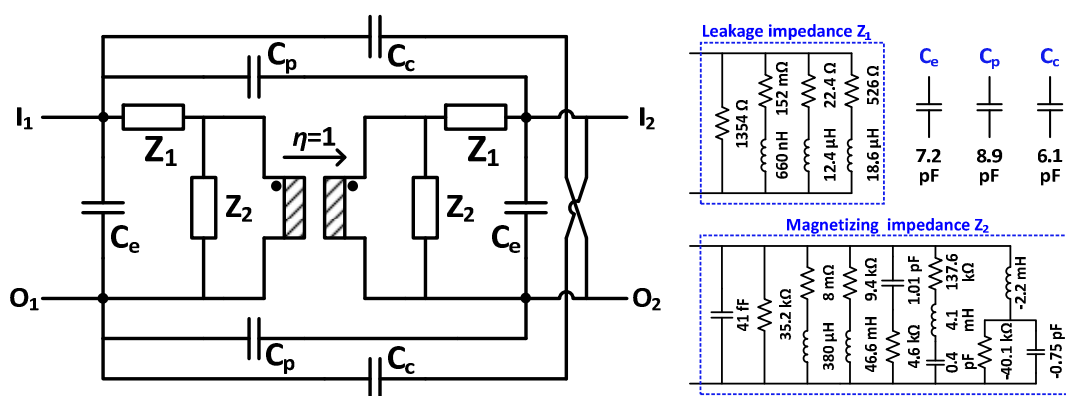

 Figure 2.16. Equivalent circuit for Z_{T2} .


Figure 2.17. Extracted equivalent circuit for the planar CM choke.

where a real pole $p = -2.1616 \times 10^8$ with negative residue $r = -9.4903 \times 10^4$ is extracted. According to the previous technique for treating negative residues, a positive $R(2.28 \text{ k}\Omega)$ - $C(2.03 \text{ pF})$ series branch is generated. The physical meaning of this circuit branch can be interpreted as the nonmagnetic HF losses in the ferrite due to the capacitive isolation of the grains [55]. The final circuit of Z_{T2} is shown in Figure 2.16.

In fact, the $L(190 \mu\text{H})$ - $R(4 \text{ m}\Omega)$ branch is the CM inductance since it corresponds to the dominant pole whose $F_i = 211$ is much larger than the others. Furthermore, this value is just about one half of the L_{CM} estimated in the initial calculation. The simulated impedance of Z_{T2} is compared with measured data in Figure 2.15 in terms of magnitude and real part. As seen, the simulated results agree well with the measurements up to 30 MHz.

With the parasitic capacitances obtained from the three measurement configurations, three linear equations expressed in (2.33) can be established, leading

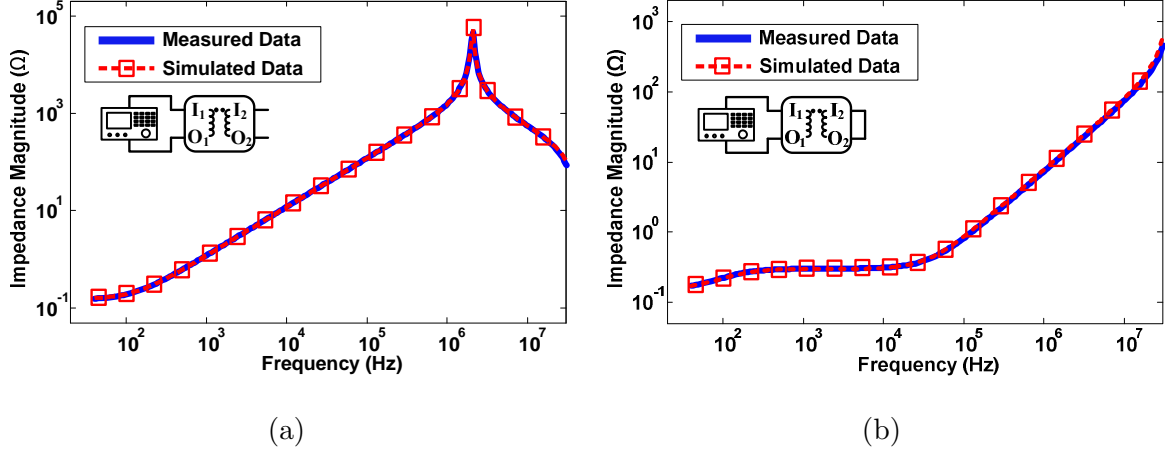


Figure 2.18. Comparison between simulations and measurements. (a) Open circuit impedance Z_0 . (b) Short circuit impedance Z_{SC} .

to the values of the parasitic capacitances: $C_c=6.1$ pF, $C_e=7.2$ pF and $C_p=8.9$ pF.

$$\begin{cases} 2C_c + 2C_p = 30 \text{ pF} \\ 2C_e + 2C_p = 32.2 \text{ pF} \\ 2C_e + 2C_c = 26.7 \text{ pF} \end{cases} \quad (2.33)$$

Finally, the equivalent circuit for the studied planar CM choke is completely identified, as illustrated in Figure 2.17. The obtained results will be validated by experimental tests in the next section.

2.5 Experimental Validations

2.5.1 Impedance Measurements and Sensitivity Analysis

To validate the extracted equivalent circuit, the schematic is simulated with Pspice software and the obtained results are compared with the measured data. For this, two other test configurations are adopted: the open circuit impedance Z_0 and the short circuit impedance Z_{SC} (see Figure 2.18). As seen, the simulated curves show good agreement with measured one, which confirms the effectiveness of the obtained model.

As there are many small-valued elements in the equivalent circuit, a sensitivity test is also performed to prove the robustness of the model. The sensitivity S is defined as the ratio of the relative change of the impedance Z to the relative change of a certain parameter X of the model, as given by the following

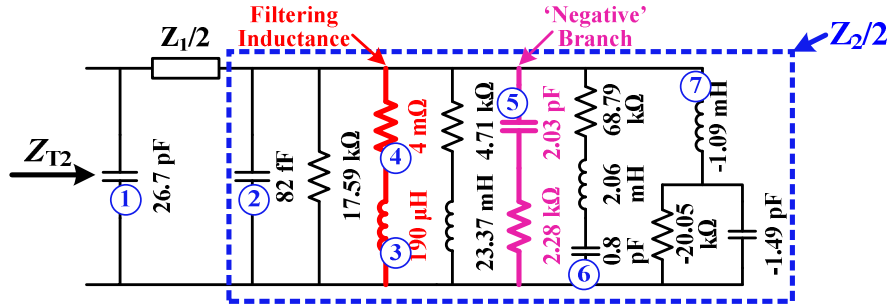


Figure 2.19. Circuit of Z_{T2} for sensitivity analysis.

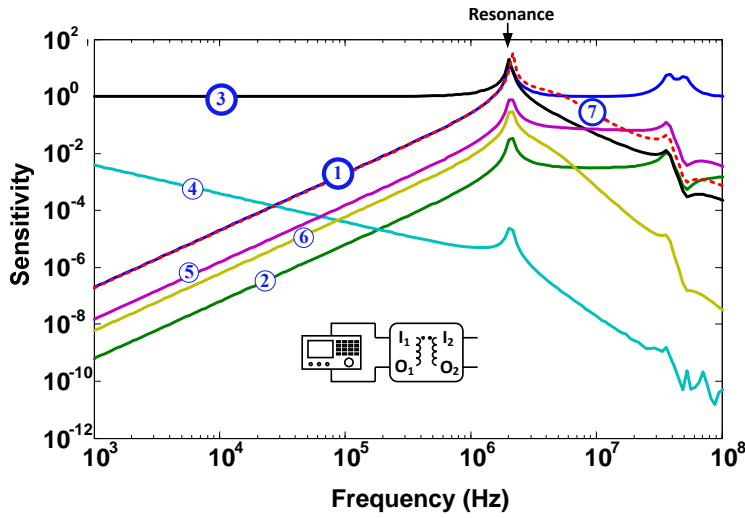


Figure 2.20. Sensitivity analysis results for Z_{T2} .

expression:

$$S(X, Z) = \lim_{\Delta X \rightarrow 0} \left(\frac{|\Delta Z / Z|}{|\Delta X / X|} \right) \quad (2.34)$$

The parameters of Z_2 are investigated and the analysis is conducted on the numbered elements shown in Figure 2.19. Simulations have been carried out by adding +5% increment ($\Delta X/X=5\%$) on the parameters. For each simulation, only one parameter is changed. The results are summarized in Figure 2.20, and lead to the following conclusions:

- a.** The three parasitic capacitances C_e , C_p and C_c in the model affect the resonances frequency and the response beyond the resonances. (Curve 1)
- b.** In Z_{T2} , the branches of dominant poles determines (190 μ H-4 m Ω branch) the behavior of the model on the inductive region (Curve 3). However, the obtained

sensitivity for this branch is unity, which implies that the model is not sensitive to the small variation of this branch.

- c. On most part of the impedance, the model is not sensitive to the parameter variation in the branches of non-dominant poles. (Curves 2,5,6,7)
- d. The resonance frequency and the impedance around the resonance are sensitive to the variation of the branch of dominant poles (Curve 3), the complex poles (Curve 7) and the parasitic capacitances (Curve 1).

The same analysis can be done on Z_{T3} and similar conclusions may be drawn. Generally speaking, the equivalent circuit model is quite robust to the small variations of its parameters. However, careful measurements and fitting are always necessary to guarantee the reliability of the results.

2.5.2 Insertion Loss Measurements

Next, an EMI filter with the topology of Figure 1.5(a) is realized with the planar CM choke, as illustrated in Figure 2.21. The leakage of the CM choke acts as DM inductances. The CM capacitors (4.7 pF) and the DM capacitor (68 nF) are measured and characterized by the IRFA method with the equivalent circuit shown in Figure 2.12(b). The IL of the filter is measured with a network analyzer (Agilent 5071C) via a four-port S parameter measurement method [56] (Figure 2.22). The S parameter matrix $[S_{ij}, i,j=1,2,3,4]$ is measured from 100 kHz to 30 MHz with logarithmic sweep. The mixed-mode S parameter S_{cc21} and S_{dd21} are derived by the following equations:

$$\begin{cases} S_{cc21} = \frac{1}{2}(S_{21} + S_{23} + S_{41} + S_{43}) \\ S_{dd21} = \frac{1}{2}(S_{21} - S_{23} - S_{41} + S_{43}) \end{cases} \quad (2.35)$$

where S_{cc21} and S_{dd21} give the CM and DM insertion loss of the filter, respectively [7]. Meanwhile, a four-port S parameter simulation is carried out with the same configuration as in Figure 2.22(a). The simulated CM IL S_{cc21_sim} and DM IL S_{dd21_sim} are calculated by (2.35) as well. The measured ILs and the simulated ones are compared in Figure 2.23. As seen, the simulated CM IL agrees well with the measured one. However, large difference on DM IL is observed beyond 3 MHz. This is due to the parasitic coupling effects among the choke, capacitors and trace loop [21], which are not considered in our model. These couplings can also be identified

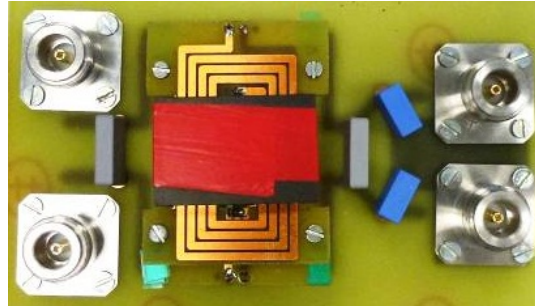


Figure 2.21. Realized EMI filter for validation

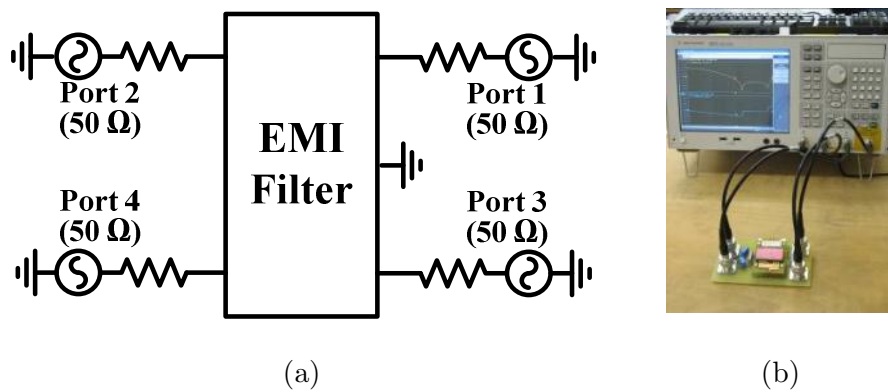


Figure 2.22. Insertion loss measurement configuration. (a) Schematic. (b) Implementation.

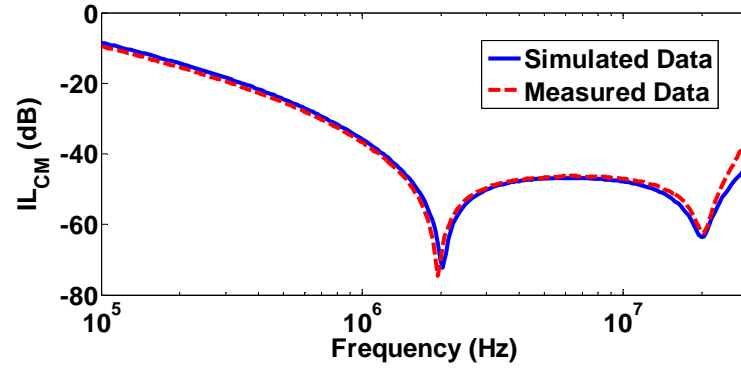
and extracted by S parameter measurements [29], but they are out of the scope of this work.

2.6 Discussion

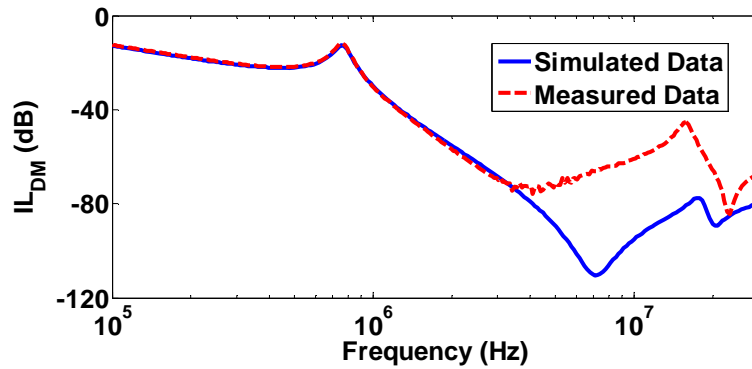
Through the IRFA method, accurate models for CM chokes can be built from three impedance measurements. However, several important aspects of the model and its characterization procedure should be addressed.

a. Passivity

Magnetic components are passive components because they do not generate any energy. However, the IRFA fitting procedure cannot guarantee the passivity of the calculated rational function. As a consequence, the passivity condition of the fitting results should be verified: an impedance $Z(s)$ is passive linear if and only if [57]:



(a)



(b)

Figure 2.23. Insertion loss comparison between measurements and simulations. (a) CM. (b) DM.

- $Z(s)$ is defined and analytic in $\text{Re}(s) > 0$;
- $Z^H(s) + Z(s)$ is a positive real for all s such that $\text{Re}\{s\} > 0$, where H denotes the conjugate transpose matrix;
- $Z(s^*) = Z^*(s)$.

The first condition relates to the stability and can be satisfied if $Z(s)$ does not contain any Right-Half-Plane poles. This is already satisfied during the fitting that the instable poles are flipped with respect to the imaginary axis. The third condition relates to the causality and it is naturally satisfied if $Z(s)$ is represented by a rational function.

The second condition is the most difficult to check and ensure. If the first condition is satisfied, the second condition implies that:

$$\operatorname{Re}[Z(j\omega)] = \frac{Z^t(j\omega^*) + Z(j\omega)}{2} \geq 0 \quad \text{for all } \omega > 0 \quad (2.36)$$

The simplest method to verify this condition is to perform a frequency sweep of $Z(j\omega)$. This method is very practice for the smoothly varied impedances as we had for magnetic components in power electronics. Moreover, a strict mathematic procedure using state-space representation is also used in [58]. If the obtained rational function from the fitting is not passive, passivity enforcement techniques can be applied to restore the passivity with very little impairment on the fitting precision [53, 58].

In this work, all the extracted results have been verified to be passive by the frequency sweep method. In practice, as CM chokes are naturally dissipative in HF due to core and copper losses, the passivity is usually respected if fitting precision is good enough.

b. Distributed Effect

Distributed effects have significant impact on the HF performances of the studied planar component because its wire length is comparable to the characteristic wave length for a commonly used PCB structure. As a consequence, using a lumped-element equivalent circuit model will not be sufficient for describing these effects. First of all, it cannot model all the HF resonances, and secondly, negative elements may appear during the circuit synthesis, just as shown previously.

The model presented in this chapter can work up to tenth of megahertz, and beyond that frequency, transmission line can be used for a better modeling accuracy. However, this kind of model is more physic than experimental so it is not studied in this work.

c. Saturation

Ideally, CM chokes are component where the DM flux is cancelled completely. However, due to leakage inductance, CM choke always work under flux bias that can lead to core saturation [15, 59]. Besides, the CM voltage-second stress will also saturate the magnetic core [60]. As a consequence, the realistic behavior of

a CM choke cannot be fully presented by a small-signal model presented in this chapter. Under working conditions, the error of the model will increase when current value rises. Nevertheless, the primary goal of this chapter is to introduce a small-signal HF model of CM chokes with a systematic synthesis procedure. As a tool for the starting the design of an EMI filter, this small-signal model can provide very rich information on the performances of the filter where the CM choke is implemented. To include the saturation effect of magnetic core, non-linear modules can be further implemented with the small-signal model. However, this requires an extensive study of the behavior of magnetic material, which is out of the concern of this work.

2.7 Conclusion

EMI filters are essential devices for the EMC compliance of power converters. In these filters, CM chokes are very critical components due to their performances. The states of art on experimental modeling methods are generally based on mathematical black-box models that have little physical meanings. Meanwhile, the reported equivalent circuit modeling techniques for CM chokes or transformers are all manually built so a lot of experience and time are required during the modeling process.

In this chapter, an improve HF equivalent circuit model for CM chokes is presented [61]. The model has more physic meanings and is extendable in circuit complexities. For extracting the parameters of the equivalent circuit model, the data of three selected impedance measurements are treated by an iterative rational function approximation fitting procedure. This procedure gives accurate fitting results from which the equivalent circuit can be systematically synthesized.

To demonstrate the parameter extraction process, an example of planar CM choke is analyzed in detail. The obtained results are further validated by impedance measurements of the studied CM choke and network measurements of the EMI filter where the CM choke is introduced. Good agreement is found between the model and the measurements, which proves the effectiveness of the model and the parameter extraction procedure.

Chapter 3. Analytical Modeling of Parasitic Capacitances of Planar Components

In Chapter 1, it has been stated that the modeling of parasitic capacitances of CM chokes has a great importance for EMI filter design. In the literature, the modeling of parasitic capacitances for planar components has not yet been extensively studied and the established models are also limited in applications. Therefore, this chapter will address this problem with a detailed analytical method and a complete procedure. Numerical methods are not the focus of this work so they will not be presented but will be used as tools for validation purposes. This chapter will start by a review of existing analytical methods for parasitic capacitances modeling. The electric field decomposition method is then introduced and extended for studying 2D configurations of the CM choke structure. Meanwhile, the influence of ferrite core is also considered via a simple transformation technique. Based on the results of 2D analysis, an energy approach is used to calculate the equivalent parasitic capacitances of the studied planar components

3.1 Review of Analytical Methods for Parasitic Capacitances Modeling

3.1.1 Plate Capacitance Formula and Other Empirical Formulas

In Figure 3.1, two identical copper plates are placed face to face (with width w and distance d) in a space of homogenous matter, which forms a plate capacitor. In common practice, the most frequently used formula for calculating its capacitance value is (3.1):

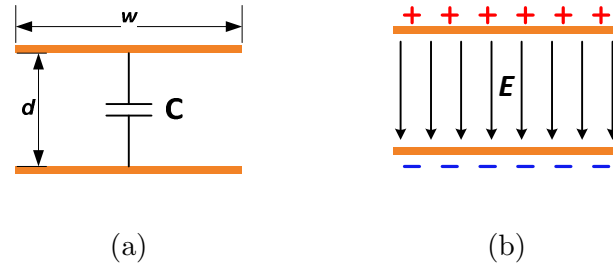


Figure 3.1. (a) Plate capacitor. (b) Uniform electric field between two electrodes.

$$C = \varepsilon_r \varepsilon_0 \frac{w}{d} \quad [\text{F/m}] \quad (3.1)$$

where ε_r and ε_0 denote the relative permittivity and the electric constant respectively. This formula considers only the electric field inside the two plates and assumes that the electric field is confined and uniform in a rectangular region. Although having a simple form, this expression has the following limitations:

- The external field outside the two plates is neglected, which sometimes is not negligible.
- The field between the two plates is not uniform at the two extremities, which is called fringe effects. The capacitance due to this fringe field has sometimes an important impact that cannot be neglected.

As long as the external field and fringe field are negligible, the formula (3.1) gives very accurate results in the following situations:

- The relative permittivity of the dielectric material between the two plates is much larger than that of the material outside the two plates.
- The w/d ratio is very large, making the plate capacitance inside the two conductors dominant with respect to the other effects.

For ordinary planar components employed in power electronics, neither the two last conditions are guaranteed. Thus, using the formula (3.1) may lead to large error in some applications.

To improve accuracy, some empirical formulas are proposed as well [62, 63]. Though more accurate, the complete empirical formulas are very limited in applications since they are not well scalable and physically interpretable.

3.1.2 Conformal Mapping

3.1.2.1 Brief review

Conformal mapping is a strict mathematic method in complex analysis and is widely used in parasitic capacitance modeling for strip-lines in microwave domains [64, 65]. In 2D electrostatic study, solving Laplace's equation may be a difficult task in the natural Cartesian coordinate system due to the complex boundaries. However, with the conformal mapping approach, one can perform coordinate transformation to solve the problem in a new plane where the boundaries are significantly simplified. As a results, the solutions can be obtained more easily.

The mathematic basis of conformal mapping is widely available in literatures [34, 66], so the theory will not be reviewed here. However, it is interesting to note the several major features of conformal mapping [34]:

1. The boundary conditions remain unchanged before and after conformal mapping.
2. The energy of the system is conserved before and after conformal mapping.

The first feature is very important since it ensure that the solution is not changed after mappings. The second feature allows carrying out some calculation directly in the transformed plane without returning to the original one. In the following part, this method will be briefly presented with an example to show its pros and cons.

3.1.2.2 Simple Example of Conformal Mapping

The example involves the calculation of the capacitance between a thin conductor and an infinite ground plate [Figure 3.2(a)]. The conductor A_1B_1 is placed perpendicularly over the ground plate in a complex plane z . The thickness of this conductor is assumed to be infinitesimal. Due to the symmetry of such structure, the problem can be simplified by considering only the first quadrant [Figure 3.2(b)]. Note that the boundaries $O-B_1$ and $A_1-\infty_y$ are called magnetic walls (M.W.) since the normal component of the electric field on them is null. Conformal mapping can be applied to transform the boundaries from z -plane to ω -plane using:

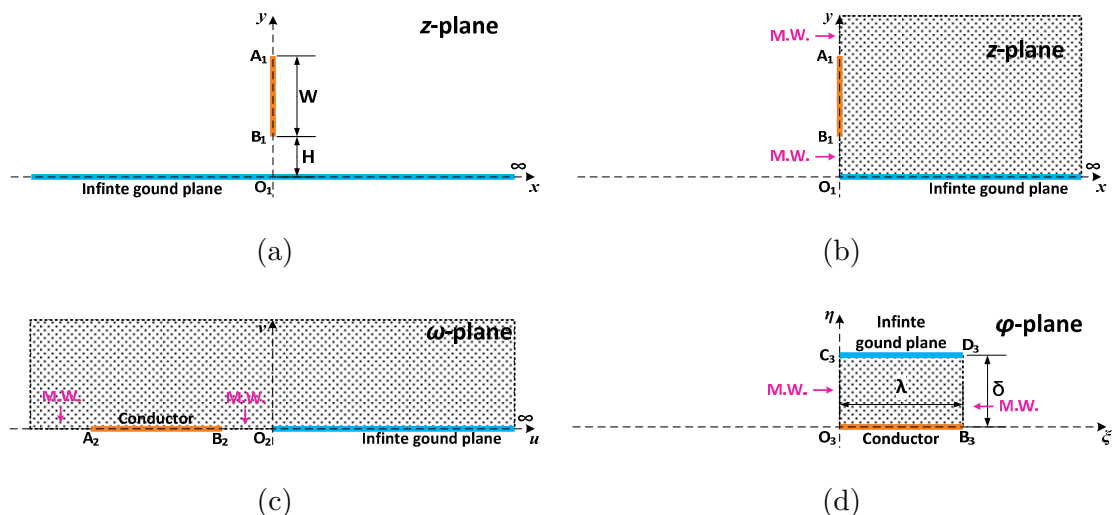


Figure 3.2. Conformal mapping of the simple example. (a) Original structure. (b) Simplified structure. (c) Mapping results in ω -plane. (d) Mapping results in φ -plane

$$\omega = \frac{z^2}{H^2} \quad (3.2)$$

where $z=x+jy$ and $\omega=u+jv$. The first quadrant of z -plane is stretched and extended to the whole up half ω -plane [see Figure 3.2(c)]. The new coordinates for the conductor is $u_{A2}=-\left(1+W/H\right)^2$ and $u_{B2}=-1$. In the next step, another conformal mapping called Schwartz-Christoffel transformation [66] (referred as SC transformation) is applied:

$$\varphi = P \int_0^\omega \frac{d\omega'}{\sqrt{(\omega' - u_{A2})(\omega' - u_{B2})\omega'}} + Q \quad (3.3)$$

This transformation can map the boundaries from ω -plane into a polygon in φ -plane with the following correspondence: $A_2 \rightarrow O_3$, $B_2 \rightarrow B_3$, $O_2 \rightarrow D_3$ and $\infty \rightarrow C_3$, as shown in Figure 3.2(d). Now the initial problem is simplified to a confined rectangular region where a plate capacitor is observed. P and Q in (3.3) are complex constants for controlling the size (λ and δ), the angle and the center position of the rectangular region. As the conformal mapping conserve the boundary conditions, the two lateral boundaries of the plate capacitor remain magnetic walls. Therefore, the electric field near the boundaries should be parallel to them. In this situation, one particular solution satisfying all the boundary conditions (B.C.) is the uniform electric field and it is the unique solution for this problem according to the theorem of uniqueness [67]. Thus, the capacitance of this structure in φ -plane can be expressed

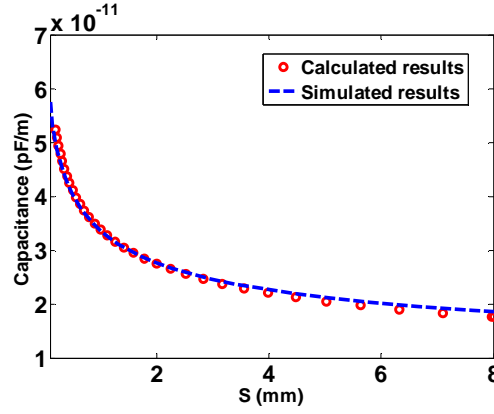


Figure 3.3. Comparison of calculated and simulated results.

as:

$$C_p = \varepsilon_r \varepsilon_0 \frac{\lambda}{\delta} \quad (3.4)$$

with

$$\frac{\lambda}{\delta} = M(k) = \begin{cases} \frac{\pi}{\ln \left(2 \frac{1 + \sqrt[4]{1-k^2}}{1 - \sqrt[4]{1-k^2}} \right)} & 0 \leq k \leq \frac{1}{\sqrt{2}} \\ \frac{1}{\pi} \ln \left(2 \frac{1 + \sqrt{k}}{1 - \sqrt{k}} \right) & \frac{1}{\sqrt{2}} \leq k \leq 1 \end{cases} \quad (3.5)$$

where $k = \sqrt{1 + 1/u_{A2}}$. The detailed derivation is omitted here but can be found in Appendix III. According to the energy conservation feature of conformal mapping, the capacitance calculated in φ -plane is the same as that in z -plane. Considering the symmetry of the structure in z -plane, the final capacitance between the conductor and the ground plane (in z -plane) is

$$C_{tot} = 2C_p = 2\varepsilon_r \varepsilon_0 \frac{\lambda}{\delta}. \quad (3.6)$$

The results from this formula are compared with those obtained from Finite Element (FEM) tool Maxwell[®], as shown in Figure 3.3. As seen, a good agreement is observed between the calculated results and the simulated ones.

Though accurate results can be achieved, the complete calculation requires three separated transformation steps, which are very complicated. For more complex structures, the analyses using conformal mapping could be very difficult or even impossible. Thus, many works have proposed to combine the conformal

mapping results with some empirical parameters to solve problems having complex structures, such as the parasitic capacitances of MOSFETS [68, 69] and interconnects [70, 71] in microelectronics. The common point of these methods is that they all decompose the electric field into several independent parts whose capacitances can be calculated by simple formulas. These methods, referred as electric field decomposition (referred as EFD), will be applied and extended in this work to PCB structures of the concerned planar components, as will be presented in the next section.

3.2 Electric Field Decomposition Method

3.2.1 Overview of EFD Method

As stated previously, the EFD method combines conformal mapping results with empirical parameters to calculate the capacitances in some problems. In this section, the basic idea of EFD method will be reviewed. In Figure 3.4, the equipotential-line diagram of one rectangular conductor (excited by 1V) over an infinite ground plane is shown. The EFD method assumes that the electric field generated by different surfaces of the upper conductor are independent to each other so that the whole field can be decomposed into different parts that are represented by separate elementary capacitances (Figure 3.5):

- C_{top} : the parasitic capacitance between the top surface of the conductor and the ground;
- C_{side} : the parasitic capacitance between the side walls of the conductor and the ground;
- C_{bot} : the parasitic capacitance between the bottom surface of the conductor and the ground;

For each of these capacitances, explicit analytical formulas are derived by conformal mapping method and the total parasitic capacitance is simply the sum of these elementary ones [68].

$$C_{tot} = C_{top} + 2C_{side} + C_{bot} \quad (3.7)$$

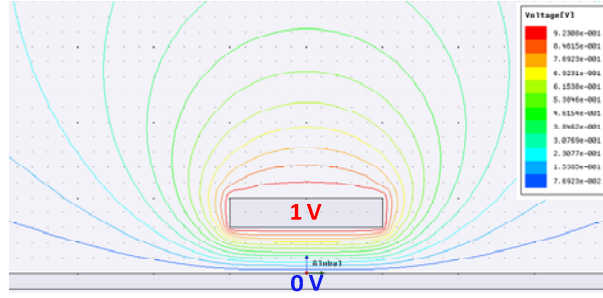


Figure 3.4. Simulated equipotential lines of one conductor over ground plane.

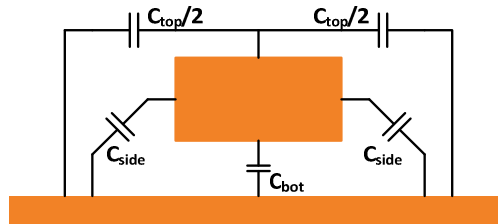


Figure 3.5. Electric field decomposition results

Note that decomposing the electric field is not physically rigorous, thus the obtained formulas still have errors, which requires fitting parameter adjustment. However, this kind of method has the following advantages:

- Decomposing a complex electric field into several simple field distributions can significantly simplify the analysis. As the method is physic-based, the derivation of the formulas is somehow easier than the complete conformal mapping formulas or empirical ones.
- The obtained formulas are scalable. As every elementary capacitance is derived by conformal mapping results, the derived formulas are scalable when the dimensions of the conductors vary. Therefore, these formulas exhibit high precision over a large range of dimensions.

3.2.2 Field-Based Stray Capacitance Modeling

Based on the EFD method, a simple and systematic method for the decomposition of electric field and the derivation of formulas is presented in [37] for modeling the parasitic capacitances of sub-65-nm on-chip interconnect in microelectronics, as will be introduced below.

3.2.2.1 Basic Elements of Electric Field Decomposition

According to Figure 3.4, three types of basic elements are introduced in [37] for decomposing the electric field of the 2D structure illustrated in Figure 3.6(a).

1. **Plate capacitance**: capacitance between two parallel surfaces;
2. **Fringe capacitance**: capacitance between the sidewall to the ground plane;
3. **Terminal capacitance**: capacitance between the corners of upper conductor and other surfaces.

The final decomposition strategy is illustrated in Figure 3.6(b). The plate capacitance C_{plate} is given by the expression (3.8).

$$\frac{C_{plate}}{\varepsilon} = \frac{W}{H} \quad (3.8)$$

The two fringe capacitances C_{fringe} from the sidewalls of the conductor to the ground is given by:

$$\frac{C_{fringe}}{\varepsilon} = \int \frac{\Delta W}{L} = \int_H^{H+T} \frac{dx}{\frac{\pi}{2}x} = \frac{2}{\pi} \ln \left(1 + \frac{T}{H} \right) \quad (3.9)$$

This integral is based on the assumption that the electric field lines in the fringe field region are circular, and it leads to a quite simple and accurate formula [68].

The terminal capacitance is approximately a constant according to the results of conformal mapping study [36, 37]. Here, the lower terminal capacitance is expressed by:

$$\frac{C_{terminal}^{lower}}{\varepsilon} = \frac{4}{\pi} \ln 2 \quad (3.10)$$

In [37], the value of terminal capacitances have been adjusted for considering the field distortion and for fitting the obtained results with simulations:

$$\frac{C_{terminal}^{lower}}{\varepsilon} = \frac{2}{\pi} \quad \text{and} \quad \frac{C_{terminal}^{upper}}{\varepsilon} = \frac{1}{\pi} \quad (3.11)$$

The capacitance from the top layer of the capacitances is treated as fringe capacitance and the following expression is obtained:

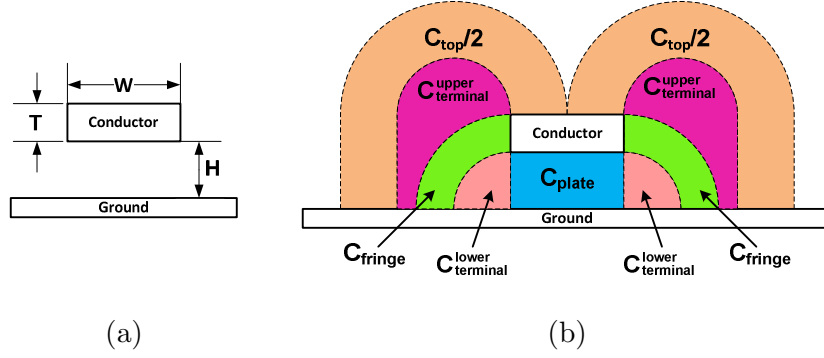


Figure 3.6. (a) Dimensions of the structure. (b) Electric field decomposition [37].

$$\frac{C_{top}}{\varepsilon} = \frac{2}{\pi} \ln \left[1 + \frac{\pi W}{2(1 + \pi)(H + T)} \right] \quad (3.12)$$

As seen, the electric field of the structure is split into several parts and the total capacitance of the structure is expressed by:

$$C_{total} = C_{plate} + 2C_{fringe} + C_{top} + 2C_{lower\ terminal}^{lower} + 2C_{upper\ terminal}^{upper} \quad (3.13)$$

Numerical simulations show that these formulas are quite accurate and scalable for calculating the parasitic capacitance of such structure [37].

3.2.2.2 Principles for Decomposition

Apart from the basic elementary capacitances, the authors have also introduced in [37] two principles for the decomposition when multiple conductors appear in the problem.

Principle 1: Charge Sharing

This principle is used to evaluate the field that is shared by two or more conductors. As seen in Figure 3.7(a), the right sidewall of conductor 1 can yield two capacitances: the fringe capacitance C_{f1g} to the ground and the plate capacitance C_{f12} to conductor 2. The electric fields of these two capacitances cause the charge sharing that can be modeled by the expression (3.14).

$$\frac{C_{p12}^*}{\varepsilon} = \int \frac{(\Delta C_{p12})^2}{\Delta C_{p12} + \Delta C_{f1g}} \quad \text{and} \quad \frac{C_{f1g}^*}{\varepsilon} = \int \frac{(\Delta C_{f1g})^2}{\Delta C_{p12} + \Delta C_{f1g}} \quad (3.14)$$

where the C_{p12}^* and C_{f1g}^* are the new capacitances considering the charge sharing

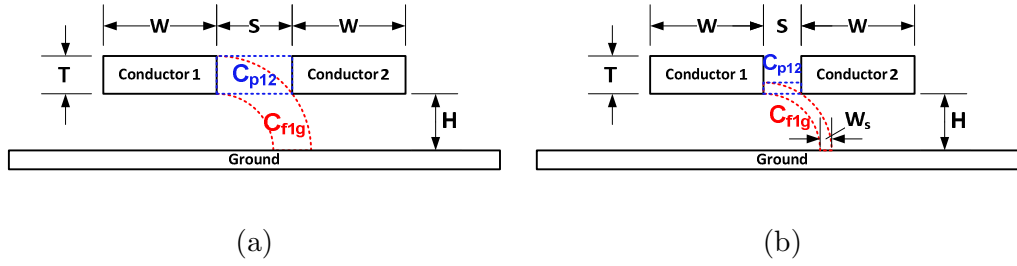


Figure 3.7. Principle for EFD method. (a) Charge sharing. (b) Field shielding [37].

effect and C_{p12} and C_{f1g} are the original capacitances without considering the charge sharing.

Principle 2: Electric Field Shielding

In Figure 3.7(b), the distance S between the two conductors is reduced. As seen, the width W_s of the shared field is also reduced to:

$$W_s = \sqrt{H^2 + S^2} - H \quad (3.15)$$

As S keeps diminishing, the fringe field from conductor 1 to the ground will finally be shielded by conductor 2.

According to these two principles, the fringe capacitance C_{f1g}^* in Figure 3.7(b) can be calculated by:

$$\begin{aligned} \frac{C_{f1g}^*}{\varepsilon} &= \int \frac{(\Delta C_{f1g})^2}{\Delta C_{p12} + \Delta C_{f1g}} = \int_H^{H+W_s} \frac{\left(\frac{2dx}{\pi x}\right)^2}{\frac{dx}{S} + \frac{2dx}{\pi x}} = \int_H^{H+W_s} \left(\frac{2}{\pi x} - \frac{2}{\pi x + 2S} \right) dx \\ &= \frac{2}{\pi} \ln \left(1 + \frac{W_s}{H} \right) - \frac{2}{\pi} \ln \left(1 + \frac{W_s}{H + \frac{2}{\pi} S} \right) \end{aligned} \quad (3.16)$$

Clearly, the first term represent the C_{f1g} without considering the charge sharing. The subtraction of the second term implies that after the charge sharing, the new capacitance is in fact reduced.

With these basic elements and the two principles, the parasitic capacitances of complex structures can be analyzed and accurate results can be expected. In this work, the EFD method will be extended for analyzing the PCB structures of planar components. More formulas and special treatments are proposed to derive the values of the parasitic capacitances.

3.3 Parasitic Capacitance Analysis of Planar Components based on EFD

The planar component under study is realized by printed circuit board with FR-4 epoxy, whose permittivity is about 5 at 10 kHz according to the measurements results with HP4294A impedance analyzer and Agilent 16451b dielectric test fixture. The thickness of the copper trace is 70 μm . As the width of the copper trace is generally in the order of several millimeters, its thickness is neglected in the following analyses. Besides, special treatment is taken in the formulations for considering the influence of the epoxy on the capacitances. Starting with some basic structures, the EFD method will then be applied on a 6-conductor PCB structure [72].

3.3.1 Basic Structures

In this section, the basic structures that might be encountered in planar components are studied. Analytical formulas will be deduced for each structure.

3.3.1.1 One Vertical Conductor over Ground Plane and Its Derived Structure

Original Problem

The structure of one vertical conductor over ground plane is already studied in the previous part using conformal mapping method. It is found that the mathematical derivation is very lengthy and complicated. Here, with the electric field decomposition method, a simplified solution can be obtained. Examining the structure shown in Figure 3.8(a), its electric field can be decomposed into four parts to yield two fringe capacitances and two terminal capacitances. The total capacitance of such structure is simply given by:

$$C_{total} = 2C_{f1} + 2C_{t1} = \varepsilon \frac{4}{\pi} \ln \left(1 + \frac{W}{H} \right) + \varepsilon \frac{8}{\pi} \ln 2 \quad (3.17)$$

The accuracy of this formula is comparable to (3.4) and (3.5) when the conductor is close to the ground plane (see Figure 3.9). As the conductor move away from the

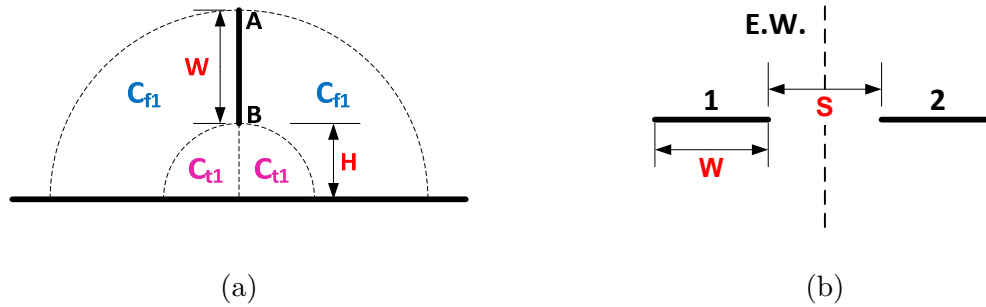


Figure 3.8. (a) One vertical conductor over ground plane. (b) Two conductors side by side.

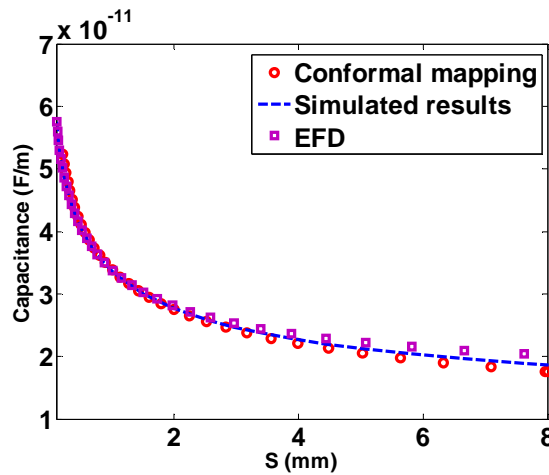


Figure 3.9. Comparison of the results of conformal mapping and EFD.

ground, the error rises. However, in this study, the PCB traces are quite close to each other, which guarantees a good precision.

Two Conductors Side by Side

In this case [Figure 3.8(b)], if conductors 1 and 2 are excited by 1V and 0V, the electric field is normal to the dashed line in the middle of these two conductors. This line is called electric wall (E.W.), which allows splitting the problem into two identical halves due to the symmetry property of the structure. As a result, this problem is transformed into the previous one. The capacitance between the two conductors is simply half of (3.17).

3.3.1.2 One Horizontal Conductor over Ground Plane and Its Derived Structures

Original Problem

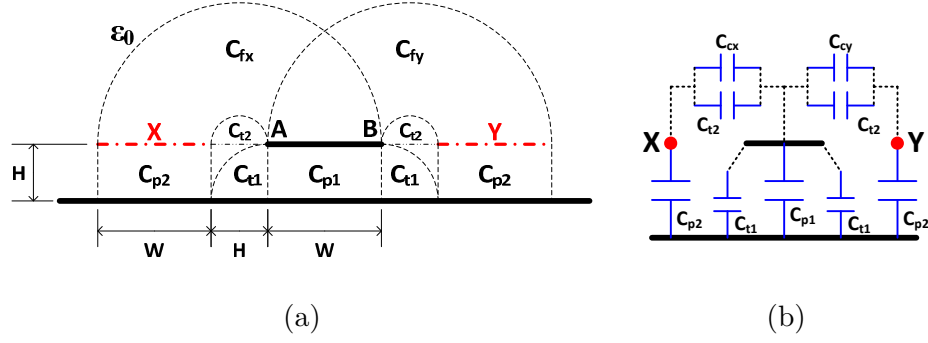


Figure 3.10. (a) Field decomposition for one conductor over ground plane. (b) The equivalent circuit for calculating the capacitance.

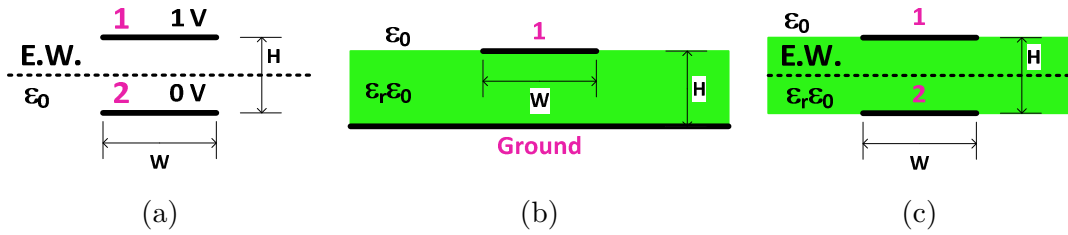


Figure 3.11. Derived cases for one conductor over ground plane. (a) Two conductors face to face. (b) One conductor over ground plane with epoxy. (c) Two conductors face to face with epoxy

This structure is illustrated in Figure 3.10. Intuitively, it is quite similar to that of Figure 3.6. However, several differences should be noted:

1. The thickness of the conductor is infinitesimal. In this case, the fringe capacitances due to the two sidewalls are neglected.
2. Two virtual conductors X and Y are added in the structure to evaluate the capacitance between the top surface of the conductor and the ground.

C_{p1} and C_{p2} are plate capacitances that can be evaluated by (3.8). The value of the lower terminal capacitance C_{t1} is given by (3.10). C_{t2} is the capacitance of the upper terminal capacitance, which can be considered as two C_{t1} in series, i.e. $C_{t1}/2$. To calculate the capacitances C_{fx} and C_{fy} , the charge sharing principle is applied, resulting in:

$$\frac{C_{fX}}{\epsilon_0} = \frac{C_{fY}}{\epsilon_0} = \int_{H/2}^{H/2+W} \frac{\left(\frac{dx}{\pi x}\right)^2}{\frac{dx}{\pi x} + \frac{dx}{\pi(H+W-x)}} = \frac{1}{\pi} \left[\ln \left(1 + \frac{2W}{H} \right) - \frac{W}{H+W} \right] \quad (3.18)$$

The final equivalent circuit of this structure can be represented by Figure

3.10(b) and the total parasitic capacitance is thereby expressed by (3.19).

$$C_{total} = 2 \frac{(C_{fX} + C_{t2})C_{p2}}{C_{fX} + C_{t2} + C_{p2}} + C_{p1} + 2C_{t1} \quad (3.19)$$

The results of (3.19) are compared with FEM simulations in Figure 3.12(a). It can be seen that this simple formula has a good match with the simulation results. This structure allows for deriving many other structures that exist in the planar components.

Two Conductors Face to Face

In Figure 3.11(a), the case of two conductors face to face is illustrated. Due to the symmetry of the structure, an electric wall can be inserted in the middle between the two conductors 1 and 2. Over this E.W., the electric field is perpendicular to it so that the problem is reduced to one conductor over ground plane whose capacitance C_{total} is given by (3.19). The final equivalent capacitance is simply $1/2C_{total}$.

One Horizontal Conductor over Ground Plane with Epoxy

When epoxy is inserted between the conductor and the ground plane, certain elementary capacitances in (3.19) have to be factored by ϵ_r , including C_{p1} , C_{p2} and C_{t1} [see Figure 3.10(a)]. The new total capacitance is given by:

$$C_{total} = 2 \frac{(C_{fX} + C_{t2})\epsilon_r C_{p2}}{C_{fX} + C_{t2} + \epsilon_r C_{p2}} + \epsilon_r C_{p1} + 2\epsilon_r C_{t1} \quad (3.20)$$

Here, the value of C_{t1} is modified to $1.5/\pi$ to fit the formula with simulated results. The calculated results show a good agreement with simulated ones in Figure 3.12(b).

Two Conductors Face to Face with Epoxy

This case is given in Figure 3.11(c), and the treatment is exactly the same as the case without epoxy. Due to the symmetry property of the problem, the obtained result is one half of (3.20).

Based on the above analyses of simple structures, the EFD method is applied

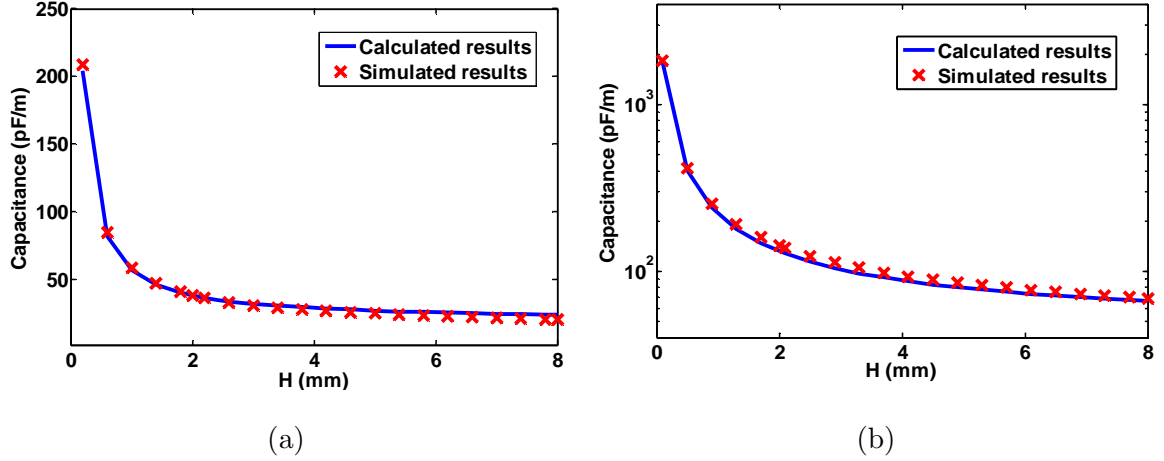


Figure 3.12. Comparison between calculation and FEM simulation. (a) One horizontal conductor over ground plane without epoxy ($W=4$ mm). (b) One horizontal conductor over ground plane with epoxy ($W=4$ mm, $\epsilon_r=5$).

to a PCB structure with 6 and 8 conductors, as will be introduced in the next section.

3.3.2 Configuration of PCB Structure with Six Conductors

The Figure 3.13 shows a PCB structure containing six conductors with the following parameters: H -thickness of the epoxy FR-4, W -width of conductors and S -distance between two neighbored conductors. Note that the capacitance matrix $[C_{ij}]$ is symmetrical, so there are 15 independent “mutual” capacitances (C_{ij} with $i \neq j$) to determine. In order to simplify the calculation, the following assumptions are proposed:

1. Due to the symmetry of the structure, the following equalities hold:

$$C_{12} = C_{23} = C_{45} = C_{56}; \quad C_{15} = C_{24} = C_{26} = C_{35}; \quad C_{14} = C_{36} \quad (3.21)$$

2. In the second assumption, it is considered that a conductor has electric coupling only with other conductors in its vicinity. Therefore, certain capacitances can be neglected:

$$C_{13} = C_{46} \approx 0; \quad C_{16} = C_{34} \approx 0 \quad (3.22)$$

These two assumptions are validated by FEM simulation of the structure presented in Figure 3.13. The parameters for the simulation are: $W=2$ mm, $H=1.5$ mm, $S=0.8$ mm and $\epsilon_r=5$, and the results are given in Table 3.1. The values in the

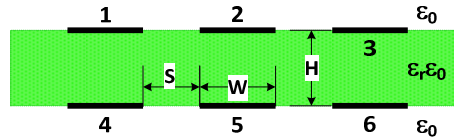


Figure 3.13. PCB structure with 6 conductors.

Table 3.1 Simulated Capacitance Matrix for the Case with 6 Conductors (Unit: pF/m).

Conductor	1	2	3	4	5	6
1	109.9	-20.3	-2.5	-69.4	-9.8	-1.8
2	-20.3	117.3	-20.3	-9.8	-57.1	-9.8
3	-2.5	-20.3	103.9	-1.8	-9.8	-69.5
4	-69.4	-9.8	-1.8	103.9	-20.3	-2.5
5	-9.8	-57.1	-9.8	-20.3	117.4	-20.3
6	-1.8	-9.8	-69.5	-2.5	-20.3	103.9

same color are verified and it can be seen that the above assumptions are quite reasonable. Note that the negative signs in Table 3.1 are due to the charge polarity according to the definition of capacitance matrix. Unless particularly mentioned, the formulas throughout this chapter give the absolute values of the “mutual” capacitances.

As a consequence, for the PCB structure with 6 conductors, we have four capacitances to determine: C_{14} , C_{15} , C_{21} and C_{25} . To calculate these capacitances, four different parts will be analyzed for each capacitance, as given below:

1. Exterior Coupling;
2. Interior Coupling;
3. Coupling of the terminal capacitances.

Note that the diagonal capacitance of C_{15} cannot be calculated by EFD method, so an empirical formula is given for obtaining its value, as will be given later. The analysis will start with the capacitance C_{21} and C_{25} .

3.3.2.1 Calculation of C_{21} and C_{25}

Part 1: Exterior Coupling

The Figure 3.14(a) shows the capacitive coupling in the exterior area of the PCB structure. The capacitances C_{f21} and C_{t21} stand for the fringe and the terminal

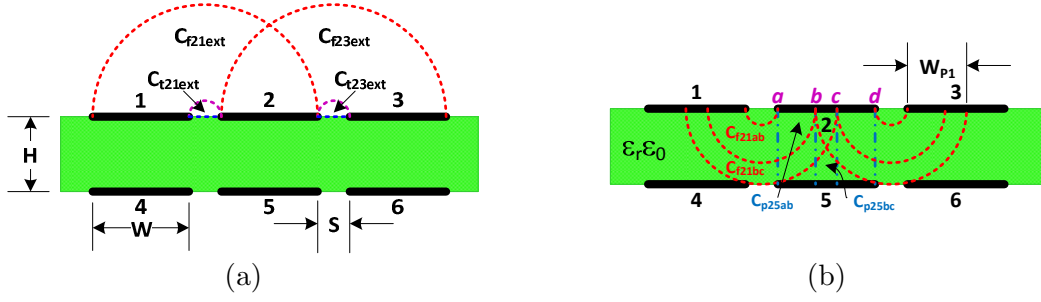


Figure 3.14. Electric field decomposition for calculating C_{21} and C_{25} . (a) Exterior coupling. (b) Interior coupling.

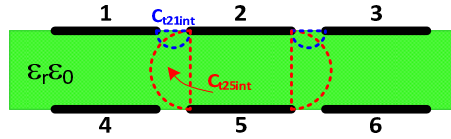


Figure 3.15. Electric field decomposition for calculating C_{21} and C_{25} : terminal capacitances between the conductors 2 and 1 in the exterior space. Their expressions are given by (3.23) and (3.24).

$$\frac{C_{f21ext}}{\epsilon_0} = \frac{C_{f24ext}}{\epsilon_0} = \frac{1}{\pi} \left[\ln \left(1 + \frac{2W}{S} \right) - \frac{W}{S+W} \right] \quad (3.23)$$

$$\frac{C_{t21ext}}{\epsilon_0} = \frac{C_{t24ext}}{\epsilon_0} = \frac{2}{\pi} \ln 2 \quad (3.24)$$

Note that during the deduction of (3.23), the charge sharing principle is applied because the field generated by conductor 2 is shared between conductors 1 and 3.

The exterior coupling between conductors 2 and 5 is neglected since the external field from conductor 2 will be “shielded” by conductors 1 and 3, as long as the conductors are very close to each other.

Part 2: Interior Coupling

The situation of the interior coupling is illustrated in Figure 3.14(b). In this case, the electric field is assumed to be confined in the region of the epoxy and relative permittivity ϵ_r of the epoxy should be accounted. It is clear that the field of segment $[ab]$ of conductor 2 is shared between conductors 1 and 5. Similar analysis holds for segment $[cd]$. Besides, the field of segment $[bc]$ is shared among conductors 1, 3 and 5. Applying again the charge sharing principle, the formulas (3.25)-(3.28)

can be derived.

$$\frac{C_{f21ab}}{\varepsilon_r \varepsilon_0} = \frac{1}{\pi} \ln \left(1 + \frac{2W_{ab}}{S} \right) - \frac{1}{\pi} \ln \left(\frac{\pi \left(\frac{S}{2} + W_{ab} \right) + H}{\pi \frac{S}{2} + H} \right) \quad (3.25)$$

$$\frac{C_{p25ab}}{\varepsilon_r \varepsilon_0} = \frac{W_{ab}}{H} - \frac{1}{\pi} \ln \left(\frac{\pi \left(\frac{S}{2} + W_{ab} \right) + H}{\pi \frac{S}{2} + H} \right) \quad (3.26)$$

$$\frac{C_{p25bc}}{\varepsilon_r \varepsilon_0} = \int_{\frac{S}{2}+W_{ab}}^{\frac{S}{2}+W_{ac}} \frac{\left(\frac{dx}{H} \right)^2}{\frac{dx}{H} + \frac{dx}{\pi x} + \frac{dx}{\pi(S+W-x)}} = \frac{W_{bc}}{H} - \int_{\frac{S}{2}+W_{ab}}^{\frac{S}{2}+W_{ac}} \frac{(S+W)dx}{(H+\pi x)(S+W) - \pi x^2} \quad (3.27)$$

$$\begin{aligned} \frac{C_{f21bc}}{\varepsilon_r \varepsilon_0} &= \int_{\frac{S}{2}+W_{ab}}^{\frac{S}{2}+W_{ac}} \frac{\left(\frac{dx}{\pi x} \right)^2}{\frac{dx}{H} + \frac{dx}{\pi x} + \frac{dx}{\pi(S+W-x)}} \\ &= \frac{1}{\pi} \ln \left(1 + \frac{2W_{bc}}{2W_{ab} + S} \right) - \int_{\frac{S}{2}+W_{ab}}^{\frac{S}{2}+W_{ac}} \frac{\left(S + W + \frac{H}{\pi} - x \right) dx}{(H + \pi x)(S + W) - \pi x^2} \end{aligned} \quad (3.28)$$

In these formulas, the dimensions W_{ab} , W_{bc} and W_{cd} are given by (3.29).

$$\begin{cases} W_{P1} = H - \frac{S}{2} \\ W_{bc} = 2W_{P1} - W = 2H - S - W \\ W_{ab} = W_{cd} = \frac{1}{2}(W - W_{P1}) = W + \frac{S}{2} - H \end{cases} \quad (3.29)$$

Note that the integration in (3.27) and (3.28) do not have explicit expressions, but they can be evaluated numerically in Matlab.

Part 3: Coupling of the Terminal Capacitances

The last elements for calculating the capacitances C_{21} and C_{25} are the terminal capacitances. It can be seen from Figure 3.15 that the terminal field from conductor 2 is shared between conductors 1 and 5. With the charge sharing principle, their formulas are expressed by:

$$\frac{C_{t21\text{int}}}{\varepsilon_r \varepsilon_0} = \frac{\left(C_{t21\text{int}}^* \right)^2}{C_{t21\text{int}}^* + C_{t25\text{int}}^*} = \frac{\left(\frac{2}{\pi} \ln 2 \right)^2}{\frac{2}{\pi} \ln 2 + \frac{2}{\pi} \ln \left(1 + \frac{S'}{S} \right)} \quad (3.30)$$

$$\frac{C_{t25\text{int}}}{\varepsilon_r \varepsilon_0} = \frac{\left(C_{t25\text{int}}^* \right)^2}{C_{t21\text{int}}^* + C_{t25\text{int}}^*} = \frac{\left[\frac{2}{\pi} \ln \left(1 + \frac{S'}{S} \right) \right]^2}{\frac{2}{\pi} \ln 2 + \frac{2}{\pi} \ln \left(1 + \frac{S'}{S} \right)} \quad (3.31)$$

with

$$S' = S \left[1 - \exp\left(-\frac{H}{\gamma S}\right) \right] \quad (3.32)$$

Note that the symbol * signifies that the original capacitance without charge sharing is considered. In particular, the formula for C_{t21int}^* depends on the thickness of epoxy H instead of being a constant [see (3.30) and (3.31)]. This can be explained by the terminal field between 2 and 1 that is also influenced by the position of conductors 4 and 5. To take into account this influence, the function (3.32) is inserted in (3.30) and (3.31). As H increases, this influence can then be neglected since $S' \rightarrow S$. The fitting parameter γ is chosen to be 1.5 to achieve a good accuracy.

Finally, by summing all the elementary capacitances, the capacitance of C_{21} and C_{25} are given by (3.33) and (3.34).

$$C_{21} = C_{f21ext} + 2C_{f21ab} + C_{f21bc} + C_{t21ext} + C_{t21int} \quad (3.33)$$

$$C_{25} = 2C_{p25ab} + C_{p21bc} + C_{t25int} \quad (3.34)$$

3.3.2.2 Calculation of C_{14}

The conductors 1 and 4 are located in the left side of the structure. The calculation of C_{14} is similar to C_{25} : only the internal coupling and the coupling of terminal capacitances are considered. The external coupling between these two conductors is neglected because the external field from 1 will mostly terminated at conductor 2.

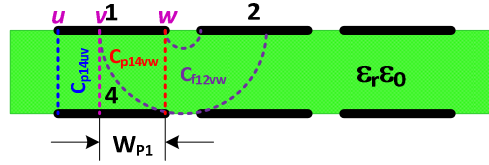
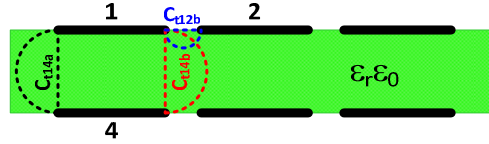
Part 1: Interior Coupling

The Figure 3.16 shows the field decomposition inside the epoxy. On the segment $[vw]$, the electric field is shared among conductors 1, 2 and 4. With the charge sharing principle, the different elementary capacitances are given by:

$$\frac{C_{p14vw}}{\varepsilon_0 \varepsilon_r} = \frac{W_{vw}}{H} \quad (3.35)$$

$$\frac{C_{p14vw}}{\varepsilon_0 \varepsilon_r} = \frac{W_{vw}}{H} - \frac{1}{\pi} \left[\ln \left(\frac{\pi \left(\frac{S}{2} + W_{vw} \right) + 1}{\pi \frac{S}{2} + 1} \right) \right] \quad (3.36)$$

where the dimension W_{vw} is expressed by:


 Figure 3.16. Electric field decomposition for calculating C_{14} : interior coupling.

 Figure 3.17. Electric field decomposition for calculating C_{14} : terminal capacitance.

$$\begin{cases} W_{P1} = H - \frac{S}{2} \\ W_{vw} = W - W_{P1} \end{cases} \quad (3.37)$$

Coupling of the Terminal Capacitances

The terminal capacitances between conductors 1 and 4 are shown in Figure 3.17. The related formulas are expressed by formulas similar to (3.31) and (3.33). Note that the charge sharing principle should be applied again. However, reasoning from the symmetry of the structure, the terminal capacitance C_{t14b} should be the same as C_{t25b} .

Finally, the capacitance C_{14} can be expressed by:

$$C_{14} = C_{p14uv} + C_{p14vw} + C_{t14a} + C_{t14b} \quad (3.38)$$

3.3.2.3 Calculation of C_{15}

The electric field decomposition method cannot be applied for the analysis of the diagonal capacitance C_{15} . In [69], an empirical formula has been introduced for this capacitance, as given in (3.39).

$$C_{15} = \frac{\varepsilon}{\pi} \sqrt{\frac{HS}{H^2 + S^2}} \quad (3.39)$$

Stemmed from this formula, an empirical formula is proposed in this work, as expressed by (3.40).

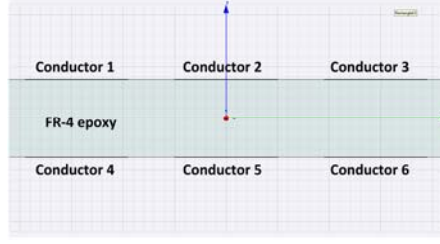


Figure 3.18. FEM model for validation.

Table 3.2 Comparison between Calculations and Simulations for the Case of 6 Conductors

	S=0.5 mm			S=0.7 mm			S=0.9 mm		
	Cal.	Sim.	Err.	Cal.	Sim.	Err.	Cal.	Sim.	Err.
C_{12}	-26.9	-27.2	1%	-22.2	-22.6	2%	-18.7	-18.8	1%
C_{14}	-67.0	-66.7	1%	-69.7	-69.3	1%	-72.2	-70.2	3%
C_{24}	-10.4	-10.2	2%	-10.1	-10	1%	-9.8	-9.6	2%
C_{25}	-53.2	-52.1	2%	-56.9	-55.8	2%	-60.4	-58.5	3%

Unit: pF/m **Cal.**=Calculation **Sim.**=Simulation **Err.**=Error

$$C_{15} = \alpha(\varepsilon_0 + \varepsilon_0\varepsilon_r)\sqrt{\sin\theta} \tanh\left(\frac{\pi W}{H+S} + 1\right) \quad (3.40)$$

where α is a fitting parameter adjusted from FEM simulation results. In this case, $\alpha=0.22$.

3.3.3 Numerical Validation

Based on the above analysis, the capacitance C_{12} , C_{14} , C_{24} and C_{25} can be calculated. To validate the developed formulas, FEM simulations are performed on the structure shown in Figure 3.18 ($W=2\text{mm}$, $H=1.5\text{ mm}$). The thickness of the conductors is set to be $10\ \mu\text{m}$. The results are compared in Table 3.2. As seen, the maximum error is less than 5%, which is sufficient for practical applications. To further improve the precision of the formulas, more fitting parameters can be used in the future work.

3.3.4 Configuration of PCB structure with Eight Conductors

In Figure 3.19, the case of a PCB structure with 8 conductors is illustrated. As seen, there are “only” 28 capacitances to determine if the symmetry of the capacitance matrix is considered. Similar to what is done in the case of six conductors, the same two assumptions can be accepted.

1. *Symmetry of the structure:* $C_{12}=C_{34}\approx C_{23}$; $C_{16}=C_{25}\approx C_{27}=C_{36}\approx C_{38}=C_{47}$; $C_{15}=C_{48}$;
 $C_{26}=C_{37}$.
2. *Negligible capacitances:* C_{13} , C_{14} , C_{17} , C_{18} , C_{24} , C_{28} , C_{35} , C_{45} and C_{46} .

In order to validate these assumptions, a FEM simulation is performed on the 8-conductor structure illustrated in Figure 3.19 with $W=2$ mm, $H=1.5$ mm, $S=0.8$ mm, Thickness= $10\ \mu\text{m}$ and $\epsilon_r=5$. The obtained results are summarized in Table 3.3. Note that the aforementioned assumptions are verified by the simulation results (colored values). Therefore, there are still four capacitances to determine: C_{12} , C_{15} , C_{16} and C_{26} . To calculate their values, the configuration of six conductors is studied again. In fact, the configuration of 8 conductors can be decomposed into two configurations of six conductors, as shown by Figure 3.20. The conductors 4 and 8 have very little impact on the capacitance matrix for the conductors group (1-2-3-5-6-7). Comparing Table 3.3 and Table 3.1, the capacitance matrix of the group (1-2-3-5-6-7) is almost the same as that of the 6-conductor configuration.

In this section, the 2D PCB structures in air are analyzed with the EFD method. When these structures are inserted into ferrite cores, the corresponding capacitance matrix will be changed due to the influence of the core. In the next section, this issue will be particularly addressed.

3.4 Influence of Ferrite Core

In the previous part, the EFD method for PCB structure in air has been presented. However, most HF magnetic components have a magnetic core so that its windings are completely or partially covered by the core. In particular, the MnZn ferrite core is concerned in this study. Normally, the ferrite core that covers the windings will influence the parasitic capacitances of the component. In this section, a simple analytical transformation technique will be presented to take into account the effects of the ferrite core.

3.4.1 Permittivity of Ferrite Core

For electrostatic studies, the permittivity of MnZn ferrite is a very important property. According to [73], the intrinsic relative permittivity of MnZn ferrite is

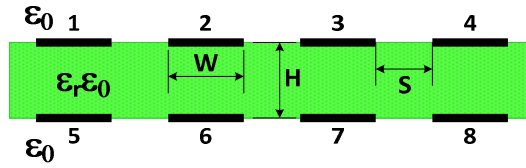


Figure 3.19. PCB structure with 8 conductors.

Table 3.3 Simulated Capacitance Matrix for the Case of 8 Conductors (Unit: pF/m).

Conductor	1	2	3	4	5	6	7	8
1	105.5	20.8	1.3	1.6	69.7	9.7	0.6	1.3
2	20.8	119.5	20.4	1.3	9.7	57.4	9.2	0.6
3	1.4	20.4	120.4	21.3	0.6	9.0	58.0	9.7
4	1.6	1.3	21.4	106.2	1.3	0.6	9.9	70.2
5	69.7	9.7	0.6	1.3	105.0	20.8	1.3	1.6
6	9.7	57.4	9.0	0.6	20.8	119.8	20.9	1.3
7	0.6	9.2	58.0	9.9	1.4	20.9	121.9	21.9
8	1.3	0.6	9.7	70.2	1.6	1.3	21.9	106.6

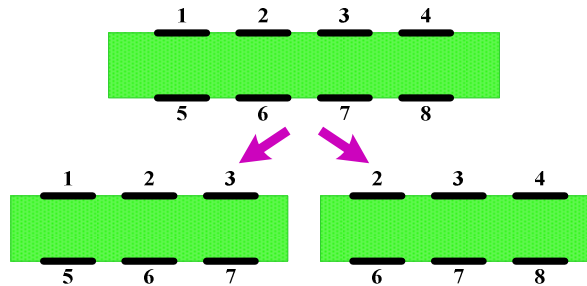


Figure 3.20. Decomposition of the configuration with 8 conductors

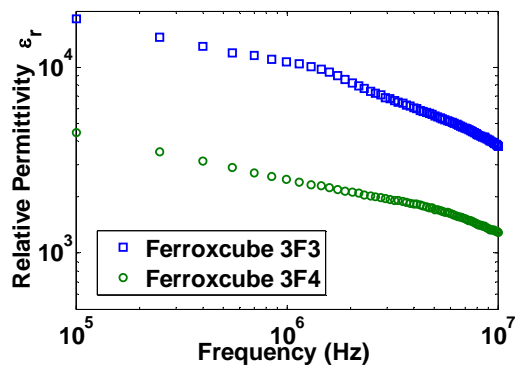
very high, usually in the order of 10^4 . For the applications in this work, the Ferroxcube 3F3 and 3F4 planar magnetic core are used. The relative permittivities of these two materials are measured by an HP4194A impedance analyzer with an Agilent 16451B dielectric measurement fixture [Figure 3.21(a)]. The obtained results are illustrated in Figure 3.21(b). As seen, the relative permittivities of the two materials are both larger than 10^3 over a large frequency range. In a word, these MnZn ferrite cores will be regarded as dielectric materials with high permittivity.

3.4.2 Perfect Electric Conductor

Perfect Electric Conductor (PEC) is a material that exhibits infinite conductivity. For PEC material, the electric field is normal to its surface in



(a)



(b)

Figure 3.21. Measurement of the relative permittivity of ferrite material. (a) Agilent 16451B fixture. (b) Measurement results.

electrostatic study. The PEC material is usually used in numerical simulations as an ideal model for highly conducting conductors and dielectric materials with high permittivity [74]. According to the measured relative permittivity of MnZn ferrite, these materials can be considered as PEC. In fact, the electric field inside a PEC is zero and the electric field is normal to the PEC surface in electrostatics, which is exactly the same situation as MnZn ferrite. As a consequence, the following assumption is proposed:

For electrostatic analysis, the ferrite core is equivalent to a floating PEC core.

Here, the term floating means that the core is isolated from any point with fixed potential and the potential of the core depends on the electric field of its surrounding environment. Concretely for planar components, this equivalence implies that the 2D capacitance matrix of a PCB structure in a ferrite core is the same as that of the same PCB structure in a floating PEC core. To verify this point, FEM simulations are performed. As seen from Figure 3.22, two PCB structures with 6 conductors are simulated. The first one is embedded in a ferrite core whereas the second one is in a floating PEC core. From the simulations results, it is clear that the two structures have almost the same capacitance matrix.

Based on above analyses, it can be concluded that, in order to find the capacitance matrix of a PCB structure surrounded by ferrite core, one can calculate this matrix in the equivalent case with a floating PEC core. Now the problem turns out to be how will the PCB structure in floating PEC core be treated.

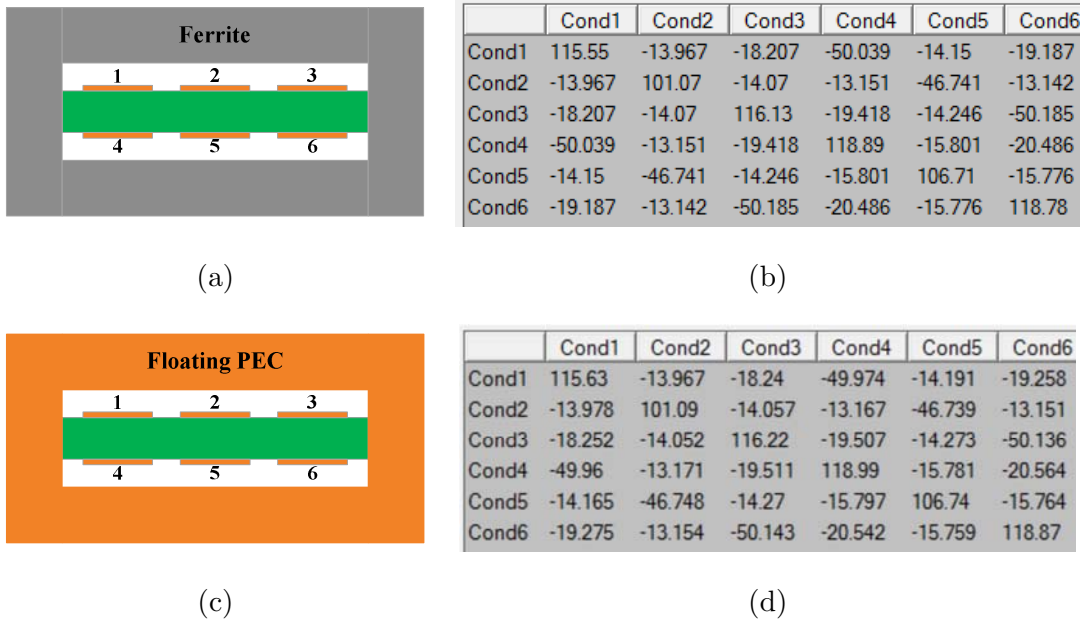


Figure 3.22. Verification of the equivalent between ferrite core and PEC core. (a) PCB structure in ferrite core. (b) Simulation results for (a). (c) PCB structure in PEC core. (d) Simulation results for (c).

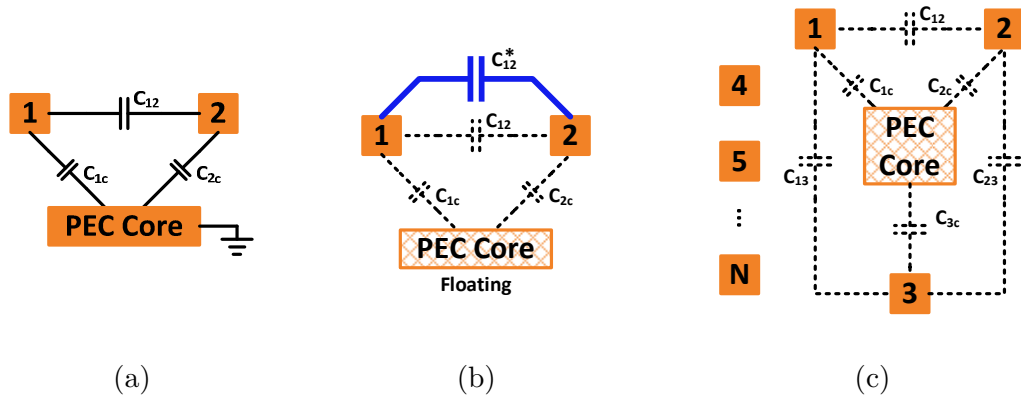


Figure 3.23. Treatment of PEC core. (a) Two conductors with grounded PEC core. (b) Two conductors with floating PEC core. (c) N conductors with floating PEC core (only the capacitances for conductors 1, 2, and 3 are drawn).

3.4.3 Transformation Technique for Handling Floating PEC Core

For better understanding, an example is described here to demonstrate the transformation technique for handling the floating PEC core [75]. The analysis begins with the case of two conductors in a grounded PEC core, as shown in Figure 3.23(a). Obviously, three capacitances can be immediately identified:

- C_{12} : the capacitance between conductors 1 and 2;

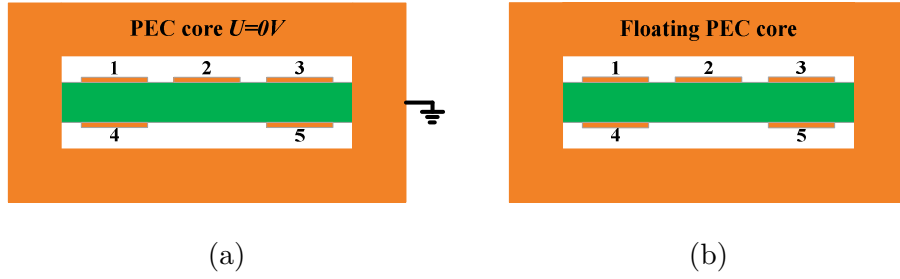


Figure 3.24. Validation of the procedure for handling ferrite core. (a) Grounded PEC core. (b) Floating PEC core.

- C_{1c} : the capacitance between conductor 1 and the grounded PEC core;
- C_{2c} : the capacitance between conductor 2 and the grounded PEC core.

Then the link between the PEC core and the ground is cut off so the core becomes floating [Figure 3.23(b)]. The new capacitance C_{12}^* between conductors 1 and 2 is simply calculated as:

$$C_{12}^* = C_{12} + \frac{C_{1c}C_{2c}}{C_{1c} + C_{2c}} \quad (3.41)$$

This formula means that the new capacitance C_{12}^* corresponds to C_{12} in parallel with the series-connected capacitances C_{1c} and C_{2c} .

More generally, in the case of N conductors in a floating PEC core [Figure 3.23(c)], a transformation formula can be obtained by applying the charge conservation principle on the PEC core, as expressed by:

$$C_{ij}^* = C_{ij} + C_{ic}C_{jc} \left(\sum_{k=1}^N C_{kc} \right)^{-1} \quad (3.42)$$

Note that in this formula, all the capacitances take their absolute values. The detailed derivation of this formula is given in Appendix IV.

To verify this formula, FEM simulations are again performed to analyze the PCB structure shown in Figure 3.24(a). This structure consists of five conductors located in a grounded PEC core [Figure 3.24(a)]. The simulated results of the capacitances are summarized in the column ‘‘Grounded PEC Core’’ of Table 3.4. On the basis of these capacitances and the transformation formula (3.42), it is also possible to calculate the value of C_{ij}^* for the case of floating PEC core [Figure

Table 3.4 Simulation Results for Grounded PEC Core and Floating PEC Core.

	Grounded PEC core (unit: pF/m)	Floating PEC core (unit: pF/m)
C_{ij}^*	$C_{12}=-7.2; C_{13}=-0.09; C_{14}=-30.7; C_{15}=-0.12;$ $C_{23}=-7.2; C_{24}=-6.2; C_{25}=-6.2;$ $C_{34}=-0.13; C_{35}=-30.7;$ $C_{45}=-0.16;$	$C_{12}^*=-19.7; C_{13}^*=-19.4; C_{14}^*=-51.3; C_{15}^*=20.7;$ $C_{23}^*=-19.7; C_{24}^*=-19.7; C_{25}^*=-19.6;$ $C_{34}^*=-20.7; C_{35}^*=-51.2;$ $C_{45}^*=-22.1;$
C_{ic}^*	$C_{1c}=95.7; C_{2c}=60.2; C_{3c}=92.7; C_{4c}=99.2;$ $C_{5c}=99.3.$	N/A

3.24(b)], for example:

$$C_{12_cal}^* = 7.2 + \frac{95.7 * 60.2}{95.7 + 60.2 + 92.7 + 99.2 + 99.3} = 20.1 \quad [\text{pF/m}] \quad (3.43)$$

$$C_{14_cal}^* = 30.7 + \frac{95.7 * 99.2}{95.7 + 60.2 + 92.7 + 99.2 + 99.3} = 51.9 \quad [\text{pF/m}] \quad (3.44)$$

Meanwhile, the same PCB structure with a floating PEC core [see Figure 3.24(b)] is also simulated and the obtained capacitances are given in the column ‘‘Floating PEC Core’’ of Table 3.4. Comparing the simulated values of C_{12}^* and C_{14}^* (as examples) to the calculated values in (3.43) and (3.44), one can find that the differences between simulation and calculation are very small (about 2%). Therefore, the transformation technique (3.42) is verified. Note that the diagonal elements C_{ij}^* ($i=j$), which represent the absolute capacitances, are not available from (3.42). However, they will not be useful in the following calculation.

3.4.4 Combination of EFD Method and Transformation Technique

In this section, the EFD method and the transformation technique are applied together to analyze a 6-conductor PCB structure in a MnZn ferrite core, as illustrated in Figure 3.25(a). As the first step, the ferrite core is replaced by a grounded PEC core.

3.4.4.1 Capacitances between Conductors and Grounded PEC Core

Plate and Terminal Capacitances between Conductor 1 and PEC Core

The decomposition of the electric field for plate and terminal capacitances are illustrated in Figure 3.25(b). First, the plate capacitance C_{pcl} between conductor 1 and the PEC core is studied. This capacitance is simply calculated by:

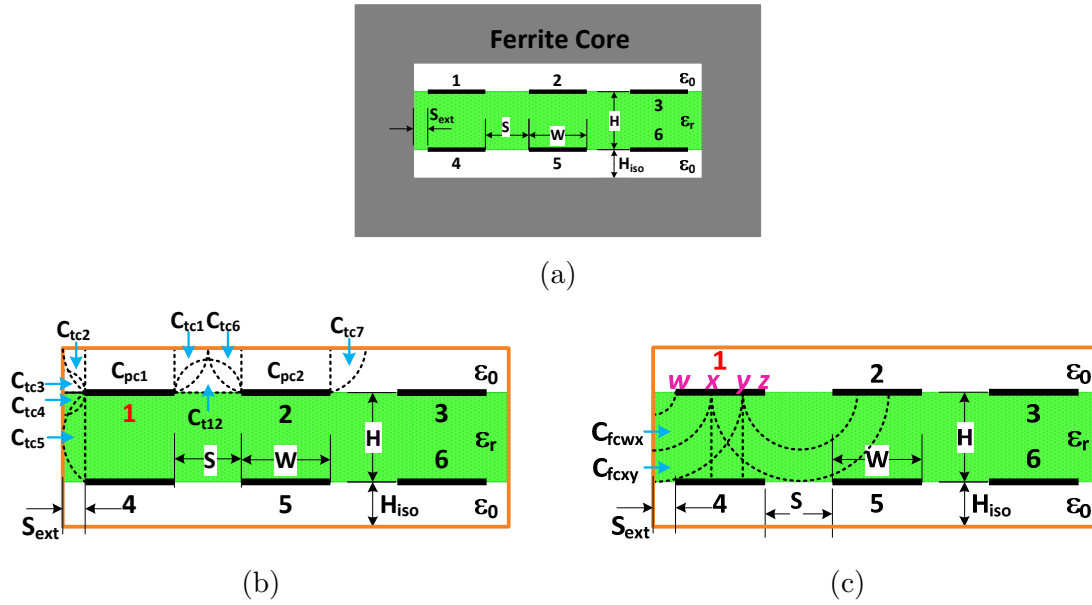


Figure 3.25. 6-conductor PCB structure in ferrite core. (a) Structure. (b) Decomposition of the field between conductors and the grounded PEC core: plate and terminal capacitances. (c) Decomposition of the field between the conductors and the grounded PEC core: fringe capacitance.

$$\frac{C_{pc1}}{\varepsilon_0} = \frac{W}{H_{iso}} \quad (3.45)$$

Next, the expressions for the terminal capacitances are derived. On the left terminal of conductor 1, the core shields a portion of terminal capacitance C_{tc2} [Figure 3.25(b)]. Thus, its formula will be changed accordingly. Here, without considering the charge sharing effect, the following expressions are established.

$$C_{tc2}^* = \frac{4}{\pi} \ln \left(1 + \frac{\min(S_{ext}, H_{iso})}{H_{iso}} \right) \quad (3.46)$$

As seen, when S_{ext} are large enough, the terminal capacitance C_{tc2}^* will no longer be influenced by the core. Besides, the value of C_{tc3} is also affected by the upper surface of the core. To evaluate this effect, the expression in (3.31) and (3.32) are reused:

$$C_{tc3}^* = \frac{4}{\pi} \ln \left(1 + \frac{S'}{S_{ext}} \right) \quad \text{with} \quad S' = S_{ext} \left[1 - \exp \left(-\frac{H_{iso}}{1.5 \cdot S_{ext}} \right) \right] \quad (3.47)$$

Now, applying the charge sharing principles, the expressions of C_{tc2} and C_{tc3} are given by:

$$\frac{C_{tc2}}{\varepsilon_0} = \frac{(C_{tc2}^*)^2}{C_{tc2}^* + C_{tc3}^*} \quad \text{and} \quad \frac{C_{tc3}}{\varepsilon_0} = \frac{(C_{tc3}^*)^2}{C_{tc2}^* + C_{tc3}^*} \quad (3.48)$$

In the epoxy, the same analysis can be applied. The left terminal field between conductors 1 and 4 is partially shielded by the core. Thus, the capacitances C_{tc4} and C_{tc5} are expressed by (3.49).

$$\frac{C_{tc4}}{\varepsilon_0 \varepsilon_r} = \frac{\left(\frac{4}{\pi} \ln 2\right)^2}{\frac{2}{\pi} \ln \left(1 + \frac{\min(S_{ext}, H/2)}{H/2}\right) + \frac{4}{\pi} \ln 2} \quad \text{and} \quad \frac{C_{tc5}}{\varepsilon_0 \varepsilon_r} = \frac{\left[\frac{2}{\pi} \ln \left(1 + \frac{\min(S_{ext}, H/2)}{H/2}\right)\right]^2}{\frac{2}{\pi} \ln \left(1 + \frac{\min(S_{ext}, H/2)}{H/2}\right) + \frac{4}{\pi} \ln 2} \quad (3.49)$$

On the right terminal of conductor 1, the terminal capacitance C_{tc1} is influenced by the terminal field of conductor 2. Thus its expression can be written as (3.50) without considering the charge sharing with C_{tl2} .

$$C_{tc1}^* = \frac{4}{\pi} \ln \left(1 + \frac{\min(S/2, H_{iso})}{H_{iso}}\right) \quad (3.50)$$

Regarding C_{tl2} , its value is also decreased by the upper surface of PEC core. Therefore, the same type expression as (3.47) is used:

$$C_{tl2}^* = \frac{4}{\pi} \ln \left(1 + \frac{S'}{S}\right) \quad \text{with} \quad S' = S \left[1 - \exp\left(-\frac{H_{iso}}{1.5 \cdot S}\right)\right] \quad (3.51)$$

After applying the charge sharing principle with C_{tl2} , its expression is given by:

$$\frac{C_{tc1}}{\varepsilon_0} = \frac{(C_{tc1}^*)^2}{C_{tc1}^* + C_{tl2}^*} \quad (3.52)$$

Fringe Capacitances between Conductor 1 and PEC Core

Next, the fringe capacitance between the conductor 1 and the core through the epoxy is analyzed [see Figure 3.25(c)]. Like the interior coupling analysis of C_{25} , the fringe capacitance between conductor 1 and the core is divided into two parts: C_{fcwx} for the segment $[wx]$ and C_{fcxy} for the segment $[xy]$. The capacitance value of C_{fcwx} is presented by:

$$\frac{C_{fcwx}}{\varepsilon_0 \varepsilon_r} = \frac{2}{\pi} \ln \left(1 + \frac{W_{wx}}{S_{ext}}\right) \quad (3.53)$$

However, to calculate $C_{f_{cxy}}$ for segment $[xy]$, the charge sharing principle should be applied among conductors 1, 2, and 4 over the segment $[xy]$ and expression (3.54) is derived:

$$\frac{C_{f_{cxy}}}{\epsilon_0 \epsilon_r} = \int_{S_{ext} + W_{wy}}^{S_{ext} + W_{wx}} \frac{\left(\frac{dx}{\pi/2 x}\right)^2}{\frac{dx}{\pi/2 x} + \frac{dx}{H} + \frac{dx}{\pi(S_{ext} + \pi/2 + W - x)}} \quad (3.54)$$

Finally, the capacitance between conductor 1 and the PEC core is simply:

$$C_{1c} = C_{pc1} + C_{tc1} + C_{tc2} + C_{tc3} + C_{tc4} + C_{fcwx} + C_{f_{cxy}} \quad (3.55)$$

The decomposition of the field between conductor 2 and the PEC core is much easier, as seen from Figure 3.25. The capacitance C_{2c} between conductor 2 and the core is:

$$C_{2c} = C_{pc2} + C_{tc6} + C_{tc7} \quad (3.56)$$

where C_{tc6} and C_{tc7} have the same expressions as C_{tc1} . Due to the symmetry of the structure, the capacitance between the other conductors and the core is also known from C_{1c} and C_{2c} .

3.4.4.2 New Inter-conductor Capacitances in Ferrite Core

The inter-conductor capacitances in the grounded PEC core can be studied similarly as is done in Section 3.3.2. However, all the exterior coupling is neglected due to the shielding effect of the PEC core and only the interior coupling in the epoxy is considered. After obtaining the capacitances between conductors C_{ij} in the grounded PEC core, the transformation formula (3.42) is applied to extract the new capacitances C_{ij}^* in the floating PEC core, i.e. the capacitances in the ferrite core.

It should be mentioned that the new diagonal capacitance C_{15}^* is given by the following formula:

$$C_{15}^* = \alpha \epsilon_0 \epsilon_r \sqrt{\sin \theta} \tanh\left(\frac{\pi W}{H + S} + 1\right) + \frac{C_{1c} C_{2c}}{4C_{1c} + 2C_{2c}} \quad (3.57)$$

where $\alpha=0.22$ remains the same as (3.40).

The capacitances such as C_{13}^* and C_{16}^* , that are originally neglected for the PCB configuration in air, can no longer be neglected in this case with ferrite core, their values are expressed by:

$$C_{13}^* = C_{16}^* = \frac{(C_{1c})^2}{4C_{1c} + 2C_{2c}} \quad (3.58)$$

3.4.4.3 Numerical Validation

To validate the method, the 6-conductor PCB structure (Figure 3.26) is simulated by Maxwell[®] with the following parameters: $W=2$ mm, $H=1.5$ mm, $H_{\text{iso}}=0.5$ mm, $S=0.8$ mm and $S_{\text{ext}}=0.3$ mm. The simulated results are compared with calculated ones in Table 3.5. As seen, a good match is found between them, which verifies the effectiveness of the introduced method.

The complete procedure for handling the PCB structure in ferrite core is summarized in Figure 3.27. The first step involves calculating the 2D capacitance matrix of the structure in a grounded PEC core. In this step, the capacitances between conductors C_{ij} and the capacitances between conductors and core C_{ic} are calculated using EFD method. Next, evaluate the capacitances matrix C_{ij}^* for the floating PEC core via the transformation formula (3.42). As discussed previously, this capacitance matrix C_{ij}^* with floating PEC core is just the one for ferrite core.

With this technique, the capacitance matrix in the core can be easily calculated. This allows a further process on the obtained 2D results, as it will be discussed in the next section.

3.5 Energy Approach

The EFD method allows the calculation of the main elements in the capacitance matrix for the 2D cross-section of a planar component. However, a planar component has a third dimension. Instead of using a full 3D analysis on the component, an energy approach will be introduced to take into account this third dimension.



Figure 3.26. Simulation model for the 6-conductor PCB structure

Table 3.5 Simulation Results for the 6-conductor PCB Structure.

Capacitance	Cal.	Sim.	Err.	Capacitance	Cal.	Sim.	Err.
<i>Capacitances between conductors and grounded PEC core</i>							
C_{1c}	106.6	102.1	4%	C_{2c}	46.0	50.2	8%
<i>New Capacitances between conductors in ferrite</i>							
C_{12}	-24.8	-23.9	4%	C_{15}	-18.5	-18.0	3%
C_{13}	-21.9	-20.4	7%	C_{16}	-21.9	-20.5	7%
C_{14}	64.9	-65.9	2%	C_{25}	-62.7	-60.4	4%
Unit: pF/m Cal. =Calculation Sim. =Simulation Err. =Erreur							

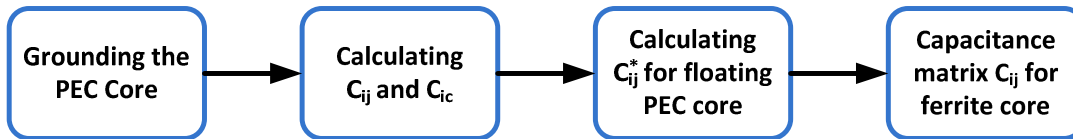


Figure 3.27. Procedure to handle ferrite core.

3.5.1 Derivation of Self-parasitic Capacitance

The resonance frequency can be considered as the frequency where the peak magnetic energy equals the peak electric energy [76]. Based on this definition, the equivalent self-parasitic capacitance C_{eq} of a single port component can be calculated with the peak electric energy, as given by (3.59):

$$C_{eq} = 2W_{elec} / U^2 \quad (3.59)$$

where W_{elec} is the electric energy and U is the peak value of input voltage. This approach is widely used for calculating the parasitic capacitances of various devices [35, 76] and it will be employed in this work for computing the equivalent parasitic capacitances of the planar components under study.

3.5.2 Calculation of Electric Energy in a Single Port Component

3.5.2.1 Basic Formulation and Assumptions

According to (3.59), the equivalent self-parasitic capacitance can be derived via the peak electric energy. In this part, the electric energy stored in a single port planar component will be introduced. This energy approach consists in combining the 2D capacitance matrix calculated previously together with the potential distribution on the studied component. In order to simplify the analysis, the following assumptions are accepted.

1. *The 2D capacitances are uniformly distributed along the third dimension of the winding trace. The edge effect on winding extremities and corners are neglected;*
2. *Without ferrite core, the potential varies linearly along the winding trace [Figure 3.28(a)];*
3. *With ferrite core, the potential varies only on the winding track covered by the core. Its variation on the winding track outside the core is negligible [Figure 3.28(b) and (c) [1].*

3.5.2.2 Procedure for Calculating the Parasitic Capacitance of Planar Inductors

Planar inductors are single-port component. The procedure for calculating the parasitic capacitance of a planar inductor consists of four steps, as will be presented below.

Step 1: Calculation of the potential profile along the winding

First, an input voltage U is fixed for the single port component. The potential distribution is calculated according to the assumptions introduced previously. For simplification, U is usually set to be 1V so that $C_{eq}=2W_{elec}$ according to (3.59).

Step 2: Calculation of the capacitance matrix for the component cross-section

In this step, the EFD method is applied to analyze the cross-section of the component inside the ferrite core and outside of the core. The main elements of the

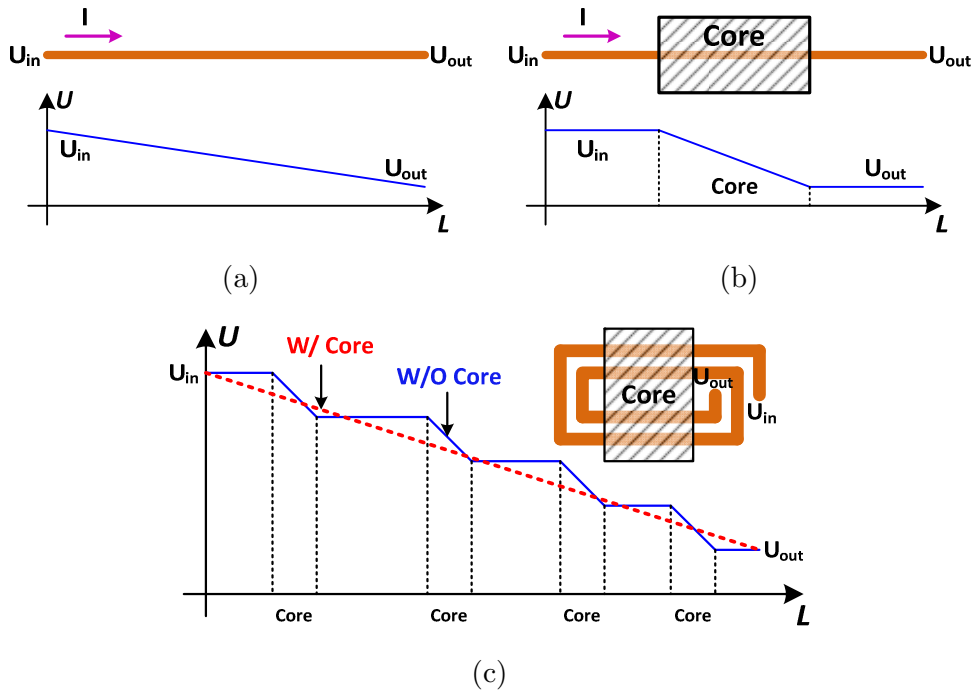


Figure 3.28. (a) Variation of potential without core. (b) Variation of potential with core. (c) Variation of potential of a 2-turn inductor: with and without core.

capacitance matrix $[C_{ij}]_{core}$ and $[C_{ij}]_{air}$ are calculated and the others, with less importance are thus neglected.

Step 3: Decomposition of the winding trace and Computation of the electric energy W_i

In this step, the winding trace of the component is decomposed into N segments at every turning point. A 6-turn inductor is taken as an example for explanation [Figure 3.29(a)]. The winding of this inductor is decomposed into 24 independent segments [Figure 3.29(b)]. After this decomposition, the electric energy between one segment and all the other parallel segments in its vicinity is calculated. The case without core is first analyzed. For example, the segment 1 has capacitive coupling with the segment 5, 18 and 22 whereas the segment 6 has capacitive coupling with segments 2, 10, 15, 19 and 23. The electric energy between two segments i and j is calculated by:

$$\Delta W_{ij} = \frac{1}{2} C_{ij} \int_0^{L_{ij}} (V_i(z) - V_j(z))^2 dz \quad (3.60)$$

where C_{ij} is the 2D capacitance calculated with the EFD method, z is the direction

along the current flow, $V(z)$ is the potential distribution calculated in the first step, and L_{ij} is the effective common length of the two segments. Note that these segments may not have the same length or not be aligned. Therefore, when calculating L_{ij} , one conductor segment j is projected onto the segment i and the length of the overlapped part is taken as L_{ij} (see Figure 3.30). Similarly, one can calculate the electric energy from segment i to the other parallel segments and the total electric energy due to segment i is:

$$W_i = \sum_{j \in NC} \Delta W_{ij} \quad (3.61)$$

where the group NC includes the conductor segments that are parallel and close to conductor segment i .

For the case with ferrite core, the winding part outside the core is still treated as before to extract its capacitance matrix. However, for the winding part covered by the core, the corresponding capacitance matrix is different from what it is outside. For example, the segment 1 will have capacitive coupling not only with segments 5, 18 and 22, but also with the segments 9 and 14 via the ferrite core, as analyzed before. Here, the coupling between the segment 1 and the conductors in the other window (16, 20, 24...) is not considered for simplification. Moreover, the coupling between two segments that is orthogonal to each other (1 and 2, 1 and 19 for example) is neglected in this study.

Step 4: Summation of ΔW_i of all the groups to obtain W_{elec}

In the step 3, the conductors in this system are analyzed in order (by number) and the electric energy stored in the component is estimated by:

$$W_{elec} = \frac{1}{2} \sum_i W_i \quad (3.62)$$

where the $\frac{1}{2}$ coefficient appears for considering the double counts of ΔW_{ij} and ΔW_{ji} .

The above-mentioned procedure is programmed in Matlab[®]. First, the winding information is loaded into the program to define the conductor segments (see Figure 3.31). Next the potential distribution is calculated at the request of the user. The decomposition of the winding and the calculation of the electric energy are realized

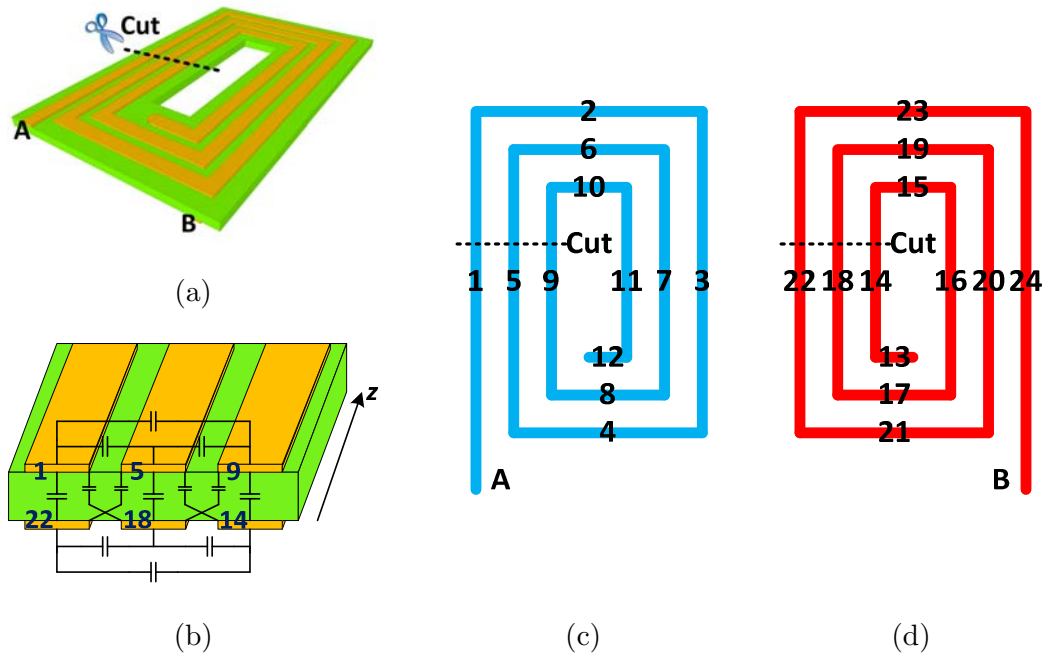


Figure 3.29. Example: 6-turn inductor without ferrite core. (a) 3D view. (b) Cross-section at the cut point. (c) Trace on the top layer. (d) Trace on the bottom layer.

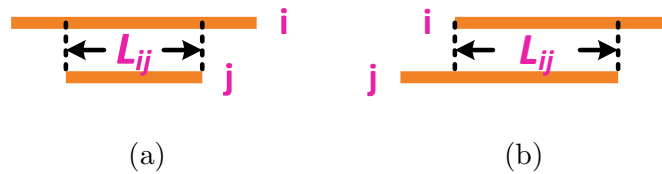


Figure 3.30. The common length L_{ij} for segments i and j . (a) Segments i and j with different lengths. (b) Segments i and j not aligned.

by a program using a function “WE()” that works as (3.60). With the capacitance matrix calculated through the EFD method, the equivalent parasitic capacitance can be determined.

3.5.3 Procedure for Calculating the Parasitic Capacitances of Planar CM Chokes

The previous approach works only for single-port components. However, it cannot be directly applied on planar CM chokes since they are two-port components. In this part, the energy approach is extended to planar CM chokes by adopting three test configurations that transform a two-port component to a single-port component.

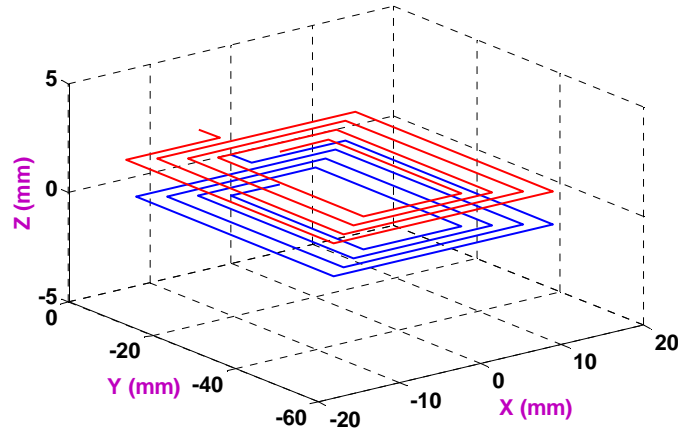


Figure 3.31. Winding structure of an 8-turn planar inductor generated in Matlab

The Figure 3.32(a) illustrates the equivalent circuit of a planar CM choke. It can be seen that there are three independent parasitic capacitances. To derive the values of these capacitances, three equations are required. Similar to what is done in the extraction procedure (see Chapter 2), the same test configurations are used for providing these three equations [Figure 3.32(b)]. However, the only difference here is that the parasitic capacitances are no longer extracted by measurements but with analytical calculations.

With each test configurations, the CM choke is transformed into a single port component. To evaluate the electric energy stored in each configuration, two kind of energy should be considered separately: (a) The energy stored in each winding W_{winding1} and W_{winding2} ; (b) The energy stored between two windings W_{inter} . For a CM choke that has symmetry structure, the total energy W is:

$$W = W_{\text{winding1}} + W_{\text{winding2}} + W_{\text{inter}} \quad (3.63)$$

Therefore, the previous procedure for single-port component can be applied again on these three configurations, resulting in three linear equations [Figure 3.32(b)]. Finally, the values of C_e , C_p and C_c are all extracted.

3.6 Applications

In this section, the applications of the EFD method together with the energy approach are introduced with detail. Three examples are given to show the

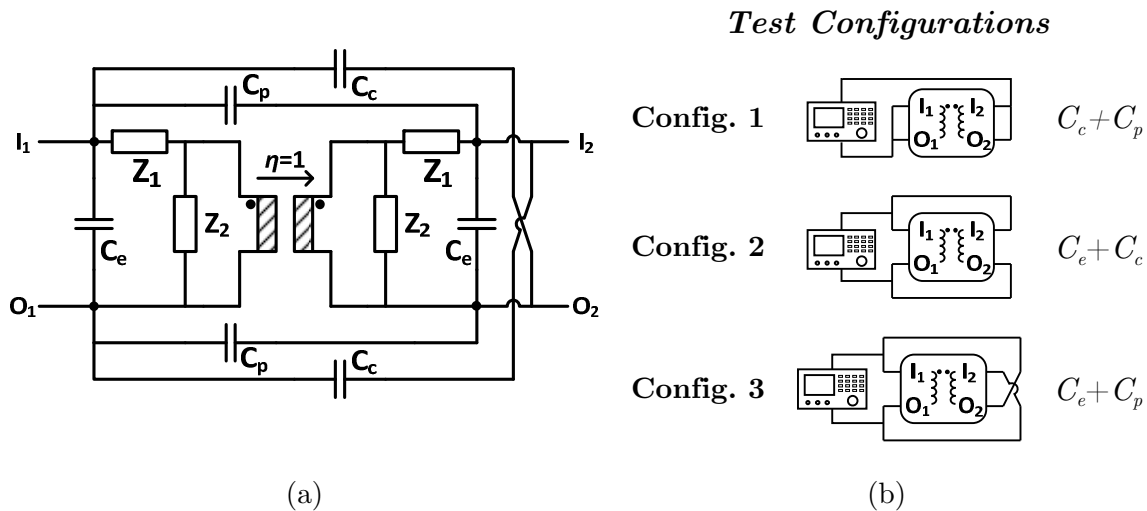


Figure 3.32. Parasitic capacitances calculation for planar CM choke. (a) Equivalent circuit for planar CM choke. (b) Test configurations.

effectiveness of the proposed analytical method for parasitic capacitance calculation.

3.6.1 Planar Inductor without Ferrite Core

The first example involves a planar inductor without ferrite core. As seen in Figure 3.33(a), the studied planar inductor has 8 turns and the ferrite core is not implemented. The cross-section of this component contains 8 conductors [Figure 3.33(b)] and can be decomposed into two 6-conductor configuration, as analyzed previously in this chapter. Based on the EFD method and the energy approach, the parasitic capacitance of the component is calculated by a Matlab program and the calculated value of the component is 11.1 pF. The measured impedance of this component is shown in Figure 3.33(c). From the resonance frequency, the parasitic capacitance can also be extracted using the following formula:

$$f_r = \frac{1}{\sqrt{C_{meas} L_{meas}}} \quad (3.64)$$

where L_{meas} is the inductance value extracted from the inductive region of the impedance curve. The experimental value of the parasitic capacitance is 10.6 pF, which is very close to the calculated one (5% difference). Note that the main difference between the EFD method and the simple formula $C = \epsilon_r W/H$ is that the former takes into account the fringe effects. If these effects were neglected by using

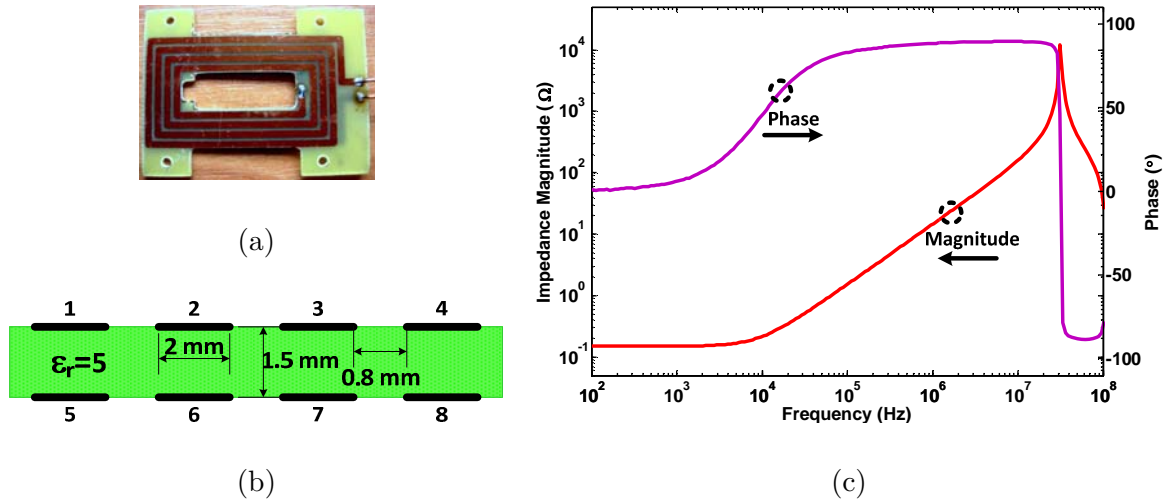


Figure 3.33. 8-turn planar inductor without ferrite core. (a) Component. (b) Cross-section. (c) Measured impedance.

only the formula (3.1), the obtained results would be 8.2 pF, which exhibits a 23% difference from the measured value. In a word, it is very important to consider the fringe effects during the parasitic capacitance calculation and the EFD method can give more accurate results.

3.6.2 Planar Inductor with Ferrite Core

Now the same inductor is implemented into a Ferroxcube 3F4 ferrite planar E38 core. The calculation begins with analyzing the 2D capacitance matrix of the cross-section of the component. As the cross-section in air of this component is already studied before, only the case in the core is treated below.

3.6.2.1 2D Analysis for the Cross-section in the Core

For handling the ferrite core, it is replaced by a grounded PEC core, and the capacitances between conductors and the core are calculated first. The cross-section in the core of the component is illustrated in Figure 3.34. As seen, a PVC cohesive tape ($\epsilon_r=3.5$, $H_T=1$ mm) is stuck on the winding part that is inside the core, to provide isolation between the winding and the core. To solve this multilayered structure, the method in [37] is employed to uniform these layers, as seen from Figure 3.35. The new PVC isolator is uniform but has an increased thickness H_i^* :

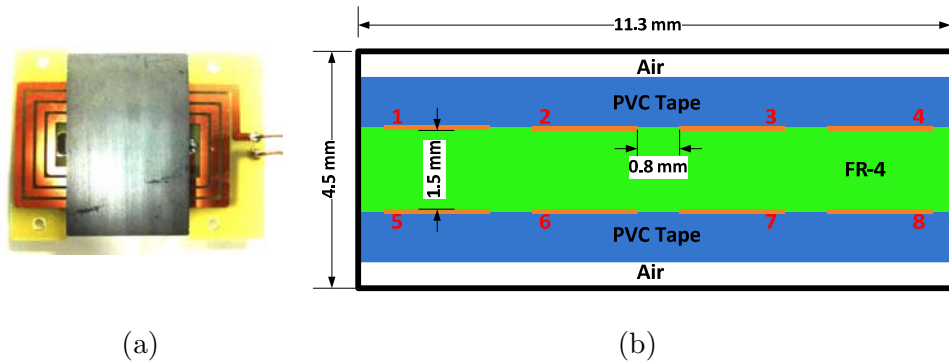


Figure 3.34. 8-turn planar inductor with ferrite core. (a) Component. (b) Cross-section in the core.

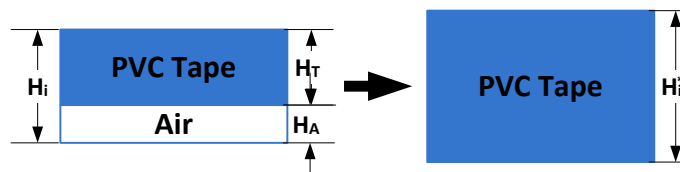


Figure 3.35. Transformation for handling the multilayered isolator.

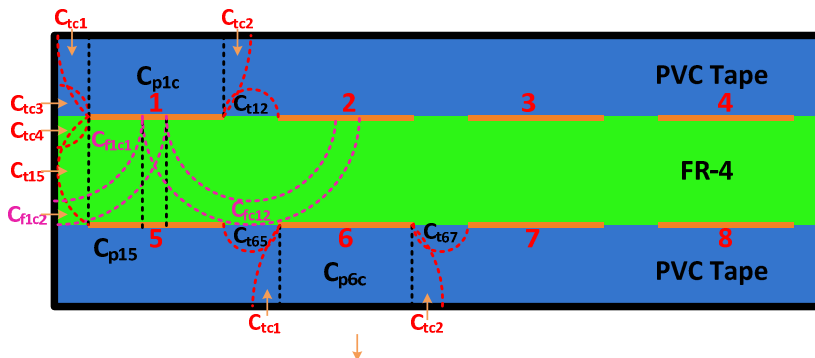


Figure 3.36. Decomposition of the field between conductors and the PEC core: conductor 1 and conductor 6.

$$H_i^* = H_i + \left(\frac{\epsilon_{PVC}}{\epsilon_0} - 1 \right) H_A = H_i + 2.5H_A \quad (3.65)$$

The decomposition of the field from conductors 1 and 6 to the PEC core is given in Figure 3.36. It is exactly the same as the case of 6-conductor PCB structure presented before. Moreover, the symmetry of the structure should be considered: The field decomposition for conductors 4, 5 and 8 is the same to 1 and the field decomposition of 2, 3 and 7 is the same to 6. After the extraction of the inter-conductor capacitances C_{ij} in the grounded PEC core and the capacitances between the conductors and the grounded PEC core C_{ic} , the transformation formula

Table 3.6 Comparison between Calculation and Simulation for the Capacitance Between Conductors and Grounded PEC Core.

Capacitance	Cal.	Sim.	Err.
$C_{1c}=C_{4c}=C_{5c}=C_{8c}$	99.2	99.0	1%
$C_{2c}=C_{3c}=C_{6c}=C_{7c}$	32.0	32.3	1%
Unit: pF/m Cal.=Calculation Sim.=Simulation Err.=Error			

Table 3.7 Comparison between Calculation and Simulation for the 8-conductor Configuration in Ferrite Core.

Capacitance	Cal.	Sim.	Err.	Capacitance	Cal.	Sim.	Err.
C_{12}	35.2	35.1	1%	C_{62}	60.7	59.7	2%
$C_{13}=C_{17}$	5.9	6.0	2%	C_{63}	10.9	11.0	1%
$C_{14}=C_{18}$	18.7	19.7	5%	$C_{64}=C_{68}$	5.9	6.0	2%
C_{15}	66.8	68.6	3%	C_{67}	31.1	31.2	1%
C_{16}	15.0	15.3	2%				
Unit: pF/m Cal.=Calculation Sim.=Simulation Err.=Error							

(3.42) is applied for finding the final capacitance matrix $[C_{ij}^*]$ in the ferrite core.

The calculated capacitances between conductors to grounded PEC core are compared with simulated values in Table 3.6. Table 3.7 compares the final capacitances matrix in ferrite core with FEM simulations results. In both tables, a good match is spotted, which further validates the presented 2D analytical formulas.

3.6.2.2 Experimental Validation

Applying again the energy approach with the calculated capacitance matrix, the parasitic capacitance of the component is determined to be 14.6 pF, which is 40% larger than the case without ferrite core. Meanwhile, the experimental value of the parasitic capacitance can also be measured from the impedance of the component, as given in Figure 3.37(c). It can be deduced that the experimental value is 18.7 pF, which is 25% higher than the calculated one. However, it should be noted that when a ferrite core is used, the dielectric characteristic between the grains will also affects the resonance frequency [55]. To consider the effects due to the ferrite core, the equivalent circuit of the core is extracted with the following steps:

1. A one-turn inductor is realized with the ferrite core and its impedance Z_{1S} is

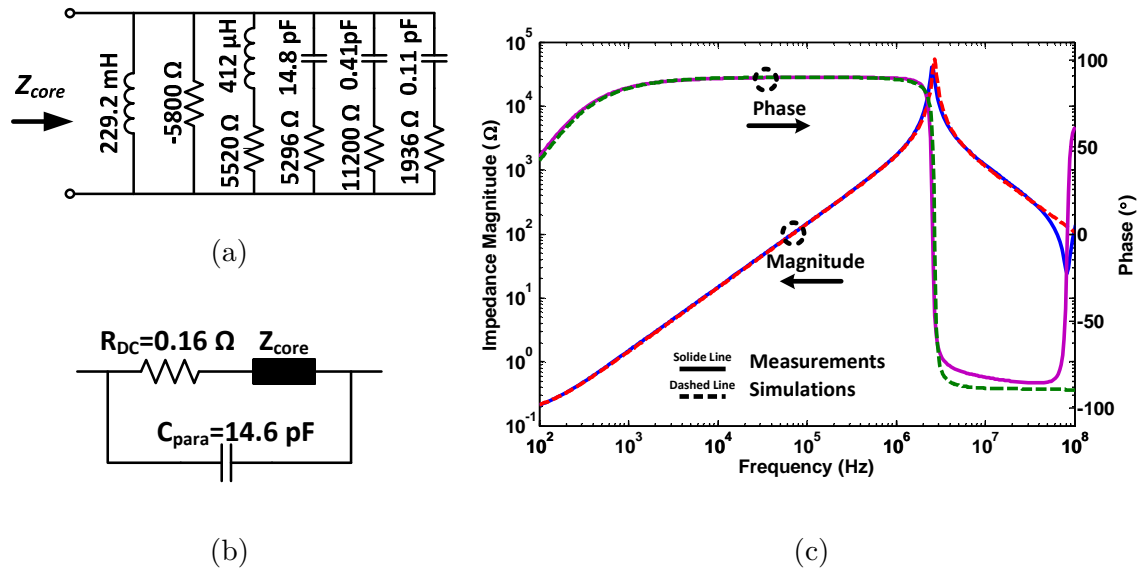


Figure 3.37. Simulation of the 8-turn planar inductor. (a) Equivalent circuit for the ferrite core. (b) Equivalent circuit for simulation. (c) Comparison between simulation and measurement.

measured with an impedance analyzer [77].

2. The impedance of an 8-turn inductor, representing the magnetizing impedance of the ferrite core, is simply:

$$Z_{8S} = 8^2 Z_{1S} \quad (3.66)$$

Using the equivalent circuit identification method introduced in Chapter 2, the equivalent circuit of Z_{8S} can be established, as illustrated in Figure 3.37(a). Now the parasitic capacitance is simulated together with the impedance Z_{8S} , as shown in Figure 3.37(b). The simulated curve is compared with the experimental one in Figure 3.37(c). It can be found that the two curves have a very good match, which validates the calculated value of the parasitic capacitance. Note that if formula (3.1) is used for this calculation without considering the fringe effects and the influence of ferrite core, the parasitic capacitance is only 10.2 pF, which exhibits a significant error.

3.6.3 Planar CM Choke with Ferrite Core

3.6.3.1 2D Analysis for the Cross-sections

The cross-section of the component out of the core is given in Figure 3.38(a).

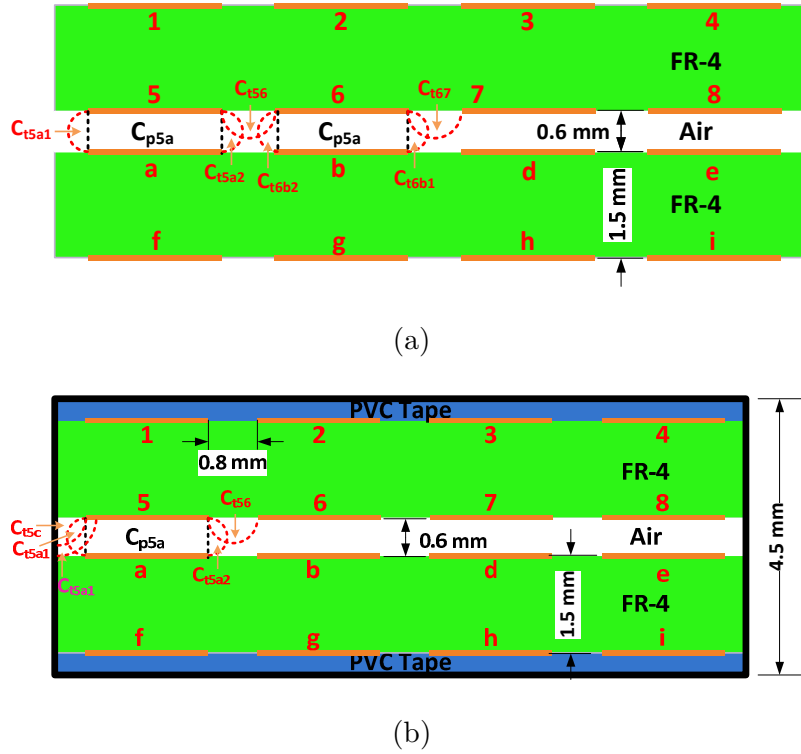


Figure 3.38. Decomposition of the field for conductor 5 and 6: (a) Cross-section in air. (b) Cross-section in core.

Some capacitances for conductors far away to each other should be neglected, such as C_{14} , C_{2e} , etc.. The capacitive coupling between the two PCBs is strong so they should be considered. As the two PCBs are very close to each other, only the plate and terminal capacitances are considered, as shown in Figure 3.38(a). The decomposition in every PCBs remains the same as the previous analyses. Here, only the conductors of 1, 2, 5 and 6 need to be analyzed. The situation for the other conductors can be studied by symmetry feature. The decomposition for conductor 5 and 6 is illustrated in Figure 3.38(a). As the two PCBs are very close, the fringe capacitances in the air layer are neglected due to field shielding effect. Note that to calculate the terminal capacitances, charge sharing principle is applied again.

The Figure 3.38(b) shows the situation in the core. Similar decomposition can be made for calculating the capacitances between conductors to core. It should be noted that the capacitance of the conductor 6, 7, b and c have negligible capacitances to the core since they are shielded from the core by other conductors. The decomposition of the field for conductor 5 is illustrated in Figure 3.38(b) while

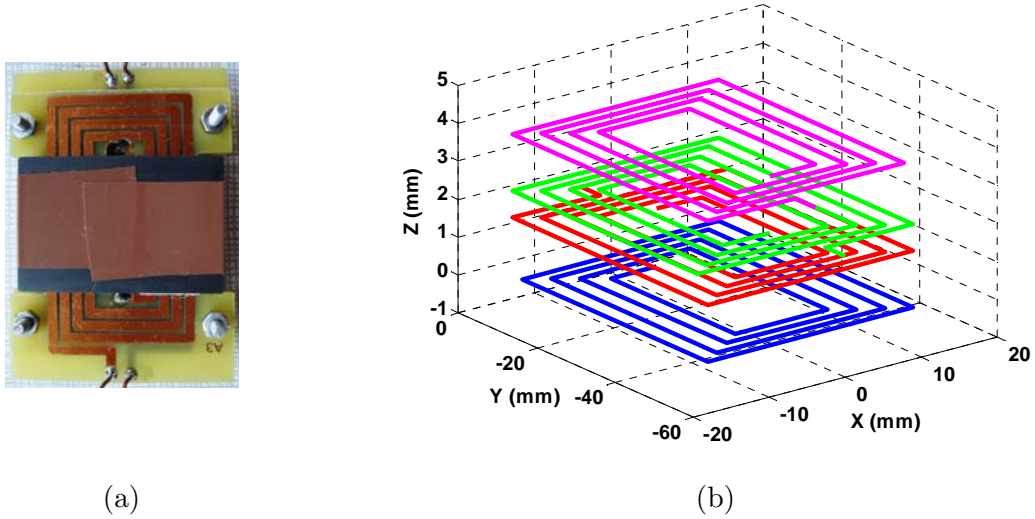


Figure 3.39. Planar CM choke under study. (a) Component. (b) Geometry models constructed in Matlab.

the one for conductor 6 remain the same to the case in air.

After the calculation, the transformation technique is applied to obtain the real capacitance matrix in ferrite core.

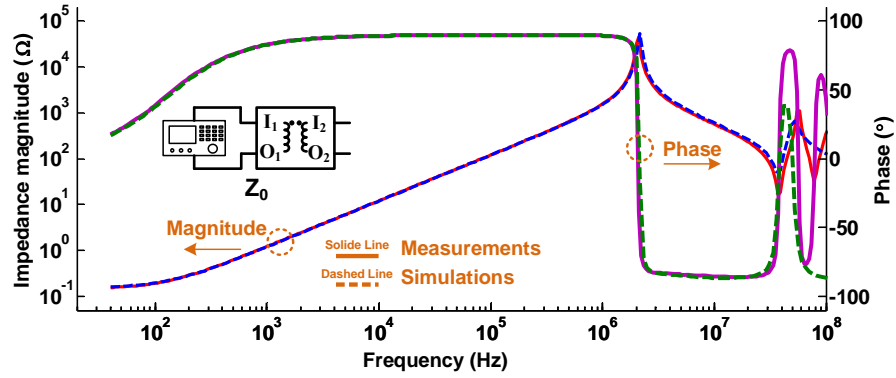
3.6.3.2 Experimental Validation

The energy approach is finally applied on the planar CM Choke under study, as given in Figure 3.39(a). Its winding segment is generated in Matlab, as given in Figure 3.39(b). According to the energy method for CM chokes, the three test configurations in Figure 3.32(b) are studied separately, lead to the following equations:

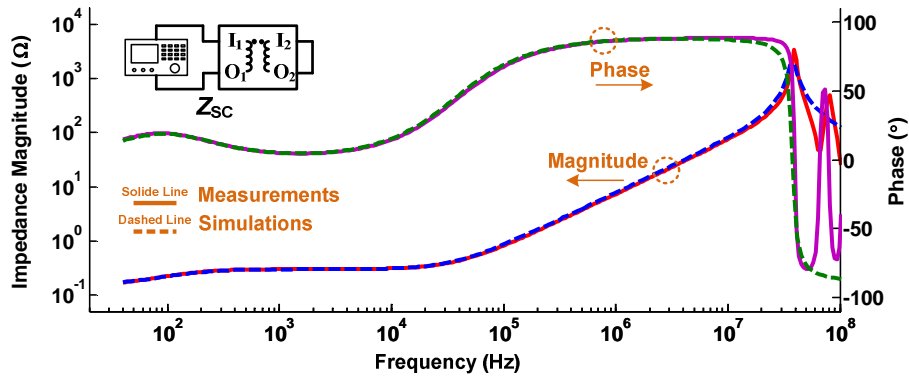
$$\begin{cases} 2C_c + 2C_p = 26.3 & \text{Config. 1} \\ 2C_e + 2C_c = 24.7 & \text{Config. 2} \\ 2C_e + 2C_p = 31.2 & \text{Config. 3} \end{cases} \quad (3.67)$$

From (3.67), the values of C_e , C_p and C_c are 7.4 pF, 8.3 pF and 4.9 pF, respectively.

For validating these values, the equivalent circuit of Figure 2.17 is used again. Note that the parasitic capacitances in this equivalent circuit are replaced by the calculated values. Similarly, the open circuit impedance Z_0 and short circuit impedance Z_{SC} is simulated and compared with measured curves, as illustrated in Figure 3.40. It can be seen that the calculated parasitic capacitances can correctly predict the resonance frequency.



(a)



(b)

Figure 3.40. Comparison between simulations and measurements for the CM choke. (a) Open-circuit impedance Z_0 . (b) Short-circuit impedance Z_{sc} .

From the above examples, it can be concluded that the developed analytical procedure based on EFD method and energy method can give quite accurate results for modeling the parasitic capacitances of planar components. As the first step in the design process, this procedure is a useful tool to guide the design.

3.7 Discussion

The proposed analytical method for calculating the parasitic capacitance works very well for the studied planar components. However, several limits should also so be underlined.

1. **Geometry of the cross-section:** This arrangement is very regular in the studied case. When using the EFD method, it is supposed that the conductors are identical, equally-spaced and well aligned. However, if the conductors are

staggered between each other, the analysis could be very cumbersome and even impossible.

2. ***Other fringe capacitances:*** To simplify the calculation, the whole method is based on 2D analysis and assumes that the 2D capacitances matrix is uniformly distributed along the third dimension. In fact, this assumption is coarse since the winding is not infinitely long along the current-flow direction. Therefore, the fringe capacitances on the extremities of every segment should be accounted in a strict sense. Besides, the capacitances between conductors that are orthogonal to each other or in different core windows are not considered in this analytical method. Anyway, the goal of this study is to provide handy calculation formulations for studying planar components, which is fast and sufficiently accurate to provide design insight. The only way to consider all the above-mentioned effects together is to employ numerical methods like PEEC or Finite-Difference, etc..
3. ***Distributed effects:*** As the method is based on the energy approach, it is valid only before the resonance where the distributed effects can be neglected. As a consequence, the method is unable to predict what happens after the first resonance. For simulating the HF resonances, distributed models should be developed in the future study.

3.8 Conclusion

In this chapter, an analytical procedure is proposed for calculating the parasitic capacitances for planar CM choke. The approach starts with 2D analysis of the cross-section of the studied component by the Electric Field Decomposition (EFD) method. Based on three elementary capacitances and two decomposition principles, the EFD method allows the derivation of accurate and scalable formulas for PCB structures encountered in the planar CM choke. To take into account the influence of the ferrite core, an effective transformation technique is then proposed. The technique treats the ferrite core as floating perfect electric conductor and uses a simple transformation formula for calculating the associated capacitances. With the EFD method, the main elements in the capacitance matrix for the cross-section

of the component can be extracted. The method for 2D analysis is validated by comparison with numerical simulations.

With 2D capacitance matrix, an energy approach is further employed to find the equivalent parasitic capacitances. The energy approach relates the parasitic capacitance to the peak electric energy stored in the component, which can be calculated by summing the electric energy stored between different conductor segments in the windings.

Complete procedure is proposed for the whole calculation of parasitic capacitance. The procedure is tested on several prototypes, including two planar inductors and a planar CM choke. The obtained results agree well with experimental ones, which validate the whole analytical procedure.

Despite of the simplicity of the proposed formulas, its accuracy cannot be guaranteed for arbitrary cross-section geometry. The lengthy decomposition makes it impossible to be implemented in optimization programs. Most importantly, the structures treated in this chapter have to be very regular and symmetrical. When conductors with different widths or staggered conductors appear in the structure, the EFD method cannot be applied. Due to these reasons, in the next chapter, a semi-analytical method based on multilayered Green's function is presented for generalizing and automating the calculation.

Chapter 4. Modeling of Parasitic Elements of Planar CM Choke via Multilayered Green's Function

The EFD method introduced in Chapter 3 has several limitations on its application area such as the requirement on the structure geometry and the complexity of the field decomposition. Therefore, a more general tool for analyzing the parasitic elements is desired. In view of this necessity, this chapter mainly treats the applications of Green's function on the modeling of the parasitic elements of planar CM chokes. The whole chapter is divided into two parts. The first part focuses on the determination of parasitic capacitances via the use of multilayered Green's function. This multilayered Green's function method allows a fast and accurate calculation on the 2D capacitance matrix of a multilayered PCB structure with random arrangement of conductors. After obtaining this 2D capacitance matrix, the same energy approach introduced in Chapter 3 can be applied again to find the equivalent parasitic capacitances of the studied component. The second part of this chapter extends the multilayered Green's function method for modeling the leakage inductance of a planar CM choke, where a FPC leakage layer is sandwiched. The method consists in solving the vector potential in the window cross-section, which allows calculation of the magnetic energy stored in the component to determine its leakage inductance.

4.1 Green's Function Theory

4.1.1 Introduction to Green's Function

The Green's function is one of the most powerful tools used in electromagnetism since it can give a closed-form solution for many types of partial differential equations [67]. In this work, its applications on Poisson's equation in

electrostatic and magnetostatic formulations are particularly interested. Here, the 2D electrostatic Poisson's equation in a region Ω is taken as an example [34]:

$$\nabla^2 U(\mathbf{r}) = -\frac{1}{\varepsilon} \rho(\mathbf{r}_s) \quad (4.1)$$

where U is the potential, \mathbf{r} and \mathbf{r}_s are respectively the coordinates of the observation and source points, ε is the permittivity of the matter and $\rho(\mathbf{r}_s)$ is the charge density distribution function for the source. Suppose that the homogenous Dirichlet boundary conditions (B.C.) are given for this problem:

$$U(\mathbf{r})|_{\partial\Omega} = 0 \quad (4.2)$$

The associated Green's function for this problem is expressed as:

$$\begin{cases} \nabla^2 G(\mathbf{r}, \mathbf{r}_s) = -\frac{1}{\varepsilon} \delta(\mathbf{r}_s) \\ G(\mathbf{r}, \mathbf{r}_s)|_{\partial\Omega} = 0 \end{cases} \quad (4.3)$$

where $\delta(\mathbf{r}_s)$ is the Dirac function.

Recalling the second Green's identity [67]:

$$\int_{\Omega} (\phi \nabla^2 \psi - \psi \nabla^2 \phi) dV = \oint_{\partial\Omega} \left(\phi \frac{\partial \psi}{\partial n} - \psi \frac{\partial \phi}{\partial n} \right) dS \quad (4.4)$$

where ϕ and ψ are two arbitrary scalar fields. Replace ϕ by U and ψ by G , the following equation is obtained:

$$\int_{\Omega} (G \nabla^2 U - U \nabla^2 G) dV = \oint_{\partial\Omega} \left(G \frac{\partial U}{\partial n} - U \frac{\partial G}{\partial n} \right) dS \quad (4.5)$$

Leading to

$$\int_{\Omega} U \delta(\mathbf{r}_s) dV = \int_{\Omega} G(\mathbf{r}, \mathbf{r}_s) \rho(\mathbf{r}_s) dV + \varepsilon \oint_{\partial\Omega} \left(G \frac{\partial U}{\partial n} - U \frac{\partial G}{\partial n} \right) dS \quad (4.6)$$

As homogenous Dirichlet B.C. is considered here, the second integral on the right side of the equation is zero. Moreover, due to the sampling property of Dirac function, the final equation is given as follows [78]:

$$U(\mathbf{r}) = \int_{\Omega} G(\mathbf{r}, \mathbf{r}_s) \rho(\mathbf{r}_s) dV \quad (4.7)$$

As seen from (4.7), the solution of the original problem (4.1) is given by a convolution. From a physical standpoint, the Green's function presents the response of an electromagnetic system to an "impulse" excitation. Concretely in this case, the Green's function gives the potential of the observation point under the influence of a Dirac source charge. In a word, the Green's function is a specially constructed function to obtain the integral form solution of the Poisson's equation (1.1).

4.1.2 2D Green's Function for Homogenous Space

In electrostatic study, the 2D Green's function is governed by the Poisson's equation below:

$$\nabla^2 G(x, y; x_s, y_s) = -\frac{1}{\varepsilon} \rho(x_s, y_s) \quad (4.8)$$

where (x, y) and (x_s, y_s) denote the coordinates of the observation and the source points, respectively. Depending on the B.C.s of the problem, different solutions can be derived from this general equation.

Green's Function for Free Space

The two dimensional Green's function of the Poisson's equation in free space has simple analytical form, as given by (4.9) [34]:

$$G(x, y; x_s, y_s) = -\frac{1}{2\pi\varepsilon} \ln \sqrt{(x - x_s)^2 + (y - y_s)^2} \quad (4.9)$$

As seen, its form is very simple, which allows the development of analytical solutions for free space problems, as will be discussed later in this chapter.

Green's Function for Rectangular Region

For a rectangular region, the Green's function should be presented by Fourier series. Here, only the case of homogenous Dirichlet BC is presented, as given in Figure 4.1. To solve this problem, two different solutions can be developed. The first one involves double series expansion approach, as given by (4.10) [34]:

$$G(x, y; x_s, y_s) = \frac{4}{\varepsilon LH} \sum_m \sum_n \frac{\sin\left(\frac{m\pi x}{L}\right) \sin\left(\frac{n\pi y}{H}\right)}{\left(\frac{m\pi}{L}\right)^2 + \left(\frac{n\pi}{H}\right)^2} \sin\left(\frac{m\pi x_s}{L}\right) \sin\left(\frac{n\pi y_s}{H}\right) \quad (4.10)$$

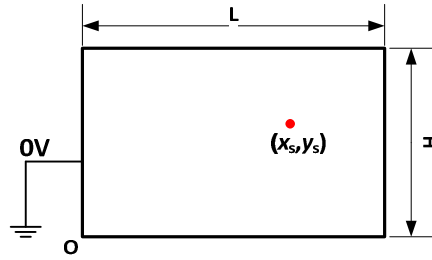


Figure 4.1. Dirac charge source in a rectangular region with homogenous Dirichlet B.C..

The obtained solution has a simple form but can be very cumbersome for computation due to its slow convergence.

The other solution is the single series expansion approach. With the separation of variable method, a closed-form formula (4.11) can be derived [34], as expressed by:

$$G(x, y | x_s, y_s) = \begin{cases} \sum_{m=1}^{\infty} \frac{2}{m\pi\epsilon} \sin\left(\frac{m\pi}{L} x_s\right) \sin\left(\frac{m\pi}{L} x\right) \frac{\sinh\left(\frac{m\pi}{L} y_s\right) \sinh\left(\frac{m\pi}{L} (H - y)\right)}{\sinh\left(\frac{m\pi H}{L}\right)} & y \geq y_s \\ \sum_{m=1}^{\infty} \frac{2}{m\pi\epsilon} \sin\left(\frac{m\pi}{L} x_s\right) \sin\left(\frac{m\pi}{L} x\right) \frac{\sinh\left(\frac{m\pi}{L} (H - y_s)\right) \sinh\left(\frac{m\pi}{L} y\right)}{\sinh\left(\frac{m\pi H}{L}\right)} & y \leq y_s \end{cases} \quad (4.11)$$

Though its form is much more complex, its computation intensity is much lower.

The above mentioned Green's functions help to solve lots of electrostatic problems. However, all these solutions require a space with homogenous matter so it cannot be easily (but possible) employed in our planar components that have a multilayered structure composed of several materials. For this reason, the method of multilayered Green's function is introduced in the following part for studying the parasitic capacitances of planar components.

4.2 Parasitic Capacitance Calculation Using Multilayered Green's Function

4.2.1 Declaration of Problem: PCB Structure with Ferrite Core

The configuration of PCB structure with ferrite core is first studied [Figure 4.2(a) (only one window is given)]. As analyzed in the previous chapter, the ferrite

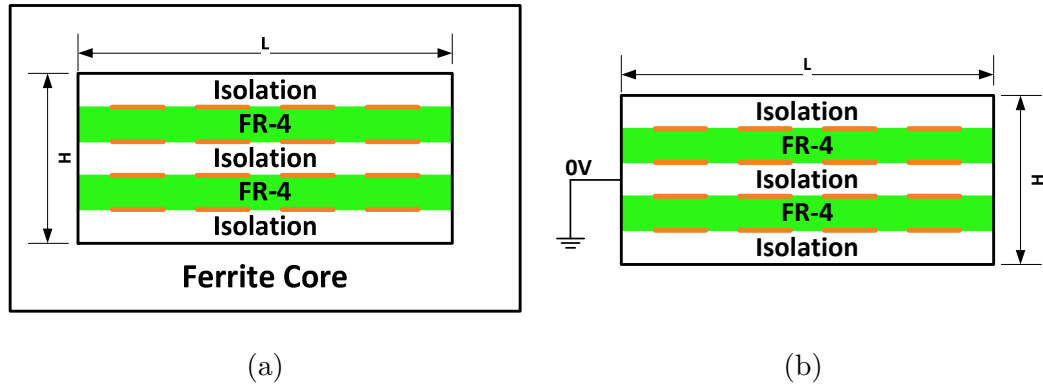


Figure 4.2. PCB structure in ferrite core. (a) Original problem. (b) Transformed Dirichlet B.C. problem.

core is treated as a floating PEC core, which can be transformed from a grounded PEC core whose potential is set to be 0 V [Figure 4.2 (b)]. Note that the configuration of grounded PEC core just forms a homogenous Dirichlet B.C..

Before studying the multilayered Green's function, the following assumptions should be accepted.

1. *The thickness of the conductors is infinitesimal.*

This assumption is reasonable because the thickness of the winding trace is negligible compared to its width. In the studied planar CM choke, the thickness of the conductors is $70 \mu\text{m}$ whereas the width is 30 times larger. With this assumption, the calculation can be significantly simplified. However, the fringe effects due to the two side walls of the conductors are not totally negligible in some cases. As will be seen later, for certain cases, the consideration of the side wall capacitance will improve the accuracy of the results obtained with the Green's function method.

2. *The conductors are located at the interfaces between layers.*

For a planar CM choke based on PCB structure, a multilayered structure composed of isolation and FR-4 epoxy layers is observed [Figure 4.2 (b)]. As the thickness of the conductors can be neglected, these conductors are assumed to be located at the interfaces of the different layers.

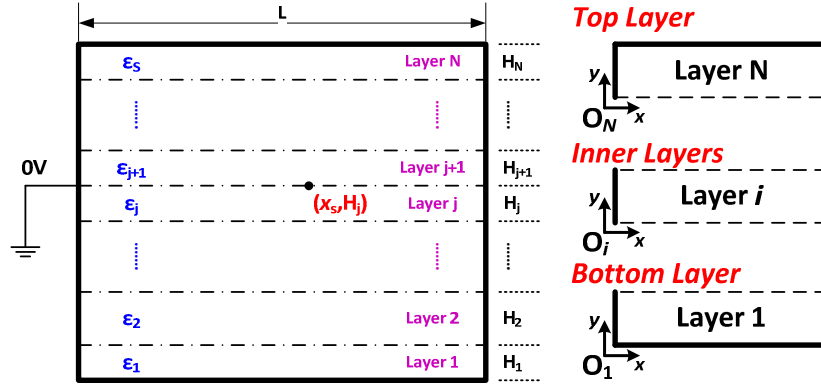


Figure 4.3. Multilayered structure under study.

4.2.2 Multilayered Green's Function for Rectangular Region

In [79], the authors have proposed a general form of Green's function for a shielded multilayered rectangular region. This method will be developed in the following parts.

As said before, the conductors are located at the interfaces between layers. To be general, considering a rectangular region composed of N layers of materials with different permittivity (see Figure 4.3). For this problem, a local coordinate is applied in each layer with the origin on the lower left vertex. Homogenous Dirichlet B.C. is applied on the boundary of the region. The Dirac charge source is positioned at $x=x_s$ on the interface between layer j and layer $j+1$ ($j < N$). As the charge source is located at the interface, the Green's function $G^i(x, y; x_s, y_s)$ in the layer i is governed by:

$$\nabla^2 G^i(x, y; x_s, y_s) = 0 \quad (4.12)$$

where (x, y) denotes the coordination of the observation point and (x_s, y_s) the source point. Meanwhile, the following B.C.s should also be satisfied:

1. *Left and right boundaries of layer i : $x=0$ and $x=L$:*

$$G^i \Big|_{x=0} = G^i \Big|_{x=L} = 0 \quad (4.13)$$

2. *Top and bottom boundaries (in layer N and layer 1):*

$$G^N \Big|_{y=H_N} = G^1 \Big|_{y=0} = 0 \quad (4.14)$$

3. Continuity conditions on the interface between layer i and layer $i+1$ ($i < N$):

$$\begin{cases} G^i \Big|_{y=H_i} - G^{i+1} \Big|_{y=0} = 0 \\ \varepsilon_i \frac{\partial G^i}{\partial y} \Big|_{y=H_i} - \varepsilon_{i+1} \frac{\partial G^{i+1}}{\partial y} \Big|_{y=0} = \delta_{ij} \delta(x - x_s) \end{cases} \quad (4.15)$$

where δ_{ij} is the Kronecker function. Using the separation of variable method, the general form of Green's function in layer i satisfying the B.C.s (4.13) is given by:

$$G^i(x, y; x_s, y_s) = \sum_{n=1}^{\infty} [\alpha_n^i \text{ch}(k_n y) + \beta_n^i \text{sh}(k_n y)] \sin(k_n x) \quad (4.16)$$

where ‘‘ch’’ and ‘‘sh’’ are the cosine and sine hyperbolic functions, α_n^i and β_n^i are the Fourier coefficients to determine and $k_n = n\pi/L$, $n=1, 2, \dots, \infty$. Note that these parameters depend on the position (x_s, y_s) of the source charge. The explicit deduction of the equations from (4.17) to (4.19) are omitted in this section but can be found in Appendix V. Only the results are given below.

The value of α_n^i and β_n^i can be derived from (4.17), where $[\mathbf{F}_n^{l,l+1}]$ and $[\mathbf{F}_n^{l,l+1}]^{-1}$ are the upward transformation matrix and downward transformation matrix for the interface of layer l and layer $l+1$, respectively, as given by (4.18) and (4.19).

$$\begin{pmatrix} \alpha_n^i \\ \beta_n^i \end{pmatrix} = \begin{cases} \begin{pmatrix} 1 \\ \prod_{l=i-1}^1 [\mathbf{F}_n^{l,l+1}] \end{pmatrix} \begin{pmatrix} 0 \\ \beta_n^1 \end{pmatrix} & i \leq j \\ \begin{pmatrix} N-1 \\ \prod_{l=i}^{N-1} [\mathbf{F}_n^{l,l+1}]^{-1} \end{pmatrix} \begin{pmatrix} -\beta_n^N \tanh(k_n H_N) \\ \beta_n^N \end{pmatrix} & i > j \end{cases} \quad (4.17)$$

$$[\mathbf{F}_n^{l,l+1}] = \frac{1}{\varepsilon_{l+1}} \begin{pmatrix} \varepsilon_{l+1} \text{ch}(k_n H_l) & \varepsilon_{l+1} \text{sh}(k_n H_l) \\ \varepsilon_l \text{sh}(k_n H_l) & \varepsilon_l \text{ch}(k_n H_l) \end{pmatrix} \quad (4.18)$$

$$[\mathbf{F}_n^{l,l+1}]^{-1} = \frac{1}{\varepsilon_l} \begin{pmatrix} \varepsilon_l \text{ch}(k_n H_l) & -\varepsilon_{l+1} \text{sh}(k_n H_l) \\ -\varepsilon_l \text{sh}(k_n H_l) & \varepsilon_{l+1} \text{ch}(k_n H_l) \end{pmatrix} \quad (4.19)$$

Values of β_n^1 and β_n^N in (4.17) are computed with the continuity conditions (4.15) on the interface of layers j and $j+1$ (where the Dirac source charge is located). This calculation results in linear equations (4.20).

$$\beta_n^N \begin{pmatrix} N-1 \\ \prod_{l=j+1}^{N-1} [\mathbf{F}_n^{l,l+1}]^{-1} \end{pmatrix} \begin{pmatrix} -\tanh(k_n H_N) \\ 1 \end{pmatrix} = \beta_n^1 \begin{pmatrix} 1 \\ \prod_{l=j}^1 [\mathbf{F}_n^{l,l+1}] \end{pmatrix} \begin{pmatrix} 0 \\ 1 \end{pmatrix} - \frac{1}{\varepsilon_{j+1}} \begin{pmatrix} 0 \\ \frac{2}{n\pi} \sin(k_n x_s) \end{pmatrix} \quad (4.20)$$

Defining:

$$\begin{cases} \begin{pmatrix} X_n \\ Y_n \end{pmatrix} = \begin{pmatrix} \prod_{l=j+1}^{N-1} [\mathbf{F}_n^{l,l+1}]^{-1} \end{pmatrix} \begin{pmatrix} -\tanh(k_n H_N) \\ 1 \end{pmatrix} \\ \begin{pmatrix} M_n \\ N_n \end{pmatrix} = \begin{pmatrix} 1 \\ \prod_{l=j}^1 [\mathbf{F}_n^{l,l+1}] \end{pmatrix} \begin{pmatrix} 0 \\ 1 \end{pmatrix} \end{cases} \quad \text{and} \quad Q_n = \frac{2}{n\pi\epsilon_{j+1}} \sin(k_n x_s) \quad (4.21)$$

The equation (4.20) can be presented as

$$\begin{pmatrix} X_n & -M_n \\ Y_n & -N_n \end{pmatrix} \begin{pmatrix} \beta_n^N \\ \beta_n^1 \end{pmatrix} = \begin{pmatrix} 0 \\ Q_n \end{pmatrix} \quad (4.22)$$

After some calculation, the following results are obtained:

$$\begin{cases} \beta_n^1 = \frac{X_n Q_n}{M_n Y_n - N_n X_n} \\ \beta_n^N = \frac{M_n Q_n}{M_n Y_n - N_n X_n} \end{cases} \quad (4.23)$$

With these two parameters known, α_n^i and β_n^i can be obtained for an arbitrary layer i through (4.17). Finally, the Green's function for the layer i is expressed by (4.16) by introducing the coefficients α_n^i and β_n^i . According to our assumptions, all the conductors are located at the interface between layers. Therefore, the associated Green's function $G_{[t,t+1]}(\mathbf{r}, \mathbf{r}_s)$ at the interface of layer t and $t+1$ can be further simplified into:

$$G_{[t,t+1]}(\mathbf{r}, \mathbf{r}_s) = G^{t+1}(x, 0; x_s, y_s) = \sum_{n=1}^{\infty} \alpha_n^{t+1} \sin(k_n x) \quad \text{with} \quad k_n = \frac{n\pi}{L} \quad (4.24)$$

4.2.3 Numerical Stability of the Green's Function

The above presented Green's function is mathematically correct but impossible to calculate with software like Matlab[®] due to its numerical stability problem. Indeed, the hyperbolic functions $\text{sh}(k_n H_i)$ and $\text{ch}(k_n H_i)$ grow exponentially with n and will thereby cause some numerical overflow in the matrix multiplications. To avoid this problem, the term $\text{ch}(k_n H_i)$ is factorized out of $[\mathbf{F}_n^{l,l+1}]$ and $[\mathbf{F}_n^{l,l+1}]^{-1}$ [see (4.18) and (4.19)], resulting in:

$$[\mathbf{F}_n^{l,l+1}] = \text{ch}(k_n H_l) \begin{pmatrix} 1 & \tanh(k_n H_l) \\ \frac{\varepsilon_l}{\varepsilon_{l+1}} \tanh(k_n H_l) & \frac{\varepsilon_l}{\varepsilon_{l+1}} \end{pmatrix} = \text{ch}(k_n H_l) [\tilde{\mathbf{F}}_n^{l,l+1}] \quad (4.25)$$

and

$$[\mathbf{F}_n^{l,l+1}]^{-1} = \text{ch}(k_n H_l) \begin{pmatrix} 1 & \frac{-\varepsilon_{l+1}}{\varepsilon_l} \tanh(k_n H_l) \\ -\tanh(k_n H_l) & \frac{\varepsilon_{l+1}}{\varepsilon_l} \end{pmatrix} = \text{ch}(k_n H_l) [\tilde{\mathbf{F}}_n^{l,l+1}]^{-1} \quad (4.26)$$

The terms $\tanh(k_n H_l)$ that appear in $[\tilde{\mathbf{F}}_n^{l,l+1}]$ and $[\tilde{\mathbf{F}}_n^{l,l+1}]^{-1}$ approach unity with the increase of n . Therefore, they can be treated numerically in the Matlab program. The factor $\text{ch}(k_n H_l)$ will not cause stability problem, as will be shown in the following part. Similarly to (4.21), one can define:

$$\begin{cases} \begin{pmatrix} \tilde{X}_n \\ \tilde{Y}_n \end{pmatrix} = \begin{pmatrix} N-1 \\ \prod_{l=j+1}^{N-1} [\tilde{\mathbf{F}}_n^{l,l+1}]^{-1} \end{pmatrix} \begin{pmatrix} -\tanh(k_n H_N) \\ 1 \end{pmatrix} \\ \begin{pmatrix} \tilde{M}_n \\ \tilde{N}_n \end{pmatrix} = \begin{pmatrix} 1 \\ \prod_{l=j}^{N-1} [\tilde{\mathbf{F}}_n^{l,l+1}] \end{pmatrix} \begin{pmatrix} 0 \\ 1 \end{pmatrix} \end{cases} \quad (4.27)$$

Again, the following relations hold:

$$\tilde{\beta}_n^1 = \frac{Q_n \tilde{X}_n}{\tilde{M}_n \tilde{Y}_n - \tilde{N}_n \tilde{X}_n} \quad \text{and} \quad \tilde{\beta}_n^S = \frac{Q_n \tilde{M}_n}{\tilde{M}_n \tilde{Y}_n - \tilde{N}_n \tilde{X}_n} \quad (4.28)$$

After introducing (4.28) into (4.17), the values of α_n^i and β_n^i can be expressed by:

$$\begin{cases} \begin{pmatrix} \alpha_n^i \\ \beta_n^i \end{pmatrix} = \begin{cases} \tilde{\beta}_n^1 \left(\prod_{m=i}^j \text{ch}(k_n H_m) \right)^{-1} \begin{pmatrix} \prod_{m=1}^i [\tilde{\mathbf{F}}_n^{l,l+1}] \end{pmatrix} \begin{pmatrix} 0 \\ 1 \end{pmatrix} & i \leq j \\ \tilde{\beta}_n^S \left(\prod_{m=j+1}^{i-1} \text{ch}(k_n H_m) \right)^{-1} \begin{pmatrix} N \\ \prod_{m=i}^N [\tilde{\mathbf{F}}_n^{l,l+1}]^{-1} \end{pmatrix} \begin{pmatrix} -\tanh(k_n H_N) \\ 1 \end{pmatrix} & i > j \end{cases} \end{cases} \quad (4.29)$$

Finally, combining all these equations, a more numerically stable version of the Green's function for the multilayered structure (Figure 4.3) is obtained, as expressed by (4.30):

$$\begin{aligned} G_{t+1}(x,0) &= \sum_{n=1}^{\infty} \alpha_n^{t+1} \sin(k_n x) = \\ &= \begin{cases} \sum_{n=1}^{\infty} \left[\tilde{\beta}_n^1 \left(\prod_{m=t+1}^j \text{ch}(k_n H_m) \right)^{-1} \begin{pmatrix} 1 \\ 0 \end{pmatrix}^T \begin{pmatrix} t+1 \\ \prod_{l=1}^{t+1} [\tilde{F}_{l,l+1}] \end{pmatrix} \begin{pmatrix} 0 \\ 1 \end{pmatrix} \right] \sin(k_n x) & t < j \\ \sum_{n=1}^{\infty} \left[\tilde{\beta}_n^S \left(\prod_{m=j+1}^t \text{ch}(k_n H_m) \right)^{-1} \begin{pmatrix} 1 \\ 0 \end{pmatrix}^T \begin{pmatrix} N \\ \prod_{l=t+1}^N [\tilde{F}_{l,l+1}]^{-1} \end{pmatrix} \begin{pmatrix} -\tanh(k_n H_N) \\ 1 \end{pmatrix} \right] \sin(k_n x) & t \geq j \end{cases} \quad (4.30) \end{aligned}$$

As seen, the terms $\text{ch}(k_n H_m)$ appear on the denominator which will no longer cause numerical overflow but will help the convergence of the series.

4.2.4 Moment Method for Calculating the Capacitance Matrix

In the previous part, the multilayered Green's function is developed for the multilayered structure. In this part, the method of moment (MoM) using point collocation (or matching) will be applied to calculate the capacitance matrix of a multilayered planar structure. According to the definition of capacitance matrix stated in Appendix IV, the capacitance C_{mn} equals the free charges on conductor n when conductor m is biased at 1V while the other conductors are biased at 0V. Thus, for calculating C_{mn} , the potentials of all the conductors are known but the free charges on the conductors have to be found.

Suppose that a system containing S horizontal conductors is studied, an arbitrary conductor i is located at the interface of layers t_i and t_{i+1} . The Y-coordinate of this conductor is y^i .

Each conductor is discretized into K segments. If K is large enough, the charge density ρ on each segment can be considered as uniform. Figure 4.4(a) gives an example of the pulse-like charge density distribution on a conductor, where the segment k is comprised in $[x_{k-1}, x_k]$ with a charge density ρ_k .

For the system with S conductors, the charge density $\rho^i(x_s, y^i)$ on conductor i is replaced by a discrete function:

$$\rho^i(x_s, y^i) = \sum_{k=1}^K \rho_k^i P_k^i(x_s) \quad (4.31)$$

where ρ_k^i is the charge density on the segment k of conductor i and $P_k^i(x_s)$ is a pulse function expressed by

$$P_k^i(x_s) = \begin{cases} 1 & x_s \in [x_{k-1}^i, x_k^i] \\ 0 & \text{otherwise} \end{cases} \quad (4.32)$$

where $[x_{k-1}^i, x_k^i]$ denotes the position of segment k on conductor i .

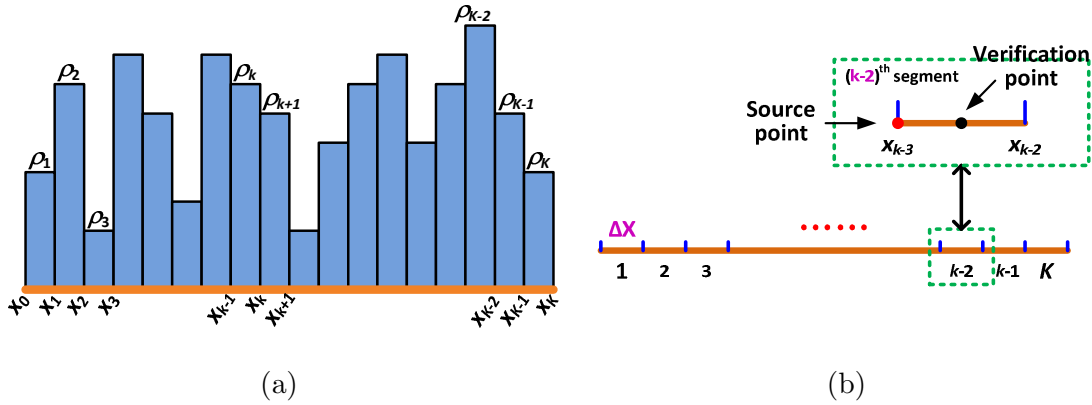


Figure 4.4. Moment method by point collocation. (a) Discretized conductor with pulse-like charge density function. (b) Source point and verification point on the segment.

Introducing (4.31) into (4.7), the potential at $(x,y)^1$ in an arbitrary layer m contributed by conductor i is given by:

$$U_i^m(x, y) = \int_{\Omega} G^m(x, y; x_s, y^i) \sum_{k=1}^K \rho_k^i P_k^i(x_s) dx_s = \sum_{k=1}^K \rho_k^i \int_{\Omega} P_k^i(x_s) G^m(x, y; x_s, y^i) dx_s \quad (4.33)$$

where $G^m(x, y; x_s, y^i)$ represents the Green's function at (x, y) in layer m due to a Dirac charge source at (x_s, y^i) on conductor i . Applying the superposition principle, the total potential at (x, y) in layer m is simply the sum of the contribution of all the conductors.

$$U^m(x, y) = \sum_{i=1}^S U_i^m(x, y) = \sum_{i=1}^S \sum_{k=1}^K \rho_k^i \int_{\Omega} G^m(x, y; x_s, y^i) P_k^i(x_s) dx_s \quad (4.34)$$

The integration of the Green's function $G^m(x, y; x_s, y^i) P_k^i(x_s)$ along x -axis on the segment k of conductor i can be realized analytically since it contains a factor $Q_n = 2\sin(k_n x_s) / (n\pi\epsilon_{j+1})$ defined by (4.21) [also see (4.28) and (4.30)].

Finally, the system (4.34) is a linear equation system of ρ_k^i containing S^*K unknowns. To solve these S^*K unknowns, S^*K independent equations are needed. Therefore, the main idea of point collocation MoM is to verify the potential U on every segment of the conductors to provide the required S^*K equations. For simplicity, the verification point \hat{x}_k^i of segment k on conductor i is set at the middle point of every segment [Figure 4.4(b)].

¹ Local coordinate in layer m

$$\hat{x}_k^i = \frac{1}{2}(x_{k-1}^i + x_k^i) \quad (4.35)$$

As said before, the potentials on the conductors are known during the calculation of the capacitance C_{mn} . Therefore, for the verification points on conductor i , the potential are given by:

$$U(\hat{x}_k^i, y^i) = \begin{cases} 1 & \text{if } i = m \\ 0 & \text{else} \end{cases} \quad (4.36)$$

To verify the potential boundary conditions on the segment l of conductor j at the interface of layer t_j and t_{j+1} . The following equation holds:

$$U(\hat{x}_l^j, 0) = \sum_{i=1}^S \sum_{k=1}^K \rho_k^i \int_{\Omega} G^{t_j+1}(\hat{x}_l^j, 0; x_s, y^i) P_k^i(x_s) dx_s \quad (4.37)$$

Defining:

$$H_{l,j}^{k,i} = \int_{\Omega} G^{t_j+1}(\hat{x}_l^j, 0; x_s, y^i) P_k^i(x_s) dx_s \quad (4.38)$$

This parameter evaluates the influence of segment k of conductor i on the potential of segment l of conductor j .

With this parameter, an S^*K equations system can be established, as given by:

$$\begin{pmatrix} H_{1,1}^{1,1} & H_{2,1}^{1,1} & \dots & H_{K,1}^{1,1} & H_{1,2}^{1,1} & \dots & H_{K,2}^{1,1} & \dots & H_{1,S}^{1,1} & \dots & H_{K,S}^{1,1} \\ H_{1,1}^{2,1} & H_{2,1}^{2,1} & \dots & H_{K,1}^{2,1} & H_{1,2}^{2,1} & \dots & H_{K,2}^{2,1} & \dots & H_{1,S}^{2,1} & \dots & H_{K,S}^{2,1} \\ \vdots & \vdots & \vdots & \vdots & \vdots & \vdots & \vdots & \vdots & \vdots & \vdots & \vdots \\ H_{1,1}^{K,1} & H_{2,1}^{K,1} & \dots & H_{K,1}^{K,1} & H_{1,2}^{K,1} & \dots & H_{K,2}^{K,1} & \dots & H_{1,S}^{K,1} & \dots & H_{K,S}^{K,1} \\ H_{1,1}^{1,2} & H_{2,1}^{1,2} & \dots & H_{K,1}^{1,2} & H_{1,2}^{1,2} & \dots & H_{K,2}^{1,2} & \dots & H_{1,S}^{1,2} & \dots & H_{K,S}^{1,2} \\ \vdots & \vdots & \vdots & \vdots & \vdots & \vdots & \vdots & \vdots & \vdots & \vdots & \vdots \\ H_{1,1}^{K,2} & H_{2,1}^{K,2} & \dots & H_{K,1}^{K,2} & H_{1,2}^{K,2} & \dots & H_{K,2}^{K,2} & \dots & H_{1,S}^{K,2} & \dots & H_{K,S}^{K,2} \\ \vdots & \vdots & \vdots & \vdots & \vdots & \vdots & \vdots & \vdots & \vdots & \vdots & \vdots \\ H_{1,1}^{1,S} & H_{2,1}^{1,S} & \dots & H_{K,1}^{1,S} & H_{1,2}^{1,S} & \dots & H_{K,2}^{1,S} & \dots & H_{1,S}^{1,S} & \dots & H_{K,S}^{1,S} \\ \vdots & \vdots & \vdots & \vdots & \vdots & \vdots & \vdots & \vdots & \vdots & \vdots & \vdots \\ H_{1,1}^{K,S} & H_{2,1}^{K,S} & \dots & H_{K,1}^{K,S} & H_{1,2}^{K,S} & \dots & H_{K,2}^{K,S} & \dots & H_{1,S}^{K,S} & \dots & H_{K,S}^{K,S} \end{pmatrix} \begin{pmatrix} \rho_1^1 \\ \rho_2^1 \\ \vdots \\ \rho_K^1 \\ \rho_1^2 \\ \rho_K^2 \\ \vdots \\ \rho_1^S \\ \rho_K^S \end{pmatrix} = \begin{pmatrix} U(\hat{x}_1^1, 0) \\ U(\hat{x}_2^1, 0) \\ \vdots \\ U(\hat{x}_K^1, 0) \\ U(\hat{x}_1^2, 0) \\ \vdots \\ U(\hat{x}_K^2, 0) \\ \vdots \\ U(\hat{x}_1^S, 0) \\ \vdots \\ U(\hat{x}_K^S, 0) \end{pmatrix} \quad (4.39)$$

By solving these linear equations, the charge density ρ_k^i can be determined and then the total free charge on the conductor j can be calculated to find the capacitance matrix, as expressed by:

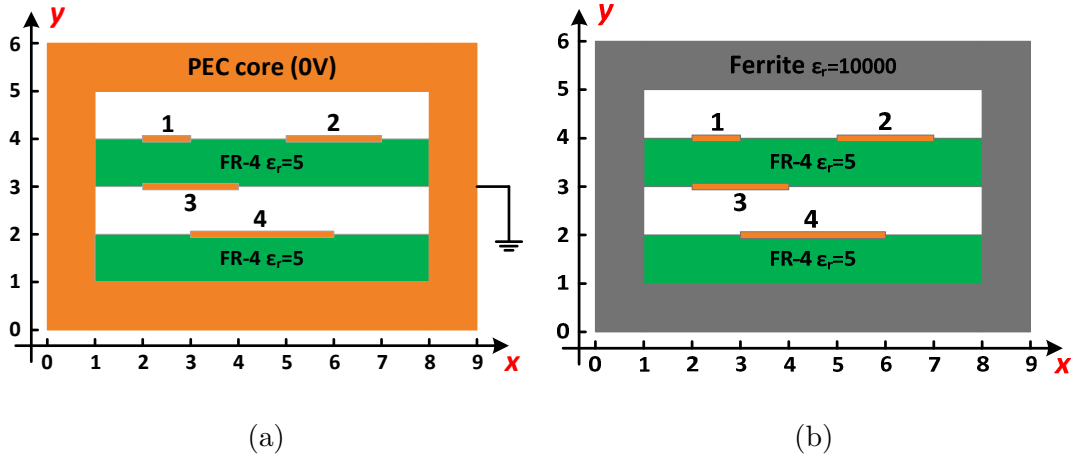


Figure 4.5. Test configuration with 4 conductors and 4 layers: (a) grounded PEC core; (b) ferrite core (unit: mm).

$$Q_j = \sum_{k=1}^K \rho_k^j (x_k - x_{k-1}) \quad (4.40)$$

It should be noted that the diagonal element in the capacitance matrix C_{ii} presents the total capacitance of conductor i to its environment. In fact, the influence of the grounded core is also included in this C_{ii} . To extract the capacitance between the conductor i and the core C_{ic} , the following formula is applied:

$$C_{ic} = \sum_{j=1}^S C_{ij} \quad (4.41)$$

Note that in this equation, the values of C_{ij} ($i \neq j$) are negative whereas C_{jj} is positive.

After solving the capacitance matrix in the grounded PEC core as well as the capacitances between the conductors and the core, the capacitance matrix for the case of floating PEC core can be derived using the transformation technique presented in Chapter 3.

4.2.5 Numerical Validation

To validate the Green's function method, a Matlab program is realized to calculate the capacitance matrix of the PCB structures illustrated in Figure 4.5. The obtained results are compared with FEM results, as given in Table 4.1. After the transformation (4.42), the capacitance matrix for ferrite core case is summarized

Table 4.1 Comparison between Calculated Results and Simulation Results for the Configuration with Grounded PEC Core.

Conductor	1			2			3			4		
	Cal.	Sim.	Err.	Cal.	Sim.	Err.	Cal.	Sim.	Err.	Cal.	Sim.	Err.
1	98.9	100.5	2%	-2.9	-2.9	0%	-60.4	-61.6	2%	-0.57	-0.54	6%
2	-2.9	-2.9	0%	92.3	95.9	4%	-17.7	-18.2	3%	-10.6	-11	4%
3	-60.4	-61.6	2%	-17.7	-18.2	3%	130	132	2%	-16.8	-17.7	5%
4	-0.57	-0.54	6%	-10.6	-11	4%	-16.8	-17.7	5%	202	205	2%

Unit: pF/m **Cal.**=Calculation **Sim.**=Simulation **Err.**=Error

Table 4.2 Comparison between Calculated Results and Simulation Results for the Configuration of Ferrite Core with High Relative Permittivity ($\epsilon_r=10^4$)

Conductor	1			2			3			4		
	Cal.	Sim.	Err.	Cal.	Sim.	Err.	Cal.	Sim.	Err.	Cal.	Sim.	Err.
1	N/A	N/A	N/A	9.9	10.1	2%	64.4	65.6	2%	20.5	20.6	1%
2	9.9	10.1	2%	N/A	N/A	N/A	24.7	25.1	2%	45.4	46.7	3%
3	64.4	65.4	2%	24.7	25.1	2%	N/A	N/A	N/A	36.8	37.3	2%
4	20.5	20.6	1%	45.4	46.7	4%	36.8	37.3	1%	N/A	N/A	N/A

Unit: pF/m **Cal.**=Calculation **Sim.**=Simulation **Err.**=Error

Table 4.3 Comparison between Calculated Results and Simulation Results for the Configuration of Ferrite Core with Lower Relative Permittivity ($\epsilon_r = 10^3$)

Conductor	1			2			3			4		
	Cal.	Sim.	Err.	Cal.	Sim.	Err.	Cal.	Sim.	Err.	Cal.	Sim.	Err.
1	N/A	N/A	N/A	-9.9	-10.0	2%	-64.4	-65.5	2%	-20.5	-20.3	1%
2	-9.9	-10.1	2%	N/A	N/A	N/A	-24.7	-24.9	1%	-45.4	-46.7	4%
3	-64.4	-65.5	2%	-24.7	-24.9	1%	N/A	N/A	N/A	-36.8	-37.0	1%
4	-20.5	-20.3	1%	-45.4	-46.7	4%	-36.8	-36.9	1%	N/A	N/A	N/A

Unit: pF/m **Cal.**=Calculation **Sim.**=Simulation **Err.**=Error

in Table 4.2. As seen, the maximum error is less than 6%. In the above simulations, the relative permittivity of the ferrite core is 10^4 . When the relative permittivity of the ferrite core decreases, the method still gives an accurate estimation on the capacitance values (see Table 4.3 where the relative permittivity is set to be 10^3). With this analytical approach, 2D capacitance matrix for the cross-section structure of a planar component can be calculated, which allows a further process on the obtained results in the energy approach developed in Chapter 3.

4.2.6 Applications on Planar Components

4.2.6.1 Planar Inductor

The cross-section in the ferrite core of the planar inductor is illustrated in Figure 4.6. The same homogenization method is applied inside the isolation region for simplification. After constructing the geometry into the Matlab program, the capacitance matrix is computed. Some of the important elements are compared with FEM simulation results in Table 4.4. As seen, good match is found between the calculation and the simulation. However, the error of C_{12} and C_{23} is relatively greater than the other ones. This is because in our model, the thickness of the conductor is neglected, which is not the case in the FEM simulation. In fact, as conductor 1 and conductor 2 are very close, the neglect the side wall effect will lead to some errors in the final results (Figure 4.7). A simple correction can be performed here using the EFD method presented before. Supposing the sidewalls between the two conductors forms a plate capacitance, the capacitance of the side wall is $C_{sw}=\epsilon_r\epsilon_0S/T$, where S is the distance between the two sidewall and T is the thickness of the conductor. In this case, $S=0.8$ mm and $T=70$ μm , so $C_{sw}=2.7$ pF/m. Adding this parameter to C_{12} or C_{23} , the error can be reduced to about 4%.

For the part outside the ferrite core, the Green's function can no longer be applied. Therefore, the capacitance matrix can be approximated by enlarge the window size to reduce the effect of the core. In this case, the size of L and H are enlarged 3 times and the isolation layers are removed. The calculated results are compared with the simulated ones in Table 4.5. As seen, good match can still be obtained using this approximation. Though a large error of C_{17} is spotted, however, its value is already negligible. Note that the value of C_{12} and C_{23} can still be corrected by the side wall capacitance, which equals 0.8 pF/m in this case. The resulting error can then be limited within 4%.

Once the capacitance matrix is obtained, the energy approach is applied to find the equivalent parasitic capacitance of the component. This is exactly the same procedure as presented in Chapter 3.

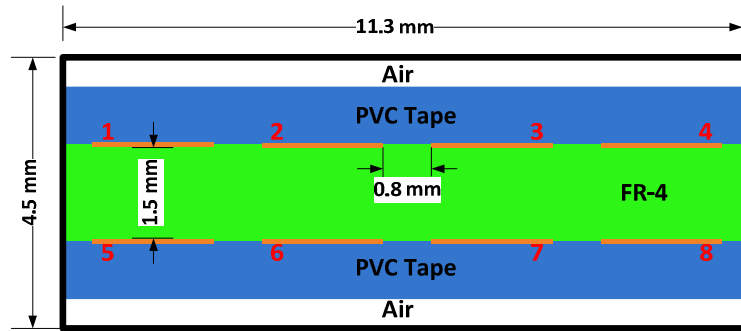


Figure 4.6 Cross-section of the 8-turn planar inductor in the ferrite core.

Table 4.4 Comparison between Calculated Results and Simulation Results for the Cross-section of the 8-turn Planar Inductor in the Core.

Capacitance	Sim.	Cal.	Err.	Capacitance	Sim.	Cal.	Err.
C_{12}	35.1	31.7+2.7	2%	C_{17}	5.9	5.8	2%
C_{13}	6.0	5.8	3%	C_{23}	31.2	28.1+2.7	2%
C_{15}	68.6	66.4	3%	C_{26}	59.7	58.8	2%
C_{16}	14.9	14.6	2%	C_{27}	11.0	10.9	1%

Unit: pF/m **Sim.**=Simulation **Cal.**=Calculation **Err.**=Error
 Note: Correction is marked in red

4.2.6.2 Planar CM Choke

Now the previous planar CM choke is analyzed with the multilayered Green's function method. The cross-section of the structure inside the core as well as the main dimensions are displayed in Figure 4.8. Using the realized program, the capacitance matrix of this structure can be determined. In Table 4.6, the calculated results are compared with simulated ones and a good agreement is observed.

For the case outside the core, the dimensions of the core are tripled, as did previously. As said in Chapter 3, in air, one conductor will only have capacitive coupling with the conductors in its vicinity. For conductor 1, only the capacitances C_{12} , C_{15} , C_{16} are non-negligible while the other capacitances from conductor 1 are almost zero. Table 4.7 compares the calculation and simulation results on some important capacitance values. As seen, with the approximation, the capacitance elements can still be accurately evaluated.

4.2.7 Discussion

The whole calculation method is semi-analytical since the analytical Green's function is coupled with a MoM method that requires the discretization on the

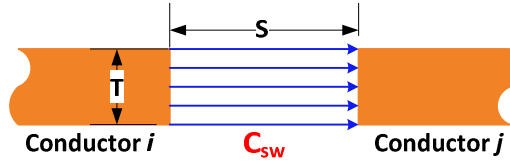


Figure 4.7. Effect of side wall.

Table 4.5 Comparison between Analytical Method and FEM Results for the Cross-section of the 8-turn Planar Inductor in Air.

Capacitance	Sim.	Cal.	Err.	Capacitance	Sim.	Cal.	Err.
C_{12}	21.2	19.7+0.8	3%	C_{17}	0.5	0.1	80%
C_{13}	1.3	1.3	0%	C_{23}	20.5	19.0+0.8	4%
C_{15}	68.9	68.3	1%	C_{26}	57.3	57.0	1%
C_{16}	9.6	9.8	2%	C_{27}	9.1	9.1	0%

Unit: pF/m **Sim.**=Simulation **Cal.**=Calculation **Err.**=Error
Note: Correction is marked in red

conductors to calculate the unknown charge density distribution. In [80], it has been assumed that the charge density is uniform on all the conductors. As a result, completely analytical formulas based on multilayered Green's function have been developed for extracting the capacitance matrix of interconnects in microelectronic circuits. This assumption gives approximate results for structures with few conductors whose sizes are small in comparison with the distance between them. However, in our case, the number of conductors is 16 and the width of the conductor is more than twice the inter-conductor distance. Therefore, the assumption of uniform charge distribution may not be appropriate for obtaining accurate results. However, for a coarse evaluation in optimization process, this assumption can still be adopted to accelerate the calculation

The Fourier series for representing the multilayered Green's function usually converge very slowly so acceleration techniques by extrapolation can be employed, such as Padé approximation [81] and Chebyshev-Toeplitz algorithm [82]. These techniques can significantly reduce the necessary number of series terms for achieving the convergence and thereby save computation time.

In conclusion, this "complex" method based on multilayered Green's function can effectively analyze the PCB structures in planar components to find their parasitic capacitances. This method is more general and accurate than the EFD

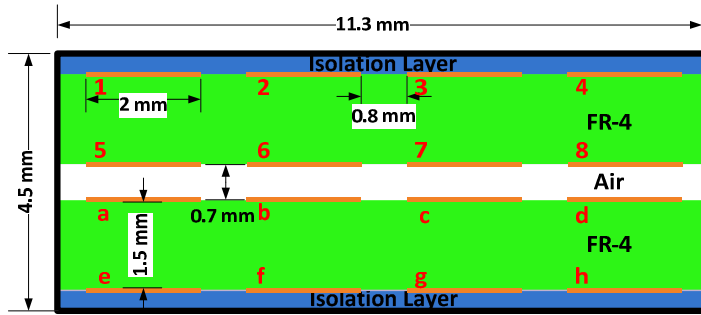


Figure 4.8. Cross-section of the planar CM choke in the ferrite core.

Table 4.6 Comparison between Calculated Results and Simulation Results for the Cross-section of the Planar CM choke in the Ferrite Core.

Capacitance	Sim.	Cal.	Err.	Capacitance	Sim.	Cal.	Err.
C_{12}	33.3	29.8+2.7	3%	C_{23}	29.7	26.7+2.7	1%
C_{13}	20.1	18.9	6%	C_{26}	55.5	53.7	3%
C_{15}	54.8	52.9	4%	C_{28}	5.4	5.3	2%
C_{16}	8.4	8.0	5%	C_{5a}	27.7	27.2	2%
C_{18}	6.5	6.3	3%	C_{5b}	1.9	2.0	5%
C_{1a}	6.1	6.0	2%	C_{5c}	0.1	0.2	100%
C_{1b}	0.8	1.1	37.5%	C_{5d}	1.6	1.6	0%
C_{1e}	0.5	0.1	80%	C_{5f}	5.0	5.0	0%
C_{1f}	19.8	18.9	5%	C_{6b}	27.7	27.2	2%
C_{1h}	24.6	23.2	5%	C_{6c}	1.8	1.8	0%

 Unit: pF/m **Sim.**=Simulation **Cal.**=Calculation **Err.**=Error

Note: Correction is marked in red

Table 4.7 Comparison between Calculated Results and Simulation Results for the Cross-section of the Planar CM choke in Air.

Capacitance	Sim.	Cal.	Err.	Capacitance	Sim.	Cal.	Err.
C_{12}	21.1	19.2+0.8	5%	C_{56}	15.8	14.6+0.8	3%
C_{13}	1.3	1	23%	C_{5a}	30.7	30.6	1%
C_{15}	66.0	63.7	4%	C_{5b}	1.8	1.9	5%
C_{16}	8.7	8.6	1%	C_{67}	15.8	14.5+0.8	3%
C_{25}	9.1	8.9	2%	C_{6b}	27.7	27.2	2%
C_{26}	56.8	55.7	2%	C_{6c}	1.8	1.8	0%

 Unit: pF/m **Sim.**=Simulation **Cal.**=Calculation **Err.**=Error

Note: Correction is marked in red

method and it can be further implemented with optimization programs for components design.

4.3 Static Leakage Inductance Calculation Using Multilayered Green's Function

For a planar CM choke, its leakage inductance can be regarded as DM inductance for noise suppression. It is thus desirable to have a large enough leakage inductance inside the planar CM choke. In order to increase the leakage inductance, leakage layers made of ferrite polymer or μ -metal can be added [1, 2]. Apart from numerical simulations, there are not adequate analytical models that are pertinent enough to evaluate the leakage inductance of planar CM choke, especially when some leakage layers are implemented. In this section, the multilayered Green's function is extended and applied on the case of planar CM choke with leakage layer. Complete formulations will be given and analyzed in the following parts.

4.3.1 Energy Base Method for Calculating Static Leakage Inductance

The existing methods for calculating the static leakage inductance rely on the evaluation of the magnetic energy stored in the component when the total ampere-turns in the component is null [40]. The relation between the leakage inductance and the magnetic energy W_{mag} is expressed by:

$$W_{mag} = \frac{1}{2} L_1 I^2 \quad (4.42)$$

To evaluate the magnetic energy, two types of integral can be used, as given by:

$$W_{mag} = \frac{1}{2} \int_{\Omega} \mathbf{B} \mathbf{H} \, dV \quad (4.43)$$

or

$$W_{mag} = \frac{1}{2} \int_{\Omega} \mathbf{A} \mathbf{J} \, dV \quad (4.44)$$

In [40], the second integration is performed since it requires only the integration on the conductors where the current density is non-zero. As a consequence, the associated calculation is much easier for the second integration than the first one that integrates until infinity.

4.3.2 Review of Existing Methods

4.3.2.1 Methods Based on Dowell's Assumption

For calculating the leakage inductance, many methods have been proposed based on Dowell's assumption [38, 83, 84] that magnetic field is tangential to the conductor. This assumption can be very close to reality when the magnetic windows are well filled with long conductors. In such cases, simple and accurate formulas can be derived to determine the leakage inductance. However, for planar components, the arrangement of the conductor can be different from one layer to another. Besides, the window is seldom fully filled due to the small size of the conductors and their non-regular arrangement. As a result, the Dowell's assumption does not correctly describe the reality and such computation will lead to inaccurate values.

4.3.2.2 Method Based on PEEC-Like Formulas

In [39, 40], the authors proposed a 2D PEEC-like formulations for calculating the leakage inductance of planar transformers. In this work, the calculation is performed on 2D by assuming that the current is perpendicular to the cross-section of the component. For a rectangular conductor carrying a current I in free space, the potential vector A_z in the space is given by (4.45):

$$A_z(x, y) = \frac{-\mu_0 I}{16\pi ab} \left[F(X, Y) \Big|_{X=x+a}^{X=x-a} \Big|_{Y=y+b}^{Y=y-b} \right] \quad (4.45)$$

with $F(X, Y) = XY \ln(X^2 + Y^2) + X^2 \arctan\left(\frac{Y}{X}\right) + Y^2 \arctan\left(\frac{X}{Y}\right)$.

With this analytical formula, the distribution of the potential vector in the space due to the rectangular current source can be determined. When there are multiple conductors, the superposition principle can be applied for the calculation. Once the information of A_z is known, the integration (4.44) is performed on the area of the conductors:

$$W_{mag} = \frac{1}{2} \iint_{\Omega} A_z J_z dx dy \quad (4.46)$$

For the conductors inside the ferrite core, image method is applied to evaluate the influence of the magnetic core. As seen from Figure 1.11(c), the field in

the magnetic window depends not only on the conductors in the window, but also on their images mirrored by the magnetic core. According to the authors, the magnetic core presents a non-negligible influence on the field in the window. In [40], the method of 4-images and 8-images are introduced. After calculating the magnetic field on the cross-section, the magnetic energy stored in the window is multiplied by a well-chosen average path L_{avg} where the peak of energy density is found. The final leakage inductance is expressed by:

$$L_f \approx \frac{2W_{mag}L}{I^2} \quad (4.47)$$

The whole procedure for calculating the leakage inductance has been programmed in Mathcad software and very accurate results can be obtained [39].

Though image method can be applied for considering the influence of the magnetic core, however, when a thin FPC layer with low permeability ($\mu_r=9$) is inserted in the cross-section window, the use of the image method can be very cumbersome, for the following reasons:

1. In the image method introduced in [40], 4 first-order images are employed due to direct reflections. 4 second order images are added due to secondary reflections. Higher order images are neglected. However, when FPC layer is implemented in the region, the reflection situation becomes much more complicated.
2. The aforementioned method assumes that the thickness of the ferrite is infinite. As long as the permeability of the ferrite material is large enough, this assumption is very close to the reality. However, since the FPC layer has a low permeability, the impact of its thickness has to be considered, which further complicates the calculation.

For the above reasons, an improved method based on multilayered Green's function has been developed and will be presented in the following part.

4.3.3 Multilayered Green's Function in Magnetostatic

4.3.3.1 Declaration of Problem

In the introduction, it is stated that the leakage layer can be inserted into planar CM choke to increase the leakage inductance for DM filtering purpose. In

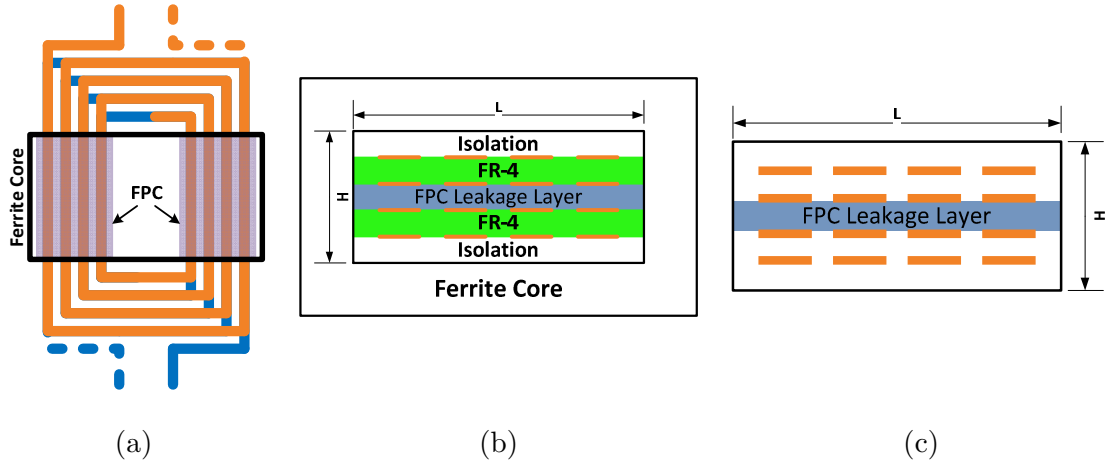


Figure 4.9. Planar CM choke with FPC leakage layer. (a) Top view (b) Cross-section (one magnetic window). (c) Cross-section for magnetostatic analysis.

this study, the target planar CM choke sandwiched a FPC leakage layer between the two PCBs only on the part covered by the magnetic core [Figure 4.9(a) and (b)]. Contrary to what is done previously, the thickness of the conductors is no longer negligible. For magnetostatic analysis, the FR-4 epoxy and isolation are considered as magnetically transparent, resulting in a cross-section given in Figure 4.9(c). As seen, a three-layered structure (Air-FPC-Air) is found inside the magnetic core.

Same to [40], the currents are supposed to be perpendicular to the cross-section and only 2D analysis is performed in this study. As a result, the corresponding Poisson's equation for magnetostatic governs the system:

$$\nabla^2 A_z = -\mu J_z \quad (4.48)$$

where A_z and J_z are the z -component of potential vector A and current density J , respectively. It can be noticed that the case of magnetostatic analysis is very similar to what has been encountered for electrostatic: a multilayered structure and the same type Poisson's equation. It is quite natural to think about using the previous multilayered Green's function. However, there is a large difference on the boundary conditions, resulting in different analytical solutions.

4.3.3.2 Boundary Conditions and Compatibility Condition

As the relative permeability of studied ferrite is very large, it is considered as

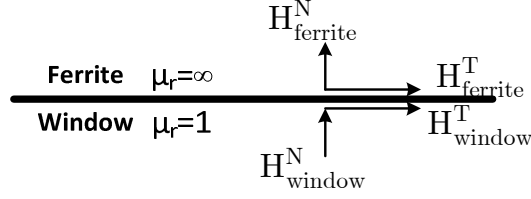


Figure 4.10. Boundary conditions on the inner surface of the magnetic window.

infinite for simplification. The associated tangential continuity condition on the inner surface of the magnetic window is (Figure 4.10):

$$H_{ferrite}^T - H_{window}^T = 0 \quad (4.49)$$

and

$$\frac{1}{\mu_{ferrite}} B_{ferrite}^T - \frac{1}{\mu_0} B_{window}^T = 0 \quad (4.50)$$

With $B_{ferrite}^T$ bounded in the core, B_{window}^T should be zero, meaning that the tangential component of magnetic induction is zero on the inner surface of the window. As a consequence, the boundary conditions of A_z on the inner interface of the core is:

$$\begin{cases} \frac{\partial A_z}{\partial y} = 0 & \text{over the horizontal surface} \\ \frac{\partial A_z}{\partial x} = 0 & \text{over the vertical surface} \end{cases} \quad (4.51)$$

A homogenous Neumann B.C. problem is thus obtained for the case under study. However, this Neumann B.C. problem must satisfy the compatibility condition (4.52) to admit solutions [67]. Concretely in this case, the compatibility condition is given as follows:

$$\int_{\partial\Omega} \frac{\partial A_z}{\partial n} dl + \mu_0 \int_{\Omega} J_z dS = 0 \quad (4.52)$$

This condition can be proved by applying Gauss Law on the equation (4.48). According to (4.51), the first integral in the equation (4.52) is zero, requiring that the second integral be zero too. This implies that the total ampere-turns in the window should be zero during the calculation, which is just the prior condition for the leakage inductance computation. As a consequence, this homogenous Neumann

B.C. admits solutions for calculating the leakage inductance. However, as it only specifies the derivation on the boundary, the obtained solution will certainly be accompanied by a constant.

4.3.3.3 Multilayered Green's Function for Magnetostatic

The mathematical representation for deriving the Green's function for this multilayered structure is given in Figure 4.11. As all the conductors are in air (or magnetically transparent matter), the multilayered Green's function is given by:

$$\nabla^2 G = -\mu_0 \delta(x_s, y_s) \quad (4.53)$$

It is desirable to provide a homogenous Neumann B.C. here to simplify the expression (4.6) (for magnetostatic case). However, this B.C. cannot be applied since it will violate the compatibility condition. This can be easily understood that, in static, the total "energy" going out of a closed region cannot be zero if a "source" is inside. In fact, the B.C.s for this Green's function problem must satisfy:

$$\int_{\partial\Omega} \frac{\partial G}{\partial n} dl = -\mu_0 \quad (4.54)$$

Therefore, the following B.C.s are proposed to simplify the calculation:

$$\begin{cases} \frac{\partial G}{\partial y} \Big|_{y=H} = -\frac{\mu_0}{L} \\ \frac{\partial G}{\partial x} \Big|_{x=0} = \frac{\partial G}{\partial x} \Big|_{x=L} = \frac{\partial G}{\partial y} \Big|_{y=0} = 0 \end{cases} \quad (4.55)$$

As seen, only the B.C. on the top edge of the rectangular region is not zero. With these B.C.s, the compatibility condition (4.54) is verified.

According to the previous analysis, the cross-section of the planar CM choke is a 3-layer structure. If a Dirac current source is introduced, the structure is further split into 4 layers. Therefore, only a 4-layered structure is studied in this work. As seen from Figure 4.11, each layer has a height H_k and a permeability μ_k . Here the local coordinates are applied again as done previously. The Dirac current source locates at the interface between layer j and $j+1$ ($j < 4$). The following boundary conditions can be written out:

1. *Left and right boundaries of layer i : $x=0$ and $x=L$:*

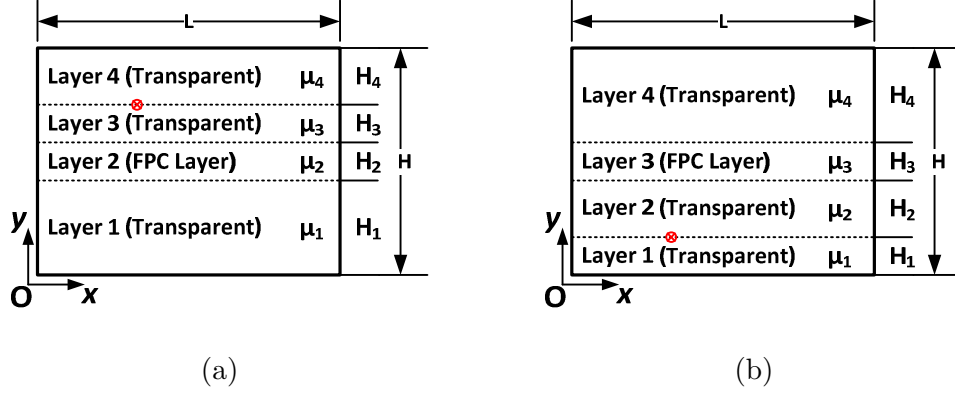


Figure 4.11. 4-layer structure for Green's function deduction. (a) Source point higher than FPC layer. (b) Source point lower than FPC Layer.

$$\left. \frac{\partial G^i}{\partial x} \right|_{x=0} = \left. \frac{\partial G^i}{\partial x} \right|_{x=L} = 0 \quad (4.56)$$

2. Top and bottom boundaries (in layer 4 and layer 1):

$$\text{Layer 1: } \left. \frac{\partial G^1}{\partial y} \right|_{y=0} = 0 \quad (4.57)$$

$$\text{Layer 4: } \left. \frac{\partial G^4}{\partial y} \right|_{y=H_4} = -\frac{\mu_0}{L} \quad (4.58)$$

3. Continuity conditions on the interface between layer i and $i+1$ ($i < 4$):

$$\begin{cases} G^i \Big|_{y=H_i} - G^{i+1} \Big|_{y=0} = 0 \\ \frac{1}{\mu_i} \frac{\partial G^i}{\partial y} \Big|_{y=H_i} - \frac{1}{\mu_{i+1}} \frac{\partial G^{i+1}}{\partial y} \Big|_{y=0} = \delta_{ij} \delta(x - x_s) \end{cases} \quad (4.59)$$

From (4.57) and (4.58), the following relations hold:

$$\begin{cases} \alpha_0^1 = 0 \quad \text{and} \quad \beta_n^1 = 0 \\ \alpha_0^4 = -\frac{\mu_0}{L} \quad \text{and} \quad \beta_n^4 = -\alpha_n^4 \tanh(k_n H_4) \end{cases} \quad (4.60)$$

The general solution in layer i can be deduced from the B.C.s (4.56), as given by:

$$G^i = \alpha_0^i y + \beta_0^i + \sum_{n=1}^{\infty} [\alpha_n^i \text{ch}(k_n y) + \beta_n^i \text{sh}(k_n y)] \cos(k_n x) \quad (4.61)$$

Note that the term $\alpha_0^i y + \beta_0^i$ appears because the eigenvalue of the equation can be zero (see Appendix V).

The next step consists in using the continuity condition to find the

parameters in (4.61). The detailed calculation is given in Appendix VI and only the final results are presented. The parameters α_0^i , β_0^i , α_n^i and β_n^i can be expressed by

$$\begin{pmatrix} \alpha_0^i \\ \beta_0^i \end{pmatrix} = \begin{cases} \begin{pmatrix} 0 \\ 0 \end{pmatrix} & i \leq j \\ \begin{pmatrix} \prod_{l=i}^{N-1} [\mathbf{F}_0^{l,l+1}]^{-1} \begin{pmatrix} -\frac{\mu_0}{L} \\ 0 \end{pmatrix} \end{pmatrix} & i > j \end{cases} \quad (4.62)$$

$$\begin{pmatrix} \alpha_n^i \\ \beta_n^i \end{pmatrix} = \begin{cases} \begin{pmatrix} \prod_{l=i-1}^1 [\mathbf{F}_n^{l,l+1}] \begin{pmatrix} \alpha_n^1 \\ 0 \end{pmatrix} \\ \prod_{l=i}^{N-1} [\mathbf{F}_n^{l,l+1}]^{-1} \begin{pmatrix} \alpha_n^4 \\ -\alpha_n^4 \tanh(k_n H_4) \end{pmatrix} \end{pmatrix} & i \leq j \\ \begin{pmatrix} \alpha_n^4 \\ -\alpha_n^4 \tanh(k_n H_4) \end{pmatrix} & i > j \end{cases} \quad (4.63)$$

With $[\mathbf{F}_n^{l,l+1}]$ and $[\mathbf{F}_n^{l,l+1}]^{-1}$ the up-going and down-going transformation matrix, respectively:

$$[\mathbf{F}_0^{l,l+1}] = \begin{pmatrix} \frac{\mu_{l+1}}{\mu_l} & 0 \\ H_l & 1 \end{pmatrix} \quad \text{and} \quad [\mathbf{F}_0^{l,l+1}]^{-1} = \begin{pmatrix} \frac{\mu_l}{\mu_{l+1}} & 0 \\ -\frac{\mu_l}{\mu_{l+1}} H_l & 1 \end{pmatrix} \quad (4.64)$$

$$[\mathbf{F}_n^{l,l+1}] = \begin{pmatrix} \text{ch}(k_n H_l) & \text{sh}(k_n H_l) \\ \frac{\mu_{l+1}}{\mu_l} \text{sh}(k_n H_l) & \frac{\mu_{l+1}}{\mu_l} \text{ch}(k_n H_l) \end{pmatrix} \quad \text{and} \quad [\mathbf{F}_n^{l,l+1}]^{-1} = \begin{pmatrix} \text{ch}(k_n H_l) & -\frac{\mu_l}{\mu_{l+1}} \text{sh}(k_n H_l) \\ -\text{sh}(k_n H_l) & \frac{\mu_l}{\mu_{l+1}} \text{ch}(k_n H_l) \end{pmatrix} \quad (4.65)$$

The parameters α_n^1 and α_n^4 in (4.63) can be derived from (4.66):

$$\prod_{l=3}^j [\mathbf{F}_n^{l,l+1}]^{-1} \begin{pmatrix} \alpha_n^4 \\ -\alpha_n^4 \tanh(k_n H_4) \end{pmatrix} = \prod_{l=1}^j [\mathbf{F}_n^{l,l+1}] \begin{pmatrix} \alpha_n^1 \\ 0 \end{pmatrix} + \begin{pmatrix} 0 \\ -\frac{2\mu_{j+1}}{n\pi} \cos(k_n x_s) \end{pmatrix} \quad (4.66)$$

The solution of this equation is quite similar to the electrostatic case and is thereby omitted in this section. Note that the same numerical stability problem arises here due to $\text{ch}(k_n H_l)$ as that in the electrostatic case. Therefore, the analysis presented before can be applied again.

4.3.3.4 Calculation of Magnetic Field from Green's Function

As a homogenous Neumann boundary condition is applied, the potential vector on the observation point can be calculated with the obtained Green's function:

$$A_z(x, y) = \int_{\Omega} G(x, y) J_z ds - \frac{1}{\mu} \oint_{\partial\Omega} A_z \frac{\partial G}{\partial n} dl \quad (4.67)$$

The first integral can be performed on the conductor area where the current is non-zero. The second term corresponds to the average value of the potential vector on the boundary of the region, which is a constant. Neglecting this constant, the first integral of (4.67) can be evaluated analytically [due to the term $\cos(k_n x_s)$ in (4.66)] along x -axis and numerically along y -axis by discretizing the conductor into K thin elements [Figure 4.12(a)]. For element k , the y coordinate of the center point $y_{sm} = (y_k + y_{k+1})/2$ is chosen for the integration along y -axis.

The magnetic induction \mathbf{B} can then be calculated by deriving A_z , as given by (4.68). Note that the parameters α_0^i , β_o^i , α_n^i and β_n^i are only dependent to the coordinate of the source point [see (4.62)-(4.66)]. This property allows the separation of the mathematical treatment on the source conductor and the observation one. Therefore, the partial derivation on G (on the observation point) in (4.68) can be performed directly on the expression whereas the integration on the source conductor is still evaluated numerically as is done before.

$$\begin{cases} B_x = \frac{\partial A_z}{\partial y} = -\mu \int_{\Omega} \frac{\partial G(x, y)}{\partial y} J ds \\ B_y = -\frac{\partial A_z}{\partial x} = \mu \int_{\Omega} \frac{\partial G(x, y)}{\partial x} J ds \end{cases} \quad (4.68)$$

The final purpose involves estimating the total energy in the cross-section via the integral (4.46). The Green's function has to be integrated both on the source conductor and the observation conductor. The integration on the source conductor is performed numerically while the integration on the observation conductor can be performed analytically according to the expression (4.61). However, three cases should be distinguished [Figure 4.12(b)]:

1. *The position of the source conductor element is higher than the observation conductor.*

In this case, the observation conductor is completely in layer $i+1$, therefore the integration is performed with the Green's function G^{i+1} for layer $i+1$.

2. *The position of the source conductor element is lower than the observation*

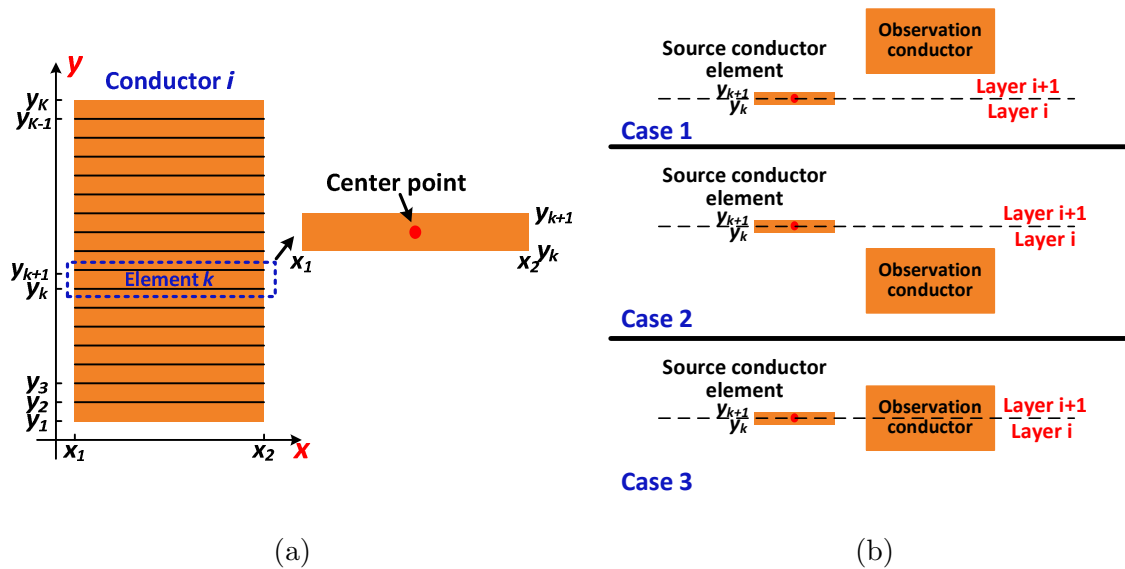


Figure 4.12. Calculation of the magnetic field. (a) Discretization along y -axis of the source conductor. (b) Analytical integration on the observation conductor-three cases

conductor.

In this case, the observation conductor is completely in layer i , the integration is thereby calculated with the Green's function G^i for layer i .

3. *The position of the source conductor element is comprised in the observation conductor.*

In this case, as the observation conductor crosses the two layers, the integration is performed by two separate parts. Both the Green's function G^i and G^{i+1} should be integrated on the corresponding parts.

Note that during the calculation of A_z , a constant is observed on the final results due to the Neumann type B.C.. However, this constant will not affect the results of (4.46) since the integral of this constant over all the conductors will be null as the total ampere-turns is compensated in the component window.

4.3.3.5 Numerical Validations

To validate the method, a Matlab program is realized. In Figure 4.13, a test configuration is given, where a FPC leakage layer with $\mu_r=9$ is implemented and the total ampere-turns in the configuration is zero. Using the Matlab program, the potential vector is calculated on two horizontal test cuts and is further compared with FEM simulation results, as given in Figure 4.14(a). Simulation results show

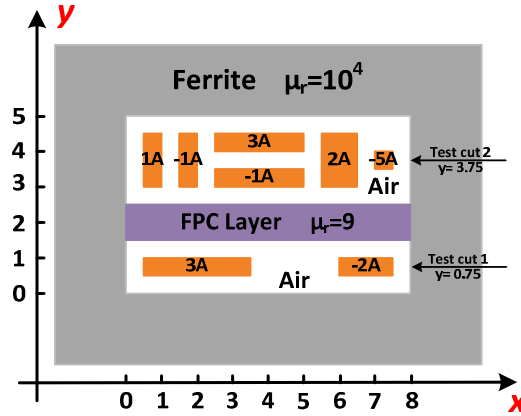


Figure 4.13. Test configurations for validation (unit: mm).

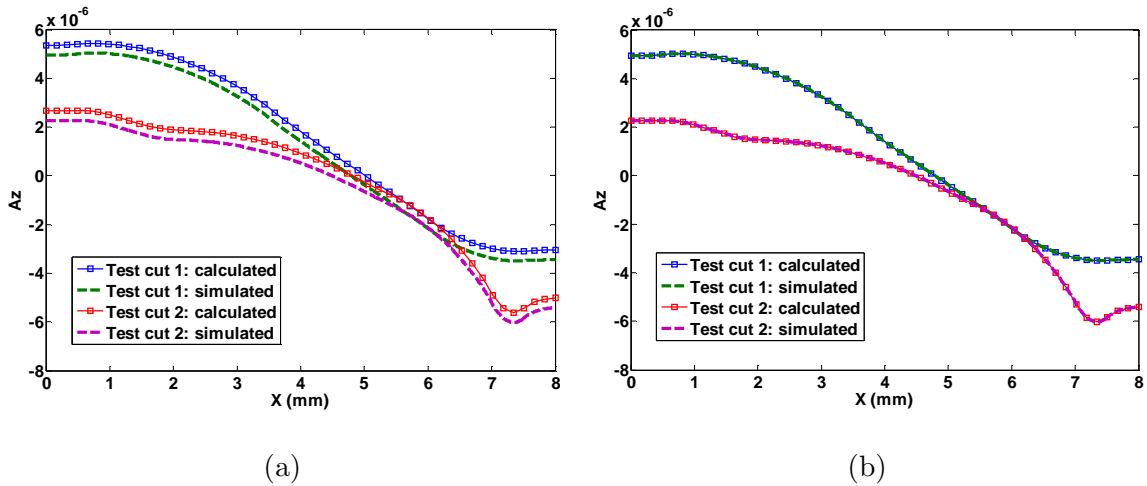


Figure 4.14. Comparison between calculated results and simulated results. (a) Before removing the constant. (b) After removing the constant.

that a constant difference ($4.01E-7$) exists between the calculated results and the simulated ones. Removing this constant, the two calculated curves can perfectly match with the simulated ones [Figure 4.14(b)]. The magnetic induction B_x and B_y are also compared between the calculation and the simulation, as illustrated by Figure 4.15. Again, close match is observed, which validate the proposed method.

After summing the magnetic energy on all the conductors in a window, the total magnetic energy can be found. According to the realized program, the magnetic energy is evaluated to be $2.29E-5$ J/m whereas the FEM simulated results gives also $2.29E-5$ J/m. It can be concluded that the proposed method can effectively calculate the magnetic field of the studied case.

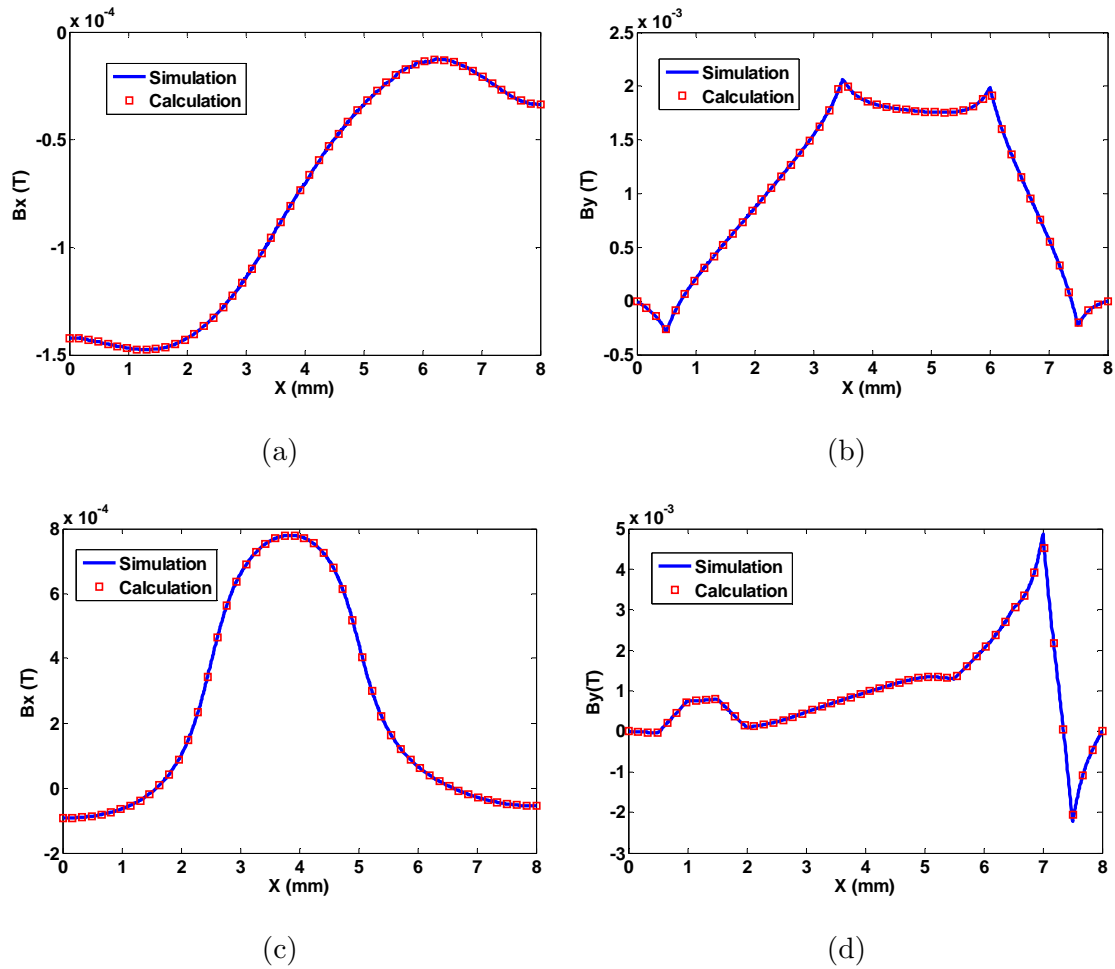


Figure 4.15. Comparison between calculated results and simulated results for the test case. (a) Test cut 1: B_x . (b) Test cut 1: B_y . (c) Test cut 2: B_x . (d) Test cut 2: B_y .

4.3.4 Application on Planar CM Choke with FPC Leakage Layer

The multilayered Green's function method is applied to study a planar CM choke with sandwiched FPC leakage layer. The window of the studied component as well the main dimensions are given in Figure 4.16. The current in each conductor higher than the FPC layer is -1A whereas the current is 1A for the conductors lower than the FPC layer. A horizontal test cut is performed on $H=1.5$ mm and the calculated results of B_x and B_y are compared with the simulated ones in Figure 4.17.

From the results of B_x and B_y , it can be concluded that the field is not tangential to the conductor on the test cut, confirming that the assumption of Dowell is not directly applicable in such case.

After numerical integration, the final energy stored in the window calculated

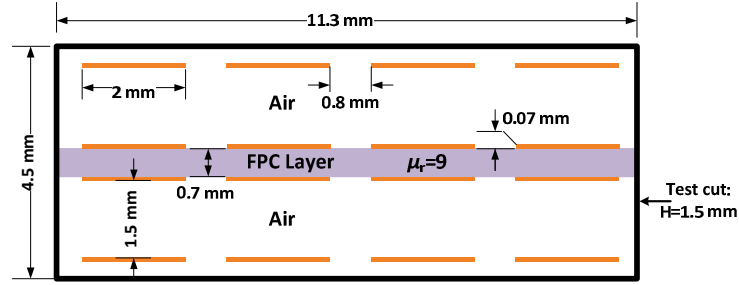
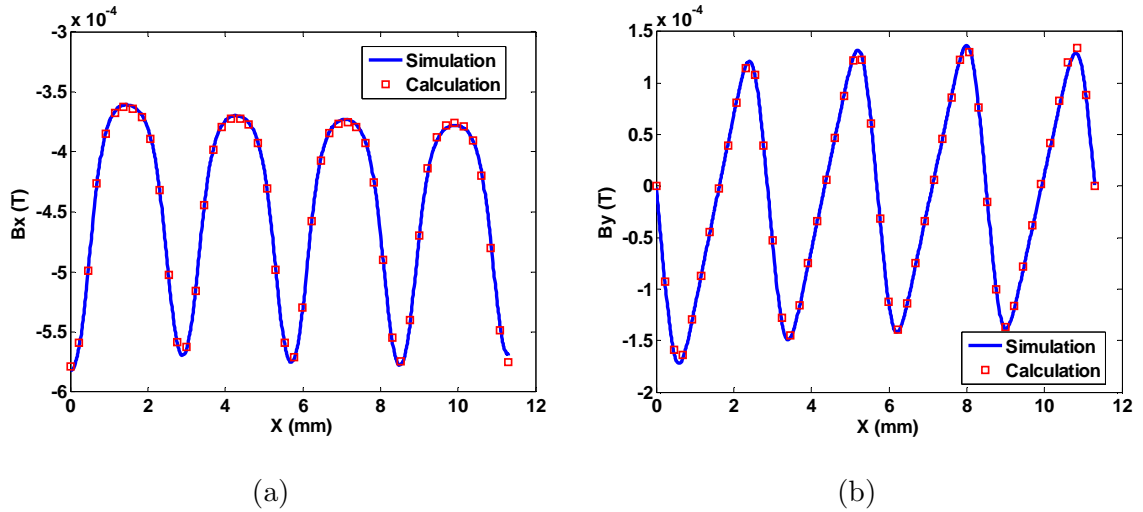


Figure 4.16. Cross-section of the studied planar CM choke.


 Figure 4.17. Comparison between calculated results and simulated results. (a) Test cut: B_x .
 (b) Test cut: B_y .

by the program is $2.43\text{E-}5$ J/m, while the simulated value is $2.57\text{E-}5$ J/m, where only 5% error is found.

4.3.5 Discussion

In the previous calculation, only the case in the core was studied since the core provides the rectangular Neumann boundary for applying the multilayered Green's function. However, for the winding part outside the core, the method cannot be applied. In our case, the FPC layer is inserted only in the winding part covered by ferrite core. Therefore, the winding part outside the core can be considered in free space so that the PEEC-like method [40] can be employed for the study. Indeed, it can be shown that the PEEC-like formulas is the integrated version of a free space Green's function on a rectangular source conductor carrying current I .

For the case where the FPC layer is also implemented in the winding part outside the core, neither method of the two can be applied easily. Using the Green's function method, one can enlarge the boundary of core to decrease the effect of the core (as we did for electrostatic case). Nevertheless, the convergence will certainly be slowed down and the results will be less accurate. Note that for a multilayered structure with $L \rightarrow \infty$, the infinite series used in the presented multilayered Green's function becomes a Fourier integral. In fact, it becomes the Fourier Transform method, which is a useful tool in electromagnetic study for problems with unbounded region. However, this requires a further work on the related topic, which has not been covered by this PhD work.

4.4 Conclusion

In this chapter, the multilayered Green's function method is studied and applied on planar components to evaluate their parasitic capacitances and/or the leakage inductance. In both studies, a 2D analysis is carried out in the first step and then an energy approach is applied for finding the equivalent parasitic capacitances or leakage inductance. For both methods, Matlab programs are realized.

For the determination of parasitic capacitances, the multilayered Green's function is employed to solve the Poisson's equation in a bounded multilayered structure with Dirichlet B.C.. Moment method with point collocation procedure is then performed to calculate the capacitance matrix for the cross-section of the component. With this capacitance matrix, the same energy approach as presented in Chapter 2 can be applied. The method is verified by comparison with FEM simulation results on several validation cases.

Regarding the calculation of leakage inductance of a planar CM choke that sandwiches a FPC leakage layer, the multilayered Green's function is constructed for a bounded 4-layer rectangular region with Neumann B.C.. Numerical integration of the Green's function is implemented in order to find the information of magnetic field including the potential vector, the magnetic induction and the energy stored in the window. Several cases have been analyzed by the proposed Green's function and

the results have a good agreement with simulated ones.

The presented methods are quite general to study a large part of planar components. The main advantage of these methods is that they can be implemented together to build the model of a planar CM choke in a short time. Moreover, the Matlab code of the two methods can also be implemented into an optimization process with further development. The work presented in this chapter, as a preliminary study, allows obtaining some encouraging results.

Chapter 5. Designs of Planar Components for EMI Filters

In this chapter, two design conceptions of magnetic chokes for EMI filters are presented. The first section introduces a conception of an improved parasitic capacitance cancellation technique for planar DM chokes. Using the structural parasitic capacitances, the proposed method allows to cancel the effect of parasitic capacitances of a planar DM choke and thereby to improve the EMI filter's performances. The second section presents a new structure of CM choke using toroid-EQ mixed structure. The CM choke associates two types of magnetic cores with different materials and geometries. With the proposed structure, the leakage inductance of the CM choke is significantly increased for DM filtering and the parasitic coupling to other components is reduced.

5.1 Improved Parasitic Capacitance Cancellation with Planar Components

As discussed in Chapter 1, the parasitic capacitances of planar magnetic components will degrade the HF performances of EMI filters. Therefore, filter designers always attempt to reduce the effect of these parasitic capacitances. Increasing the distance between winding trace or using staggered structures can effectively diminish the parasitic capacitances [1]. As shown in Figure 5.1(a), the conductors in different layers of a staggered structure are no longer face to face. However, the volume of such component will certainly be increased, which is not desirable for the miniaturization of filter. Recently, an alternating winding strategy [see Figure 5.1(b)] has been proposed for reducing the parasitic capacitances of planar components [85]. Though this method is very effective for planar components, it requires a very complex winding trace design and fabrication process. In a word, all these methods are limited by the design or fabrication

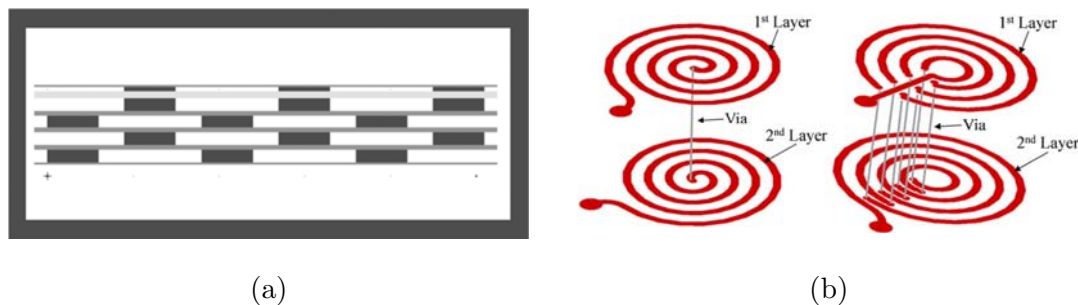


Figure 5.1. Methods for reducing parasitic capacitances. (a) Staggered winding structure [1]. (b) Alternating winding: left-traditional winding; right-alternating winding [85].

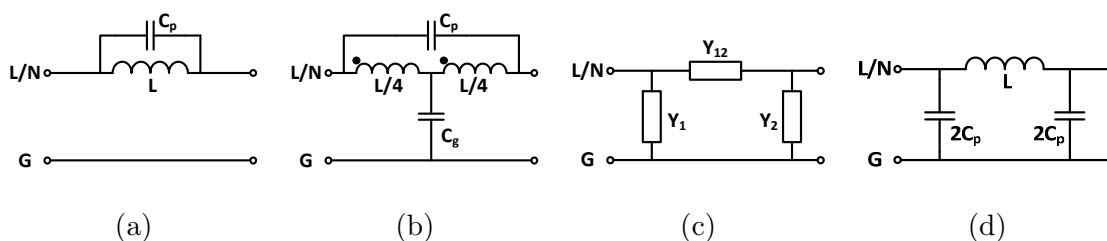


Figure 5.2. Parasitic capacitance cancellation technique for CM chokes.

constraints, and most importantly, the parasitic capacitance always exists as a physical fact and thereby can never be eliminated.

5.1.1 Overview of Parasitic Capacitance Cancellation Techniques

Parasitic capacitance cancellation involves several elegant techniques that are reported in the past ten years [1, 86, 87]. Completely different from the traditional methods based on “reduction”, these methods, as named, are based on cancellation. In view of network analysis, this cancellation implies that the negative effect of the parasitic capacitances is compensated by additional circuitry so that the whole component works as if the parasitic capacitances do not exist. In the following part, two major parasitic capacitance cancellation techniques are briefly introduced.

5.1.1.1 Parasitic Capacitance Cancellation for CM Chokes

The Figure 5.2(a) illustrates an inductor L with its parasitic capacitance C_p . To realize the cancellation, an additional capacitor C_g is added between the center point of the inductor L and the ground in [1], as presented by Figure 5.2(b).

Suppose that the two halves of winding have a perfect magnetic coupling, this circuit is equivalent to a new π network [Figure 5.2(c)] after a Y- Δ transformation [1], with Y_1 , Y_2 and Y_{12} expressed by (5.1) and (5.2).

$$Y_1 = Y_2 = \frac{1}{2}j\omega C_g \quad (5.1)$$

$$Y_{12} = \frac{1 + \omega^2 L \left(\frac{C_g}{4} - C_p \right)}{j\omega L} \quad (5.2)$$

From (1.1), it can be deduced that if $C_g=4C_p$, $Y_{12}=(j\omega L)^{-1}$, so it is equivalent to an ideal inductance. This implies that, from an external view, the whole circuit becomes a perfect LC π -type filter without parasitic capacitances. The two capacitances $2C_p$ on the right and left legs of the network act as Y-capacitance for filtering CM noises. Indeed, the current that passes through the parasitic capacitances C_p is compensated by the current drawing from ground through the additional capacitance C_g . This method is very practical since C_g can be realized with a discrete capacitor easily. In [1], instead of using a discrete capacitor, the authors have sandwiched a ground layer in a planar CM choke to yield the C_g in a distributed way, resulting in a very compact component.

It should be mentioned that this method only works well if the winding are strongly coupled. In the deduction of (5.1) and (5.2), the coupling coefficient between the two halves of windings is supposed to be unity, which is never the case in reality. In common practice, the leakage between the two halves of winding deteriorates the performances of this cancellation technique. As a consequence, having a strong coupling becomes a prior condition for applying this cancellation technique.

5.1.1.2 Parasitic Capacitance Cancellation for DM Inductors

The Figure 5.3 shows two identical DM inductors L with their parasitic capacitances C_p . To cancel these parasitic capacitances, the cancellation method reviewed before can be applied again. Two additional capacitors C_g are added between the center point of each inductor and the ground [Figure 5.3(b)]. As the inductors are studied in DM, no current actually flows into the ground. Therefore, the ground is indeed a neutral point that can be floating. Finally, the two

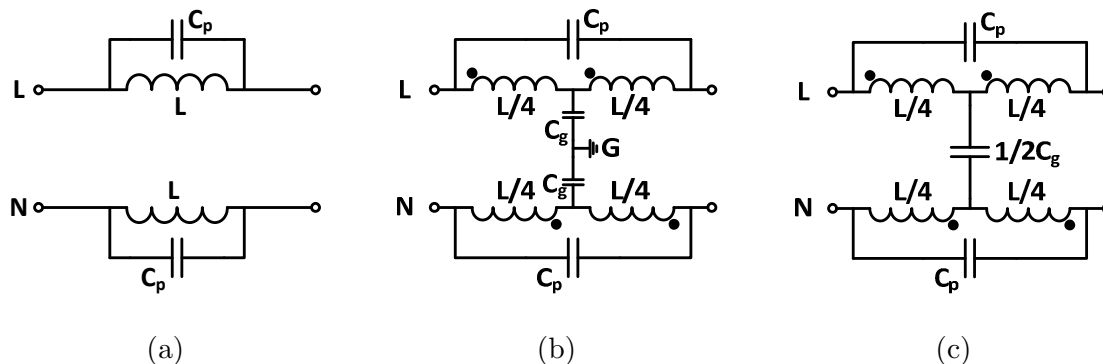


Figure 5.3. Parasitic capacitance cancellation technique for DM inductors: method 1.

additional capacitors become series-connected, which can be simplified by a new capacitor $C_c=1/2C_g=2C_p$ that connects the two center points of the two DM inductors [Figure 5.3(c)]. Just like the previous method, the performances of this cancellation technique also depend on the coupling strength of the windings.

An alternative solution that is independent of the coupling strength is proposed in [86]. Noted that these two DM inductors with their parasitic capacitances form a two-port network whose Y-parameter matrix is given by (5.3).

$$Y_{IND} = \begin{bmatrix} \frac{1}{2}(Y_L + Y_{C_p}) & \frac{-1}{2}(Y_L + Y_{C_p}) \\ \frac{-1}{2}(Y_L + Y_{C_p}) & \frac{1}{2}(Y_L + Y_{C_p}) \end{bmatrix} = \begin{bmatrix} \frac{1}{2}\left(\frac{1}{sL} + sC_p\right) & \frac{-1}{2}\left(\frac{1}{sL} + sC_p\right) \\ \frac{-1}{2}\left(\frac{1}{sL} + sC_p\right) & \frac{1}{2}\left(\frac{1}{sL} + sC_p\right) \end{bmatrix} \quad (5.3)$$

In [86], the authors have proposed to add an additional X compensation network for the cancellation, as illustrated by Figure 5.4(a). The Y-parameter matrix for this network is expressed by (5.4).

$$Y_X = \begin{bmatrix} \frac{1}{2}Y_{C_X} & \frac{1}{2}Y_{C_X} \\ \frac{1}{2}Y_{C_X} & \frac{1}{2}Y_{C_X} \end{bmatrix} = \begin{bmatrix} \frac{1}{2}sC_X & \frac{-1}{2}sC_X \\ \frac{-1}{2}sC_X & \frac{1}{2}sC_X \end{bmatrix} \quad (5.4)$$

This network is connected in parallel with the DM inductors, as shown in Figure 5.4(b), and the complete Y-parameter matrix for this final circuit [Figure 5.4(b)] is written as (5.5).

$$Y_{DM} = Y_{IND} + Y_X = \begin{bmatrix} \frac{1}{2}\left[\frac{1}{sL} + s(C_p + C_X)\right] & \frac{-1}{2}\left[\frac{1}{sL} + s(C_p - C_X)\right] \\ \frac{-1}{2}\left[\frac{1}{sL} + s(C_p - C_X)\right] & \frac{1}{2}\left[\frac{1}{sL} + s(C_p + C_X)\right] \end{bmatrix} \quad (5.5)$$

This matrix can be further represented by a symmetrical π -type network, as shown in Figure 5.4(c). In this network, a negative capacitance $-C_X$ is connected in parallel with C_p and it can be used for canceling C_p . If the relation $C_X=C_p$ is satisfied, the

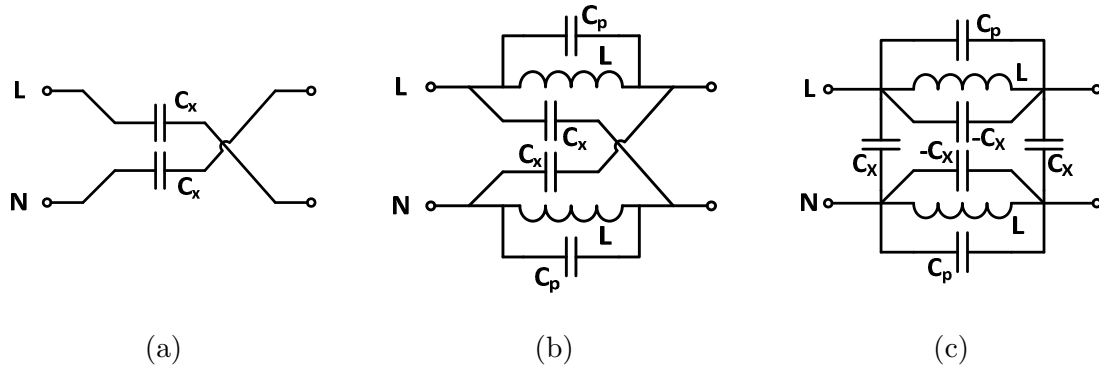


Figure 5.4. Parasitic capacitance cancellation technique for DM inductors: method 2.

parasitic capacitances C_p are eliminated, implying that the cancellation is done.

One of the main advantages of this cancellation technique is that it does not depend on the coupling strength of the inductors, which is very interesting for improving the performances of DM filters. Consider a case of an L filter [Figure 5.3(a)], where $L=100 \mu\text{H}$ and $C_p=20 \text{ pF}$. According to the cancellation technique, two capacitances C_x are added, as illustrated in Figure 5.4(b). In order to observe the effect of this cancellation on the filter IL (with $50 \Omega/50 \Omega$ source and load impedances), several simulations are performed by modifying the values of C_x . The obtained results are summarized in Figure 5.5. Without the cancellation, the filter does not work ideally beyond 3.5 MHz due to the parallel resonance of L and C_p . When the cancellation technique is applied, with $C_x < C_p$, the larger C_x is, the farther the filter's limit frequency can be pushed away. However, if $C_x > C_p$, the increase of C_x will be adverse to the IL of the filter. When $C_x = C_p$, the perfect cancellation is achieved and the filter can have the best performances. Defining:

$$K = \frac{C_x}{C_p} \quad (5.6)$$

Two different zones can be identified accordingly: $K < 1$ for the zone of under-cancellation and $K > 1$ for the zone of over-cancellation. The ideal situation is to make $K \rightarrow 1$ to optimize the HF performances of the filter.

From a physical viewpoint, the noise current that bypasses the inductor L through the parasitic capacitance C_p is canceled by the noise current that is coupled by C_x from the other line. In order to achieve a good cancellation, the two noise

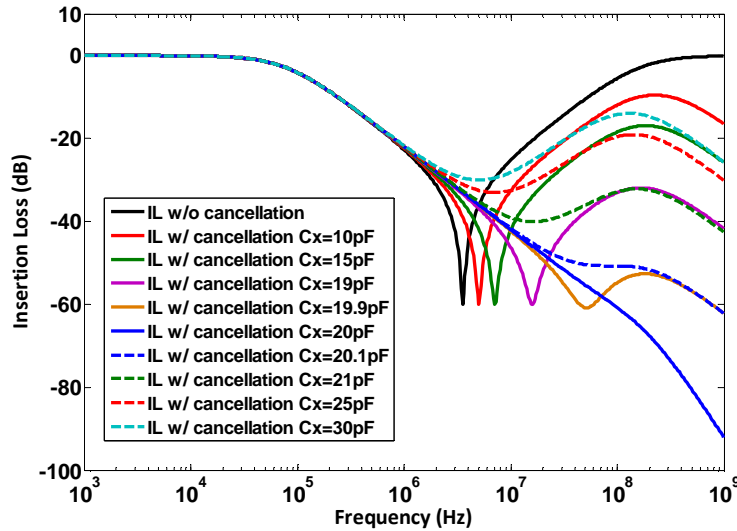


Figure 5.5. Simulation results of the parasitic cancellation technique for DM inductors: method 2.

currents should be identical in magnitude but opposite in phase (naturally satisfied in DM). This requirement leads to the equality between C_p and C_X .

5.1.2 Improved Parasitic Capacitance Cancellation for Planar DM Chokes

5.1.2.1 Basic Idea

In the aforementioned cancellation technique for DM inductors, two additional capacitors C_X are needed, resulting in an increase of the component volume and failure risk. To avoid using these discrete components, an improved parasitic capacitance cancellation using structural parasitic elements has been developed for planar DM chokes [75].

The equivalent circuit for coupled DM chokes is presented in Figure 5.6. As seen, it is almost the same as that of CM chokes except that the coupling direction is opposite. Z_l and Z_m are the leakage and magnetizing impedances, respectively. C_1 , C_2 and C_3 are the parasitic capacitances of the DM choke. In fact, only C_1 and C_3 are not desirable since they impair the HF performances of the choke. However, C_2 can be regarded as DM capacitances for attenuating DM noises. Comparing Figure 5.6 and Figure 5.4(b), it can be found that C_1 and C_3 are connected in the same way as C_p and C_X . Intuitively, it seems possible to use C_3 to cancel the effect of C_1

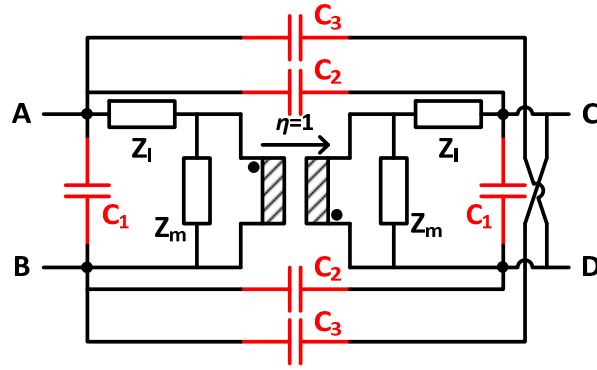


Figure 5.6. Equivalent circuit for DM chokes

Table 5.1 Test Configurations for Calculating the Parasitic Capacitances

<i>Term</i>	$C_2 + C_3$	$C_1 + C_2$
<i>Test Configuration</i>		

by establishing the equality $C_3 = C_1$, just as demonstrated previously. To achieve this equality, C_2 is added to both sides of the equation, leading to:

$$C_2 + C_3 = C_1 + C_2 \quad (5.7)$$

Recalling the parasitic capacitance calculation procedure presented in Chapter 3, $C_2 + C_3$ and $C_1 + C_2$ can be calculated by two different test configurations, as given in Table 5.1. The above analysis implies that the cancellation using structural elements is possible if the electric energies stored in the two test configurations are equal. In the following parts, the cancellation technique is applied on a planar DM choke. Two different cases are discussed separately: DM choke without ferrite core [Figure 5.7(b)] and DM choke with ferrite core in [Figure 5.7(a) and (c)]. The geometry dimensions and material parameters of this component are summarized in Table 5.2.

Case 1: DM Choke without Ferrite Core

The cross-section of the structure (one window) is given in Figure 5.7(b). In this case, $C_2 + C_3$ stands for the capacitive coupling between the two windings 1 and 2. In fact, its value depends strongly on the distance H_{iso} between the two PCBs, as

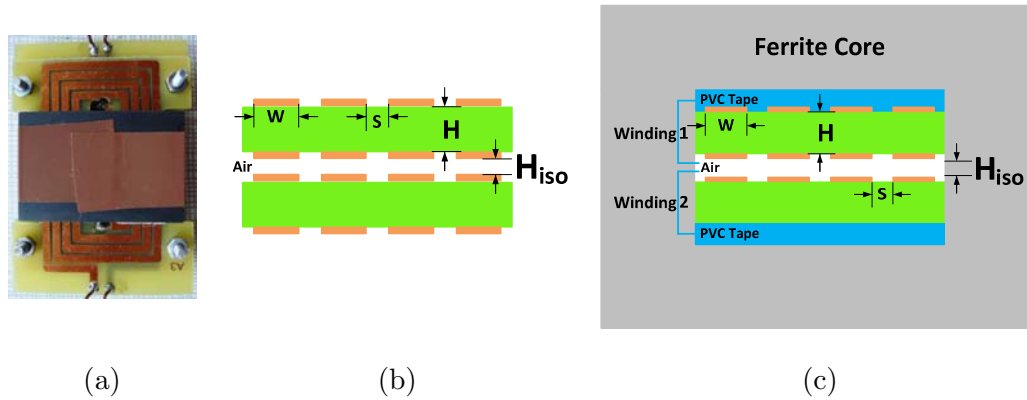


Figure 5.7. Parasitic capacitance cancellation for planar DM choke. (a) Realized DM choke. (b) Cross-section without core. (c) Cross-section with core.

Table 5.2 Geometry and Material Properties of the Component

<i>Geometry characteristics</i>	<i>Material properties</i>
W=2 mm	Ferroxcube 3F4 Ferrite Planar E38
S=0.8 mm	ϵ_r of ferrite: 10^3 - 10^4
$S_{\text{ext}}=0.5$ mm	ϵ_r of epoxy: 5
H=1.5 mm	ϵ_r of PVC tape: 3.5

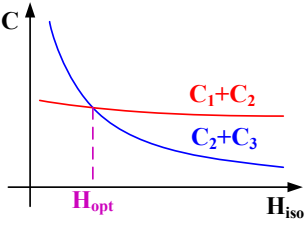
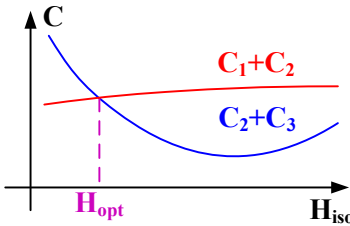
shown in Figure 5.7(b). It is easy to understand that this capacitance is a plate-type capacitance (two conductors face to face). Therefore, its value is a linear function of $(H_{iso})^{-1}$, as illustrated in Table 5.3. C_1+C_2 presents the parasitic capacitance in each winding and the DM capacitive coupling between the two windings. As H_{iso} increases, the two PCBs will become independent to each other, so C_1+C_2 will finally stabilize to a constant. On the other hand, as H_{iso} decreases, this value will slowly increase since the electric coupling between the two PCBs is strengthened.

Case 2: DM Choke with Ferrite Core:

If a ferrite core is implemented [Figure 5.7(c)], the value of C_2+C_3 will decrease at first when H_{iso} increases. However, the two PCBs will approach the ferrite core when H_{iso} is large enough. As the ferrite core is considered as a good dielectric material, the value of C_2+C_3 will increase due to the capacitive coupling through the ferrite core. Similarly, the value C_1+C_2 will also rise slowly with an increasing H_{iso} [see Table 5.3].

In both cases, when approaching the two PCBs (by reducing H_{iso}), the values of C_1+C_2 and C_2+C_3 will intersect at a point where the equality (5.7) is verified.

Table 5.3 Variation of the Capacitances with H_{iso}

Case	W/O Ferrite Core	W/ Ferrite Core
Variation Curves		

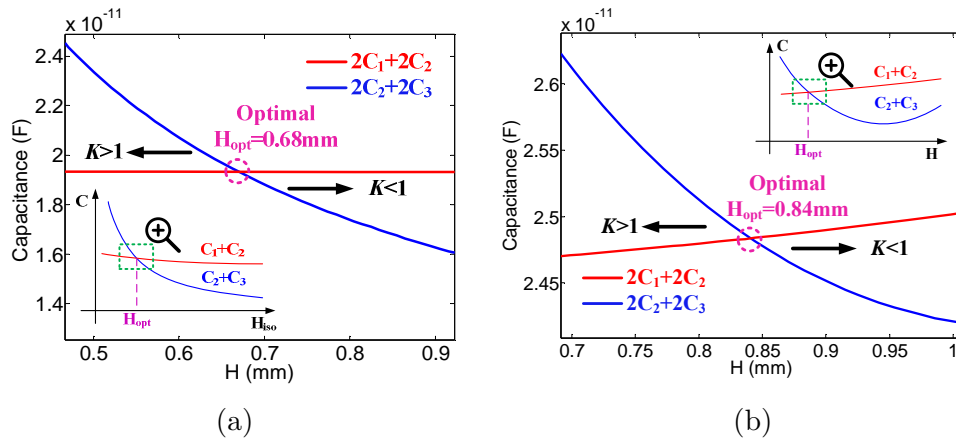


Figure 5.8. Calculated variation of the capacitances. (a) Without ferrite core. (b) With ferrite core.

This point H_{opt} is the optimal one for the parasitic cancellation because $K=1$. With the program of the parasitic capacitances calculation for planar components, the curves of C_1+C_2 and C_2+C_3 can be drawn so that this optimal point can be found. The calculated curves are shown in Figure 5.8. The optimal values of H_{iso} are 0.68 mm and 0.84 mm for the cases without ferrite core and with ferrite core, respectively.

5.1.3 Experimental Validations

5.1.3.1 Tests on L filter

To validate the cancellation technique, the 8-turn planar DM choke [Figure 5.7(a)] with Ferroxcube 3F4 ferrite core is tested using a network analyzer (Agilent 5071C ENA). The test setup is shown in Figure 5.9(b). Two $50\Omega/50\Omega$ baluns are used for the differential mode measurements.

As the DM choke works under high current value, air gap is needed for the

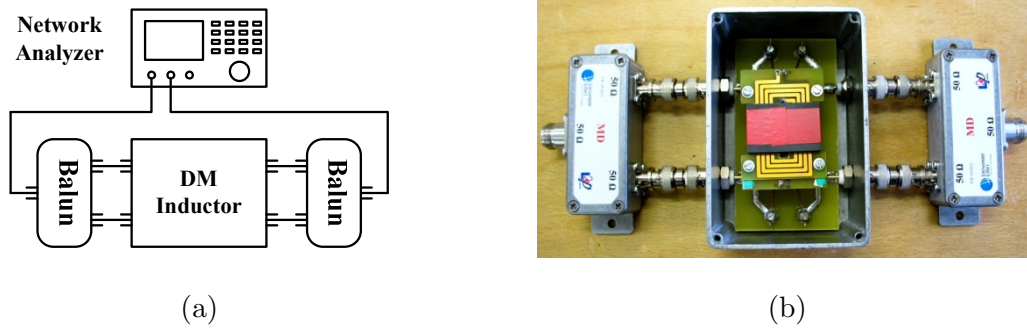


Figure 5.9. Test setup for the cancellation. (a) Schematic. (b) Photo of the fixture.

ferrite core to avoid saturation of the ferrite. Two extreme cases are chosen to show the validity of the method: (a) without ferrite core; (b) with ferrite core but without air-gap. The measurement results on the DM inductor without ferrite core are shown in Figure 5.10(a). The insertion loss for under-cancellation, over-cancellation and optimal cancellation are compared to the case without cancellation. As seen, when the optimal cancellation is achieved, the resonance is moved from 30MHz to about 40MHz. Figure 5.10(b) illustrates the measured results when the ferrite core is incorporated. Without the cancellation (two separated inductors), the insertion loss presents a resonance close to 2.3 MHz. While with the optimal cancellation, the resonance is moved to 8.3 MHz. As illustrated, the improvement in HF for the DM inductor is significant.

To achieve the best cancellation performance, the experimental H_{opt} may differ from its calculated value due to the measurement setup and the parasitic elements of the testing fixture. In Table 5.4, the calculated H_{opt} for cancellation is compared with the measured ones. It can be found that the computed value can still give a good starting point to guide the design.

Though this cancellation technique does not have any requirement on the coupling strength on each inductor, the coupling strength between the two inductors is very important for the effectiveness of the method. It should be noted that the leakage inductance of the inductor will also limit the HF performance of the cancellation. It can be spotted from all the measurements that the insertion loss will decrease towards 0 beyond tenth of megahertz. This is due to the resonances from the leakage inductance and the parasitic capacitances of the component. In fact, the lower the leakage inductance is, the better the cancellation will be, as

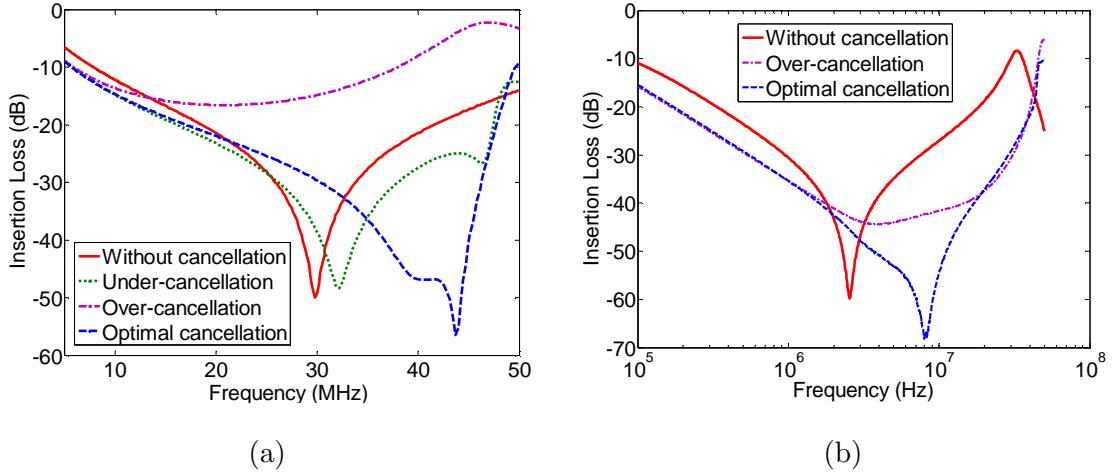


Figure 5.10. Measurement results for the parasitic cancellation technique. (a) Without ferrite core. (b) With ferrite core.

Table 5.4 H_{opt} for the Cancellation

	<i>Computed Value</i>	<i>Measured Value</i>
<i>W/O Ferrite Core</i>	0.68 mm	0.85 mm
<i>W/ Ferrite Core</i>	0.84 mm	0.75 mm

addressed in [87].

5.1.3.2 Tests on LC Filter

The cancellation technique is further tested on a simple LC DM filter using the previous planar DM choke. As seen from Figure 5.11, the capacitance of the DM capacitor is 68 nF. A four-port measurement method is used to evaluate the IL of the filter with a network analyzer (Agilent 5071C). The DM IL is given by the value S_{dd21} that is expressed by (2.35) and it is illustrated in Figure 5.12. It can be seen that the resonance is about 2 MHz without a good cancellation, whereas it is pushed to about 7 MHz. The IL of the filter is improved by 10-20 dB from 2 MHz to 30 MHz. It can be concluded that with an optimal design of the DM choke winding, the performance of the filter can be significantly improved without using any additional components.

5.1.4 Discussion

In this section, the idea of using structural parasitic elements to realize the parasitic cancellation has been presented. Though some preliminary tests show

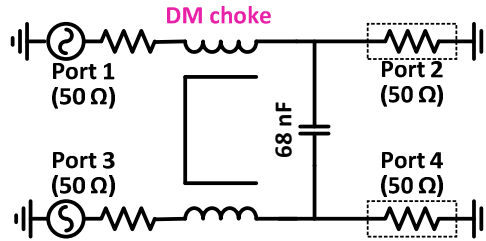


Figure 5.11. Measurement setup for testing the LC filter.

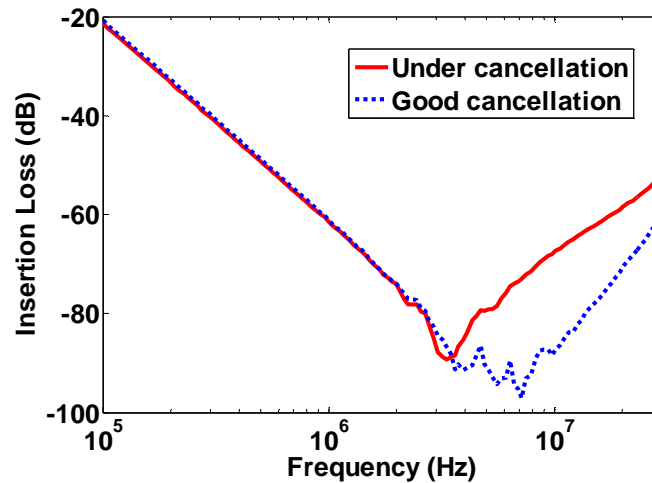


Figure 5.12. Measured IL of the LC filter.

some encouraging results, several aspects of the parasitic cancellation technique should be addressed.

1. **Sensibility and robustness:** In this part, the capacitance cancellation technique is realized by varying the values of H_{iso} . From the test results, it can be concluded that H_{opt} is usually very small, making the cancellation relatively sensible to the variations of H_{iso} . In practice, the design parameter H_{iso} should be defined on a small region where the performances of the filter will be optimized. Moreover, in this work, the isolation between the two PCBs is not taken into account. For safety purpose, isolation layer such as Kapton should be added.
2. **Effects of environment:** The values of C_p and C_x are dependent to the environment where the component locates, especially the metallic fixture used for measurement. A test in a large metallic box can lead to a different H_{opt} from that of a test in a smaller metallic box. As the cancellation requires a good match between C_p and C_x , their values should be calculated by taking account

of their environment. However, this will make the theoretical analysis very cumbersome.

3. **Saturation:** As DM choke works under flux bias, air-gapped core or powder material should be applied for avoid core saturation. In this study, the air-gap is not used; therefore this DM choke should be used in an AC-DC converter where a large smoothing inductor is implemented at the input.

5.2 Toroid-EQ Mixed Structured CM Choke

During the past decades, many research works have addressed the integration issue of EMI filter. Numerous techniques have been proposed for the integration of chokes with different technology, such as planar, toroid and foil. This section introduces a CM choke that combines two technologies: planar and toroid. This choke is composed of two different magnetic cores with different materials and geometries. The design and characteristics of such component is very interesting for EMI filtering applications, as will be described hereinafter.

5.2.1 Review of Integration Techniques of CM and DM Chokes

According to Chapter 1, the CM choke L_{CM} in an EMI filter is realized by coupled inductors whereas the DM chokes L_{DM} can be yielded by independent discrete coils or by the leakage inductance of the CM choke. Recently, numerous techniques have been proposed to integrate L_{CM} and L_{DM} together [88, 89, 90, 91, 1]. In [88], flexible multilayered foils are wound on two UU ferrite cores to integrate CM capacitances, L_{CM} and L_{DM} , resulting in a miniaturized EMI filter [see Figure 5.13(a)]. Nevertheless, the closely wound foil layers leads to large parasitic capacitances that degrade the HF characteristics of the filter. In [1], an FPC layer is sandwiched inside a planar CM choke for providing the leakage path and thereby enlarging the L_{DM} [see Figure 5.13(b)].

It should be mentioned that toroidal cores are still the most commonly used for chokes in commercial EMI filters due to their low cost and wide availability [30]. In the past ten years, several integration techniques have also been reported for those toroidal cores. In [89, 90], CM and DM chokes are realized by combination of

toroidal cores with different radius. The DM choke with smaller core is embedded into the inner space of the larger CM choke [see Figure 5.13(c) and (d)]. These methods integrate the CM and DM chokes into the same component and thereby significantly reduce the volume of the filters.

Another integration technique involves increasing the leakage inductance of a toroidal CM choke for DM noise suppression [91]. For a toroidal CM choke, its leakage inductance is approximately calculated by [92]:

$$L_{\text{DM}} = \mu_{\text{DM}_e} \frac{0.4\pi N^2 A_e}{l_e \sqrt{\left[\left(\frac{\theta}{360}\right) + \left(\frac{\sin(\theta/2)}{\pi}\right)\right]}} \quad (5.8)$$

where μ_{DM_e} is the effective permeability for leakage flux, N is the number of turns in the winding, θ is the winding angle, A_e is the effective cross section area and l_e is the effective mean length of the core. From (5.8), it can be concluded that L_{DM} mainly depends on the number of turns N , the geometry of the core, and the effective permeability for DM leakage flux. Usually, the values of L_{DM} are very small. Recently, nanocrystalline cores receive more concern in EMI filtering applications [33, 93]. In comparison to MnZn ferrite, nanocrystalline material presents a very high initial permeability μ_0 , high saturation level B_{sat} , high operating temperature T_{max} and low temperature sensibility. As a result, to attain the same inductance L_{CM} for a given current, using nanocrystalline core allows minimizing the filter with a smaller core and less winding turn number, resulting in an even smaller L_{DM} , which is not desirable for DM noise suppression. In [91], a CM choke is coated with magnetic epoxy mixture [see Figure 5.13(e)]. This mixture coat can raise the value of μ_{DM_e} in (5.8) and thereby increase the leakage inductance L_{DM} . However, the fabrication of the magnetic epoxy mixture and the coating process make this kind of integrated components expensive for practical use.

In the following part, a new CM choke with toroid-EQ (referred as T-EQ) mixed structure is introduced [94]. This component is indeed the association of two magnetic cores with different geometries and materials (i.e. nanocrystalline toroid and ferrite EQ cores). The first nanocrystalline core plays the role of CM choke to yield L_{CM} whereas the ferrite EQ core increases the leakage inductance of the nanocrystalline CM choke, namely L_{DM} for attenuating the DM noises. Besides, this

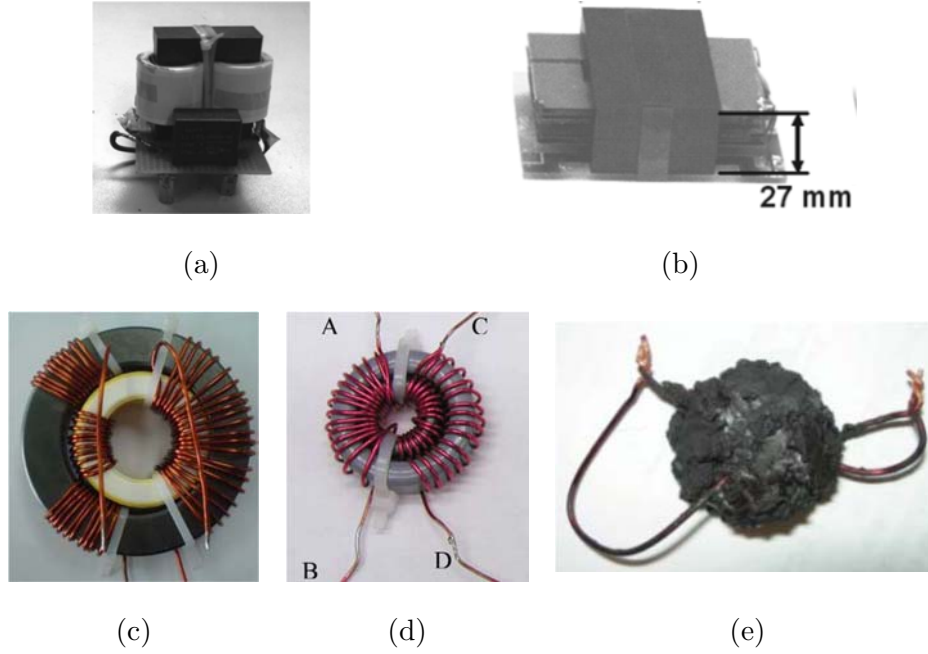


Figure 5.13. Integration techniques for EMI filters. (a) [88]. (b) [1]. (c) [89]. (d) [90]. (e) [91].

T-EQ CM choke exhibits less parasitic magnetic coupling between itself and neighboring capacitors. Last but not least, the fabrication of such CM choke is relatively easy. To validate the conception and show its benefits, measurements and performance comparisons are carried out on realized prototypes.

5.2.2 Design of the Toroid-EQ CM Choke

5.2.2.1 Design Description

In order to augment L_{DM} one can increase the effective permeability for leakage flux μ_{DM_e} according to (5.8). The T-EQ CM choke described in this section associates a nanocrystalline toroidal core as CM choke and a ferrite EQ core for increasing the value of μ_{DM_e} . The Figure 5.14 illustrates the main conception of this component. As seen, the toroidal CM choke is first wound normally and then it is implemented into a ferrite EQ core. The fabrication of this T-EQ CM choke is easy because it does not need any particular winding or fabrication process. Just like an ordinary toroidal CM choke, the flux generated by DM currents is cancelled out in the toroidal core. The CM inductance L_{CM} of this choke is expressed by:

$$L_{CM} = A_L N^2 \quad (5.9)$$

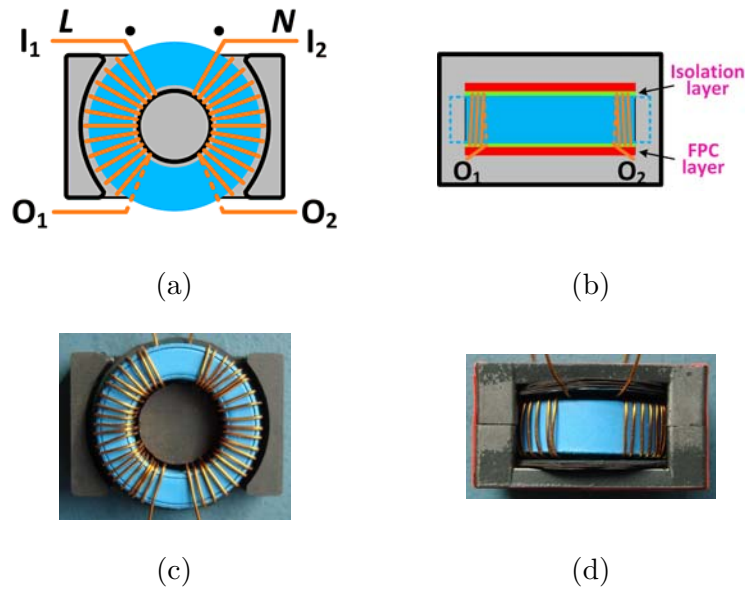


Figure 5.14. T-EQ CM choke. (a) Structure: top view. (b) Structure: front view. (c) Realized T-EQ choke: top view. (d) Realized T-EQ choke: front view.

Table 5.5 Parameters of the Magnetic Cores Used in the T-EQ CM Choke

	<i>Nanocrystalline core</i>	<i>Ferrite EQ core</i>
<i>Reference</i>	Magnetec M-307	EPCOS EQ30 N97
<i>Dimensions</i>	OD=22.5 mm ID=12.5 mm H=7.5 mm	L=30 mm W=20 mm H=16mm
<i>Initial Permeability</i>	30000	2300
<i>Saturation Level</i>	1.2 T	0.4~0.5 T

where A_L stands for the inductance ratio of the toroidal core and N stands for the number of turns in the winding. Meanwhile, the leakage inductance of the CM choke acts as L_{DM} for DM noise attenuation. Due to the MnZn ferrite EQ core that surrounds the CM toroidal core, μ_{DM_e} is significantly increased.

On the basis of this conception, a prototype is realized [Figure 5.14(c) and (d)]. The toroidal core for CM choke uses Nanoperm alloy from Magnetec [95] whereas the EQ ferrite core uses EPCOS N97 material [96]. The main characteristics of both cores are summarized in Table 5.5. The windings of the toroidal CM choke owns 21 turns of 0.4 mm (radius) copper wire. The inner surface of the EQ core is coated with a layer of silicone varnish to isolate the windings from the core. Moreover, the space between the CM choke and the EQ core is filled by EPCOS ferrite polymer composite (FPC) C350 material [96] to further increase

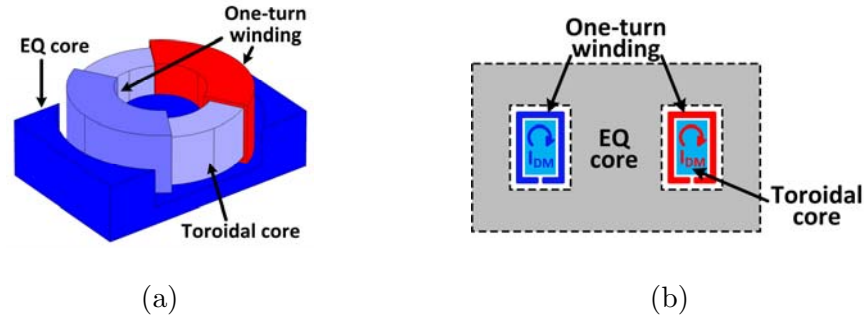


Figure 5.15. T-EQ CM choke model for simulation. (a) One-turn equivalent model. (b) Cross section view.

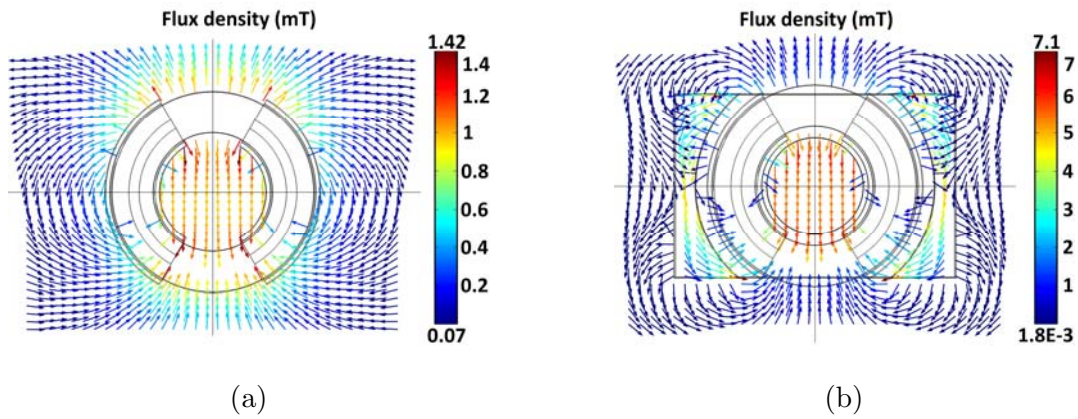


Figure 5.16. Finite element simulation results for the CM choke models. (a) Ordinary toroidal choke. (b) T-EQ choke.

μ_{DM_e} .

5.2.2.2 Component Characteristics

First, numerical simulations are performed for studying the characteristics of the component. According to [59], the windings of the toroidal choke can be modeled by two one-turn coils having the same winding angle and the same ampere-turns, as illustrated in Figure 5.15. On the basis of this approximation, the introduced component is modeled and analyzed by COMSOL[®] multiphysics software in collaboration with Carlos Cuellar, PhD student of L2EP. Magnetostatic simulations are carried out for this analysis. Suppose that DM currents passing through the 21-turn CM choke is 0.5 A (peak), the DM currents in the one-turn model are thereby 10.5 A for having the same value of ampere-turns. Comparison of the performance of an ordinary toroidal CM choke and the T-EQ CM choke is

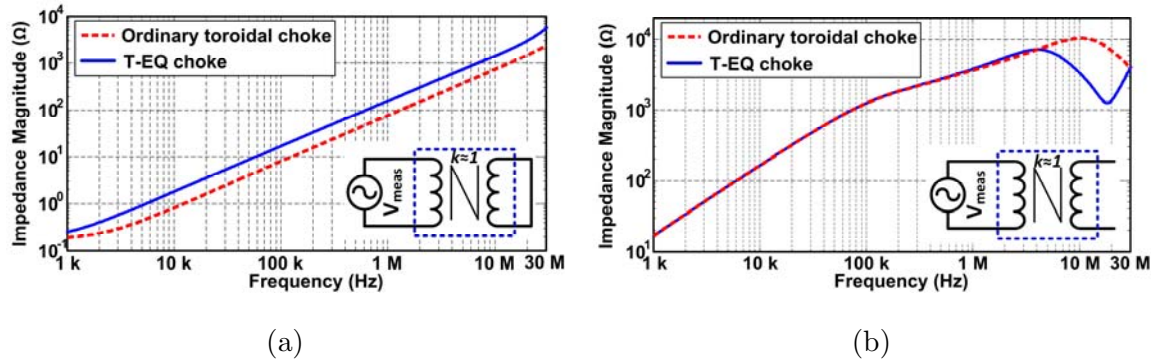


Figure 5.17. Impedance measurement results. (a) Short-circuit configuration. (b) Open-circuit configuration.

Table 5.6 Parameters of the Chokes

	<i>Ordinary choke</i>	<i>T-EQ choke</i>
<i>Number of turns</i>	21	21
L_{CM} (@10 kHz)	2.6 mH	2.6 mH
L_{DM} (@100 kHz)	6.3 μ H	13.6 μ H
<i>Volume</i>	4.3 cm ³	9.6 cm ³

carried out. The Figure 5.16 illustrates the simulated flux densities on the median cross-sections of the two components (without the flux density in the toroidal core). It can be seen that the leakage flux of the T-EQ choke mainly travels through the central cylinder leg and is well confined inside the EQ core. As a consequence, the flux density outside the T-EQ CM choke is significantly reduced. In this configuration, the saturation of the EQ core is avoided thanks to the space between the toroid and the EQ cores, which forms an air-gap.

Next, impedance analyses of the T-EQ CM choke are performed on an impedance analyzer (HP4294A). The values of the CM inductance and leakage one are evaluated with short and open circuit impedance measurements, respectively.

The Figure 5.17 compares the obtained results of the T-EQ CM choke to those of an ordinary CM choke. Accordingly, the main parameters of the T-EQ CM choke and the ordinary CM choke are summarized in Table 5.6. The leakage inductance of the T-EQ choke is 13.6 μ H, twice as much as that of the ordinary one. Meanwhile, the CM inductances measured at 10 kHz in both cases are 2.6 mH. It is stated in Chapter 3 that the relative permittivity ϵ_r of MnZn ferrite is normally in the order of 10^4 . As a result, the parasitic capacitances of the T-EQ CM choke

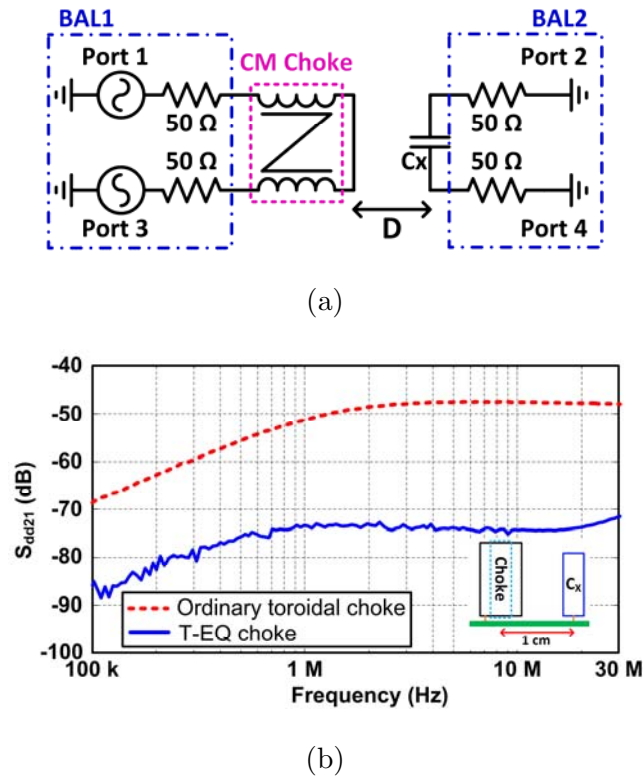


Figure 5.18. Measurements of the parasitic magnetic coupling between the choke and DM capacitors. (a) Test setup. (b) Measurement results.

are increased. Due to this raise of the parasitic capacitances, the resonance of the T-EQ CM choke's open-circuit impedance is shifted to a lower frequency [Figure 5.17(b)]. However, according to the previous section in this chapter, the parasitic capacitance cancellation techniques can be applied to alleviate this parasitic capacitance problem.

5.2.2.3 Parasitic Magnetic Coupling between CM Choke and Filtering Capacitors

As said in the introduction, parasitic elements can considerably impair the HF characteristics of an EMI filter. Apart from the well-known self-parasitic elements, parasitic coupling between components in an EMI filter is also very critical for its performances [21]. In practice, magnetic shield such as μ -metal can be applied for reducing the parasitic coupling [14, 21]. In the studied T-EQ CM choke, the ferrite EQ core acts as a shield surrounding the CM toroidal choke. Therefore, a large part of the leakage flux is confined in the EQ core instead of circulating in air, leading to a decreased magnetic coupling between the choke and its neighbored

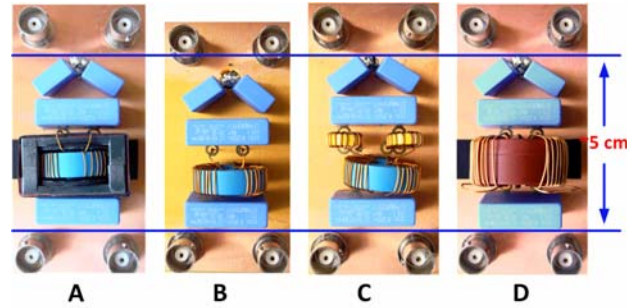


Figure 5.19. Four different EMI filters for comparison.

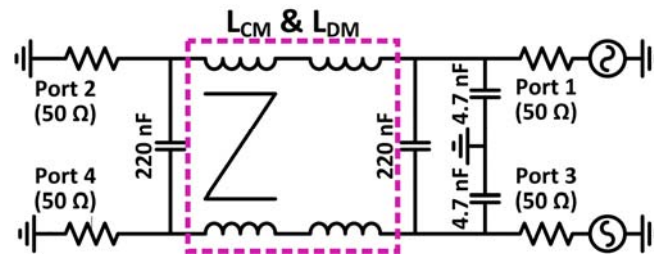


Figure 5.20. Configuration of the four-port mixed-mode S parameter measurements.

components. This is verified by the simulation results illustrated in Figure 5.16. Since the flux density outside the T-EQ CM choke is significantly reduced in comparison with that of the ordinary one, the parasitic coupling between the choke and capacitors is also reduced.

To further verify the simulation results, experimental tests are carried out. Four-port mixed-mode S parameter measurements are performed with a vector network analyzer (Agilent E5071C) to evaluate the small-signal characteristics of filters. The BAL-BAL mode fixture simulator is enabled in the analyzer with port 1 and 3 being BAL1 and port 2 and 4 being BAL2. The distance D between the choke and the capacitor is fixed to be 1 cm, as shown in Figure 5.18(a). The CM choke is excited by the balanced RF outputs (BAL1) while the balanced RF input (BAL2) receives the RF signal coupled from the choke to the DM capacitor C_x . The measured value of S_{dd21} from the analyzer indicates the magnetic coupling strength between the two components, as shown Figure 5.18(b). As seen, coupling between the choke and the capacitor is significantly reduced in the T-EQ choke case than in the ordinary choke case.

5.2.3 Experimental Validations and Discussion

5.2.3.1 Comparison of Different Solutions for Increasing L_{DM}

In practice, many solutions can be used to increase L_{DM} for EMI filtering. In order to show the benefits of the T-EQ CM choke conception, four different EMI filters of the same topology (Figure 1.5) are compared in Figure 5.19: (A) the proposed T-EQ CM choke; (B) the same toroidal CM choke without EQ core; (C) the same toroidal CM choke with independent DM inductors; (D) a larger toroidal CM choke for increasing L_{DM} . The values of the filtering capacitors are the same for all the filters: $C_X=220$ nF and $C_Y=4.7$ nF. In filter (C), to achieve comparable L_{DM} as (A) and to avoid saturation, two MULTICOMP 8.2 μ H/2A iron powder inductors are chosen for realizing the DM coils. In filter (D), a larger Magnetec M-449 nanocrystalline core is wound with 26 turns so that it has the same L_{DM} as filter (A). However, its CM inductance ($L_{CM}=6.4$ mH@10 kHz) is greater than filter (A). In Figure 5.19, filter (B) has the smallest volume whereas filters (A), (C) and (D) occupy nearly the same PCB area. It should also be noted that filter (C) increases the length of the winding wire by 45% (from 110 cm to 160 cm) and solution (D) raise the height by 25% (from 2.4 cm to 3 cm) and almost doubles the winding length (from 110 cm to 210 cm).

5.2.3.2 Small Signal Insertion Loss Measurements

Among the four filters, only filter (A) uses a ferrite EQ core to cover the toroidal CM choke. According to the previous analysis, the magnetic coupling between the choke and the filtering capacitors should be significantly reduced due to the shielding effects of the ferrite EQ core, which improves the HF performances of the EMI filter. To verify this property, four-port mixed-mode S parameter measurements are carried out again with the Agilent E5071C network analyzer to obtain the IL of the four EMI filters from 100 kHz to 30 MHz. Figure 5.20 shows the measurement setup and Figure 5.21 presents the measured results, where S_{dd21} denotes the DM IL whereas S_{cc21} denotes the CM IL. According to the DM IL curves of filters (A) and (B), it can be concluded that the use of EQ ferrite core results in an improvement of more than 8 dB from 100 kHz to 30 MHz, because of

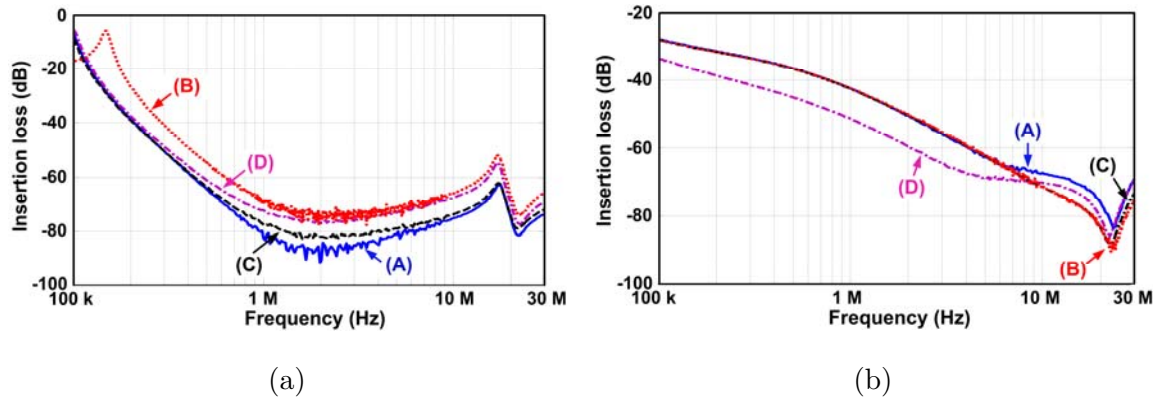


Figure 5.21. Comparison of the insertion losses of the four EMI filters. (a) DM. (b) CM.

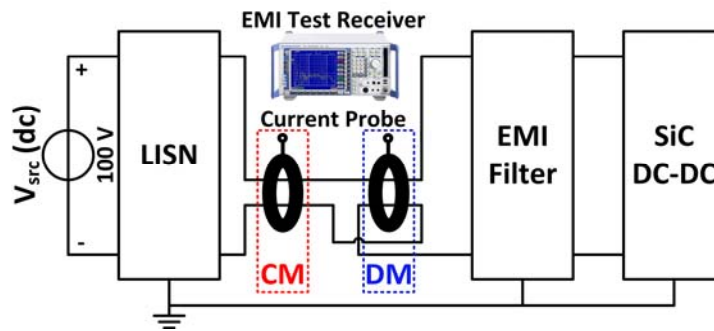
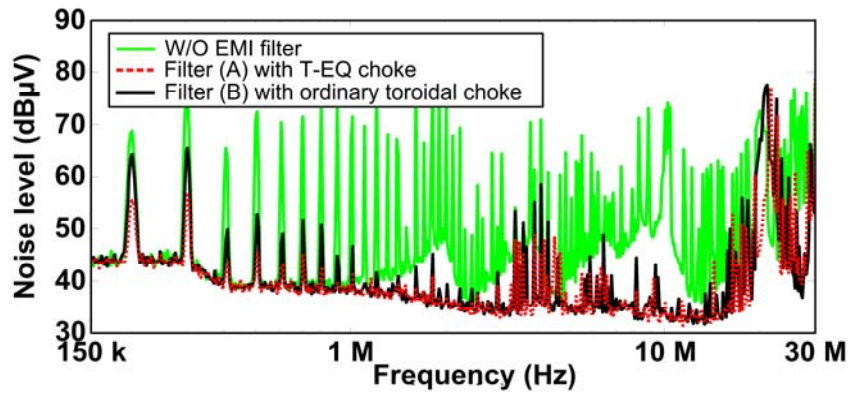


Figure 5.22. Setup for conducted noise measurements.

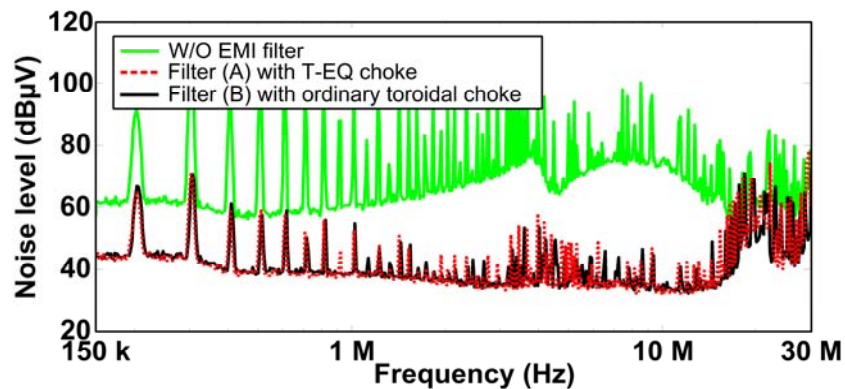
the increased L_{DM} and diminished parasitic magnetic coupling between components. Moreover, filters (A), (C) and (D) exhibit the same L_{DM} , so they have almost the same DM ILs below 400 kHz. However, the magnetic parasitic coupling between the choke and the DM capacitors still deteriorates the performances of filters (C) and (D) beyond 1 MHz [21]. Concerning the CM ILs, almost the same CM ILs below 5 MHz are observed for the filters (A), (B) and (C). However, beyond 5 MHz, the parasitic capacitances of the CM choke in filter (A) degrade its IL for about 8 dB. As filter (D) has greater CM inductance due to the larger toroidal core, it exhibits better CM attenuation below 8 MHz.

5.2.3.3 EMI Conducted Noises Measurements

In this step, the EMI filters (A) and (B) are implemented with a DC-DC converter using SiC power semiconductor that operates at 100 kHz. A $R(30\ \Omega)$ - $L(6\ \text{mH})$ load is used at the output. The input voltage is $100\ V_{DC}$ and the input current is about 1 A. Figure 5.22 illustrates the measurement setup. A current probe (FCC



(a)



(b)

Figure 5.23. Conducted noise measurement results. (a) DM noise. (b) CM noise.

F-35, 100 Hz–100 MHz) is used to send the DM and CM noises to an EMI test receiver (ROHDE & SCHWARZ, 9 kHz–3 GHz). The detection mode is chosen as peak detection and the noises are measured from 150 kHz–30 MHz. After correction, the final DM and CM conducted noise levels are compared in Figure 5.23. The DM IL of filter (A) using T-EQ CM choke is improved by 6–8 dB from 150 kHz to 10 MHz compared to the filter (B) with the ordinary toroidal choke. Besides, the ferrite EQ core has no evident influence on the CM IL of the filter since both filters exhibit almost the same attenuation for CM (see Figure 5.23).

5.2.4 Discussion

As two different cores are used in the T-EQ CM choke, there are many design freedoms to further improve the performances of the choke. First of all, additional winding can be wound on the EQ core to achieve a higher inductance

value. Many choices are also available: winding on the central leg or winding directly outside the EQ core. The former solution yields a coupled DM inductor which has saturation problem. Therefore, air-gap should be added on its central cylinder leg.

Besides, additional magnetic shield (copper or μ -metal foil) can be stuck directly on the flat surface of the EQ core to reduce the parasitic coupling between components, which is not possible with toroidal core.

The EQ core used in this work can be replaced by other cores including P core, PQ core, etc., which enable to confine the leakage flux of the toroidal CM choke. Though a large variety of core geometry can be selected, cores with customized sizes and material can also be employed for thicker wire and higher current.

5.3 Conclusion

In this chapter, two different conception ideas for EMI filter are presented. First, an improved parasitic capacitance cancellation technique for planar coupled DM choke is introduced. The technique, attempting to find the optimal geometry arrangement, uses the structural parasitic elements of the component to achieve the cancellation. This optimal geometry arrangement is calculated based on the parasitic capacitance calculation technique presented in Chapter 3. With this technique, additional components for the cancellation are avoided. Measurement results show that the cancellation technique can effectively reduce the parasitic capacitance effect and thus improve the HF performances of the planar DM choke.

Secondly, a CM choke with toroidal and EQ mixed structure is introduced. The CM choke using toroidal nanocrystalline core is implemented into a MnZn ferrite EQ core that increases the leakage inductance for DM filtering. The proposed structure can effectively augment the leakage inductance with an easy fabrication process. Besides, the parasitic coupling between this T-EQ CM choke and the other components is significantly reduced due to the use of the ferrite EQ core, which works as a magnetic shield. Numerical simulations and experimental tests are carried out and show that this conception is very interesting for EMI

filtering applications.

Conclusion and Perspectives

EMI filters are essential parts of power converters for the conformity with strict EMC standards. Recently, the pursuit of integration and miniaturization of such filters makes planar components a very promising technology for realizing more compact systems. This dissertation focuses on the modeling issues of planar components in PCB technology for EMI filters. The main goal of this dissertation is to provide some tools to establish the model of a planar CM choke, especially the parasitic elements such as parasitic capacitances and leakage inductance. Both experimental methods and theoretical ones are studied in this work. Moreover several design conceptions are also proposed at the end of this dissertation.

Realized Work

In Chapter 2, an experimental approach for building the HF equivalent circuit of a planar CM choke via impedance measurements is presented. Unlike the traditionally-used method based on observations and manual parameter extraction that might be very slow and exhausting, the introduced method incorporates a fitting scheme for fast parameter extraction. The algorithm called Iterative Rational Function Approximation (IRFA) is applied for the fitting process and a systematic equivalent synthesis method is also introduced for generating an accurate equivalent circuit from fitting results. An improved HF equivalent circuit for CM chokes is suggested to adapt to the fitting algorithm. The major elements in the model are extendable depending on the fitting results. A detail extraction procedure is presented for explaining the use of the IRFA algorithm and the improved model. With them, an accurate broadband equivalent circuit of planar CM chokes can be synthesized in a short time.

One of the main objectives of this PhD work is to build a physical model for calculating the parasitic capacitances of planar components. Chapter 3 thereby presents a complete analytical procedure to determine these parasitic capacitances. The analysis begins with 2D analysis where a method named Electric Field

Decomposition (EFD) is employed. The EFD method, originally developed in microelectronics, is significantly extended in this study for analyzing PCB structures encountered in planar components. This method is based on several conformal mapping results, decomposition principles and some fitting parameters. With this EFD method, scalable formulas with good accuracy can be derived. To consider the effect of ferrite core, a transformation technique that treats the ferrite core as a perfect electric conductor (PEC) is proposed with simple formulas. Based on the combination of the EFD and the transformation technique, the capacitance matrix for the cross-section of a planar component can be derived for both cases with core and without core. After obtaining the capacitance matrix, an energy approach is applied for calculating the equivalent parasitic capacitance(s) of a single-port component or a planar CM choke. Measurements results show that the proposed procedure can effectively extract the values of capacitances for the planar components of interest.

Despite of the simplicity of the formulas proposed in Chapter 3, the method still presents some limits. In particular, it requires a very regular and symmetrical geometry on the cross-section of the component. Besides, the analysis requires some insight on the field decomposition so it seems to be more adapted for handy analysis than automated calculation. It is for this reason that a semi-analytical method using Green's function is developed in Chapter 4.

In Chapter 4, the multilayered Green's function method is studied for calculating the parasitic elements of a planar CM choke, i.e. the parasitic capacitances and the leakage inductance. First, the parasitic capacitances are studied. The multilayered Green's function is applied for solving a 2D Poisson's equation in electrostatic over a multilayered rectangular region with homogenous Dirichlet boundary conditions. With the obtained Green's function, the Moment method with point collocation is applied for finding the charge density distribution on the conductors. With the charge density known, the capacitance matrix can be obtained with high accuracy, which can be further processed in the energy approach presented in Chapter 3. Next, the multilayered Green's function is extended to magnetostatic case for extracting the leakage inductance of a CM choke with a ferrite polymer leakage layer. Some special treatments are suggested for solving the

Green's function for the original Neumann boundary condition problem. Numerical integration is implemented for calculating the magnetic field and the energy stored in the cross-section window. Finite-elements simulations show that the method can accurately calculate the magnetic field information of the studied structure, allowing some further process in the calculation of the leakage inductance via an energy approach. The Green's function method presented in this chapter is general and accurate, which allows to think of its implementation with optimization process in the future.

Apart from the modeling topics, this PhD work has also introduced two new conceptions of planar components for EMI filtering applications. The first involves an improved parasitic capacitance cancellation method for planar DM choke, which is stemmed from a reported parasitic capacitance cancellation technique. The difference in this work is that, instead of realizing the cancellation via two additional discrete capacitors, the structural parasitic elements of the component are used to achieve the cancellation by finding the optimal geometry configuration. Measurement results show that the proposed method can effectively improve the HF performances of the studied planar DM choke without using additional component. The second conception presented in this chapter concerns a T-EQ mixed structure CM choke. This choke consists in the association of two magnetic cores with different geometries and materials. The nanocrystalline toroidal core is wound as an ordinary CM choke and it is embedded inside a planar EQ ferrite core that serves for increasing the leakage inductance of the choke and reducing the parasitic magnetic coupling between the choke and the other nearby filter components. Small-signal measurements and tests on a SiC Buck converter show that the T-EQ CM choke presents some interesting features for EMI filter integration.

Future Work

As a preliminary work on modeling and design of planar components for EMI filtering applications, some encouraging results are obtained in this study. However, there are still many aspects that need to be improved or continued in the

future.

Regarding the equivalent circuit extraction method for CM chokes, a human-machine interface should be made to facilitate the users in a short term. This interface has been developed by an engineer student Arnaud Fuchs of Ecole Centrale de Lille [97]. Some improvements on this interface have to be made to further enhance its performances and robustness. The parameter extraction via impedance measurements requires multiple tests and addition connections, which will add uncertainty and error in the final results. From a long term view, the identification with network analyzer can be expected. The measurement required with this method is one-shot and the results are believed to be more reliable. However, further study on the extraction methodology from network parameters (Z , Y or S matrix) should be performed in the future. Moreover, the extraction algorithm has been performed on a planar CM choke but it can also be extended to other arbitrary 2-winding transformers or N -winding transformers. Therefore, more studies should be done for this extension.

Regarding the parasitic capacitances modeling of planar components, the formula generated by EFD method should be further simplified and systematized, which will make the handy analysis more accessible to the users. In this work, the decomposition of component's winding in the energy approach is manually performed. Therefore, the energy approach should be automated by programs which can analyze the structure intelligently. The methods presented in Chapter 4 seem very interesting for automated modeling of planar CM choke since they are all based on generalized formulations. Thus, complete analysis for parasitic elements of a planar CM choke can be realized via this method with more code developments. However, some of the formulations still have to be improved such as the Fourier transformation method for unbounded case, as addressed in Chapter 4.

As a great part of this PhD study concerns the modeling aspects of planar CM choke, its validity should be tested on more components with larger variety. More test cases should be performed, especially on a planar CM choke that has larger number of turns and smaller volume. The realization of such components is the objective for the work of the next PhD student.

The conceptions introduced in the last chapter requires more experimental tests and design considerations to make them mature for practical use. For example, proper layout design and isolation should also be addressed. Moreover, as the T-EQ CM choke incorporates two different cores, the design freedom of such component is very large comparing to traditional ones. Therefore, more work is expected on the improved designs stemmed from this T-EQ CM choke.

Appendix

Appendix I. Householder Transformation

The Householder transformation involves the notion of vector reflection. Given a vector a and a specific plane \mathbf{P} whose normal vector is v , the reflection b of the vector a with respect to the plane \mathbf{P} is given by:

$$b = (\mathbf{I} - 2vv^T)a = \mathbf{H}a \quad (\text{I.1})$$

where $\mathbf{H} = \mathbf{I} - 2vv^T$ is called the householder matrix. Simply speaking, the obtained vector b is the image of vector a mirrored by the plane \mathbf{P} .

The goal here is to solve the equations $\mathbf{A}\mathbf{X} = \mathbf{B}$, where all the columns of \mathbf{A} are regarded as vectors in N dimensional space. The main idea of the Householder transformation consists of choosing special matrix \mathbf{H} to reflect a column vector a on the first axis of its vector space (referred as e_1) so that all the elements in e_1 is zero except for the first one, as given by (I.1).

$$e_1 = (1 \ 0 \ \dots \ 0)^T \quad (\text{I.2})$$

After a series of Householder transformation, the matrix \mathbf{A} will be transformed into an upper-triangle matrix so that Gauss-elimination can be applied to obtain the solution \mathbf{X} .

The detailed analysis on the reflection method of Householder transformation is omitted here but can be found in literature [46]. The following part will present the algorithm of Householder transformation.

Algorithm of Householder Transformation

1. $\mathbf{A}_1\mathbf{X} = \mathbf{B}_1$ is given as the original problem with \mathbf{A}_1 a matrix of dimension $M \times N$ ($M \geq N$).
2. The Householder transformation \mathbf{H}_1 is applied on \mathbf{A}_1 so that all the elements in the first column of $\mathbf{H}_1\mathbf{A}_1$ are zero except for the first element a_{11} . The

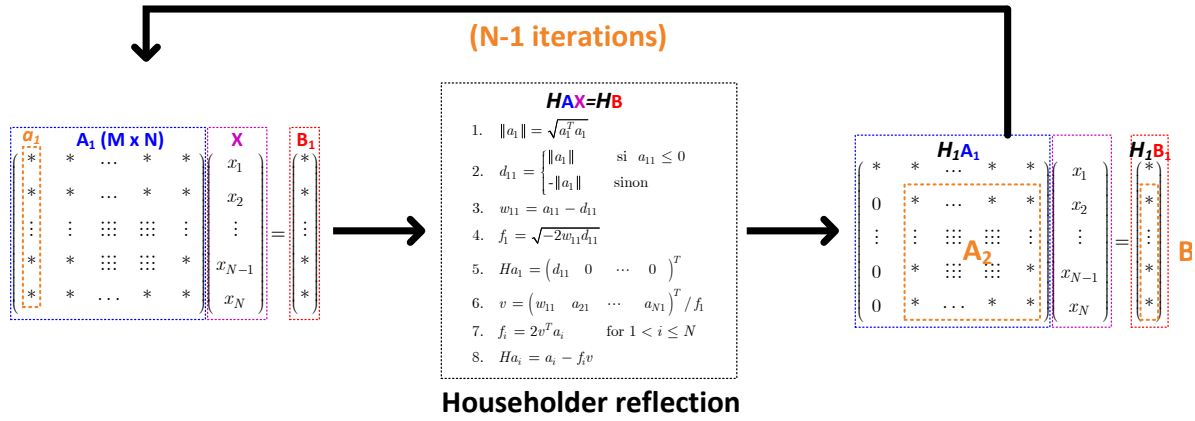


Figure I.1 Householder transformation algorithm.

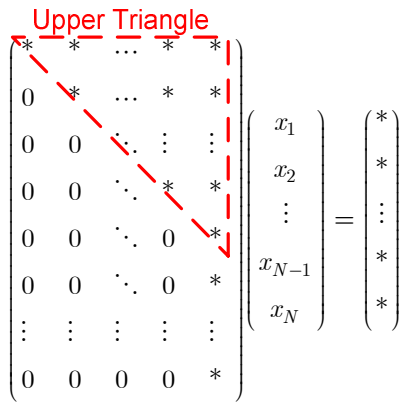


Figure I.2 Final system after a series of Householder transformation.

vector \mathbf{B}_1 is also transformed into $\mathbf{H}_1\mathbf{B}_1$.

3. Defining \mathbf{A}_2 the $(M-1) \times (N-1)$ sub-matrix of $\mathbf{H}_1\mathbf{A}_1$ by deleting the first row and the first column, the Householder transformation \mathbf{H}_2 is applied on the sub-matrix \mathbf{A}_2 with keeping the first row and the column of $\mathbf{H}_1\mathbf{A}_1$. Similar operation is performed on $\mathbf{H}_1\mathbf{B}_1$, as shown by Figure I.1.
4. Repeat the step 3 on $\mathbf{H}_2\mathbf{A}_2$ and $\mathbf{H}_2\mathbf{B}_2$ and so on until the matrix \mathbf{A}_1 is transformed into an upper triangle matrix.
5. Solve the final system as given by Figure I.2.

Appendix II. Derivation of (2.16)-(2.17)

According to the SK iteration, the denominator of the iteration $t-1$ $D^{[t-1]}(s_k)$ is divided at both sides of the equation (2.6) of the iteration t , resulting in (2.13) and

$$\frac{N^{[t]}(s_k)(D^{[t-1]}(s_k))^*}{|D^{[t-1]}(s_k)|^2} = \frac{Z_{meas}(s_k)D^{[t]}(s_k)(D^{[t-1]}(s_k))^*}{|D^{[t-1]}(s_k)|^2} \quad (\text{II.1})$$

where the superscript $*$ denotes the complex conjugate. For magnetic components, the imaginary part of the impedance ($Z \approx \omega L$) is much larger than its real part (losses) in the inductive region. This unbalance will lead to a low fitting quality for the real part during the least square process. In order to achieve a balanced fitting precision between the real part and the imaginary part, the real and imaginary parts of (2.13) are normalized respectively by $1/\text{Re}[Z^{[t-1]}(s_k)]$ and $1/\text{Im}[Z^{[t-1]}(s_k)]$ as weighting factors:

$$\begin{cases} \frac{1}{\text{Re}[Z^{[t-1]}(s_k)]} = \frac{|D^{[t-1]}(s_k)|^2}{\text{Re}[N^{[t-1]}(s_k)(D^{[t-1]}(s_k))^*]} \\ \frac{1}{\text{Im}[Z^{[t-1]}(s_k)]} = \frac{|D^{[t-1]}(s_k)|^2}{\text{Im}[N^{[t-1]}(s_k)(D^{[t-1]}(s_k))^*]} \end{cases} \quad (\text{II.2})$$

Combining the SK iteration (2.13) with the weighting factors (II.2), the final formulations (2.16) and (2.17) are derived.

Appendix III. Derivation of Eq.(3.5)

III.1 Elliptic Integral of the First Kind

Before demonstrating the formula, the elliptical integral should be introduced at first place. The Jacobian elliptic integral of the first kind is given by

$$F(t, k) = \int_0^t \frac{dz}{\sqrt{(1-z^2)(1-k^2z^2)}} \quad (\text{III.1})$$

This integral is called complete elliptic integral of the first kind $K(k)$ when $t=1$

$$K(k) = \int_0^1 \frac{dz}{\sqrt{(1-z^2)(1-k^2z^2)}} \quad (\text{III.2})$$

Its complementary integral $K'(k)$ is defined as:

$$K'(k) = \int_1^{\frac{1}{k}} \frac{dz}{\sqrt{(z^2-1)(1-k^2z^2)}} \quad (\text{III.3})$$

If we define $k' = \sqrt{1-k^2}$ as the complementary modulus of k , the following two equalities can be proved [34]

$$\begin{cases} K'(k) = K(k') \\ K'(k') = K(k) \end{cases} \quad (\text{III.4})$$

Another identity that will be used in the following part is:

$$\begin{aligned} F\left(\frac{1}{k}, k\right) &= \int_0^{\frac{1}{k}} \frac{dz}{\sqrt{(1-z^2)(1-k^2z^2)}} \\ &= \int_0^1 \frac{dz}{\sqrt{(1-z^2)(1-k^2z^2)}} + \int_1^{\frac{1}{k}} \frac{dz}{\sqrt{(1-z^2)(1-k^2z^2)}} \\ &= K(k) - jK'(k) \end{aligned} \quad (\text{III.5})$$

To evaluate the complete elliptic integral of the first kind, the Matlab function “ellipke” can be used. However, the ratio between $K(k)$ and $K'(k)$ are more frequently encountered during the calculation, which can be evaluated by the following formula with a very high accuracy [34]:

$$\frac{K(k)}{K'(k)} = \frac{K(k)}{K(k')} = \begin{cases} \frac{1}{\pi} \ln \left(2 \frac{1+\sqrt{k}}{1-\sqrt{k}} \right) & \frac{\sqrt{2}}{2} \leq k \leq 1 \\ \pi / \ln \left(2 \frac{1+\sqrt{k'}}{1-\sqrt{k'}} \right) & 0 \leq k < \frac{\sqrt{2}}{2} \end{cases} \quad (\text{III.6})$$

III.2 Demonstration of (3.4) and (3.5)

The SC transformation is shown by the following integral

$$\varphi = P \int_0^\omega \frac{d\omega'}{\sqrt{(\omega' - u_{A2})(\omega' - u_{B2})\omega'}} + Q \quad (\text{III.7})$$

Suppose $\omega' = -t^2$, we have:

$$\begin{aligned} \varphi &= P \int_0^{\sqrt{-\omega}} \frac{dt}{\sqrt{(-u_{A2} - t^2)(-u_{B2} - t^2)(-t^2)}} + Q = P \int_0^{\sqrt{-\omega}} \frac{\frac{2j}{\sqrt{-u_{A2}}} dt}{\sqrt{(1-t^2) \left(1 - \left(\frac{t}{\sqrt{-u_{A2}}}\right)^2\right)}} + Q \\ &= P \frac{2j}{\sqrt{-u_{A2}}} F\left(\sqrt{-\omega}, \frac{1}{\sqrt{-u_{A2}}}\right) + Q \end{aligned} \quad (\text{III.8})$$

Defining $P' = 2jP(-u_{A2})^{-1/2}$ and studying the correspondences between $A_2 \leftrightarrow O_3$, $B_2 \leftrightarrow B_3$ and $O_2 \leftrightarrow D_3$, the following equations are obtained:

$$\begin{cases} P'F\left((-u_{A2})^{\frac{1}{2}}, (-u_{A2})^{-\frac{1}{2}}\right) + Q = 0 \\ P'F\left(1, (-u_{A2})^{-\frac{1}{2}}\right) + Q = \lambda \\ P'F\left(0, (-u_{A2})^{-\frac{1}{2}}\right) + Q = \lambda + j\delta \end{cases} \quad (\text{III.9})$$

Solving the equation, we get:

$$\begin{cases} P = \frac{\lambda}{F\left(1, (-u_{A2})^{-\frac{1}{2}}\right) - F\left((-u_{A2})^{\frac{1}{2}}, (-u_{A2})^{-\frac{1}{2}}\right)} \\ Q = \frac{-\lambda F\left((-u_{A2})^{\frac{1}{2}}, (-u_{A2})^{-\frac{1}{2}}\right)}{F\left(1, (-u_{A2})^{-\frac{1}{2}}\right) - F\left((-u_{A2})^{\frac{1}{2}}, (-u_{A2})^{-\frac{1}{2}}\right)} \\ \delta = \frac{j\lambda F\left(1, (-u_{A2})^{-\frac{1}{2}}\right)}{F\left(1, (-u_{A2})^{-\frac{1}{2}}\right) - F\left((-u_{A2})^{\frac{1}{2}}, (-u_{A2})^{-\frac{1}{2}}\right)} \end{cases} \quad (\text{III.10})$$

Using the last equation and the relations (III.4), (III.6) and (III.10), we get:

$$\frac{\lambda}{\delta} = \frac{F\left(1, (-u_{A2})^{-\frac{1}{2}}\right) - F\left((-u_{A2})^{\frac{1}{2}}, (-u_{A2})^{-\frac{1}{2}}\right)}{jF\left(1, (-u_{A2})^{-\frac{1}{2}}\right)} = \frac{K'\left((-u_{A2})^{-\frac{1}{2}}\right)}{K\left((-u_{A2})^{-\frac{1}{2}}\right)} = \frac{K(\sqrt{1+1/u_{A2}})}{K'(\sqrt{1+1/u_{A2}})} \quad (\text{III.11})$$

According to (III.6) and (III.11), the formulas (3.4) and (3.5) are derived.

Appendix IV. Derivation of (3.45)

The value of C_{ij} between conductor i and j is defined as the charge induced on conductor j when the potential of conductor i is 1V and the potentials of all the other conductors are 0V:

$$C_{ij} = \frac{Q_j}{U_i - U_j} \Big|_{U_i=1, U_j=0} = Q_j \quad (\text{IV.1})$$

All the inter-conductor capacitances C_{ij} and the capacitances between conductor-PEC core capacitances C_{ic} are already known. Make the PEC core floating and the capacitances C_{ij}^* is analyzed. According to the definition, the potential of conductor i is set to be 1V while all the other conductors are biased at 0V. As the PEC core is floating, the total charges on it will always be zero according to the charge conservation principle. As a consequence, it is not difficult to find the potential of the floating PEC core U_c :

$$\sum_{k=1}^N C_{kc} (U_k - U_c) = 0 \quad (\text{IV.2})$$

After a few manipulation, we get:

$$C_{ic} (1 - U_c) - \sum_{k=1, k \neq i}^N C_{kc} U_c = 0 \quad (\text{IV.3})$$

Finally, the potential of the floating PEC core U_c is given by:

$$U_c = \frac{1V \cdot C_{ic}}{\sum_{k=1}^N C_k} = \frac{C_{ic}}{\sum_{k=1}^N C_k} \quad (\text{IV.4})$$

The total charges Q_j induced on conductor j come from two parts: the first part is induced directly by conductor i and the second part is induced by the PEC core. Accordingly, Q_j can be calculated by:

$$Q_j = C_{ij} (U_i - U_j) + C_{jc} (U_c - U_j) = C_{ij} + C_{ic} C_{jc} \left(\sum_{k=1}^N C_k \right)^{-1} \quad (\text{IV.5})$$

According to the definition (IV.1), the equation (3.45) is proved.

Appendix V. Derivation of Multilayered Green's Function for Electrostatic

V.1 General Solution by Separation of Variable

If the observation point is not at the position of the Dirac source, the following 2D Laplace's equation governs:

$$\nabla^2 G(x,y)=0 \quad (\text{V.1})$$

The eigenvalue equation should be solved to derive the general solution of (V.1). This eigenvalue equation is given by:

$$\nabla^2 \Phi(x,y)=0 \quad (\text{V.2})$$

Using the separation variable method and supposing $\Phi(x,y)=X(x)Y(y)$, we can cast the equation into:

$$X(x)\frac{\partial^2 Y(y)}{\partial y^2} + Y(y)\frac{\partial^2 X(x)}{\partial x^2} = 0 \quad (\text{V.3})$$

Reformulate the equation (V.3) by adding the eigenvalue λ .

$$X(x)\frac{\partial^2 Y(y)}{\partial y^2} = -Y(y)\frac{\partial^2 X(x)}{\partial x^2} = \lambda \quad (\text{V.4})$$

Depending on the eigenvalue of λ , three type general solutions may be obtained for the equations

Case 1: $\lambda < 0$

$$X(x) = \alpha \cos(\sqrt{-\lambda}x) + \beta \sin(\sqrt{-\lambda}x) \quad \text{and} \quad Y(y) = A \text{ch}(\sqrt{-\lambda}y) + B \text{sh}(\sqrt{-\lambda}y) \quad (\text{V.5})$$

Case 2: $\lambda > 0$

$$X(x) = \alpha \text{ch}(\sqrt{\lambda}x) + \beta \text{sh}(\sqrt{\lambda}x) \quad \text{and} \quad Y(y) = A \cos(\sqrt{\lambda}y) + B \sin(\sqrt{\lambda}y) \quad (\text{V.6})$$

Case 3: $\lambda = 0$

$$X(x) = \alpha X + \beta \quad \text{and} \quad Y(y) = Ay + B \quad (\text{V.7})$$

These three general solutions are chosen depending on the boundary conditions that are given.

V.2 Derivation of (4.16)-(4.19)

According to the boundary conditions (4.13), only (V.6) admit a non-zero solution. Introducing the boundary conditions into (V.6), the general form of the Green's function in layer i is:

$$G^i(\mathbf{r}, \mathbf{r}_s) = \sum_{n=1}^{\infty} [\alpha_n^i \operatorname{ch}(k_n y) + \beta_n^i \operatorname{sh}(k_n y)] \sin(k_n x) \quad \text{with} \quad k_n = n\pi / L \quad (\text{V.8})$$

The continuity conditions (V.9) are used for derive the parameters α_n^i and β_n^i .

$$\begin{cases} G^i \Big|_{y=H_i} - G^{i+1} \Big|_{y=0} = 0 \\ \varepsilon_i \frac{\partial G^i}{\partial y} \Big|_{y=H_i} - \varepsilon_{i+1} \frac{\partial G^{i+1}}{\partial y} \Big|_{y=0} = \delta_{ij} \delta(x - x_s) \end{cases} \quad (\text{V.9})$$

Recall that the source point locates at the interface between layer j and $j+1$ and the observation point is at the interface between layer i and $i+1$. If $i \neq j$, $\delta_{ij}=0$. In this case, the Dirac charge source does not locate on the interface of the observation point. The condition (V.9) can be expressed by:

$$\begin{cases} \alpha_n^{i+1} = \alpha_n^i \operatorname{ch}(k_n H_i) + \beta_n^i \operatorname{sh}(k_n H_i) \\ \varepsilon_{i+1} \beta_n^{i+1} = \varepsilon_i \alpha_n^i \operatorname{sh}(k_n H_i) + \varepsilon_i \beta_n^i \operatorname{ch}(k_n H_i) \end{cases} \quad (\text{V.10})$$

which can be expressed in a matrix form:

$$\begin{pmatrix} \alpha_n^{i+1} \\ \beta_n^{i+1} \end{pmatrix} = \begin{pmatrix} \operatorname{ch}(k_n H_i) & \operatorname{sh}(k_n H_i) \\ \frac{\varepsilon_i}{\varepsilon_{i+1}} \operatorname{sh}(k_n H_i) & \frac{\varepsilon_i}{\varepsilon_{i+1}} \operatorname{ch}(k_n H_i) \end{pmatrix} \begin{pmatrix} \alpha_n^i \\ \beta_n^i \end{pmatrix} = [\mathbf{F}_n^{i,i+1}] \begin{pmatrix} \alpha_n^i \\ \beta_n^i \end{pmatrix} \quad (\text{V.11})$$

Or in its inverse matrix form:

$$\begin{pmatrix} \alpha_n^i \\ \beta_n^i \end{pmatrix} = \begin{pmatrix} \operatorname{ch}(k_n H_i) & -\frac{\varepsilon_{i+1}}{\varepsilon_i} \operatorname{sh}(k_n H_i) \\ -\operatorname{sh}(k_n H_i) & \frac{\varepsilon_{i+1}}{\varepsilon_i} \operatorname{ch}(k_n H_i) \end{pmatrix} \begin{pmatrix} \alpha_n^{i+1} \\ \beta_n^{i+1} \end{pmatrix} = [\mathbf{F}_n^{i,i+1}]^{-1} \begin{pmatrix} \alpha_n^{i+1} \\ \beta_n^{i+1} \end{pmatrix} \quad (\text{V.12})$$

Here, the matrix $[\mathbf{F}]$ and $[\mathbf{F}]^{-1}$ are defined as the upward and downward transformation matrix. Given the parameters of a layer, these matrixes allow for deriving the parameters of its superior and inferior layers.

If $i=j$, $\delta_{ij}=1$. In this case, the Dirac charge source locates on the studied interface. The condition (V.9) becomes:

$$\begin{cases} \alpha_n^{j+1} = \alpha_n^j \operatorname{ch}(k_n H_j) + \beta_n^j \operatorname{sh}(k_n H_j) \\ -\varepsilon_{j+1} \sum_{n=1}^{\infty} \beta_n^{j+1} k_n \sin(k_n x) + \varepsilon_j \sum_{n=1}^{\infty} [\alpha_n^j \operatorname{sh}(k_n H_j) + \beta_n^j \operatorname{ch}(k_n H_j)] k_n \sin(k_n x) = \delta(x - x_s) \end{cases} \quad (\text{V.13})$$

Multiplying the second equation of (V.13) by $\sin(k_n x)$ and integrate the equation over $[0, L]$, we obtain:

$$-\varepsilon_{j+1} \beta_n^{j+1} k_n + \varepsilon_j (\alpha_n^j k_n \operatorname{sh}(k_n H_j) + \beta_n^j k_n \operatorname{ch}(k_n H_j)) = \frac{2}{L} \sin\left(\frac{k_n x_s}{L}\right) \quad (\text{V.14})$$

Recombine the first equation of (V.10) and (V.14), the following system is obtained.

$$\begin{pmatrix} \alpha_n^{j+1} \\ \beta_n^{j+1} \end{pmatrix} = \begin{pmatrix} \operatorname{ch}(k_n H_j) & \operatorname{sh}(k_n H_j) \\ \frac{\varepsilon_j}{\varepsilon_{j+1}} \operatorname{sh}(k_n H_j) & \frac{\varepsilon_j}{\varepsilon_{j+1}} \operatorname{ch}(k_n H_j) \end{pmatrix} \begin{pmatrix} \alpha_n^j \\ \beta_n^j \end{pmatrix} - \begin{pmatrix} 0 \\ \frac{2 \sin(k_n x_s)}{n \pi \varepsilon_{j+1}} \end{pmatrix} = [\mathbf{F}_n^{j,j+1}] \begin{pmatrix} \alpha_n^j \\ \beta_n^j \end{pmatrix} - \begin{pmatrix} 0 \\ \frac{2 \sin(k_n x_s)}{n \pi \varepsilon_{j+1}} \end{pmatrix} \quad (\text{V.15})$$

With the boundary conditions on the top and bottom layer (4.14), the following relations can be obtained

$$\alpha_n^1 = 0 \quad \text{and} \quad \alpha_n^N = -\beta_n^N \tanh(k_n H_S) \quad (\text{V.16})$$

Based on these relations, the equation (V.15) can be transformed into (V.17) by using the transformation matrix $[\mathbf{F}]$ and $[\mathbf{F}]^{-1}$

$$\begin{pmatrix} \prod_{l=j+1}^{N-1} [\mathbf{F}_n^{l,l+1}]^{-1} \end{pmatrix} \begin{pmatrix} -\beta_n^N \tanh(k_n H_N) \\ \beta_n^N \end{pmatrix} = \beta_n^1 \begin{pmatrix} 1 \\ \prod_{l=j}^{N-1} [\mathbf{F}_n^{l,l+1}] \end{pmatrix} \begin{pmatrix} 0 \\ \beta_n^1 \end{pmatrix} - \begin{pmatrix} 0 \\ \frac{2 \sin(k_n x_s)}{n \pi \varepsilon_{j+1}} \end{pmatrix} \quad (\text{V.17})$$

Solving this equation, the values of β_n^1 and β_n^N are known. The parameters of any layer i α_n^i and β_n^i can be derived by:

$$\begin{pmatrix} \alpha_n^i \\ \beta_n^i \end{pmatrix} = \begin{cases} \begin{pmatrix} 1 \\ \prod_{l=i-1}^{N-1} [\mathbf{F}_n^{l,l+1}] \end{pmatrix} \begin{pmatrix} 0 \\ \beta_n^1 \end{pmatrix} & i \leq j \\ \begin{pmatrix} \prod_{l=i}^{N-1} [\mathbf{F}_n^{l,l+1}]^{-1} \end{pmatrix} \begin{pmatrix} -\beta_n^N \tanh(k_n H_N) \\ \beta_n^N \end{pmatrix} & i > j \end{cases} \quad (\text{V.18})$$

Appendix VI. Derivation of Multilayered Green's Function for Magnetostatic

Recall the general solution of Green's function in layer i

$$G^i = \alpha_0^i y + \beta_0^i + \sum_{n=1}^{\infty} [\alpha_n^i \operatorname{ch}(k_n y) + \beta_n^i \operatorname{sh}(k_n y)] \cos(k_n x) \quad (\text{VI.1})$$

and the continuity conditions on the interface between layer i and $i+1$ ($i < 4$)

$$\begin{cases} G^i \Big|_{y=H_i} - G^{i+1} \Big|_{y=0} = 0 \\ \frac{1}{\mu_i} \frac{\partial G^i}{\partial y} \Big|_{y=H_i} - \frac{1}{\mu_{i+1}} \frac{\partial G^{i+1}}{\partial y} \Big|_{y=0} = \delta_{ij} \delta(x - x_s) \end{cases} \quad (\text{VI.2})$$

If $i \neq j$, $\delta_{ij} = 0$. In this case, the Dirac current source does not locate on the interface to analyze. The condition (VI.2) can be expressed by:

$$\begin{cases} \alpha_0^i H_i + \beta_0^i + \sum_{n=1}^{\infty} [\alpha_n^i \operatorname{ch}(k_n H_i) + \beta_n^i \operatorname{sh}(k_n H_i)] \cos(k_n x) = \beta_0^{i+1} + \sum_{n=1}^{\infty} \alpha_n^{i+1} \cos(k_n x) \\ \frac{1}{\mu_i} \left\{ \alpha_0^i + \sum_{n=1}^{\infty} [\alpha_n^i k_n \operatorname{sh}(k_n H_i) + \beta_n^i k_n \operatorname{ch}(k_n H_i)] \cos(k_n x) \right\} = \frac{1}{\mu_i} \left\{ \alpha_0^{i+1} + \sum_{n=1}^{\infty} \beta_n^{i+1} k_n \cos(k_n x) \right\} \end{cases} \quad (\text{VI.3})$$

Based on the equality of the coefficients term by term, the following matrix systems can be derived:

$$\begin{pmatrix} \alpha_0^{i+1} \\ \beta_0^{i+1} \end{pmatrix} = \begin{pmatrix} \frac{\mu_{i+1}}{\mu_i} & 0 \\ H_i & 1 \end{pmatrix} \begin{pmatrix} \alpha_0^i \\ \beta_0^i \end{pmatrix} = [\mathbf{F}_0^{i,i+1}] \begin{pmatrix} \alpha_0^i \\ \beta_0^i \end{pmatrix} \quad (\text{VI.4})$$

$$\begin{pmatrix} \alpha_n^{i+1} \\ \beta_n^{i+1} \end{pmatrix} = \begin{pmatrix} \operatorname{ch}(k_n H_i) & \operatorname{sh}(k_n H_i) \\ \frac{\mu_{i+1}}{\mu_i} \operatorname{sh}(k_n H_i) & \frac{\mu_{i+1}}{\mu_i} \operatorname{ch}(k_n H_i) \end{pmatrix} \begin{pmatrix} \alpha_n^i \\ \beta_n^i \end{pmatrix} = [\mathbf{F}_n^{i,i+1}] \begin{pmatrix} \alpha_n^i \\ \beta_n^i \end{pmatrix} \quad (\text{VI.5})$$

Here the up-going transformation matrix $[\mathbf{F}]$ is similarly defined as for the electrostatic case. Its inverse matrix $[\mathbf{F}^{-1}]$ can also be calculated, as given by:

$$\begin{pmatrix} \alpha_0^i \\ \beta_0^i \end{pmatrix} = \begin{pmatrix} \frac{\mu_i}{\mu_{i+1}} & 0 \\ -\frac{\mu_i}{\mu_{i+1}} H_i & 1 \end{pmatrix} \begin{pmatrix} \alpha_0^{i+1} \\ \beta_0^{i+1} \end{pmatrix} = [\mathbf{F}_0^{i,i+1}]^{-1} \begin{pmatrix} \alpha_0^{i+1} \\ \beta_0^{i+1} \end{pmatrix} \quad (\text{VI.6})$$

$$\begin{pmatrix} \alpha_n^i \\ \beta_n^i \end{pmatrix} = \begin{pmatrix} \text{ch}(k_n H_i) & -\frac{\mu_i}{\mu_{i+1}} \text{sh}(k_n H_i) \\ -\text{sh}(k_n H_i) & \frac{\mu_i}{\mu_{i+1}} \text{ch}(k_n H_i) \end{pmatrix} \begin{pmatrix} \alpha_n^{i+1} \\ \beta_n^{i+1} \end{pmatrix} = [\mathbf{F}_n^{i,i+1}]^{-1} \begin{pmatrix} \alpha_n^{i+1} \\ \beta_n^{i+1} \end{pmatrix} \quad (\text{VI.7})$$

If $i=j$, $\delta_{ij}=1$. In this case, the Dirac current source locates on the studied interface. The condition (VI.2) becomes:

$$\begin{cases} \alpha_0^j H_j + \beta_0^j + \sum_{n=1}^{\infty} [\alpha_n^j \text{ch}(k_n H_j) + \beta_n^j \text{sh}(k_n H_j)] \cos(k_n x) = \beta_0^{j+1} + \sum_{n=1}^{\infty} \alpha_n^{j+1} \cos(k_n x) \\ \frac{1}{\mu_j} \left\{ \alpha_0^j + \sum_{n=1}^{\infty} [\alpha_n^j k_n \text{sh}(k_n H_j) + \beta_n^j k_n \text{ch}(k_n H_j)] \cos(k_n x) \right\} - \frac{1}{\mu_j} \left[\alpha_0^{j+1} + \sum_{n=1}^{\infty} \beta_n^{j+1} k_n \cos(k_n x) \right] = \delta(x - x_s) \end{cases} \quad (\text{VI.8})$$

Integrate the second equation of (VI.8) on $[0, L]$:

$$\frac{L}{\mu_j} \alpha_0^j - \frac{L}{\mu_{j+1}} \alpha_0^{j+1} = 1 \quad (\text{VI.9})$$

Multiply the two sides of the second equation of (VI.8) by $\cos(k_n x)$, and integrate it on $[0, L]$:

$$\frac{1}{\mu_j} \sum_{n=1}^{\infty} [\alpha_n^j \text{sh}(k_n H_j) + \beta_n^j \text{ch}(k_n H_j)] - \frac{1}{\mu_{j+1}} \beta_n^{j+1} = \frac{2}{n\pi} \cos(k_n x_s) \quad (\text{VI.10})$$

Rearrange the equation (VI.9), (VI.10) and the first equation of (VI.8), the following matrix system are obtained:

$$\begin{pmatrix} \alpha_0^{j+1} \\ \beta_0^{j+1} \end{pmatrix} = \begin{pmatrix} \frac{\mu_{j+1}}{\mu_j} & 0 \\ H_j & 1 \end{pmatrix} \begin{pmatrix} \alpha_0^j \\ \beta_0^j \end{pmatrix} + \begin{pmatrix} -\frac{\mu_{j+1}}{L} \\ 0 \end{pmatrix} = [\mathbf{F}_0^{j,j+1}] \begin{pmatrix} \alpha_0^j \\ \beta_0^j \end{pmatrix} + \begin{pmatrix} -\frac{\mu_{j+1}}{L} \\ 0 \end{pmatrix} \quad (\text{VI.11})$$

$$\begin{pmatrix} \alpha_n^{j+1} \\ \beta_n^{j+1} \end{pmatrix} = \begin{pmatrix} \text{ch}(k_n H_j) & \text{sh}(k_n H_j) \\ \frac{\mu_{j+1}}{\mu_j} \text{sh}(k_n H_j) & \frac{\mu_{j+1}}{\mu_j} \text{ch}(k_n H_j) \end{pmatrix} \begin{pmatrix} \alpha_n^j \\ \beta_n^j \end{pmatrix} + \begin{pmatrix} 0 \\ -\frac{2\mu_{j+1}}{n\pi} \cos(k_n x_s) \end{pmatrix} = [\mathbf{F}_n^{j,j+1}] \begin{pmatrix} \alpha_n^j \\ \beta_n^j \end{pmatrix} + \begin{pmatrix} 0 \\ -\frac{2\mu_{j+1}}{n\pi} \cos(k_n x_s) \end{pmatrix} \quad (\text{VI.12})$$

To solve the value of α_0^i , β_0^i , α_n^i and β_n^i , the equations (VI.11) and (VI.12) are solved. On the interface between layers j and $j+1$ ($j < 4$), the following equations hold:

$$\prod_{l=3}^j [\mathbf{F}_0^{l,l+1}]^{-1} \begin{pmatrix} -\frac{\mu_0}{L} \\ \beta_0^4 \end{pmatrix} = \prod_{l=1}^j [\mathbf{F}_0^{l,l+1}] \begin{pmatrix} 0 \\ \beta_0^1 \end{pmatrix} + \begin{pmatrix} -\frac{\mu_{j+1}}{L} \\ 0 \end{pmatrix} \quad (\text{VI.13})$$

$$\prod_{l=3}^j [\mathbf{F}_n^{l,l+1}]^{-1} \begin{pmatrix} \alpha_n^4 \\ -\alpha_n^4 \tanh(k_n H_4) \end{pmatrix} = \prod_{l=1}^j [\mathbf{F}_n^{l,l+1}] \begin{pmatrix} \alpha_n^1 \\ 0 \end{pmatrix} + \begin{pmatrix} 0 \\ -\frac{2\mu_{j+1}}{n\pi} \cos(k_n x_s) \end{pmatrix} \quad (\text{VI.14})$$

It can be shown that $\beta_0^1 = \beta_0^2 = \beta_0^3 = \beta_0^4 = \text{constant}$, which agree with feature of a homogenous Neumann B.C. problem that an arbitrary constant will appear in the final solutions. In this study, they are set to be zero for simplicity. It is explained in the text that their value will not influence the final leakage inductance. Once the values of α_n^1 and α_n^4 are obtained, the following equation is applied to find all the parameters α_0^i , β_0^i , α_n^i and β_n^i .

$$\begin{pmatrix} \alpha_0^i \\ \beta_0^i \end{pmatrix} = \begin{cases} \begin{pmatrix} 0 \\ 0 \end{pmatrix} & i \leq j \\ \left(\prod_{l=i}^{N-1} [\mathbf{F}_0^{l,l+1}]^{-1} \right) \begin{pmatrix} -\frac{\mu_0}{L} \\ 0 \end{pmatrix} & i > j \end{cases} \quad (\text{VI.15})$$

$$\begin{pmatrix} \alpha_n^i \\ \beta_n^i \end{pmatrix} = \begin{cases} \left(\prod_{l=i-1}^1 [\mathbf{F}_n^{l,l+1}] \right) \begin{pmatrix} \alpha_n^1 \\ 0 \end{pmatrix} & i \leq j \\ \left(\prod_{l=i}^{N-1} [\mathbf{F}_n^{l,l+1}]^{-1} \right) \begin{pmatrix} \alpha_n^4 \\ -\alpha_n^4 \tanh(k_n H_4) \end{pmatrix} & i > j \end{cases} \quad (\text{VI.16})$$

References

- [1] R. Chen, J. V. Wyk, S. Wang et W. Odendaal, "Improving the Characteristics of integrated EMI filters by embedded conductive Layers," *IEEE Trans. Power Electron.*, vol. 20, p. 610–619, May 2004.
- [2] J. Biela, A. Wirthmueller, R. Waespe, M. Heldwein, K. Raggl et J. Kolar, "Passive and Active Hybrid Integrated EMI Filters," *Power Electronics, IEEE Transactions on*, vol. 24, pp. 1340–1349, May 1999.
- [3] M. Ali, E. Labouré, F. Costa et B. Revol, "Design of a Hybrid Integrated EMC Filter for a DC–DC Power Converter," *IEEE Trans. Power Electron.*, vol. 27, p. 4380–4390, Nov. 2012.
- [4] H. Ott, *Electromagnetic Compatibility Engineering*, NJ, USA: John Wiley & Sons, Inc., 2009.
- [5] J.-L. Cocquerelle, *C.E.M et Electronique de Puissance*, Paris: Edition Technip, 1999.
- [6] C. Paul, *Introduction to Electromagnetic Compatability*, 2nd éd., NJ, USA: John Wiley & Sons, Inc., 2006.
- [7] C.I.S.P.R., *Information Technology Equipment—Radio Disturbance Characteristics—Limits and Methods of Measurement—Publication 22*, Geneva, Switzerland, 1997.
- [8] K. Mainali et R. Oruganti, "Conducted EMI Mitigation Techniques for Switch-Mode Power Converters: A Survey," *IEEE Trans. Power Electron.*, vol. 25, p. 2344–2356, Sep. 2010.
- [9] H. Chung, S. Hui et K. Tse, "Reduction of power converter EMI emission using soft-switching technique," *IEEE Trans. Electromagn. Compat.*, vol. 40, p. 282–287, Aug. 1998.
- [10] X. Wu, J. Yang, H. Chen et Z. Qian, "Analysis and design considerations for EMI and losses of RCD snubber in flyback converter," in *Proceeding of Twenty-Fifth Annual IEEE Applied Power Electronics Conference and Exposition*, Palm Springs, CA, 2010.
- [11] J. Balcells, A. Santolaria, A. Orlandi, D. Gonzalez et J. Gago, "EMI reduction in switched power converters using frequency Modulation techniques," *IEEE Trans. Electromagn. Compat.*, vol. 47, p. 569–576, 2005.
- [12] Y.-C. Son et S.-K. Sul, "Generalization of active filters for EMI reduction and harmonics compensation," *IEEE Trans. Ind. App.*, vol. 42, p. 545–551, Apr. 2006.
- [13] A. Roc'h, R. Iannarelli, F. Leferink "New materials for inductors," in *Proceeding of International Symposium on Electromagnetic Compatibility - EMC Europe*, Athens, 1999.
- [14] M. Hartmann, H. Ertl et J. Kolar, "EMI Filter Design for a 1 MHz, 10 kW Three-Phase/Level PWM Rectifier," *IEEE Trans. Power Electron.*, vol. 26, p. 1192–1204, Apr. 2011.
- [15] Y. Maillet, R. Lai, S. Wang, F. Wang, R. Burgos et D. Boroyevich, "High-Density EMI Filter Design for DC-Fed Motor Drives," *IEEE Trans. Power Electron.*, vol. 25, p. 1163–1172, May 2010.

- [16] B. Toure, J. Schanen, L. Gerbaud, T. Meynard, J. Roudet et R. Ruelland, "EMC Modeling of Drives for Aircraft Applications: Modeling Process, EMI Filter Optimization and Technological choice," *IEEE Trans. Power Electron.*, 2013 - To be published.
- [17] F. Shih, D. Chen, Y. Wu et Y. Chen, "A procedure for designing EMI filters for AC line applications," *IEEE Trans. Power Electron.*, vol. 11, p. 170–181, Jan. 1996.
- [18] D. Zhang, D. Chen, M. Nave et D. Sable, "Measurement of noise source impedance of off-line converters," *IEEE Trans. Power Electron.*, vol. 15, p. 820–825, Sep. 2000.
- [19] V. Tarateeraseth, B. Hu, K. Y. See et F. G. Canavero, "Accurate Extraction of Noise Source Impedance of an SMPS Under Operating Conditions," *IEEE Trans. Power Electron.*, vol. 25, p. 111–117, Jan. 2010.
- [20] V. Tarateeraseth, Y. Kye, F. Canavero et R. Chang, "Systematic Electromagnetic Interference Filter Design Based on Information From In-Circuit Impedance Measurements," *IEEE Trans. Electromagn. Compat.*, vol. 52, p. 588–598, Aug. 2010.
- [21] S. Wang, F. Lee, D. Chen et W. Odendaal, "Effects of parasitic parameters on EMI filter performance," *IEEE Trans. Power Electron.*, vol. 19, p. 869–877, May 2004.
- [22] Ferroxcube Inc., "Data Handbook Soft Ferrites and Accessories," 08 2011. [online]. Available: <http://www.ferroxcube.com/>. [Access: 2012 Sep.].
- [23] Coil Winding Specialist, Inc., "MPP, Sendust, Kool Mu[®], High Flux and Iron Powder Core Properties and Selection Guide," Jan. 2008. [online]. Available: http://www.coilws.com/index.php?main_page=page&id=49. [Access: 2012 Jul.].
- [24] K. Zhao, "Magnetic Components in Switched Mode Power Supply," Nanjing University of Aeronautics and Astronautics, Nanjing, 2004.
- [25] ITACA Srl., "Samwha catalogue of ferrite cores," [online]. Available: <http://www.itacasrl.it/>. [Access 2012 Sep.].
- [26] F. Forest, E. Laboure, T. Meynard et M. Arab, "Analytic Design Method Based on Homothetic Shape of Magnetic Cores for High-Frequency Transformers," *IEEE Trans. Power Electron.*, vol. 22, pp. 2070–2080, May. 2007.
- [27] S. Wang et C. Xu, "Design Theory and Implementation of Planar EMI Filter Based on Annular Integrated Inductor-Capacitor Unit," *IEEE Trans. Power Electron.*, 2013-To be published.
- [28] A.-M. Sánchez, A. Pérez, J. Regué, M. Ribó, P. Rodríguez-Cepeda et F. J. Pajares, "A Modal Model of Common-Mode Chokes for Conducted Interference Prediction," *IEEE Trans. Electromagn. Compat.*, vol. 52, p. 749–752, Aug. 2010.
- [29] S. Wang, F. C. Lee et W. G. Odendaal, "Characterization and Parasitic Extraction of EMI Filters Using Scattering Parameters," *IEEE Trans. Power Electron.*, vol. 20, p. 502–510, Mar. 2005.
- [30] J.-L. Kotny, X. Margueron et N. Idir, "High Frequency Model of the coupled inductors used in EMI Filters," *IEEE Trans. Power Electron.*, vol. 27, p. 2805–2812, Jun. 2012.
- [31] A. Watson, D. Melendy, P. Francis, K. Hwang et A. Weisshaar, "A comprehensive compact-modeling methodology for spiral inductors in silicon-based RFICs," *IEEE Trans. Microwave Theory Tech.*, vol. 52, p. 849–857, Mar. 2004.
- [32] C. Coelho, J. Phillips et L. Silveira, "A convex programming approach for generating guaranteed passive approximations to tabulated frequency-data," *IEEE Trans. Computer-Aided Design*, vol. 23, pp. 293–301, Feb. 2004.
- [33] M. Kovacic, Z. Hanic, S. Stipetic, S. Krishnamurthy et D. Zarko, "Analytical

- Wideband Model of a Common-Mode Choke," *IEEE Trans. Power Electron.*, vol. 27, p. 3173–3185, Jul. 2012.
- [34] R. Garg, *Analytical and Computational Methods in Electromagnetics*, London: Artech House, 2008.
- [35] L. Zhao et J. van Wyk, "Wideband modeling of integrated power passive structures: the series resonator," *IEEE Trans. Power Electron.*, vol. 19, p. 523–530, Mar. 2004.
- [36] F. Stellari et A. Lacaita, "New formulas of interconnect capacitances based on results of conformal mapping method," *IEEE Trans. Electron Device*, vol. 47, p. 222–231, Jan. 2000.
- [37] W. Zhao, X. Li, S. Gu, S. Kang, M. Nowak et Y. Cao, "Field-Based Capacitance Modeling for Sub-65-nm On-Chip Interconnect," *IEEE Trans. Electron Devices*, vol. 56, p. 1862–1872, Sep. 2009.
- [38] R. Chen, W. S., J. van Wyk et W. Odendaal, "Integration of EMI filter for distributed power system (DPS) front-end converter," in *Proceeding of IEEE 34th Annual Power Electronics Specialist Conference*, 2003.
- [39] X. Margueron, A. Besri, P.-O. Jeannin, J.-P. Keradec et G. Parent, "Complete Analytical Calculation of Static Leakage Parameters: A Step Toward HF Transformer Optimization," *IEEE Trans. Ind. App.*, vol. 46, p. 1055–1063, May 2010.
- [40] X. Margueron, J.-P. Keradec et D. Magot, "Analytical Calculation of Static Leakage Inductances of HF Transformers Using PEEC Formulas," *IEEE Trans. Ind. App.*, vol. 43, p. 884–892, Jul. 2007.
- [41] A. Schellmanns, K. Berrouche et J.-P. Keradec, "Multiwinding transformers: a successive refinement method to characterize a general equivalent circuit," *IEEE Trans. Instrum. Meas.*, vol. 47, p. 1316–1321, Oct. 1998.
- [42] R. Pintelon, P. Guillaume, Y. Rolain, J. Schoukens et H. Van Hamme, "Parametric identification of transfer functions in the frequency domain—a survey," *IEEE Trans. Autom. Control*, vol. 39, p. 2245–2260, Nov. 1994.
- [43] J. Nocedal et S. J. Wright, *Numerical Optimization*, New York, USA: Springer-Verlag New York, Inc., 1999.
- [44] E. Levy, "Complex-curve fitting," *IRE Trans. Automat. Contr.*, Vols. AC-4, p. 37–44, 1959.
- [45] M. Elzinga, K. Virga, L. Zhao et J. L. Prince, "Pole-residue formulation for transient simulation of high-frequency interconnects using householder LS curve-fitting techniques," *IEEE Trans. Adv. Packag.*, vol. 25, p. 142–147, May 2000.
- [46] W. Press, S. Teukolsky, W. Vetterling et B. Flannery, *Numerical Recipes: The Art of Scientific Computing*, 3rd éd., New York, USA: Cambridge University Press, 2007.
- [47] C. K. Sanathanan et J. Koerner, "Transfer function synthesis as a ratio of two complex polynomials," *IEEE Trans. Autom. Control*, Vols. AC-8, p. 56, Jan. 1963.
- [48] B. Gustavsen et A. Semlyen, "Rational approximation of frequency domain responses by vector fitting," *IEEE Trans. Power Deliv.*, vol. 14, p. 1052–1061, Jul. 1999.
- [49] G. Antonini, "Spice equivalent circuits of frequency domain responses," *IEEE Trans. Electromagn. Compat.*, vol. 45, p. 502–512, Aug. 2003.
- [50] Z. Ye et Z. Yu, "Passive-assured rational function approach for compact modeling of on-chip passive components," in *Proceeding of International Conference on Solid-State and Integrated Circuits Technology*, 2004.

- [51] S. Prabhakaran et C. Sullivan, "Impedance-analyzer measurements of high-frequency power passives: techniques for high power and low impedance," in *Proceeding of 37th Industry Application Society Annual Meeting*, Pittsburgh, USA, 2002.
- [52] S. Mei et Y. Ismail, "Modeling skin and proximity effects with reduced realizable RL circuits," *IEEE Trans. VLSI Systems*, vol. 12, p. 437–447, Apr. 2004.
- [53] B. Gustavsen et A. Semlyen, "Enforcing passivity for admittance matrices approximated by rational functions," *IEEE Trans. Power Systems*, vol. 16, p. 97–104, Jan. 2001.
- [54] The Institute for Interconnecting and Packaging, "Controlled Impedance Circuit Boards and High Speed Logic Design Electronic Circuits," IPC, Northbrook, Illinois, USA, 1996.
- [55] A. Schellmanns, P. Fouassier, J.-P. Keradec et J.-L. Schanen, "Equivalent circuits for transformers based on one-dimensional propagation: accounting for multilayer structure of windings and ferrite losses," *IEEE Trans. Magn.*, vol. 36, p. 3778–3784, Sep. 2000.
- [56] K. S. Kostov et J. Kyrrä, "Insertion loss in terms of four-port network parameters," *IET Science, Measurement and Technology*, vol. 3, p. 208–216, May 2009.
- [57] P. Triverio, S. Grivet-Talocia, M. Nakhla, F. Canavero et R. Achar, "Stability, Causality, and Passivity in Electrical Interconnect Models," *IEEE Trans. Adv. Packag.*, vol. 30, p. 795–808, Nov. 2007.
- [58] D. Saraswat, R. Achar et M. Nakhla, "Global passivity enforcement algorithm for macromodels of interconnect subnetworks characterized by tabulated data," *IEEE Trans. VLSI Systems*, vol. 13, p. 819–832, Jul. 2005.
- [59] H. Chen, Z. Qian, Y. S. et C. Wolf, "Finite-Element Modeling of Saturation Effect Excited by Differential-Mode Current in a Common-Mode Choke," *IEEE Trans. Power Electron.*, vol. 24, pp. 873–877, Mar. 2009.
- [60] F. Luo, S. Wang, W. F., D. Boroyevich, N. Gazel, K. Y. et A. Baisden, "Analysis of CM Volt-Second Influence on CM Inductor Saturation and Design for Input EMI Filters in Three-Phase DC-Fed Motor Drive Systems," *IEEE Trans. Power Electron.*, vol. 25, pp. 1905–1914, Jul. 2010.
- [61] W. Tan, C. Cuellar, X. Margueron et N. Idir, "A High Frequency Equivalent Circuit and Parameter Extraction Procedure for Common Mode Choke in EMI Filter," *IEEE Trans. Power Electron.*, 2013 - To be published.
- [62] T. Sakurai et K. Tamaru, "Simple formulas for two- and three-dimensional capacitances," *IEEE Trans. Electron Devices*, vol. 30, pp. 183–185, Feb. 1983.
- [63] P. Chan, C. Lee et S. Hui, "Stray capacitance calculation of coreless planar transformers including fringing effects," *Electronics Letters*, vol. 43, Nov. 2007.
- [64] E. Carlsson et S. Gevorgian, "Conformal mapping of the field and charge distributions in multilayered substrate CPWs," *IEEE Trans. Microwave Theory and Tech.*, vol. 47, pp. 1544–1552, Aug 1999.
- [65] C.-H. Wan et J.-X. Zheng, "Accurate solution of periodic microstrips for digital applications," *IEEE Trans. Microwave Theory and Tech.*, vol. 51, pp. 1003–1008, Mar. 2003.
- [66] Z. Nehari, *Conformal Mapping*, New York, USA: Dover Publication, Inc., 1952.
- [67] P. Olver, *Introduction to Partial Differential Equations*, Minnesota, USA, 2012.
- [68] K. Suzuki, "Parasitic capacitance of submicrometer MOSFET's," *IEEE Trans. Electron Devices*, vol. 46, pp. 1895–1900, Sep. 1999.

- [69] A. Bansal, B. Paul et K. Roy, "Modeling and optimization of fringe capacitance of nanoscale DGMOS devices," *IEEE Trans. Electron Devices*, vol. 52, n° 1256–262, Feb. 2005.
- [70] F. Stellari et A. Lacaita, "New formulas of interconnect capacitances based on results of conformal mapping method," *IEEE Trans. Electron Devices*, vol. 47, pp. 222–231, Jan. 2000.
- [71] B. A., P. B.C. et R. K., "An Analytical Fringe Capacitance Model for Interconnects Using Conformal Mapping," *IEEE Trans. Comput.-Aided Design Integr. Circuits Syst.*, vol. 25, pp. 2765–2774, Dec. 2006.
- [72] W. Tan, X. Margueron, T. Duquesne et N. Idir, "Approche Energétique pour le Calcul en 3D des Capacités Parasites des Composants Planar," in *Proceeding of Electronique de Puissance du Futur*, Bordeaux, 2012.
- [73] R. Huang et D. Zhang, "Experimentally Verified Mn–Zn Ferrites' Intrinsic Complex Permittivity and Permeability Tracing Technique Using Two Ferrite Capacitors," *IEEE Trans. Magn.*, vol. 43, pp. 974–981, 2007.
- [74] I. Lindell et A. Sihvola, "Transformation method for problems involving perfect electromagnetic conductor (PEMC) structures," *IEEE Trans. Antennas Propag.*, vol. 53, pp. 3005–3011, Sep. 2005.
- [75] W. Tan, X. Margueron, T. Duquesne et N. Idir, "An Improved Parasitic Capacitance Cancellation Method for Planar Differential Mode Inductor in EMI Filters," in *Proceeding of 7th International Conference on Integrated Power Electronics Systems*, Nuremberg, Germany, 2012.
- [76] A. Zolfaghari, A. Chan et B. Razavi, «Stacked inductors and transformers in CMOS technology," *IEEE J. Solid-State Circuits*, vol. 36, pp. 620–628, Apr. 2001.
- [77] C. Cuellar, W. Tan, X. Margueron, A. Benabou et N. Idir, "Measurement method of the complex magnetic permeability of ferrites in high frequency," in *Proceeding of IEEE International Instrumentation and Measurement Technology Conference*, Graz, Aus., 2012.
- [78] G. Arfken et H. Weber, *Mathematical Methods for Physicists*, 6th éd., Burlington, MA, USA: Elsevier Inc., 2005.
- [79] K. Li, K. Atsuki et T. Hasegawa, "General analytical solutions of static Green's functions for shielded and open arbitrarily multilayered media," *IEEE Trans. Microwave Theory. and Tech.*, vol. 45, p. 2–8, Jan. 1997.
- [80] H. N. B. Ymeri et K. Maex, "Computation of capacitance matrix for integrated circuit interconnects using semi-analytic Green's function method," *Integration, the VLSI Journal*, vol. 30, p. 55–63, Nov. 2000.
- [81] J. Zheng et Z. Li, "Efficient parameter computation of 2-D multiconductor interconnection lines in layered media by convergence acceleration of dielectric Green's function via Padé approximation," *IEEE Trans. Microwave Theory and Tech.*, vol. 46, pp. 1339–1343, Sep. 1998.
- [82] S. Singh et R. Singh, "On the use of Chebyshev-Toeplitz algorithm in accelerating the numerical convergence of infinite series," *IEEE Trans. Microwave Theory and Tech.*, vol. 40, pp. 171–173, Jan. 1992.
- [83] P. Dowell, "Effects of eddy currents in transformer windings," *Proceedings of the Institution of Electrical Engineers*, vol. 113, pp. 1387–1394, Aug. 1966.
- [84] Z. Ouyang, O. Thomsen et M. Andersen, "The analysis and comparison of leakage inductance in different winding arrangements for planar transformer," in *Proceeding of International Conference on Power Electronics and Drive Systems*, Taipei, 2009.

- [85] C. K. Lee, Y. Su et S. Hui, "Printed Spiral Winding Inductor With Wide Frequency Bandwidth," *IEEE Trans. Power Electron.*, vol. 26, pp. 2936–2945, Oct. 2012.
- [86] S. Wang, F. Lee et J. van Wyk, "Inductor winding capacitance cancellation using mutual capacitance concept for noise reduction application," *IEEE Trans. Power Electron.*, vol. 48, pp. 311–318, May 2006.
- [87] S. Wang, F. Lee, J. van Wyk et J. van Wyk, "A Study of Integration of Parasitic Cancellation Techniques for EMI Filter Design With Discrete Components," *IEEE Trans. Power Electron.*, vol. 23, pp. 3094–3102, Nov. 2008.
- [88] X. Wu, D. Xu, Z. Wen, Y. Okuma et K. Mino, "Design, Modeling, and Improvement of Integrated EMI Filter With Flexible Multilayer Foils," *IEEE Trans. Power Electron.*, vol. 26, p. 1344–1354, May 2011.
- [89] P. Boonma, V. Tarateeraseth et W. Khan-ngern, "A new technique of integrated EMI inductor using optimizing inductor-volume approach," in *Proceeding of International Power Electronic Conference*, 2005.
- [90] R. Lai, Y. Maillet, F. Wang, S. Wang, R. Burgos et D. Boroyevich, "An integrated EMI choke for differential-mode and common-mode noises suppression," *IEEE Trans. Power Electron.*, vol. 25, p. 539–544, Mar. 2010.
- [91] F. Luo, D. Boroyevich, P. Mattevelli, K. Ngo, D. Gilham et N. Gazel, "An integrated common mode and differential mode choke for EMI suppression using magnetic epoxy mixture," in *Proceeding of Twenty-Sixth Annual IEEE Applied Power Electronics Conference and Exposition*, Fort Worth, TX, USA, 2011.
- [92] M. Nave, "On modeling the common mode inductor," *Proc. IEEE Trans. Electromagn. Compat.*, p. 452–457, 1991.
- [93] T. Chailloux, M. Raulet, C. Martin, C. Joubert, F. Sixdenier et L. Morel, "Magnetic Behavior Representation Taking Into Account the Temperature of a Magnetic Nanocrystalline Material," *IEEE Trans. Magn.*, vol. 48, pp. 455–458, Feb. 2012.
- [94] W. Tan, C. Cuellar, X. Margueron et N. Idir, "A Common-Mode Choke Using Toroid-EQ Mixed Structure," *IEEE Trans. Power Electron.*, vol. 28, pp. 31–35, Jan. 2013.
- [95] Magnetec, Inc, "Product specification for inductive components: M-307," Oct. 2006. [online]. Available: <http://www.magnetec.us>.
- [96] EPCOS, Inc., "Ferrites and accessories," Sep. 2006. [online]. Available: <http://www.epcos.de>.
- [97] A. Fuchs, W. Tan, X. Margueron et N. Idir, "Méthodologie et Logiciel pour l'Identification Automatique des Schémas Equivalents de Composants Magnétiques," in *Proceeding of Electronique de Puissance du Futur*, Bordeaux, France, 2012.

Remerciements

Les remerciements sont la dernière chose à faire pour terminer ce manuscrit. Ça me fait encore plus de plaisir d'écrire cette partie que les autres... même si je pense qu'il est toujours difficile de synthétiser les remerciements de manière complète et en français ! Cette thèse a abouti grâce à de nombreuses personnes, et pardonnez-moi si je vous oublie dans ce texte.

J'ai l'honneur d'avoir eu un jury dont les membres sont très reconnus dans divers domaines de la recherche en Electronique de puissance et en Compatibilité Electromagnétique. Je tiens à remercier tout d'abord M. Forest, Professeur des universités à l'Université de Montpellier 2, pour avoir présidé le jury de ma soutenance de thèse. Ensuite, je remercie M. Labouré, Professeur des universités à l'Université de Paris SUD 11 et M. Schanen, Professeur des universités à l'Institut Polytechnique de Grenoble, pour avoir rapporté sur mon mémoire de thèse et pour les diverses questions et remarques qu'ils ont apportées sur ces travaux ainsi que sur le manuscrit. Je voudrais aussi remercier M. Schellmanns, Maître de conférences à l'Université de Tours et M. Martin, Maître de conférences de l'Université de Lyon 1, pour avoir examiné mes travaux et participé à ma soutenance.

Je souhaite remercier sincèrement mon encadrant M. Margueron, pour sa gentillesse, ses conseils scientifiques, les nombreux heures passées avec moi et aussi les innombrables corrections de Français qu'il a faites pour moi (y compris ces remerciements...) pendant ces trois années passées. De 4 ans plus âgé que moi, Xavier est une personne très dynamique et passionnée par la recherche, la musique et la bière. Je suis très heureux de l'avoir connu et d'avoir travaillé avec lui pour ma thèse.

Je voudrais adresser mes remerciements chaleureux à mon directeur de thèse, M. Idir, pour son soutien et sa disponibilité, pour toutes les questions, idées et remarques scientifiques et techniques qu'il m'a données mais aussi pour toute l'aide qu'il m'a offerte pendant ma thèse. En tant que directeur de thèse, Nadir non seulement m'a dirigé avec sa grande compétence dans sa spécialité de recherche, mais m'a aussi donné de nombreux conseils pertinents pour ma carrière.

Je voudrais exprimer mes remerciements à M. Duquesne et M. Thomy pour toutes les cartes de circuits imprimés qu'ils ont tirés, ainsi qu'à M. Cimetière, pour son assistance technique dans le laboratoire.

Mes remerciements vont à mes collègues de bureau, François, Sophie, Laurent, Ye, Dimitry, Rija, Vera, Pierre, Patricio; à mes collègues au laboratoire P2, Ke, Carlos et Clément, ainsi qu'à tous mes collègues du L2EP, pour leur amitié et l'ambiance très agréable de travail.

J'aimerais également remercier tous mes amis chinois avec qui j'ai eu la chance de partager cette expérience de vie en France. Les nombreux voyages et soirées qu'on a faits seront toujours de bons trésors gardés dans mes souvenirs.

Ces remerciements ne seraient pas complets sans pensées pour ma copine, Yue, pour m'avoir soutenu et poussé pendant la rédaction et la période de soutenance. Je suis heureux de l'avoir rencontrée à Lille et d'écrire une nouvelle page de ma vie, avec elle, en Chine.

Enfin, un immense merci à mes parents, pour m'avoir donné la vie, nourri, cultivé et surtout, pour m'avoir tout le temps soutenu, encouragé et m'avoir fait confiance. Sans eux, cette thèse n'aurait jamais pu voir le jour.

Modélisation et Conception des Composants Passifs Planar pour Filtres CEM

Résumé: Les composants magnétiques en technologie planar répondent aux exigences actuelles de l'Electronique de Puissance (EP), à savoir la montée en fréquence de commutation des structures d'EP et la réduction du volume des convertisseurs. La première tendance impose des contraintes fortes en termes de compatibilité électromagnétique (CEM) des équipements. Ces dernières doivent être prises en compte par les ingénieurs dès la phase conception des convertisseurs en se basant sur des modèles fiables, peu développés pour les composants planar dans la littérature scientifique.

Ce travail de thèse porte ainsi sur la modélisation des composants planar pour applications aux filtres CEM. Différentes méthodes sont développées au cours de cette thèse pour arriver à évaluer de manière fine les éléments parasites des inductances planar de mode commun : capacités parasites et inductances de fuite. Une partie du travail a porté sur la modélisation par circuits équivalents du comportement fréquentiel des inductances de MC. Une approche automatisée, basée sur un algorithme de fitting a ainsi été développée pour élaborer des circuits équivalents fiables et robustes. Des approches analytiques (Décomposition du Champ Electrique) et semi-analytiques (Fonctions de Green) ont aussi été proposées pour évaluer les valeurs des éléments parasites. La dernière partie de la thèse est plus orientée conception, avec la réalisation de deux structures de composants innovantes, la première se basant sur une technique de compensation des capacités parasites à l'aide d'éléments parasites structuraux et la seconde sur l'association de deux noyaux magnétiques, possédants matériaux et géométries différentes.

Mots-clés: Modélisation analytique, inductance de mode commun, filtre compatibilité électromagnétique, circuit équivalent, intégration, inductance de fuite, capacité parasite, composant planar.

Modeling and Design of Passive Planar Components for EMI Filters

Abstract: The magnetic components with planar technology join in the current trends in Power Electronics (PE), namely increasing the switching frequency of PE structures and reducing the size of the power converters. The first tendency imposes strong constraints in terms of electromagnetic compatibility of equipments. The latter has to be considered by engineers at the beginning of the design of Power converters on the basis of reliable models, which are not sufficiently developed for planar components in scientific literature.

This PhD work thereby focuses on the modeling of planar components for the applications of EMI filters. Different methods are developed during this study in order to accurately evaluate the parasitic elements of planar common-mode chokes: parasitic capacitances and leakage inductances. A part of this dissertation concerns the equivalent circuit modeling of the frequency behavior of CM chokes. An automated approach, based on a fitting algorithm developed for elaborating reliable and robust equivalent circuits. Analytical approaches (Electric Field Decomposition) and semi-analytical (Green's Function) are proposed as well for calculating the values of these parasitic elements. The last part of this dissertation is oriented to conception, with the realization of two structures of innovative components, the first one based on a parasitic capacitance cancellation technique using structural parasitic elements and the second one on the association of two magnetic cores with different materials and geometries.

Keywords: Analytical modeling, common-mode choke, electromagnetic filter, equivalent circuit, integration, leakage inductance, parasitic capacitance, planar component